Structure and properties of ice templated macroporous particle-polymer hybrid assemblies

Thesis Submitted to AcSIR for the Award of
the Degree of
DOCTOR OF PHILOSOPHY
in Engineering Sciences

By

Karthika S
Reg. No. 20EE13A26046

Under the Guidance of
Dr. Guruswamy Kumaraswamy

Polymer Science and Engineering Division

CSIR-National Chemical Laboratory,
Pune-411008, India

JULY, 2018

सीएसआयआर–राष्ट्रीय रासायनिक प्रयोगशाला
(वैज्ञानिक तथा औद्योगिक अनुसंधान परिषद)
डॉ. होमी भाभा मार्ग, पुणे – 411 008. भारत
CSIR-NATIONAL CHEMICAL LABORATORY
(Council of Scientific & Industrial Research)
Dr. Homi Bhabha Road, Pune - 411008. India

CERTIFICATE

This is to certify that the work incorporated in this Ph.D. thesis entitled **"Structure and properties of ice templated macroporous particle-polymer hybrid assemblies"** submitted by **Ms. Karthika S** to Academy of Scientific and Innovative Research (AcSIR) in fulfilment of the requirement for the award of the Degree of **Doctor of Philosophy**, embodies original research work under my guidance. We further certify that this work has not been submitted to any other University or Institution in part or full for the award of any degree or diploma. Research material obtained from other sources has been duly acknowledged in the thesis. Any text, illustration, table etc., used in the thesis from other sources have been duly cited and acknowledged.

Karthika S

Reg. No. **20EE13A26046**

Dr. Guruswamy Kumaraswamy

(Research Supervisor)

Date: 31 July 2018

Place: Pune

Communications Channels
NCL Level DID : 2590
NCL Board No. : +91-20-25902000
Four PRI Lines : +91-20-25902000
FAX
Director's Office : +91-20-25902601
COA's Office : +91-20-25902660
SPO's Office : +91 20 25902664
WEBSITE
www.ncl-india.org

DECLARATION BY RESEARCH SCHOLAR

I hereby declare that the thesis entitled **"Structure and properties of ice templated macroporous particle-polymer hybrid assemblies"** submitted by me for the Degree of Doctor of Philosophy to Academy of Scientific & Innovative Research (AcSIR) is the record of work carried out by me at Polymer Sciences & Engineering Division (PSE), CSIR-National Chemical Laboratory, Pune - 411008, India, under the supervision of Dr. Guruswamy Kumaraswamy (research supervisor). The work is original and has not formed the basis for the award of any degree, diploma, associateship and fellowship titles in this or any other university or other institute of higher learning. I further declare that the material obtained from other resources has been duly acknowledged in the thesis.

Karthika S

July 2018

Polymer Science & Engineering Division
CSIR-National Chemical Laboratory
Dr. Homi Bhabha Road, Pashan
Pune – 411008
Maharashtra, India

Dedicated to:

Badrinath A Menon

Dr. Malik Abdul Wahid

Adv. Radhamani Mariyil

Acknowledgement

It is a matter of pride and honour for me to be in a position to write this acknowledgement for all the people who have directly or indirectly contributed towards achieving this ultimate academic goal.

First and foremost in the list is my ever supporting family. I am hugely indebted to my family members for elevating me to the position I am at present. My parents pertinacious efforts to ensure my quality education towards realisation of this big goal of mine, finds no other match. I am highly indebted to my dear 'Achan- Suresh N N' and 'Amma- Saraswathy V T'. I am extremely thankful to my 'Brother-Anish S' for being a very strong support throughout this journey. I am equally thankful to my 'Sister-in-law- Aswathy' for her excellent comradeship. It will be all worthless if I fail to pay thanks to my dearest little 'Badri' for making this period far so pleasant.

My earnest, deepest and most sincere thanks to my supervisor Dr. Guruswamy Kumaraswamy for nurturing me to the level I am at present. Dr. Guru possesses a sparkling persona with a lot to emulate. I am extremely thankful to him for his concerns and inputs for changing a raw science student to a well grown researcher. I strongly acknowledge him for his rigorous training on how to define a scientific problem, how to think for solving that problem, how to design an experiment, how to critically analyse the results, how to write a scientific paper and how to present our work to a specific and to a general community. I would also like to thank him for funding numerous conferences and also for his patience with me. His classes on SAXS and Polymer physics were really helpful to build my basics in those subjects.

I express my gratitude to my collaborators for letting me a free hand on the sophisticated instrumentation in their respective labs. I express my sincere gratitude towards Dr. P R Rajamohanan, Dr. T G Ajith Kumar and Athulya (NMR team at NCL) for their support with NMR. I am equally thankful to Prof. Shivprasad Patil (IISER-Pune) for AFM facilities and timely discussions. I am extremely grateful to Prof. Arindam Chowdhury (Single particle tracking, IIT Bombay) for access to fluorescence microscope and also for teaching me the basics of single particle tracking. I am equally thankful to Dr. V K Aswal, Dr. Sugam Kumar and Dr. Debes Roy from BARC-Mumbai for allowing SANS measurements and also for many fruitful discussions. I

would also like to thank Prof. Basavaraj Madivala Gurappa, Dr. Venkateshwar Rao Dugyala, Hisay Lama from IIT Madras for their help in the synthesis of Hematite particles of different shapes and sizes. I would like to specially thank Dr. Ravi Kumar (CSIR-NCL) for helping me with wavelet transform. I deeply acknowledge him for his patience to teach me the basics of wavelet transform. I would also like to thank Dr. M V Badiger, Arun Torris, Fayis K P for access to X-ray computed micro-tomography instrument and also for giving me an opportunity to learn tomography image analysis and GeoDict software. I would also like to thank Drs. Kadhiravan Shanmuganathan, and Sreekumar Kurungot (CSIR-NCL) Dr. Rahul Banerjee (IISER-Kolkata), Prof. David Diaz Diaz and Marleen Haring (University of Regensburg), Prof. Nicholas Kotov (University of Michigan) for involving me also in their various projects. These collaborations gave (or giving) me lot of insights about various fields.

I extend my gratitude to the doctoral advisory committee for guiding my way through to the final stage. Dr. Mugdha Gadgil, Dr. T G Ajith Kumar, Dr. Ashish Orpe and Dr. Sayam Sengupta (IISER- Kolkata) have been really helpful throughout this period and have contributed through their timely discussions and valuable suggestions. Thanks all for being there whenever I needed the professional guidance.

Special thanks to my NCL Technology and Entrepreneurship Club (NCL-TEC) headed by Dr. Premnath Venugopal and Dr. Soma Chattopadhyay. It was really an ideal platform to learn how a lab scale science can be taken into market as well as to the society. The student associates involving Aniket Thosar, Bhagyasree, Ramendra Pandey, Pravin Shinde, Emmanual Joseph and Viswanath were fantastic to work with. Another platform of equal importance which I can't hold without a mention here is our team of Aspiring Saturday's. Thanks a lot guys for allowing me a free entry and opportunity to speak in front of you. I would like to extend my thanks to Sachin Dubey, Maya and Usman (Module Innovations, Pune team) and Poonam Yadav for letting me in.

I would like to pay my sincere thanks to my professional colleagues: Kiran K J (special thanks to him for directing me to NCL and to the Dr. Guru's lab), Drs. Ramya C and Dharmendar Kumar Sharma (for helping me with epifluorescence microscopy at IIT Bombay), Amandeep (IISER Pune) for many fruitful discussions about AFM and its basics, Dr.Anees, Dr. Venugopal Edakkal, Anju Julius, Dr. Yogesh Gawli (thanks for your all support; technical as well as intellectual), Dr. Dhanya Puthussery, Dr. Rounak Naphade (for his initial guidance for the project "compressible piezoelectric

materials from ice templating"), Dr. Soumyajyoti Chatterjee (for his all the academic guidance), Yogesh Marathe, Dr. Mohan Raj Mani, Harshal (for the technical help with SEM), Sonal, Dr. Amey, Abdul Khayum (being a student collaborator of late), Saurabh Usgaonkar (for being a collaborator of the recent 3D printing project). Aakash Sharma and Bipul Biswas (for being helpful labmates and help regarding arrangement of comfortable and safe journey and stay during our trip to US for APS March meeting); Dr.Amruta Kulkarni, Dr. Samruddhi Kamble, Krishnaroop Chowdhuri, Dr. Subhadarsinee Sahoo (my friend cum contemporary); Profesar Kamdi (our Prof. Kamdi), Bhavana Vyas, Sameer Hupriker, Aniket Gudadhe, Subrajeet, Gadha Mathew, Dr. Nirmalya Bachhar, Dr. Divya Nagaraj (for special considerations) and Dr. Chayanika Das. Here I would like to make a special mention of Dr. Neha Tiwari for extending a helpful hand at the outset by arranging my accommodation and being kind and helpful.

I also take it as an opportunity to thank my friends at NCL Pune; Maya, Salim Dar, Manzoor Dar, Prabhu D and Manoj Sharma, for their bounteous and able company. Your associateship was the one which benefitted me personally and academically. Discussions and parties were worth remembering. I also would like to thank my B.Tech friends who kept on ringing my phone without blaming me for not picking up!.

At the end I would like thank my close ones for their affection and bounteous love. I would like to express my thanks to Kannolil family, Adv. Radhamani Mariyil and family. I would like to make a special mention of Dr. Malik Abdul Wahid whom I owe a gratitude of highest degree for his selfless companionship and guidance. Thanks for being there.

Karthika

Table of Contents

List of Figures

are compared with wet sponges (where the sponges are soaked in excess water, so that all the voids contain water).

Figure 2.8: SEM images of **(a)** elastic sponge and **(b)** plastic monolith prepared using silica nanoparticles. The scale bar represents 100 μm.

Figure 2.9: (a) SAXS data from an elastic sponge and a plastic monolith while they were held at -15^{o}C to allow the polymer to crosslink. Data are vertically offset for clarity. The solid line represents SAXS from a dilute dispersion of the 22 nm silica particles that were used to prepare the monoliths. **(b)** Normalizing the SAXS data from the monoliths by the dilute solution scattering from silica nanoparticles allows us to determine an apparent structure factor, $S_A(q)$ for nanoparticles in the monoliths. The solid line through the first peak represents a fit[30] to the data to obtain the nearest neighbour spacing. Here too, data is vertically offset for clarity.

Figure 2.10: (a) TGA temperature-dependent weight loss data for the elastic sponge, the plastic monolith and for the as-received 22 nm silica particles used to prepare the scaffolds. **(b)** ^{13}C NMR spectra of elastic sponge and plastic monolith. The peak at 26.3 ppm (marked *) is attributed to the carbon nuclei in the -(CH2-CH2)- group present in the crosslinker 1, 4-butanediol diglycidyl ether.

Figure 2.11: Storage (G′, filled circles) and loss moduli (G″, open circles) from rheological measurements in the linear regime for **(a)** elastic sponge (black) and for plastic monoliths (red) prepared using uncrosslinked 1μm polystyrene (PS) particles. **(b)** G′ and G″ for crosslinked PEI gel obtained from elastic sponge (black) and from plastic monolith (red) after dissolution of the PS latex particles.

Figure 2.12: (a) SEM micrograph of monoliths prepared using uncrosslinked polystyrene particles of size 1μm (inset: high resolution micrograph of the wall of the monolith) and **(b)** SEM of gel obtained after washing with cyclohexane. Note that the scale bar in this image is 4 μm. The polystyrene particles appear to be completely dissolved and are not observed in this image.

Figure 2.13: Compression-expansion behaviour of pure crosslinked polymer scaffold at 60 % compressive strain. Note that the monoliths recover elastically independent of whether the crosslinking is done in the presence of ice or after lyophilization.

Figure 2.14: Compression-expansion behaviour of monoliths prepared using an aqueous dispersion of 1µm silica particles, where the PEI is crosslinked in the **(a)** presence and **(b)** absence of ice crystals (viz. after lyophilization of the ice). Nominal stress as a function of nominal strain for the compressive strains from 10% to 80%.

Figure 2.15: (a) Surface topography and **(b)** phase shift images of elastic (left) and plastic (right) monoliths. We extracted height and phase angle profiles along several line cuts across these images. We present one such profile of the **(c)** height trace and the **(d)** phase shift trace as an example. Profiles obtained for other line cuts were qualitatively similar. Comparing the height traces for the elastic and plastic monoliths, we note that there is a similar height variation as we go across the sample (and over multiple particles) for the two scaffolds. When we examine the phase shift trace for the elastic scaffold, we observe a variation from about -50^{o} to $+50^{o}$ as we go across the sample. In contrast, the phase shift trace for the plastic monolith exhibits a larger variation (by a factor of ≈2), from about 0 to 230^{o}. Again, we note that the data presented is representative of differences between elastic and plastic monoliths in Φ–variations across the sample.

Figure 2.16: AFM height image for **(a)** elastic sponge and **(b)** plastic monolith. We select regions between the particles (marked *) to probe the nature of the crosslinked polymer mesh that bonds the particles in the monoliths. **(c)** Energy dissipation per cycle as a function of normalized amplitude calculated for the interparticle regions in elastic sponges and plastic monoliths. Dynamic energy dissipation measurements are made at several interparticle points using independent samples for both monoliths. **(d)** Distribution of the work of adhesion from contact mode force-displacement measurements performed on several interparticle points on elastic sponges and plastic monoliths.

Figure 2.17: Energy dissipation per cycle for polymer films with different crosslinking density.

Figure 2.18: Extension (blue)-retraction (dark red) curve showing the dependence of cantilever deflection (that is related to the force on the cantilever) as a function of tip-sample distance for **(a)** elastic sponge **(b)** plastic monolith. The work of adhesion is calculated from the hysteretic area between these extension-retraction curves. This data is shown as an example of how the work of adhesion was calculated. We performed this at over 50 points using 10 independent samples of both elastic and plastic scaffolds.

Figure 3.9: The effect of different thresholding levels on the trend signal. The 4 level thresholding showed the best filtering of high frequency signal from low frequency signal.

Figure 3.10: Comparison between the results of analysis using the Origin and MATLAB. In Origin we have used 4^{th} order Daubechies basis set and threshold level =4 for denoising the mother signal. In MATLAB, through wavelet transform, the mother signal is deconvoluted into 11 scales. Scales 6-11 represent low frequency signal (trend signal) and scales 1-5 represent detrend signal. (**a**) Mother signals of multiple particles (**b**) and (**c**) taking a representative signal and splitting that signal into trend and detrend signals using MATLAB code and Origin software respectively. (**d**) and (**e**) are the high frequency detrend signals obtained after denoising using MATLAB code and Origin software respectively. (**f**) Comparison between the data obtained through MATLAB code and Origin software in terms of jump distribution. The jump distribution obtained after wavelet transform either through MATLAB code or Origin matches well.

Figure 3.11: The van Hove jump distribution of 9 particles. The jump distribution calculated for time step (**a**) 1 s, (**b**) 2 s and (**c**) 4 s. The comparison of Figures a, b and c shows the resolution is independent of time step and in all cases the dynamical resolution is less than 4nm.

Figure 3.12: X and Y coordinates of two particles present in elastic sponge obtained from a movie. The particles show directional movement along with small jumps per frame.

Figure 3.13: Microscopy investigation of elastic sponges. **(a)** Particle trajectory of a single probe particle from fluorescence microscopy. The trajectory is color coded to show the time scale of motion. **(b)** Particle motion along X and Y coordinates (defined arbitrarily, as shown in (a)) as a function of time. **(c)** & **(d)** Trajectory and position of a particle after elimination of stage drift using wavelet transform. **(e)** van Hove jump distribution for a particle along X and Y coordinates, fit to a Gaussian form. **(f)** MSD for particle movement in the X-Y plane. We calculate MSD based on frames collected over about 10 minutes of imaging, but restrict our interpretation to only the first 5% of the lag time, τ, to ensure statistical reliability.

Figure 3.14: Microscopy investigation of plastic monoliths. **(a)** Particle trajectory of a single probe particle from fluorescence microscopy. The trajectory is color coded to show the time scale of motion. **(b)** Particle motion along X and Y coordinates (defined arbitrarily, as shown in (a)) as a function of time. **(c)** & **(d)** Trajectory and position of a particle after elimination

List of Tables

Chapter 1

Introduction

1.1 Introduction

Porous colloidal assemblies made from polymeric latex, metal and inorganic particles are interesting since they combine low density with favorable thermal, electrical and mechanical properties.[1-7] However, the usage of porous colloidal assemblies is greatly restricted by their brittleness.[8-11] The catastrophic failure of these colloidal assemblies is governed by the natureof interparticle bonds that hold the assembly together. Therefore, it is important to develop methods to engineer the interparticle bonds to develop new damage resistant particle assemblies.

Recently, Rajamanickam et al. discovered a new class of flexible particle/polymer hybrid assemblies.[12] These materials are comprised primarily of inorganic particles (over 90% by weight) but are remarkably flexible. These could readily be compressed to one-tenth of their original dimension, and displayed a complete recovery upon removal of load. Surprisingly, this mechanical response was independent of the chemistry of the particles, polymer and crosslinking method employed. The practical implication of this is that it opens up the possibility of preparing materials for a wide range of applications based on assemblies of functional particles. Thus, these materials have tremendous promise and have already found applications as separation media,[13] low-flammability structural sponges[14] and as flexible supercapacitors.[15] However, the origin of their remarkable mechanical properties remains incompletely understood. In this thesis, we explore the microstructural underpinnings of the remarkable compressibility of these ice templated particle- polymer hybrid structures.

1.2 Colloids

Colloids are small particles ranging from a few nanometers to a few microns in size, dispersed in a medium. According to the IUPAC Gold book, "the term *colloidal* refers to a state of subdivision, implying that the molecules or polymolecular particles dispersed in a medium have at least in one direction a dimension roughly between 1nm and 1μm, or that in a system discontinuities are found at distances of that order".[16] The range of materials that are colloidal in nature is vast and this is because of the broad definition of a colloidal particle. Common examples of colloids include milk, paint, bacteria, viruses and globular proteins. Sol- gel particle formation,[17] microfluidic fabrication,[18] emulsion polymerization,[19] mini and micro emulsion polymerization,[20] precipitation polymerization[21] and suspension polymerization[22] are a few colloid synthesis methods.

Colloidal particles are comprised of diverse materials including polymers, minerals, clays, organic compounds, ceramics, semiconductors and metals. The field of colloidal chemistry has matured so that there are well established routes to the synthesis of colloids with well controlled size distribution, shape, and surface chemistry. For example, patchy colloids, viz., particles that exhibit heterogeneous surfaces with a patchy architecture have recently been synthesized.[23] Further, particles with even more complex architectures have been synthesized including Janus particles,[24] composite particles,[25] core shell and hollow capsule systems,[26] non-spherical particles,[27] well-defined particle clusters[28] and colloidosomes[29].

The assembly of colloidal particles is guided by different forces. Colloidal assembly is determined by the size, shape and material composition of the particle and dispersion medium. The shape of the particle is directly connected to the symmetry of the assembled structures. For example, monodisperse spherical colloids form ordered face centred cubic or hexagonal close packed structures whereas monodisperse cubic particles organize into simple cubic lattice symmetries.

1.3 Colloidal assembly and the forces involved

Individual colloids can assemble into complex structures either through self assembly or through guided assembly. Self assembly is the self-governing organization of components into patterns or structures without human intervention.[30] This process is common throughout Nature and this is one of the practical strategies for making ensembles of nanostructures. Self assembly can be classified intostatic self assembly and dynamic self assembly. Static self assembly involves systems that are at global or local equilibrium and do not dissipate energy. Colloidal crystals and liquid crystals are examples of static self assembly.[30] In static assembly, the formation of ordered structure may require energy (for example, in the form of stirring), but it is stable once it is formed. In dynamic self assembly, the interactions between components responsible for the formation of structures or patterns occur only if the system is dissipating energy. Bacterial colonies are examples for this. Templated assembly is another variant of self assembly. Here, the interactions between components and regular features in their environment determine the structure that forms. Crystallization of colloids in three dimensional optical fields is an example.[30] Thus, self assembly reflects information coded in individual attributes such as shape, surface properties, charge, polarisability, magnetic dipole, mass etc. These characteristics determine the interactions between individual entities.

In guided assembly, interfaces, templates or external fields can guide the process of particle organization toward desirable geometries. Layer by Layer (LBL) assembly and light, electrical or magnetic field induced assembly of particles come in the category of guided assembly. LBL involves the alternate deposition of high molecular weight species to make coatings and macroscale free standing sheets.[31] In LBL, colloidal particles are often combined with polymers to produce composites.

Field activated particle assemblies involve light sensitised particle assembly, electric field and magnetic field activated particle assemblies. Light sensitised particle assembly relies on optical confinement and irradiation induced changes in photoactive ligands present on particle surface.[32] Here, the dipolar interactions between particles triggers particle assembly into ordered 3D arrays. Electric field driven assembly occur from induced polarization of particles. Adjacent particles interact through dipole-dipole interactions and form chains aligned parallel to field lines. Particles can also be assembled by AC field by dielectrophoresis (DEP).[33] DEP can be used for the assembly of different types of particles in a variety of liquids without undesired effect caused by electro-osmosis and electrolysis. Magnetic field driven assemblies originate from particle association via magnetic dipoles when torque exerted by a magnetic field exceeds particle thermal excitation energy.[34] Magnetic particles can form chains or 3D superlattices.

Next, we will summarise various forces involved in colloidal system along with their nature, source, range and governing formulae. Detailed explanations about these forces can be found in these two references[35, 36].

1.3.1 Various forces associated with colloidal assembly

Table 1.1: Summary of forces acting between a pair of identical colloidal particles or an individual particle in a liquid medium.

Forces/ Nature	**Source**	**Range**	**Formula**
Electrical double layer/ Repulsive	Surface charges, adsorption of ions, dissolved ions and solvent.	Can be up to hundreds of nanometers depending on surface charge density, particle size and solvent ion concentrations.	$F(D) \approx 2\pi R\varepsilon\varepsilon_0\kappa\Psi_0^2 e^{-\kappa D} = 2\pi R\sigma^2 e^{-\kappa D}/\kappa\varepsilon\varepsilon_0$

Van der Waals/ Attractive	Quantum fluctuations of dipole moment. This includes following interactions: Dipole- dipole dipole- induced dipole induced dipole- induced dipole	Can be up to hundreds of nanometers depending on the Hamaker constant and particle size.	Between two spheres: $F(D) = \frac{-A}{6D^2}[\frac{R_1 R_2}{R_1 + R_2}]$ $A = \pi^2 C \rho_1 \rho_2$
Solvation force (Oscillatory)/ Attractive or repulsive	Arises once there is a change in the liquid density at the particles surface and/ or the midplane as two particles approach each other.	Short, 5-10 solvent molecular diameters	$F(D) = f_0 \cos(2\pi D/\sigma) e^{-D/\sigma}$
Steric hydration force between fluid like surfaces/ Repulsive	Entropy driven, induced by steric overlap of adsorbed species.	Short, 1-2 nm with an exponential decay length of 0.1-0.3 nm. If the adsorbed species is polymeric, repulsion extends to about $10R_g$	$F(D) = f_0 e^{-D/\lambda_0}$
Hydration force between solid hydrophilic surfaces/ Repulsive	Surface groups strongly hydrogen bonded and solvated by water	Interaction range: 3-5 nm, with a decay length ~ 1nm	$F(D) = f_0 e^{-D/\lambda_0}$

Hydrophobic interaction (between two hydrophobic surfaces in water)/ Attractive	Several models for this, including vapor bridges model, water structure model and electrostatic model. Details of these models can be found in reference[36].	Long, 0-10 nm with decay length 1-2 nm. Based on the solvent, it may be effective up to several tens of nanometers.	$F(D) = -{2\gamma_i}/{\lambda_0}\, e^{-D/\lambda_0}$
Inter-segment force/ Attractive	Occurs when two polymer coated surfaces come together in a poor solvent. Temperature and solvent dependent	Short, decay length ~ R_g	
Bridging force/ Attractive	Any polymer that naturally adsorbs to a surface from solution has the potential to form a bridge between two such surfaces.	Short, decay length ~ R_g	Force between spherical particle and a planar surface: $F(D) = {-4\pi R\varepsilon\Gamma(L_c - D)}/{l}$
Depletion force/ Attractive	Entropic origin, polymer is not adsorbed on particle surface, arises from osmotic pressure between the bulk solution that contains polymer and the polymer-depleted zone		For two spheres: $F(D) = -\pi R R_g \rho kT$

	between two particle surfaces that is free of polymer.		
Capillary force/ Attractive	Surface tension of suspending liquid, wetting behaviour and overlap of the interfacial deformation.	Long (could be up to millimeters) and strong	Normal capillary force for spheres on plane: $F = -2\pi\gamma R(cos\theta_s + cos\theta_p)$
Hydrodynamic or drag force/ in fluid flow direction	Viscous friction		$F_D = 6\pi\mu R\upsilon$
Brownian force, not directional	Bombardment from thermal molecules in the fluid.		Over time, $\sum F_B$=0
Buoyancy force/ opposite to gravitational field	Due to the pressure of the fluid and gravity.		$F_{buoyancy} = \rho_f Vg$
Gravity force/ in the direction of gravitational field	Earth acting on particle	Force is very weak for small particles, Particle sediments when gravity works against the sum of buoyancy force and fluid drag force.	$F_{gravity} = \rho_p Vg$

R: particle radius, κ: inverse Debye length, $\varepsilon, \varepsilon_0$: dielectric constant and permittivity of the suspending medium respectively, Ψ: surface charge potential, D: distance between two surfaces, A: Hamaker constant, ρ_1, ρ_2: number of atoms per unit volume in the two bodies, C: coefficient in the atom- atom pair potential, R_1, R_2: radii of two spheres, f_0 : force at $D = 0$, σ: molecular diameter, λ_0 : characteristic exponential decay length, R_g: radius of gyration of the polymer coil, γ_i: surface- water interfacial energy, Γ: polymer chain tail density, ε: polymer chain segment length, L_c: contour length, ρ: number density, k: Boltzmann constant, T: temperature, γ: the liquid surface tension, θ_s: mean slope angle of meniscus on sphere

with respect to plane of contact line, θ_p: same but for plane, υ: relative velocity between liquid and particle, μ: viscosity of fluid, ρ_f: density of the fluid, g: the gravitational constant, V: the volume of the fluid element and ρ_p: density of particle.

1.3.2 Particle assembly

Particle assembly and resultant structure is critical in many applications including catalysis, solar energy conversion and optoelectronics. Figure 1.1 shows some of the possible structures that can be obtained from spherical building blocks. The assembly of particles into chains followed by oriented attachment leads to connectivity between initially separated particles. This lattice connectivity is essential for energy storage devices. For example, Kotov et al. have made copper nanoparticle films by field stimulated assembly of copper nanoparticles.[37] Here, the lattice to lattice connectivity in self assembled nanoparticles enabled fast charge transport and therefore these materials can be used as current collectors in lithium ion batteries. Control over these particle assemblies is essential to attain desired properties. For example, controlling the filler particle assembly in a composite is critical to its performance.[38] Synthesis of particles with controlled size, shape, composition and surface chemistry is important in achieving control over their assemblies. It is now possible to synthesise materials with desired size distribution, chirality and surface functionalization. Particle attributes that result from synthesis, along with any imposed stimuli or external fields then dictate the nature of assembly.

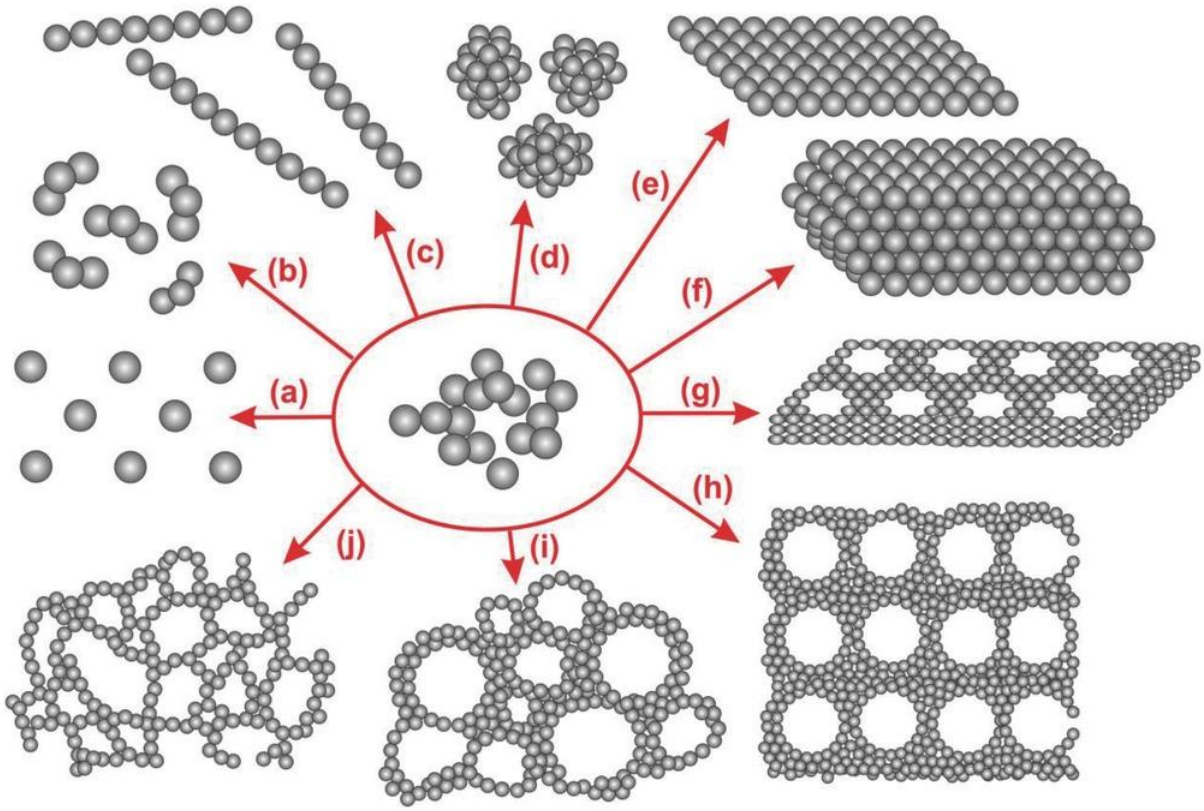

Figure 1.1: Assembly of spherical colloidal particles into various structures. **(a)**single particle arrays **(b)** colloidal molecules **(c)** colloidal chains **(d)** colloidal clusters **(e)** colloidal monolayer **(f)** colloidal 3D assembly **(g)** porous colloidal assemblies **(h)** inverse opals **(i)** foams and **(j)** aerogels. *(Reprinted with permission from reference[39]. Copyright © 2017, John Wiley and Sons.)*

Interparticle forces help in growing nanomaterials from nanometers to microns, millimeters, and may be meters while controlling the geometry of self-organized one- (1D), two- (2D), and three dimensional (3D) superstructures. Particle assembly along one direction leads to colloidal chains. The formation of such chain like structures is analogous to polymerization of organic molecules. Examples include nanoparticle chains of Ag,[40] Au,[41] CdTe[42] or Co.[43] In these examples, particle surfaces were grafted with organic ligands that provide stability against coalescence and ultimately lead to the formation of pearl necklace like structures. Mann et al. had shown that these linear assemblies are formed by the ligand exchange induced dipole driven assembly mechanism.[41]

The assembly of two dimensional arrays of particles creates surface patterns with a resolution determined solely by the size of the colloids. These monolayers can be directly deposited onto solid substrates via evaporation driven convective assembly[44], spin coating[45], electric field assisted deposition[46] or mechanical rubbing of dry powders[47]. Particles can also be assembled at a liquid interface and subsequently transferred to a solid substrate.[48] These

colloidal monolayers are valuable as masks or templates for etching or evaporation processes to create coatings or functional surface nanostructures.[49] Three dimensional assemblies are predominantly prepared by convective assembly in which colloidal particles are deposited from a dispersion via a receding meniscus.[50] Methods to assemble colloidal particles into three dimensional arrays include sedimentation[51], Langmuir- Blodgett[52], spin coating[53], evaporative deposition[54] and shear alignment[55]. This three dimensional assembly of particles finds applications in surface coatings including anti- reflective and self- cleaning coatings,[56] hydrophobic surfaces,[57] and low surface tension liquids.[58] Colloidal assemblies have also been exploited to understand structural color and mimic colorations occurring in Nature.[59, 60] A detailed description of these methods is beyond the scope of this Chapter. Since this work is mainly focused on porous colloidal assemblies, we now examine in detail the preparation methods, important features, applications and major limitations of porous particle assemblies.

1.4 Porous colloidal assemblies

Colloid based porous materials are interesting because they are light in weight and find application in various areas of practical importance including separation, catalysis, low dielectric constant materials, etc.[61] By definition, porous materials are materials with pores (interstices, cavities and channels). The characteristics of porous materials vary depending on the size, arrangement, shape of the pores as well as the porosity and composition of the material itself. The attributes of a porous solid are shown in Table 1.2. This thesis is focused on porous materials made by assembling particles and therefore the discussions are restricted to porous colloidal assemblies.

Pores in colloidal assemblies can be either ordered or disordered. Ordered porous structures are mainly generated from the packing voids of monodisperse colloids. These ordered porous structures are mainly used in optical devices, for example; ordered micropores in a high refractive index matrix such as titania can be used to make photonic crystals with a full photonic band gap (PBG).[62] Applications of these PBG materials include waveguides, omnidirectional mirrors and suppression or enhancement of spontaneous emission.[63]

Table 1.2: Definition of terms used to characterize porous materials.

Term	Definition
Porosity	$\frac{Total\ pore\ volume}{Apparent\ volume\ of\ the\ material}$
Pore shape	Spherical, cylindrical, funnel, slit shaped etc...
Pore accessibility	Closed or open pores
Pore size and transport phenomena	➢ <2 nm : micropores: activated transport ➢ 2-50 nm : mesopores: capillary transport, Knudsen diffusion,[64] surface diffusion through pore walls ➢ > 50 nm: macropores: molecular diffusion
Density	➢ Bulk density: mass per total volume (where, total volume= volume of pores + volume of pore walls) ➢ Pore wall density: density of solid network in the pore wall

Irregular porous structures are mainly prepared using chemical processes like sol- gel method which controls the generation and aggregation of the particles. In a sol- gel process, colloidal sol particles dispersed in a liquid transition to form a 3D sponge like gel network.[65] The sol to gel transition is called gelation which occurs over a period of time. In a 3D network, if the liquid medium that is gelled is water or alcohol, the resulting gels are known as hydrogels or alcogels. Replacement of the liquid phase with air while preserving the porous structure gives aerogels. Kistler et al. in 1931 prepared the first aerogel from polysaccharides where they removed solvent using supercritical drying.[66] Other methods used to remove solvent include freeze drying and ambient- pressure drying. If the liquid is removed by freeze drying, then that material is known as a cryogel. Xerogels are obtained upon conventional drying of wet gels either by increasing temperature or by decreasing pressure. However, drying in this manner typically leads to a significant shrinkage due to capillary forces experienced during drying.

Among all these porous structures, aerogels have the highest porosity with open pore structure (porosity ~90% with overall density of 0.004 g/cc to 0.5 g/cc). They are characterized by high inner surface area, large open pores, extremely low thermal conductivity, low sound velocity combined with high optical transparency.[67] Moreover, researchers have varied the pore size in aerogels to create mesoporous to macroporous structures.[68, 69] These pores are surrounded by solid networks comprising, typically oxides of silicon, aluminium, iron, tin, thorium or tungsten.[70] Researchers have also prepared aerogels using polymers like cellulose, cellulose nitrate and gelatine.[71] These exhibit very interesting properties like ultra light weight, extremely low thermal conductivity, low sound velocity or high optical transparency.[10] These unique material properties arise from the special fractal arrangement of their solid phase. Researchers have investigated aerogel structure using small angle X- ray scattering (SAXS) and small angle neutron scattering (SANS) techniques.[10, 72] Studies showed that, in contrast to compact particle aggregates, in which the mass (M) varies with length L as: $M \sim L^3$, the length of the fractal object related to M through $M \sim L^{d_f}$; where d_f represents the fractal dimension.[73] The knowledge of the fractal dimension gives information on the spatial arrangement of the solid network and it can be related to the particle aggregation mechanism leading to this structure. The density of the fractal can be written as $\rho(L) \propto L^{d_f-3}$. Real materials can be fractal only over a limited length range, from a lowest limit set by the size of the primary particle (a) to a maximum limit (ξ) above which the material is homogeneous and the density approaches the bulk density. Therefore the fractal density can be defined as $\rho(\xi) = \rho(a)[\xi/a]^{d_f-3}$. The fractal dimension is related to the particle assembly process. It has been reported that the least dense structure forms for a diffusion limited aggregation in which particles stick irreversibly and permanently at contact. These systems exhibit smaller d_f with value ~ 1.8.[35] However when apotential barrier must be overcome for aggregation, an incoming particle will explore an aggregate for some time before it sticks. In this case, it is more likely to reach the interior of the aggregate and stick there. This leads to a more compact structure and a larger d_f is observed experimentally. This is called reaction limited aggregation. Here, the larger d_f increases the density of the porous material and correspondingly affects other properties such asporosity. Aerogels have been used in a variety of fields such as in energy storage devices (example V_2O_5 as a cathode in lithium ion batteries[74]), in electrocatalysis (MoO2),[75] ecologically sound insecticides,[76] cosmic dust collectors[77] and as scaffolds in tissue engineering.[12]

1.5 Mechanical robustness of porous particle assemblies

We have seen that particle assemblies are interesting with many exciting properties and applications. However, these assemblies are extremely brittle and exhibit catastrophic failure even at modest deformations (Figure 1.2). Kim et al. had classified particle assemblies based on their elongation; when elongation > 200%, they termed this as superplasticity, when elongation was in the range of 50-200%, these were super plastic like materials, 3-50% elongation were ductile materials and <3% were brittle materials.[78] The brittleness of aerogels limits their use in many applications, for example, in membrane filtration. Brittleness of a material is related to the amount of energy that can be absorbed or dissipated in the form of deformation before it fractures from the imposed stress. Narkis et al. had shown a relationship between material's brittleness and elongation at break through an equation: $B = \frac{1}{\varepsilon_b E'}$, where, ε_b is the elongation at break and E' is the dynamic modulus obtained from dynamic mechanical analysis. Therefore, the brittleness of a material can be quantified from the stress-strain curve.[79] In the low strain portion of the curve, materials obey Hooke's law so that stress is proportional to strain with the constant of proportionality being the modulus of elasticity (E'). As strain is increased, materials eventually deviate from this linear proportionality, the point of departure being termed the proportional limit. This nonlinearity usually arises from stress-induced "plastic" flow in the material. Here, the material undergoes a rearrangement of its internal molecular or microscopic structure, such that atoms are moved to new equilibrium positions. This plasticity requires a mechanism for molecular mobility, which in crystalline materials can arise from dislocation motion. For materials lacking this mobility, for instance due to internal microstructures that block dislocation motion, failure is brittle rather than ductile. The stress-strain curve for brittle materials is typically linear over their full range of strain, eventually terminating in fracture without appreciable plastic flow. The amount of energy required to crack a material is often expressed in terms of toughness and which can be obtained as the area under the stress-strain curve. Along with lower ε_b and toughness, brittle materials also exhibit low Poisson's ratio ($\nu = \frac{-\varepsilon_{\text{lateral}}}{\varepsilon_{\text{longitudinal}}}$, where ε is the strain).[79] The appropriate values of Poisson's ratio of major classes of engineering materials are; rubber ≈ 0.5, plastics ≈ 0.4, metals ≈ 0.3, ceramics ≈ 0.2.[79] It should be noted that the materials appear to become more flexible as the Poisson's ratio increases. This is because, the ability of material to contract laterally as it is extended

longitudinally is related to its molecular mobility - rubber can stretch due to a large number of molecular conformations. However, ceramics are tightly bonded.

On applying force to porous particle assemblies like aerogels, very little deformation (ε_b< 3%) is possible before the applied stress results in collapse of the sample. The gas trapped inside the open pores is pushed outwards during collapse of the system, however, its energy dissipation is very small.[80] Therefore, the energy applied on an aerogel is primarily absorbed through collapse of particle network structure.[11, 81-84]

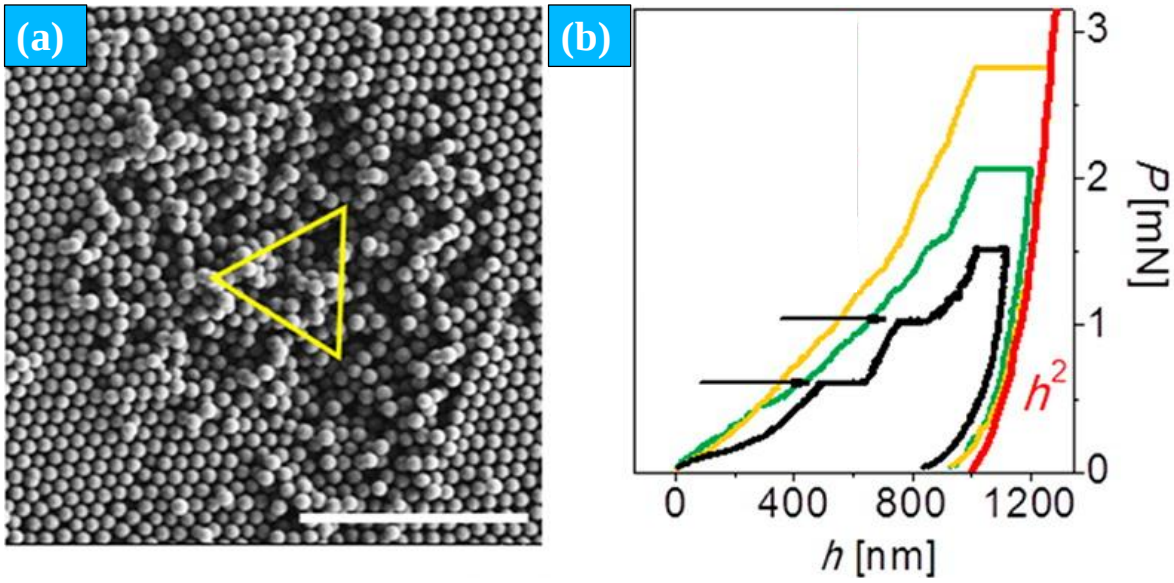

Figure 1.2: Nanoindentation on silica colloidal crystals (CC). Here, silica particles are connected by capillary bridges where the water is physisorbed on the hydrophilic silica surface under controlled temperature and humidity conditions. **(a)** SEM micrograph of residual indents: surface morphology ofCC after nanoidentation with penetration depth (h_{max}) of 500 nm (scale bar 5 μm). Colloids are uplifted with compression force. (**b**) Load-depth curves with h_{max} = 1000 nm performed at different load rates (5, 50, and 500 μN/s − black, green, and orange lines, respectively). *(Reprinted with permission from reference[85]. Copyright (2012) American Chemical Society.)*

The elasto-mechanical behaviour of brittle assemblies has been experimentally studied using various techniques including dynamic mechanical analysis (compression, tension, three point bending), nanoindentation, and sound velocity measurements. The fracture mechanics of particle assemblies has shown that the deformability of these materials is strongly dependent on the characteristics of interparticle bridges. For example, Lopez et al. had shown that the capillary bridges between colloids influence its mechanical properties.[85]

They prepared colloidal crystals (CCs) using hydrophilic silica particles by vertical deposition of dilute colloidal suspension on a glass substrate under controlled temperature and humidity. Capillary bridges are formed between particles by the uptake of water from ambient moisture. They characterized the micromechanical properties of these CCs by nanoindentation. They showed that the capillary bridges between colloids failed under compression and led to disruption of colloidal assembly. They also performed temperature dependent nanoindentation of CCs with controlled content of adsorbed water. They showed that CC structure becomes more compliant upon water desorption. Similarly, it has been reported that sintered ceramics fail abruptly even at smaller deformations (~2%) due to failure of contact points between particles.[86] Therefore, it is clear that interparticle bridges determine the mechanical robustness of particle assemblies. We now examine the literature on crack formation at interfaces and the important parameters that influence crack propagation in general.

According to the linear elastic fracture mechanics, fracture occurs as a result of stress concentration at the crack tip.[82, 87] When stressed, a brittle material is characterized by stress intensity factor (K_I), where,

$$K_I = \sigma_a Y \sqrt{\pi a}$$

where, σ_a is the applied stress, Y is the geometrical factor depending on location and defect shape and a is the defect size.

Material fracture occurs when σ_a or a or both increase in such a way that K_I reaches a critical stress intensity factor, K_{Ic}. Therefore, K_{Ic} is a measure of toughness.[79] Toughness of samples can be experimentally measured using single edge notched beam technique. Figure 1.3 depicts the variation of crack propagation velocity (V) as a function of K_I. Three different regimes can be identified in this. The material remains uncracked as long as $K_I < K_{Ii}$, where K_{Ii} is the stress factor when the crack velocity is zero. Region 1 shows subcritical propagation. Here, the crack growth is slow and the life time of the material depends mainly on the crack rates. Once $K_I > K_{Ii}$, the crack starts growing. Region 2 represents the crack rate plateau where slight increase in (K_I) arises from an increase in either applied stress (σ_a) or crack length (a). Finally, further increase in stress leads to the rapid propagation of cracks (Regime 3) and reaches the critical stress value (K_{Ic}). Therefore, to improve the reliability of particle assemblies, control of flaw size or increase in fracture toughness is required.

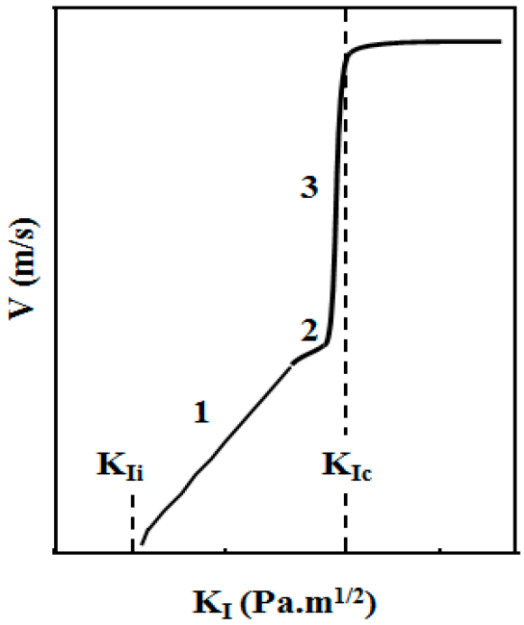

Figure 1.3: Profile of crack propagation velocity (v) variation as a function of stress intensity factor (K_1).*(Reprinted with permission from reference[82].)*

1.6 How to overcome brittleness in particle assemblies

Typically, high mineral content leads to brittleness. However, some natural structures like bone, hexactinellid, seashells and tooth enamel are tough despite their high mineral content (mineral content of bone is 30-70 vol%, seashell 95 vol% and tooth enamel and sea urchin spines 99 vol%).[88] In all these, the mineral phases are in the forms of micro or nano size rods, layers, grains or platelets, bonded by soft organic materials like proteins or polysaccharides (Figure 1.4). While the mineral phase provides stiffness, it also contributes to brittleness. In composites, the mineral-organic interface allows for energy dissipation, and thus controls crack propagation by deflecting or guiding the cracks towards regions of the material where the crack energy can be dissipated and therefore the overall toughness can be improved. The phenomenon is well exemplified in natural nacre, where 95 vol% is brittle aragonite (a crystalline form of calcium carbonate, 0.1- 0.9 μm thick) and 5 vol% is an organic material (30nm thick layer of a compound of polysaccharide and protein). In this system the organic materials are strongly bonded with inorganic platelets in the form of fine networks organized around mineral nanograins. This brick and mortar type microstructure of nacre provides a combination of stiffness, strength and toughness. Under tension, the stress in inorganic tablets of nacre is transferred to the neighbouring platelets through soft organic interfaces enclosing the tablet. However, these inorganic plates are brittle. The toughness and energy absorption capability of the structure arises from other mechanisms operative at the

interface, such as interlocking of nano-asperities, inelastic shear deformation of organic phase and microscale waviness.[89] Single molecule force spectroscopy study using atomic force microscopy (AFM) showed that the energy dissipation of organic layer is by the reversible unfolding of macromolecules and rupture of sacrificial bonds.[89, 90]

Nature is a perennial source of inspiration for scientists. To overcome the brittleness of particle assemblies, the concept of introducing ductile phases into particulate matrix in different ways has been employed as a successful strategy. These hybrid structures can be classified into two categories; class I and class II, based on the nature of interaction and link between the organic and inorganic components.[91] Class I hybrids are those, where both phases interact through weak forces like van der Waals forces, electrostatic forces and hydrogen bonding. The inorganic–organic phases bonded through strong chemical bonds like covalent or iono- covalent bonds form class II structures. These organic phases absorb energy by dissipation due to macromolecular motions. Consequently, hybrid structures are more resistant to cracks and fracture.

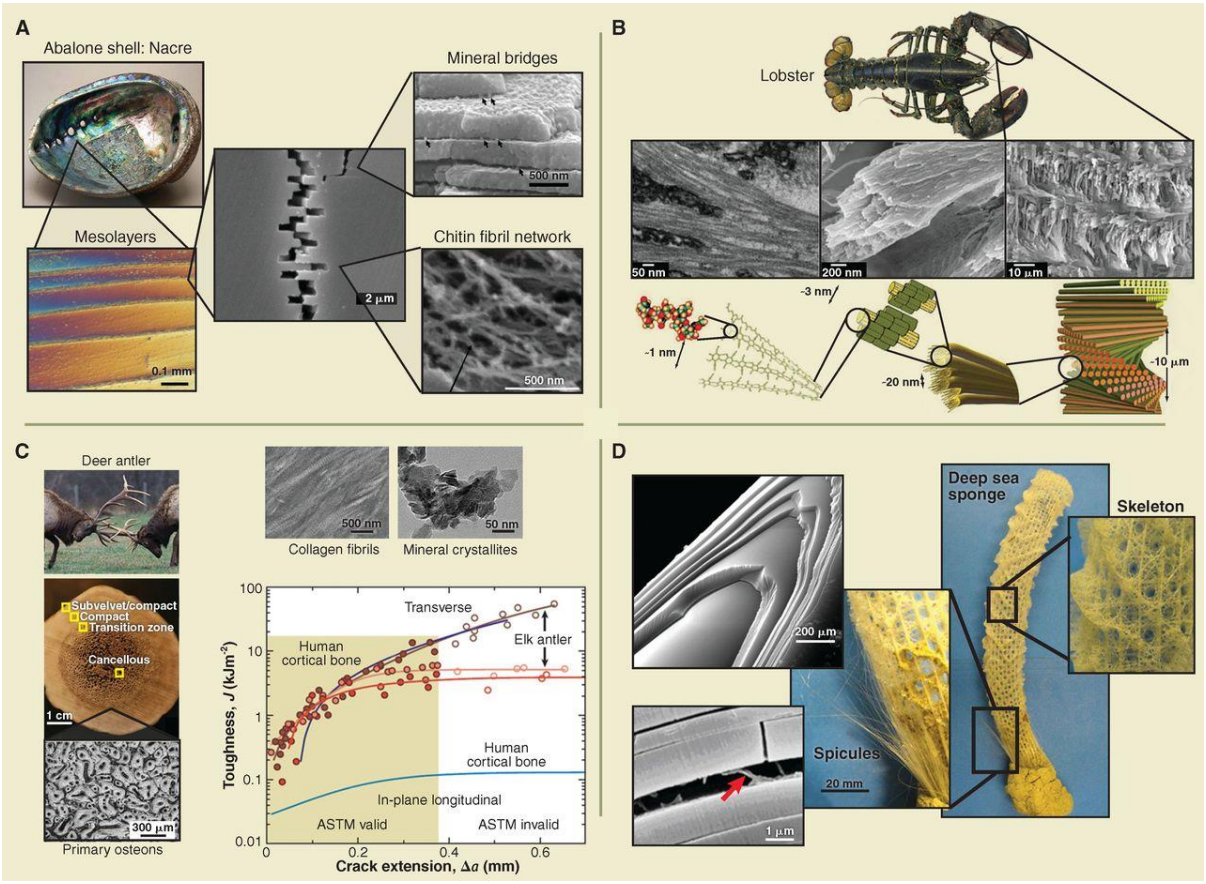

Figure 1.4: Examples of tough biological materials. **(a)** Abalone nacre with mesolayers, mineral bridges between mineral plates and asperities on the plate surface. The chitin network fibrils form the backbone of inorganic layer. Also, image shows that cracks show tortuous propagation around tiles rather than through the tiles. **(b)** Lobster exoskeleton with twisted plywood structure of the chitin and the tubules which extend from chitin layers. **(c)** Antler bone with porous bone and a surrounding hard cortical bone. Collagen fibrils are in one direction and nanocrystalline minerals dispersed in and around the fibrils. **(d)** Deep sea sponge and scaffold of spicules. Each spicule is rod-like with circumferential layers. The interface between layers helps in arresting crack propagation. Organic silicates act as bridge between silica layers. *(Reprinted with permission from reference[88]. Copyright © 2013, American Association for the Advancement of Science.)*

1.6.1 Hybridization of particle phase with ductile phase

Ductile phases are incorporated into particle assemblies either physically or through chemical reactions. In normal polymer composites, the polymer phase is doped with inorganic fillers to improve stiffness (but the toughness reduces with increase in filler loading) and thermal properties. However, Leventis et al. doped a majority filler phase with a

polymer.[7] They soaked wet silica gel in solution containing di-isocyanate followed by heating of the gel. The two reactive end groups of di-isocyanate reacted with hydroxyl groups on nearby nanoparticles and formed a carbamate bond. This bond acted as a glue between particles and allowed the formation of an aerogel that could be flexed without breaking. Such structures are known as crosslinked hybrid structures. These hybrid structures are used as light weight thermal insulators, acoustic insulation, armour, run flat tyres, optical sensors and membranes for fuel cells. Similarly, Schiraldi et al. also used polymer to overcome the brittleness of clay aerogels.[92] They made aerogel by combining water soluble epoxy monomers with clay in water. This was then freeze dried into polymer – aerogel prepregs and then thermally cured to produce thermoset composites. Here, the polymerization happened along with the aerogel formation. These aerogels were capable of recovering elastically from compression to 80% strain.

In the two aforementioned cases, flexible aerogels are formed by crosslinking wet gels prior to supercritical or freeze drying. It is also possible to reinforce dry particle gels. This has been done through atomic layer deposition (ALD) or chemical vapour deposition (CVD) by coating conformal polymer throughout the interior portions of an aerogel. For example, Boday et al. have employed this protocol to coat silica aerogel with methyl cyanoacrylate using ambient temperature CVD method.[93] They reported that this led to a 30-fold increase in strength of the aerogel with only a 3-fold increase in density.

To improve the flexibility of inorganic aerogels, another approach used was the adsorption of inorganic particles on the skeleton of flexible aerogels to form organic-inorganic composite aerogels.[94, 95] For example, Berglund et al. have made flexible porous magnetic aerogels by adsorbing ferromagnetic cobalt ferrite nanoparticles on flexible bacterial cellulose nanofibril aerogel.[95] They initially made a flexible aerogel template from bacterial cellulose hydrogel by freeze drying, then dipped this in $FeSo_4$/ $CoCl_2$ solution at room temperature followed by heating at 90^oC. Thermally precipitated nonmagnetic metal hydroxides/ oxides on templates were converted into ferrite crystal nanoparticles on immersion in NaOH/ KNO_3 solution at 90^oC. They have shown that in the composites, these nanoparticles were located on the bacterial cellulose nanofibril surfaces. They demonstrated that these magnetic aerogels were comprised of 79 wt% nanoparticles and yet exhibited elastic compressibility upto 80% strain.

Researchers have also used fibre mats to make flexible aerogels. Here, a wet particle gel is infiltrated into a porous, flexible fibre mat (fibrous batting) and super critically dried or freeze dried to produce a composite porous particle assembly.[96] For example, Xiang et al.

made flexible composite aerogels with interpenetrating network microstructure by a sol-gel process.[97] Here, they incorporated cellulose fibres in a three dimensional web like form, where the branching points were fixed solidly by a large number of hydrogen bonds between fibres, into silica sol. Silica particles diffused into the fibre matrix and an inorganic gel skeleton formed within the fibrous matrix during gelation. Freeze drying of this interpenetrated network structure gave a flexible aerogel composite. The major applications of flexible composite aerogels are in sub-sea oil pipe lines, thermal insulation, in shoe soles and house interior walls, hydrophobic surfaces and in laminates.

Rao et al. have shown another strategy to make flexible aerogels without the addition of polymer ductile phase. Here, they made highly flexible, super hydrophobic, thermally stable (~530 K) silica aerogels using methyltrimethoxysilane (MTMS) by a two step acid-base sol- gel process.[98, 99] The three methoxy groups of MTMS undergo hydrolysis and condensation. As condensation progressed, the ≡Si-CH_3 hydrophobic groups increased compared to ≡Si-OH leading to an inorganic- organic hybrid silica network which was flexible (compression ~60% by volume) and superhydrophobic. They have also shown that hydrolysis in presence of acid catalyst and condensation in presence of base catalyst is essential for the formation of continuous network required for flexibility. These hybrids have been used for absorption of toxic chemicals and non-polar compounds.

Apart from toughness improvement, addition of ductile phase to particle assemblies affects the rheology and glass transition of the system.[100] For example, class I hybrids having polymeric ductile phase showed an increase in glass transition temperature, corresponding to a loss in segmental mobility in the soft phase. Also, hybrids made from inorganic particles with excess polymer ductile phase have decreased materials stiffness along with high temperature stability. For example, materials exhibiting highest toughness are comprised of atleast 20 vol% of a polymeric phase which restricts its high temperature use to 200^{o}C or less.[101]

To overcome these limitations, Deville et al. have made nacre–like damage resistant ceramics purely from mineral constituents.[101] They have fabricated dense ceramic materials with five structural features spanning several length scales: closely packed ceramic platelets of dimensions identical to nacre (500 nm thick and 0.9 μm diameter), ceramic bridges linking the platelets, nano-asperities at the surface of platelets and a secondary phase with lower stiffness ensuring crack deflection, delamination and load redistribution. 100 nm size aluminium particles acted like a bridge between platelets and provided nano asperities. 20 nm

size silica or calcia particles filled the remaining gap between the platelets. The synthesis process was multistep, comprising preparation of colloidal suspension, ice templating to drive the platelet assembly followed by a pressure assisted synthesis at high temperature (~ 1500^{o}C). The tough ceramic that formed could sustain high temperature in contrast to organic phase filled hybrid structures. However, the drawback of this protocol is that it is a multistep process requiring high temperature sintering.

In 2014, Rajamanickam et al. reported a general protocol to make flexible particle assemblies using a very simple, single step ice templating process.[12] The materials they report are class I flexible inorganic–organic hybrid structures, with < 20 wt% organic content. This thesis focuses on understanding the structural underpinnings of the mechanical response of these flexible particle assemblies. We now present a detailed account of the synthesis, features and applications of these flexible sponges.

1.7 Elastically recoverable soft colloidal scaffolds

Rajamanickam et al. have demonstrated a one-step freezing method to make elastic, macroporous particle-polymer assemblies.[12] These materials can recover their shape after being compressed to less than 15% of their original size even though the material is composed of 90 wt% of particles. These materials were prepared using a modification of the classical ice templating process. They started with particles and a polymer-crosslinker mixture dispersed in water and froze this dispersion. This process is known as ice templating. The polymer physically adsorbed on the particle surface and was crosslinked in the frozen state. After crosslinking the polymer for a day, the ice crystals were removed by room temperature thawing to yield a hybrid assembly. Before discussing the interesting features and applications of this material, the physics of the ice templating process will be discussed first.

1.7.1 Ice templating: A simple and versatile method to generate macroporosity

The use of solvent crystals to prepare porous materials is known as crystal templating. In 1987, Nakazawa et al. introduced freezing as a protocol to control the porous structure of clay aerogels.[102] Apart from water, solidification of a variety of solvents has been used to template the organization of dispersed solutes.[103] Crystallization of a solvent containing colloids differs from pure solvent crystallization. The presence of colloids changes its freezing point because of change in chemical potential.[103] The chemical potential of a particle dispersion can be given as:

$$\mu_1^A = \mu^f(T,P) - \frac{\pi(T,\varphi)}{\rho_f}$$

where, μ^f is the chemical potential of pure solvent, π; osmotic pressure, ρ_f; solvent density, T; temperature, P; pressure and φ is the concentration of colloids.

The freezing point of the dispersion is; $T_f = T_m(1+m\varphi z)^{-1}$, where, T_m is the melting point of the pure solvent, $m = \frac{k_B {T_m}^2}{v_p \rho_f L_f}$, k_B is the Boltzmann constant, v_p is the volume of a particle, L_f the latent heat and z is the compressibility factor which accounts for particle-particle interactions. Therefore, the freezing point of a colloidal suspension is a function of fraction and size of colloids. For example, it has been predicted that for an aqueous suspension, the freezing point drops to -10°C from 0°C when colloid fraction changes from 0.4 to 0.6.[103]

The nucleation of ice crystals happens when the suspension temperature reaches its freezing point. Typically, nucleation is heterogeneous in a colloidal suspension and happens when energetically favourable sites are available for the formation of nuclei. The surface of solid particles, surface of the cold substrate where the suspension is stored or impurities can act as nucleation sites. The formation of nuclei occurs when the change of free energy that accompanies the formation of the nuclei is negative. This variation in free energy is the sum of contributions coming from the formation of new surfaces (ΔG_s) and the change in volume (ΔG_v), where the (ΔG_s) is always positive and (ΔG_v) is always negative. The free energy change for the homogeneous formation of a spherical nucleus is, $\Delta G_{homo} = \sigma 4\pi r^2 + \Delta g \frac{4}{3}\pi r^3$ and the free energy change for the heterogeneous nucleation is ΔG_{homo} weighted by a factor, $f(\theta)$ that depends on contact angle between impurity and the nucleus, θ, i.e. $\Delta G_{hetero} = \Delta G_{homo} f(\theta)$.[103]

$$f(\theta) = \frac{2-3\cos\theta+\cos^3\theta}{4},$$

where, r is the radius of the nucleus; σ is the surface tension; Δg is the volumetric free energy change between the liquid and solid phases. When the size of the nucleus, r, is greater than a critical size (r_c) (correspondingto the metastable state of the system), the nucleus will grow and if $r < r_c$the nucleus will dissolve to reduce the free energy. Once the nucleus dimension reaches r_c, a rapid growth of crystal occurs. These crystals can grow from a few microns to a few mm in dimension based on the system and conditions. If the surface for nucleation is large enough then nucleation can occur at several locations. Each one of these crystals will grow independently and form a domain until it impinges on another domain.

Once these crystals impinge, the boundaries of the domains are relatively stable. However, when colloids are present in the solution, they will be either expelled or engulfed by the growing crystals depending on the freezing rate. In those cases, the morphology and stability of the crystal–particle interface strongly depend on freezing front velocity and size of the colloids. Deville et al. have represented the chance of particle localization for different interface velocity and colloidal size in the form of a "phase" diagram (Figure 1.5).[103]

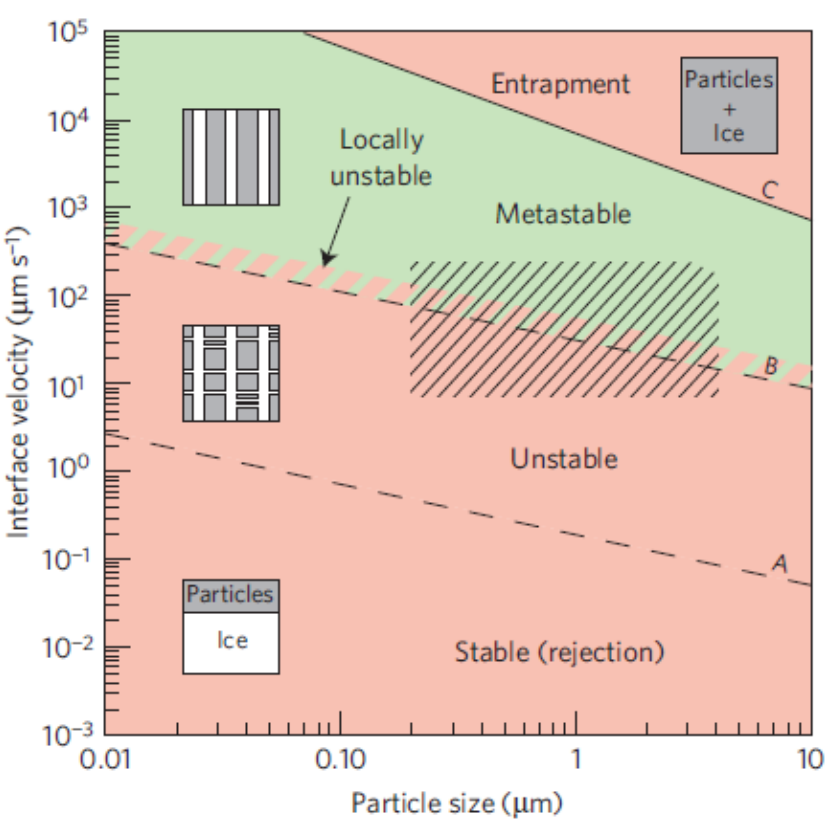

Figure 1.5: General stability and structure diagram of freezing colloidal dispersion. The green regions indicate the metastable conditions suitable for processing homogeneous and defect free cellular materials. Red areas are not suitable for the processing of defect free ice templated materials. *(Reprinted with permission from reference[104]. Copyright © 2009, Springer Nature.)*

They find that, for low growth front velocities (< 1μm/s) and small particle size, the water-ice interface is planar and all colloids are rejected. If the velocity is very high (> 1mm/s), then the interface morphology does not change from planar but it encapsulates all the particles without any redistribution. At intermediate velocities (1μm/s– 1mm/s) and particle sizes, a cellular interface forms and two sub-domains of stable and unstable growth conditions are found (Figure 1.5). Rejection of colloidal particles during the cellular growth of ice crystals

(Figure 1.6) results in particles getting trapped between crystals. Sublimation of the ice crystals leads to a porous structure with pore walls made of particles. This technique has been extensively used in the ceramic community to make porous structures. The pore size and shape is set by the crystal morphology which in turn can be tuned by varying freezing solvents and growth rate.[103] The directionality of pores can be controlled by adjusting the temperature gradient in the freezing system. The pore wall thickness increases with colloid concentration which in turn decreases the pore size.

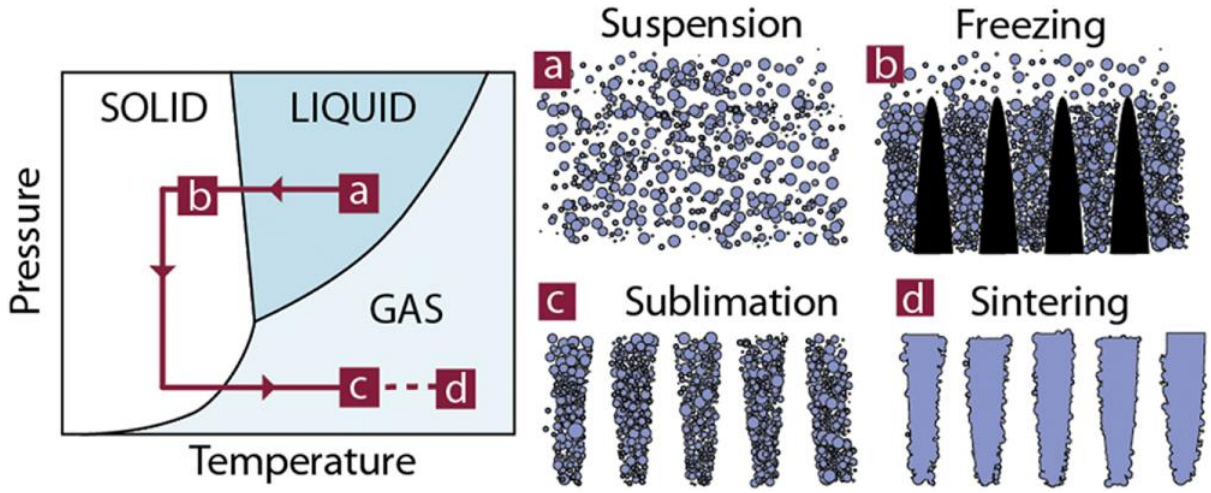

Figure 1.6: Schematic representation of unidirectional ice templating followed by sublimation of ice crystals and sintering. *(Reprinted with permission from reference[105].)*

The spatial arrangement of particles concentrated by crystals plays a key role in controlling the structure and physical properties of the ice templated materials. It has been reported that for low interface velocity, monodisperse hard spheres form an ordered arrangement (colloidal crystals) near the water-ice interface and that there is a transformation to a disordered assembly as the velocity increases.[103] The factors which account for the organization of particles are: a) nature and magnitude of the interaction between particles b) solvent characteristics, which include ionic strength, pH and type of solvent c) shape and size distribution of particles and d) crystal growth kinetics. To bring the particles in contact, growing crystals exert sufficient pressure to overcome the electrostatic repulsion between those particles. Once these particles are in contact, van der Waals interactions help to retain the structure even after the removal of ice through sublimation. However, this pressure is not sufficient to make strong particle aggregates. Therefore, the ice templated samples are sintered after sublimation or binders are added to retain the templated structures after removal of ice.

The major advantages of ice templating are: a) wide range of porosity (40-99.99%) and pore size (4-500 μm) can be obtained by this method. b) This method doesn't require any additional chemicals to generate pores or any additional thermal treatment step to remove porogens. c) Ice templating is not limited to pure phases and it can also be used for making porous composites; d) the pore size and shape can be easily tuned by various additives including antifreeze proteins, ethanol, glycerol etc. These additives either change the phase diagram of solvent used or they modify the properties of the suspension or the growth kinetics of crystals by blocking certain crystallographic growth directions or planes. However, ice templating is not a suitable method to obtain macroporous materials with low porosity (lower than 40%). Ice templated porous materials have been extensively used for membranes, in biomedical applications, as armour, as piezoelectric materials and as impact resistant materials.[103]

1.7.2 Interesting features and applications of ice templated particle- polymer hybrids

Rajamanickam et al. have shown the preparation of ice templated particle-polymer hybrids that can recover from 90% compressive strain and are stable over multiple compression-expansion cycles.[12] These sponges have a foam-like morphology with interconnected pores. The pore walls are made of particles embedded in crosslinked polymer (Figure 1.7 a-b). They have reported materials with pore volume of 0.9 cc/cc and bulk density of 0.13 g/cc. However, the Young's modulus was significantly lower (~20 kPa) than for highly filled particle composites. Therefore, it is clear that the mechanical properties of the hybrids reflect a combined effect of polymer and particles. Another very interesting feature they have reported was that the monolith mechanical response is entropic in origin: the modulus of this sponge increases with temperature over a temperature range of 140^{o}C (Figure 1.7c). This behaviour is well known for polymer rubbers and indicates that the elasticity is entropic in origin.[106]

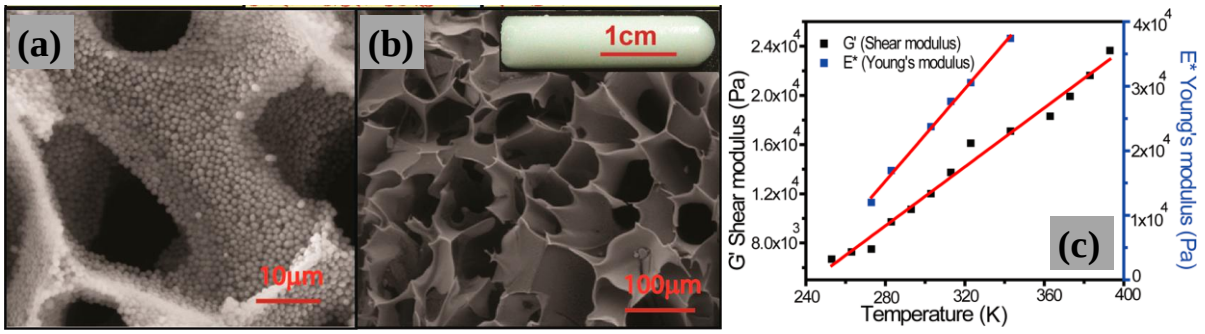

Figure 1.7: Features of ice templated sponges. (**a**)-(**b**) Scanning electron micrographs showmacroporous morphology and pore walls are made of particles embedded in polymer. (**c**) Variation of modulus of these sponges as a function of temperature. *(Reprinted with permission from reference[12]. Copyright (2014), American Chemical Society.)*

Most importantly, Rajamanickam et al. have shown that the elastic response of these ice templated crosslinked assemblies is obtained for particles with different composition, for different polymers and for different crosslinking chemistries.[12]

Chatterjee et al. have used ice templating to prepare omniphilic sponges.[13] They report chemically modified omniphilic sponges that absorb over 10 fold their dry weight of either water or hexane. They have shown the potential of ice templated hybrid sponges as compressible super capacitors[15] and as environmentally friendly fire retardant foams[14]. Rajamanickam et al. have demonstrated the use of ice templated biocompatible materials as tissue engineering scaffolds.[12] While it is clear that ice templated macroporous hybrids represent platform materials with a wide variety of uses, the structural underpinning of their superflexibility in ice templated hybrids remained unclear.

1.8 Objective of Thesis

Ice templated hybrid structures address a major drawback of particle assemblies, i.e., brittleness. Therefore, understanding structure-property relations in such materials is of interest. In this study, we try to understand the detailed microstructure of the ice templated inorganic/organic hybrids and try to address the reasons for their elasticity. Ice templated materials are characterized by structural features at a wide variety of length scales: from the crosslinked polymer films that separate particles and that are about ten nanometers in width, to the micron sized inorganic particles, to the 100 micron sized void structures and the centimeter scale size of the macroscopic foams. Similarly, dynamics in these materials span from the nanosecond time scales of polymer segmental motions to the millisecond time scales of particle Brownian motions. The dynamics of foam deformation and macroscopic recovery take place over a time scale of seconds. We chose to use a multi-pronged strategy by

investigating the material at these various length and time scales, using different experimental tools. Finally, we combine the results from these different studies to present a unified picture of the microstructure of these materials.

1.9 Outline of Thesis

Chapter 1: In this chapter, we provide background literature to motivate our investigations on the origin of elasticity in ice templated particle- polymer hybrid structures.

Chapter 2: We study the effect of template on the elasticity of ice templated hybrid structures. Our study shows that the synthesis of elastic particle based sponges is determined by the template. Elastic sponge forms only if the polymer is crosslinked in presence of ice crystal templates. Polymer crosslinking in absence of ice crystals leads to plastic monoliths which cannot sustain even small deformations. We characterise elastic and plastic monoliths using various techniques:

- Compression- expansion behaviour of scaffolds: Rheometry
- Morphology: Scanning electron microscopy
- Structure: Small angle X-ray scattering
- Total organic content: Thermogravimetric analysis
- Crosslinker to polymer ratio: ^{13}C Nuclear Magnetic Resonance spectroscopy
- Overall crosslinking density: Shear rheology
- Nanoscale energy dissipation: Amplitude modulation- atomic force microscopy

Our study shows that the crosslinking in presence of ice crystal modulates the properties of the polymer mesh that connects the particles in the assembly and determines its mechanical properties.

Chapter 3: We study the microstructure-property relationships in elastic sponge and plastic monolith. To obtain the local structure and property, we investigate the colloidal dynamics in elastic sponge and plastic monolith using single particle tracking technique. Since, these are particle filled systems, colloidal motions in these assemblies are sluggish. Therefore, particle tracking is sensitive to imaging artefacts such as stage drift. To obtain the thermal vibrations of particles, we have to eliminate those artefacts. In this chapter, we demonstrate that:

- Use of wavelet transform applied to trajectories of probe particles from fluorescence microscopy eliminates stage drift, allowing a dynamical resolution of about 2 nm.

- Mean square displacement and van Hove jump distribution obtained from particles motions show that the plastic monoliths are characterised by significantly larger spatial heterogeneity when compared with the elastic sponges.
- Microrheology shows wider distribution of local modulus for plastic monoliths as compared to elastic sponges.

Our study shows that the ice crystals set the spatial distribution of mechanical properties in ice templated scaffolds.

Chapter 4: We study the microstructure of elastic sponge and plastic monolith during compression using X-ray computed micro-tomography and single particle tracking. Studies show that the crosslinking in presence of ice crystals lead to flexible interparticle bridges which allow the elastic deformation of pore walls when it is compressed. Flexible bridges also allow them to recover during release of load. However, crosslinking in absence of ice crystals leads to formation of plastic domains. These domains concentrate stress when the monolith is compressed and massive failure of these domains occur at moderate deformations. Therefore, bigger cracks propagate through the sample and the entire assembly fails in contrast to elastic sponges. This study confirms that the properties of polymer which connects particles decide the overall mechanical properties of particle- polymer hybrids.

Chapter 5: We systematically vary the organic content in scaffolds crosslinked in presence and absence of ice crystals by keeping the particle content fixed. We further study the mechanical properties, nanoscale structure, colloidal dynamics and molecular structure of these scaffolds using rheometry, small angle X-ray scattering, single particle tracking and solid state nuclear magnetic resonance spectroscopy respectively. Our study shows that, at higher organic loading, scaffolds crosslinked in absence of ice crystals show a transition from plastic to elastic. The spatial heterogeneity found in plastic monoliths disappears at higher organic loading. Our Solid state NMR study shows a difference in the amount of water cluster in scaffolds crosslinked in presence and absence of ice crystals. We presume that the polymer crosslinking reaction will be affected by the extent of neighbouring water molecules in these systems. This affects the spatial crosslinking density and therefore the local mechanical properties.

Chapter 6: We study the effect of interaction between polymer and particle on elasticity of ice templated sponges. We tune the interaction between polymer and particle by changing the pH of the solution where the scaffolds are dipped. We have made scaffolds with silica

spherical particles and these particles exhibit an isoelectric point in the range of 3-4. Compression expansion study shows that the sponges are elastic at all pH. However, a threefold decrease in mechanical stiffness is observed when the pH is below the isoelectric point. Similar results are obtained for sponges prepared using hematite spherical particles where the isoelectric point is at pH near 8. We hypothesize that the reduction in mechanical stiffness could be because of desorption of the polymer from spherical particle surface when the particle surface charge becomes positive.

Chapter 7: Provides a concise summary of the work presented in the thesis.

1.10 References

1. Phillips, K. R.; England, G. T.; Sunny, S.; Shirman, E.; Shirman, T.; Vogel, N.; Aizenberg, J., A colloidoscope of colloid-based porous materials and their uses. *Chem. Soc. Rev.* **2016,** 45, 281-322.

2. Iskandar, F.; Mikrajuddin, a.; Okuyama, K., In situ production of spherical silica particles containing self-organized mesopores. *Nano Lett.* **2001,** 1, 231-234.

3. Iskandar, F.; Mikrajuddin, a.; Okuyama, K., Controllability of pore size and porosity on self-organized porous silica particles. *Nano Lett.* **2002,** 2, 389-392.

4. Arachchige, I. U.; Brock, S. L., Sol-gel methods for the assembly of metal chalcogenide quantum dots. *Acc. Chem. Res.* **2007,** 40, 801-809.

5. Sharma, K. P.; Ganai, A. K.; Gupta, S. S.; Kumaraswamy, G., Self-standing three-dimensional networks of nanoparticles with controllable morphology by dynamic templating of surfactant hexagonal domains. *Chem. Mater.* **2011,** 23, 1448-1455.

6. Rhodes, K. H.; Davis, S. A.; Caruso, F.; Zhang, B.; Mann, S., Hierarchical Assembly of Zeolite Nanoparticles into Ordered Macroporous Monoliths Using Core-Shell Building Blocks. *Chem. Mater.* **2000,** 12, 2832-2834.

7. Leventis, N.; Sotiriou-Leventis, C.; Zhang, G.; Rawashdeh, A.-M. M., Nanoengineering strong silica aerogels. *Nano Lett.* **2002,** 2, 957-960.

8. Stein, A.; Schroden, R. C., Colloidal crystal templating of three-dimensionally ordered macroporous solids: Materials for photonics and beyond. *Curr. Opin. Solid State Mater. Sci.* **2001,** 5, 553-564.

9. Gibson, L. J.; Ashby, M. F., *Cellular solids: Structure and Properties*. Cambridge university press: **1999**.

10. Pierre, A. C.; Pajonk, G. M., Chemistry of aerogels and their applications. *Chem. Rev.* **2002,** 102, 4243-4266.

11. Husing, N.; Schubert, U., Aerogels-airy materials: Chemistry, structure, and properties. *Angew. Chem., Int. Ed.* **1998,** 37, 22-45.

12. Rajamanickam, R.; Kumari, S.; Kumar, D.; Ghosh, S.; Kim, J. C.; Tae, G.; Sen Gupta, S.; Kumaraswamy, G., Soft colloidal scaffolds capable of elastic recovery after large compressive strains. *Chem. Mater.* **2014,** 26, 5161-5168.

13. Chatterjee, S.; Sen Gupta, S.; Kumaraswamy, G., Omniphilic polymeric sponges by ice templating. *Chem. Mater.* **2016,** 28, 1823-1831.

14. Chatterjee, S.; Shanmuganathan, K.; Kumaraswamy, G., Fire-Retardant, Self-Extinguishing Inorganic/Polymer Composite Memory Foams. *ACS Appl. Mater. Interfaces* **2017,** 9, 44864-44872.

15. Das, C.; Chatterjee, S.; Kumaraswamy, G.; Krishnamoorthy, K., Elastic Compressible Energy Storage Devices from Ice Templated Polymer Gels treated with Polyphenols. *J. Phys. Chem. C* **2017,** 121, 3270-3278.

16. Everett, D. H., Manual of symbols and terminology for physicochemical quantities and units, appendix II: Definitions, terminology and symbols in colloid and surface chemistry. *Pure Appl. Chem.* **1972,** 31, 577-638.

17. Stober, W.; Fink, A.; Bohn, E., Controlled growth of monodisperse silica spheres in the micron size range. *J. Colloid Interface Sci.* **1968,** 26, 62-69.

18. Tumarkin, E.; Kumacheva, E., Microfluidic generation of microgels from synthetic and natural polymers. *Chem. Soc. Rev.* **2009,** 38, 2161-2168.

19. Xia, Y.; Gates, B.; Yin, Y.; Lu, Y., Monodispersed colloidal spheres: Old materials with new applications. *Adv. Mater.* **2000,** 12, 693-713.

20. Landfester, K.; Bechthold, N.; Tiarks, F.; Antonietti, M., Formulation and stability mechanisms of polymerizable miniemulsions. *Macromolecules* **1999,** 32, 5222-5228.

21. Tseng, C. M.; Lu, Y. Y.; El-Aasser, M. S.; Vanderhoff, J. W., Uniform polymer particles by dispersion polymerization in alcohol. *J. Polym. Sci. Part A: Polym. Chem.* **1986,** 24, 2995-3007.

22. Hohenstein, W. P.; Mark, H., Polymerization of olefins and diolefins in suspension and emulsion. Part I. *J. Polym. Sci. A: Polym. Chem.* **1946,** 1, 127-145.

23. Groschel, A. H.; Walther, A.; Lobling, T. I.; Schacher, F. H.; Schmalz, H.; Muller, A. H. E., Guided hierarchical co-assembly of soft patchy nanoparticles. *Nature* **2013,** 503, 247.

24. Nie, Z.; Li, W.; Seo, M.; Xu, S.; Kumacheva, E., Janus and ternary particles generated by microfluidic synthesis: Design, synthesis, and self-assembly. *J. Am. Chem. Soc.* **2006,** 128, 9408-9412.

25. van den Brom, C. R.; Anac, I.; Roskamp, R. F.; Retsch, M.; Jonas, U.; Menges, B.; Preece, J. A., The swelling behaviour of thermoresponsive hydrogel/silica nanoparticle composites. *J. Mater. Chem.* **2010,** 20, 4827-4839.

26. Still, T.; Sainidou, R.; Retsch, M.; Jonas, U.; Spahn, P.; Hellmann, G. P.; Fytas, G., The "Music" of Core-Shell Spheres and Hollow Capsules: Influence of the Architecture on the Mechanical Properties at the Nanoscale. *Nano Letters* **2008,** 8, 3194-3199.

27. Rossi, L.; Sacanna, S.; Irvine, W. T. M.; Chaikin, P. M.; Pine, D. J.; Philipse, A. P., Cubic crystals from cubic colloids. *Soft Matter* **2011,** 7, 4139-4142.

28. Manoharan, V. N.; Elsesser, M. T.; Pine, D. J., Dense packing and symmetry in small clusters of microspheres. *Science* **2003,** 301, 483-487.

29. Dinsmore, A. D.; Hsu, M. F.; Nikolaides, M. G.; Marquez, M.; Bausch, A. R.; Weitz, D. A., Colloidosomes: Selectively permeable capsules composed of colloidal particles. *Science* **2002,** 298, 1006-1009.

30. Whitesides, G. M.; Grzybowski, B., Self-assembly at all scales. *Science* **2002,** 295, 2418-2421.

31. Ariga, K.; Hill, J. P.; Ji, Q., Layer-by-layer assembly as a versatile bottom-up nanofabrication technique for exploratory research and realistic application. *Phys. Chem. Chem. Phys.* **2007,** 9, 2319-2340.

32. Klajn, R.; Bishop, K. J. M.; Grzybowski, B. A., Light-controlled self-assembly of reversible and irreversible nanoparticle suprastructures. *PNAS* **2007,** 104, 10305-10309.

33. Hermanson, K. D.; Lumsdon, S. O.; Williams, J. P.; Kaler, E. W.; Velev, O. D., Dielectrophoretic assembly of electrically functional microwires from nanoparticle suspensions. *Science* **2001,** 294, 1082-1086.

34. Tripp, S. L.; Dunin-Borkowski, R. E.; Wei, A., Flux Closure in Self-Assembled Cobalt Nanoparticle Rings. *Angew. Chem. Int. Ed.* **2003,** 42, 5591-5593.

35. Evans, D. F.; Wennerstrom, H., The colloidal domain: Where physics, chemistry, biology, and technology meet. **1999,** Second Edition, Wiley- VCH.

36. Israelachvili, J. N., *Intermolecular and surface forces*. Academic press: **2011**.

37. Liu, L.; Choi, B. G.; Tung, S. O.; Hu, T.; Liu, Y.; Li, T.; Zhao, T.; Kotov, N. A., Low-current field-assisted assembly of copper nanoparticles for current collectors. *Faraday Discuss.* **2015,** 181, 383-401.

38. Schmidt, G.; Malwitz, M. M., Properties of polymer-nanoparticle composites. *Curr Opin Colloid Interface Sci.* **2003,** 8, 103-108.

39. Niederberger, M., Multiscale Nanoparticle Assembly: From Particulate Precise Manufacturing to Colloidal Processing. *Adv. Funct. Mater.* **2017,** 27, 1703647.

40. Giersig, M.; Pastoriza-Santos, I.; Liz-Marzan, L. M., Evidence of an aggregative mechanism during the formation of silver nanowires in N, N-dimethylformamide. *J. Mater. Chem.* **2004,** 14, 607-610.

41. Li, M.; Johnson, S.; Guo, H.; Dujardin, E.; Mann, S., A Generalized Mechanism for Ligand-Induced Dipolar Assembly of Plasmonic Gold Nanoparticle Chain Networks. *Adv. Funct. Mater.* **2011,** 21, 851-859.

42. Wei, Q. H.; Su, K. H.; Durant, S.; Zhang, X., Plasmon resonance of finite one-dimensional Au nanoparticle chains. *Nano Lett.* **2004,** 4, 1067-1071.

43. Keng, P. Y.; Shim, I.; Korth, B. D.; Douglas, J. F.; Pyun, J., Synthesis and self-assembly of polymer-coated ferromagnetic nanoparticles. *ACS Nano* **2007,** 1, 279-292.

44. Born, P.; Munoz, A.; Cavelius, C.; Kraus, T., Crystallization mechanisms in convective particle assembly. *Langmuir* **2012,** 28, 8300-8308.

45. Jiang, P.; Prasad, T.; McFarland, M. J.; Colvin, V. L., Two-dimensional nonclose-packed colloidal crystals formed by spincoating. *Appl. Phys. Lett.* **2006,** 89, 011908.

46. Giersig, M.; Mulvaney, P., Preparation of ordered colloid monolayers by electrophoretic deposition. *Langmuir* **1993,** 9, 3408-3413.

47. Park, C.; Lee, T.; Xia, Y.; Shin, T. J.; Myoung, J.; Jeong, U., Quick, Large-Area Assembly of a Single-Crystal Monolayer of Spherical Particles by Unidirectional Rubbing. *Adv. Mater.* **2014,** 26, 4633-4638.

48. Retsch, M.; Zhou, Z.; Rivera, S.; Kappl, M.; Zhao, X. S.; Jonas, U.; Li, Q., Fabrication of Large-Area, Transferable Colloidal Monolayers Utilizing Self-Assembly at the Air/Water Interface. *Macromol. Chem. Phys.* **2009,** 210, 230-241.

49. Ye, X.; Qi, L., Two-dimensionally patterned nanostructures based on monolayer colloidal crystals: Controllable fabrication, assembly, and applications. *Nano Today* **2011,** 6, 608-631.

50. Malaquin, L.; Kraus, T.; Schmid, H.; Delamarche, E.; Wolf, H., Controlled particle placement through convective and capillary assembly. *Langmuir* **2007,** 23, 11513-11521.

51. Vos, W. L.; Megens, M.; van Kats, C. M.; Bosecke, P., X-ray diffraction of photonic colloidal single crystals. *Langmuir* **1997,** 13, 6004-6008.

52. Bardosova, M.; Pemble, M. E.; Povey, I. M.; Tredgold, R. H., The Langmuir-Blodgett Approach to Making Colloidal Photonic Crystals from Silica Spheres. *Adv. Mater.* **2010,** 22, 3104-3124.

53. Mihi, A.; Ocana, M.; Miguez, H., Oriented Colloidal-Crystal Thin Films by Spin-Coating Microspheres Dispersed in Volatile Media. *Adv. Mater.* **2006,** 18, 2244-2249.

54. Vasquez, Y.; Kolle, M.; Mishchenko, L.; Hatton, B. D.; Aizenberg, J., Three-phase co-assembly: In situ incorporation of nanoparticles into tunable, highly ordered, porous silica films. *ACS Photonics* **2013,** 1, 53-60.

55. Pursiainen, O. L. J.; Baumberg, J. J.; Winkler, H.; Viel, B.; Spahn, P.; Ruhl, T., Shear-Induced Organization in Flexible Polymer Opals. *Adv. Mater.* **2008,** 20, 1484-1487.

56. Li, Y.; Zhang, J.; Zhu, S.; Dong, H.; Jia, F.; Wang, Z.; Sun, Z.; Zhang, L.; Li, Y.; Li, H., Biomimetic surfaces for high-performance optics. *Adv. Mater.* **2009,** 21, 4731-4734.

57. Park, S.-G.; Lee, S. Y.; Jang, S. G.; Yang, S.-M., Perfectly hydrophobic surfaces with patterned nanoneedles of controllable features. *Langmuir* **2010,** 26, 5295-5299.

58. Vogel, N.; Belisle, R. A.; Hatton, B.; Wong, T.-S.; Aizenberg, J., Transparency and damage tolerance of patternable omniphobic lubricated surfaces based on inverse colloidal monolayers. *Nat. Commun.* **2013,** 4, 2176.

59. Park, C.; Koh, K.; Jeong, U., Structural color painting by rubbing particle powder. *Sci. Rep.* **2015,** 5, 8340.

60. Chung, K.; Yu, S.; Heo, C. J.; Shim, J. W.; Yang, S. M.; Han, M. G.; Lee, H.-S.; Jin, Y.; Lee, S. Y.; Park, N., Flexible, Angle-Independent, Structural Color Reflectors Inspired by Morpho Butterfly Wings. *Adv. Mater.* **2012,** 24, 2375-2379.

61. Davis, M. E., Ordered porous materials for emerging applications. *Nature* **2002,** 417, 813.

62. Wijnhoven, J. E. G. J.; Bechger, L.; Vos, W. L., Fabrication and characterization of large macroporous photonic crystals in titania. *Chem. Mater.* **2001,** 13, 4486-4499.

63. Subramanian, G.; Manoharan, V. N.; Thorne, J. D.; Pine, D. J., Ordered macroporous materials by colloidal assembly: A possible route to photonic bandgap materials. *Adv. Mater.* **1999,** 11, 1261-1265.

64. Malek, K.; Coppens, M.-O., Effects of surface roughness on self-and transport diffusion in porous media in the Knudsen regime. *Phys. Rev. Lett.* **2001,** 87, 125505.

65. Hench, L. L.; West, J. K., The sol-gel process. *Chem. Rev.* **1990,** 90, 33-72.

66. Kearby, K.; Kistler, S. S.; Swann, S., Aerogel Catalyst Conversion of Alcohols to Amines. *Ind. Eng. Chem.* **1938,** 30, 1082-1086.

67. Husing, N.; Schubert, U., Aerogels-Airy Materials: Chemistry, Structure, and Properties. *Angew. Chem. Int. Ed.* **1998,** 37, 22-45.

68. Yao, N.; Cao, S.; Yeung, K. L., Mesoporous TiO2-SiO2 aerogels with hierarchal pore structures. *Microporous Mesoporous Mater.* **2009,** 117, 570-579.

69. Baumann, T. F.; Satcher Jr, J. H., Template-directed synthesis of periodic macroporous organic and carbon aerogels. *J. Non-Cryst. Solids* **2004,** 350, 120-125.

70. Suh, D. J.; Park, T.-J., Sol-Gel strategies for pore size control of high-surface-area transition-metal oxide aerogels. *Chem. Mater.* **1996,** 8, 509-513.

71. Aegerter, M. A.; Leventis, N.; Koebel, M. M., *Aerogels handbook*. Springer Science & Business Media: **2011**.

72. Yasumori, A.; Kawazoe, H.; Yamane, M., The structural evolution of alkoxy-derived gel during drying. *J. Non-Cryst. Solids* **1988,** 100, 215-219.

73. Woignier, T.; Phalippou, J.; Vacher, R.; Pelous, J.; Courtens, E., Different kinds of fractal structures in silica aerogels. *J. Non-Cryst. Solids* **1990,** 121, 198-201.

74. Li, H.; He, P.; Wang, Y.; Hosono, E.; Zhou, H., High-surface vanadium oxides with large capacities for lithium-ion batteries: From hydrated aerogel to nanocrystalline VO_2 (B), V_6O_{13} and V_2O_5. *J. Mater. Chem.* **2011,** 21, 10999-11009.

75. Pajonk, G. M., Aerogel catalysts. *Appl. Catal.* **1991,** 72, 217-266.

76. Vincent, C.; Hallman, G.; Panneton, B.; Fleurat-Lessard, F., Management of agricultural insects with physical control methods. *Annu. Rev. Entomol.* **2003,** 48, 261-281.

77. Burchell, M. J.; Graham, G.; Kearsley, A., Cosmic dust collection in aerogel. *Annu. Rev. Earth Planet Sci.* **2006,** 34, 385-418.

78. Kim, B. N.; Hiraga, K.; Morita, K.; Sakka, Y., A high-strain-rate superplastic ceramic. *Nature* **2001,** 413, 288.

79. Roylance, D., Introduction to fracture mechanics. *MIT, Cambridge* **2001,** 1.

80. Carraher Jr, C. E., *Introduction to polymer chemistry*. CRC press: **2017**.

81. Woignier, T.; Hafidi Alaoui, A.; Primera, J.; Phalippou, J. In *Mechanical Properties of Aerogels: Brittle or Plastic Solids?*, Key Eng. Mater., **2009**; Trans Tech Publ: **2009**; pp 27-44.

82. Woignier, T.; Primera, J.; Alaoui, A.; Etienne, P.; Despestis, F.; Calas-Etienne, S., Mechanical properties and brittle behavior of silica aerogels. *Gels* **2015,** 1, 256-275.

83. Tam, E.; Podsiadlo, P.; Shevchenko, E.; Ogletree, D. F.; Delplancke-Ogletree, M.-P.; Ashby, P. D., Mechanical properties of face-centered cubic supercrystals of nanocrystals. *Nano Lett.* **2010,** 10, 2363-2367.

84. Pejchal, V.; Zagar, G.; Charvet, R.; Denereaz, C.; Mortensen, A., Compression testing spherical particles for strength: Theory of the meridian crack test and implementation for microscopic fused quartz. *J. Mech. Phys. Solids* **2017,** 99, 70-92.

85. Gallego-Gomez, F.; Morales-Florez, V.; Blanco, A.; de la Rosa-Fox, N.; Lopez, C., Water-dependent micromechanical and rheological properties of silica colloidal crystals studied by nanoindentation. *Nano Lett.* **2012,** 12, 4920-4924.

86. Quinn, J. B.; D Quinn, G., Indentation brittleness of ceramics: A fresh approach. *J. Mater. Sci.* **1997,** 32, 4331-4346.

87. Williams, J. G., Introduction to linear elastic fracture mechanics. In Elsevier: **2001**.

88. Meyers, M. A.; McKittrick, J.; Chen, P.-Y., Structural biological materials: Critical mechanics-materials connections. *Science* **2013,** 339, 773-779.

89. Smith, B. L.; Schaffer, T. E.; Viani, M.; Thompson, J. B.; Frederick, N. A.; Kindt, J.; Belcher, A.; Stucky, G. D.; Morse, D. E.; Hansma, P. K., Molecular mechanistic origin of the toughness of natural adhesives, fibres and composites. *Nature* **1999,** 399, 761.

90. Zhou, X.; Guo, B.; Zhang, L.; Hu, G.-H., Progress in bio-inspired sacrificial bonds in artificial polymeric materials. *Chem. Soc. Rev.* **2017,** 46, 6301-6329.

91. Sanchez, C.; Belleville, P.; Popall, M.; Nicole, L., Applications of advanced hybrid organic-inorganic nanomaterials: From laboratory to market. *Chem. Soc. Rev.* **2011,** 40, 696-753.

92. Arndt, E. M.; Gawryla, M. D.; Schiraldi, D. A., Elastic, low density epoxy/clay aerogel composites. *J. Mater. Chem.* **2007,** 17, 3525-3529.

93. Boday, D. J.; DeFriend, K. A.; Wilson Jr, K. V.; Coder, D.; Loy, D. A., Formation of Polycyanoacrylate-Silica Nanocomposites by Chemical Vapor Deposition of Cyanoacrylates on Aerogels. *Chem. Mater.* **2008,** 20, 2845-2847.

94. Korhonen, J. T.; Hiekkataipale, P.; Malm, J.; Karppinen, M.; Ikkala, O.; Ras, R. H. A., Inorganic Hollow Nanotube Aerogels by Atomic Layer Deposition onto Native Nanocellulose Templates. *ACS Nano* **2011,** 5, 1967-1974.

95. Olsson, R. T.; Samir, M. A. S. A.; Salazar-Alvarez, G.; Belova, L.; Strom, V.; Berglund, L. A.; Ikkala, O.; Nogues, J.; Gedde, U. W., Making flexible magnetic aerogels and stiff magnetic nanopaper using cellulose nanofibrils as templates. *Nat. Nanotech.* **2010,** 5, 584.

96. Karatum, O.; Steiner Iii, S. A.; Griffin, J. S.; Shi, W.; Plata, D. L., Flexible, mechanically durable aerogel composites for oil capture and recovery. *ACS Appl. Mater. Interfaces* **2015,** 8, 215-224.

97. Sai, H.; Xing, L.; Xiang, J.; Cui, L.; Jiao, J.; Zhao, C.; Li, Z.; Li, F., Flexible aerogels based on an interpenetrating network of bacterial cellulose and silica by a non-supercritical drying process. *J. Mater. Chem. A* **2013,** 1, 7963-7970.

98. Rao, A. V.; Bhagat, S. D.; Hirashima, H.; Pajonk, G. M., Synthesis of flexible silica aerogels using methyltrimethoxysilane (MTMS) precursor. *J Colloid Interface Sci.* **2006,** 300, 279-285.

99. Nadargi, D. Y.; Latthe, S. S.; Hirashima, H.; Rao, A. V., Studies on rheological properties of methyltriethoxysilane (MTES) based flexible superhydrophobic silica aerogels. *Microporous Mesoporous Mater.* **2009,** 117, 617-626.

100. Tan, J. C.; Cheetham, A. K., Mechanical properties of hybrid inorganic-organic framework materials: Establishing fundamental structure-property relationships. *Chem. Soc. Rev.* **2011,** 40, 1059-1080.

101. Bouville, F.; Maire, E.; Meille, S.; Van de Moortele, B.; Stevenson, A. J.; Deville, S., Strong, tough and stiff bioinspired ceramics from brittle constituents. *Nat. Mater.* **2014,** 13, 508.

102. Nakazawa, H.; Yamada, H.; Fujita, T.; Ito, Y., Texture control of clay-aerogel through the crystallization process of ice. *Clay Sci.* **1987,** 6, 269-276.

103. Deville, S., *Freezing colloids: Observations, principles, control, and use: Applications in materials science, life science, earth science, food science, and engineering*. Springer: **2017**.

104. Deville, S.; Maire, E.; Bernard-Granger, G.; Lasalle, A.; Bogner, A.; Gauthier, C.; Leloup, J.; Guizard, C., Metastable and unstable cellular solidification of colloidal suspensions. *Nat. Mater.* **2009,** 8, 966.

105. Deville, S.; Meille, S.; Seuba, J., A meta-analysis of the mechanical properties of ice-templated ceramics and metals. *Sci. Technol. Adv. Mater.* **2015,** 16, 043501.

106. Treloar, L. R. G., The elasticity and related properties of rubbers. *Rep. Prog. Phys.* **1973,** 36, 755.

Chapter 2

The Template Determines Whether Chemically Identical Nanoparticle Scaffolds Show Elastic Recovery or Plastic Failure

Subtle variations in the preparation of ice-templated nanoparticle assemblies yield monoliths that are chemically identical, but that exhibit qualitatively different mechanical behaviour. We ice template aqueous dispersions to prepare macroporous monoliths comprising largely of silica nanoparticles held together by a crosslinked polymer mesh. When the polymer is crosslinked in the presence of ice crystals, we obtain an elastic sponge that is capable of recovery after imposition of large compressive strains (up to 80%). If, however, the ice is lyophilized before the polymer is crosslinked, we obtain a plastic monolith that fails even for modest strains (less than 10%). The elastic sponge and plastic monoliths are chemically identical, so that they have the same organic content, the same ratio of polymer-to-crosslinker and the same average crosslink density. Atomic force microscopy (AFM) was used to probe local mechanical properties of the crosslinked polymer mesh. These measurements indicate that plastic monoliths dissipate significantly more energy and have a larger spatial variation in local mechanical response relative to the elastic sponges. We believe that this behaviour might correlate with a wider spatial distribution of crosslinks in plastic scaffolds relative to elastic scaffolds.

The content of this chapter is published in,

"*Langmuir* 2016, 32,11623-11630".

2.1 Introduction

Nanoparticle assemblies are anticipated to find application as optical materials, in electronics as well as sensors.[1] The mechanical properties of nanoparticle assemblies are important for the use of such materials in practical applications. There are now several reports[2-7] on the formation of mechanically robust ultrathin two-dimensional sheets comprised of nanoparticles. As discussed in Chapter 1, these sheets are formed either by interdigitation of the ligands that cap the nanoparticles[4-7] or by "crosslinking" the sheet using bifunctional link molecules[2] or by employing nanoparticles capped with crosslinkable ligands.[3] However, very few studies have focused attention on the mechanical properties of three dimensional nanoparticle assemblies. Unlike single nanoparticle thick sheet-like assemblies, three dimensional assemblies of nanoparticles typically exhibit a plastic response.[8-12] The plasticity of nanoparticle assemblies has been exploited to produce molded macroscopic objects.[13] However, in most applications, a mechanically robust assembly is desirable. The mechanical response of three dimensional nanoparticle assemblies has been investigated using nanoindentation measurements.[14] The force exerted by the nanoparticle assemblies increases as the nanoindenter is pressed into the sample. However, on retracting the nanoindenter, the force rapidly decays to zero and the sample exhibits residual plastic deformation. Previous investigations have attributed this plastic failure of nanoparticle assemblies to the nature of the interparticle links formed by the organic ligand shell around the particles.[8, 9, 15]

Preparation of mechanically robust three-dimensional nanoparticle assemblies has focused on engineering the strength of the interparticle links. Layer-by-layer assembly of clay and poly(vinylalcohol), followed by crosslinking of the polymer, was demonstrated[16] to yield nacre-like ultra-tough composites that were mechanically superior to those held together purely through electrostatic interactions.[17] Super compressible DNA gold nanoparticle assemblies that could be osmotically compressed to reduce lattice size by a factor of 1.8 have been reported.[18] However, we note that in assemblies of gold nanoparticles using DNA tethers, the nanoparticles occupy only a small volume fraction of the entire metal/DNA assembly. In other work, researchers have used atom transfer radical polymerization (ATRP) to grow polymer brushes off silica nanoparticles to produce densely grafted particles.[19] These surface-grafted polymer chains entangle in nanoparticle assemblies to yield materials that are tough and fracture-resistant. However, these entanglements are in sufficient to produce

materials that remain elastic on subjecting to large deformations. Free radical polymerization initiated from the surface of aerogels has been demonstrated to render aerogel monoliths tough.[20] Mechanically robust aerogels have been produced by covalently linking the nanoparticles that comprise the aerogel.[21, 22] For example, aerogel monoliths obtained by crosslinking of amine modified silica aerogels using multifunctional epoxies[23] exhibit enhanced strength relative to typical brittle aerogels. Flexible aerogels that recover from compression have also been synthesized by using a fraction of trialkoxysilanes during sol-gel synthesis of aerogel monoliths.[24, 25]

Recently, our group has reported[26] a general route to prepare large, centimeter-sized macroporous particle aggregates that are capable of elastic recovery after repeated imposition of large compressive strains. These scaffolds are formed by ice-templating. Ice templating has emerged as a versatile technique for assembly of nanoparticles. Recent advances[27-29] in ice-templating have focused on employing directional cooling techniques to control nanoparticle organization. We do not use directional cooling. Rather, we have demonstrated[26] monolith formation by the consolidation of particles, polymer and crosslinker at the boundaries of ice crystals when an aqueous dispersion is frozen. Crosslinking of the polymer is effected in the frozen state. After crosslinking is complete, the sample is thawed to obtain a self-standing monolith with a macropore structure determined by the ice crystal templates. We have reported that monoliths comprised of 90% by weight of inorganic can recover from multiple cycles of compressive strains of up to 90%. Remarkably, we obtain elastic monoliths using this protocol, independent of the chemistry of the particles and polymer, independent of the particle size and polymer molecular weight and for different crosslinking chemistries. We had attributed the elastic recovery of the monoliths to the structure of the inorganic-crosslinked polymer hybrid. In this Chapter, we demonstrate that the synthesis of elastic nanoparticle-based sponges is determined by the template. Elastic sponges form only if the polymer is crosslinked in the presence of the ice crystal templates. We demonstrate that crosslinking in the presence of ice crystals modulates the properties of the polymer mesh that connects the nanoparticles in the assembly and determines its mechanical response.

2.2 Experimental Section

2.2.1 Materials:

Silica particles, trade name Ludox-TM (manufacturer specified size = 22 nm) are obtained as a 50% (w/v) dispersion and are used as received. Uncrosslinked PS latex was generously supplied as a gift by Microparticles GmbH (Germany). 1μm silica particles were obtained from Richen Industries (Hong Kong). Polyethylenimine (PEI, 25 kg/mol) and 1,4-butanediol diglycidyl ether were obtained from Sigma Aldrich. All materials were used as received. Structures of all the chemicals used in the experiments are shown in Figure 2.1.

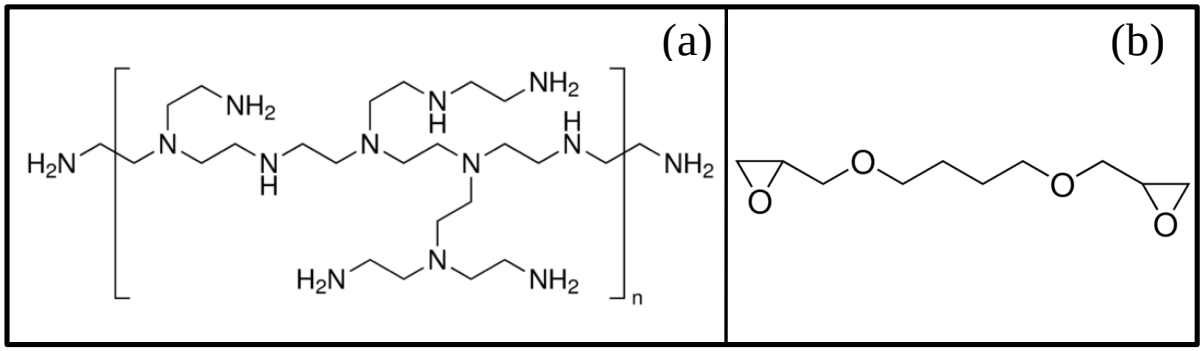

Figure 2.1: Chemical structure of (**a**) polyethylenimine and (**b**) 1,4-butanediol diglycidyl ether crosslinker.

2.2.2 Sample Preparation:

Synthesis of silica scaffolds: General protocol for the preparation of macroporous assemblies: 60 mg of the silica particles were dispersed in 560 μL of DI water (corresponding to a concentration of 10 % w/v) and sonicated for 20 min followed by 10 min of vortexing. To this aqueous dispersion was added 30μL of 100mg/mL aqueous PEI stock solution and was vortexed for 5 min. To this was added 10 mg of 1,4-butanediol diglycidyl ether, followed by vortexing for 3 min. This sample was subjected to either of the following protocols. (a) This sample was placed in a freezer maintained at approximately -15^{o}C, for 24h to prepare elastic sponges. (b) For preparation of plastic monoliths, the sample was frozen for 30 min at -15^{o}C. Subsequently, the frozen sample was lyophilized at -110^{o}C to sublime the ice crystals. After 6h of lyophilization, the sample was stored at -15^{o}C for 24h to allow crosslinking. In both protocols, the sample was allowed to crosslink over 24h at -15^{o}C. Subsequently, the samples were removed from the freezer and thawed. Finally, the

monoliths were washed multiple times with water to remove unreacted polymer and crosslinker.

Synthesis of uncrosslinked polystyrene (PS) particle scaffold, and dissolution of PS particles to obtain gel: To 10 wt% dispersion of 1µm uncrosslinked PS latex particles (Micro particles, GmbH, Germany) in aqueous medium was added 3 mg (30µl stock solution) of PEI (25 kDa). This was vortexed for 10 min so that the PEI adsorbs on the particle surface through electrostatic interactions. To this, 10 mg of 1,4-butanediol diglycidyl ether was added and vortexed for 3 min. The sample was frozen at -15^{o}C for 24 h to prepare an elastic monolith. To prepare a plastic monolith, after 30 min freezing at -15^{o}C for 30 min, the frozen sample was lyophilized for 6h, followed by 24h of crosslinking at -15^{o}C. After proper drying, the crosslinked scaffold was immersed in cyclohexane to dissolve the uncrosslinked polystyrene particles. After thorough repeated washing to remove the PS, we obtain a gel comprised of crosslinked PEI.

Synthesis of polymer scaffolds: 10 mg PEI (25 kDa) was dispersed in 575 µl of water and was vortexed for 30 min. To this aqueous dispersion was added 13 mg of 1,4-butanediol diglycidyl ether and vortexed for 5 min. The sample was frozen at -15^{o}C for 24 h to allow crosslinking in presence of ice crystals. To crosslink in absence of ice crystals, the aqueous dispersion was frozen for 30 min and the frozen assembly was lyophilized for 6 h followed by crosslinking at -15^{o}C for 24 h. Finally the self standing scaffold was removed and washed with excessive water to remove unreacted polymer and crosslinker. We note that self standing monoliths are formed only when a high concentration of PEI is used (10 mg of PEI in 575µl water). Self standing scaffolds do not form when ice templating at lower PEI concentrations in the absence of particles (for example, at 3 mg of PEI in 575µl water – that is typically used to prepare scaffolds using silica particles).

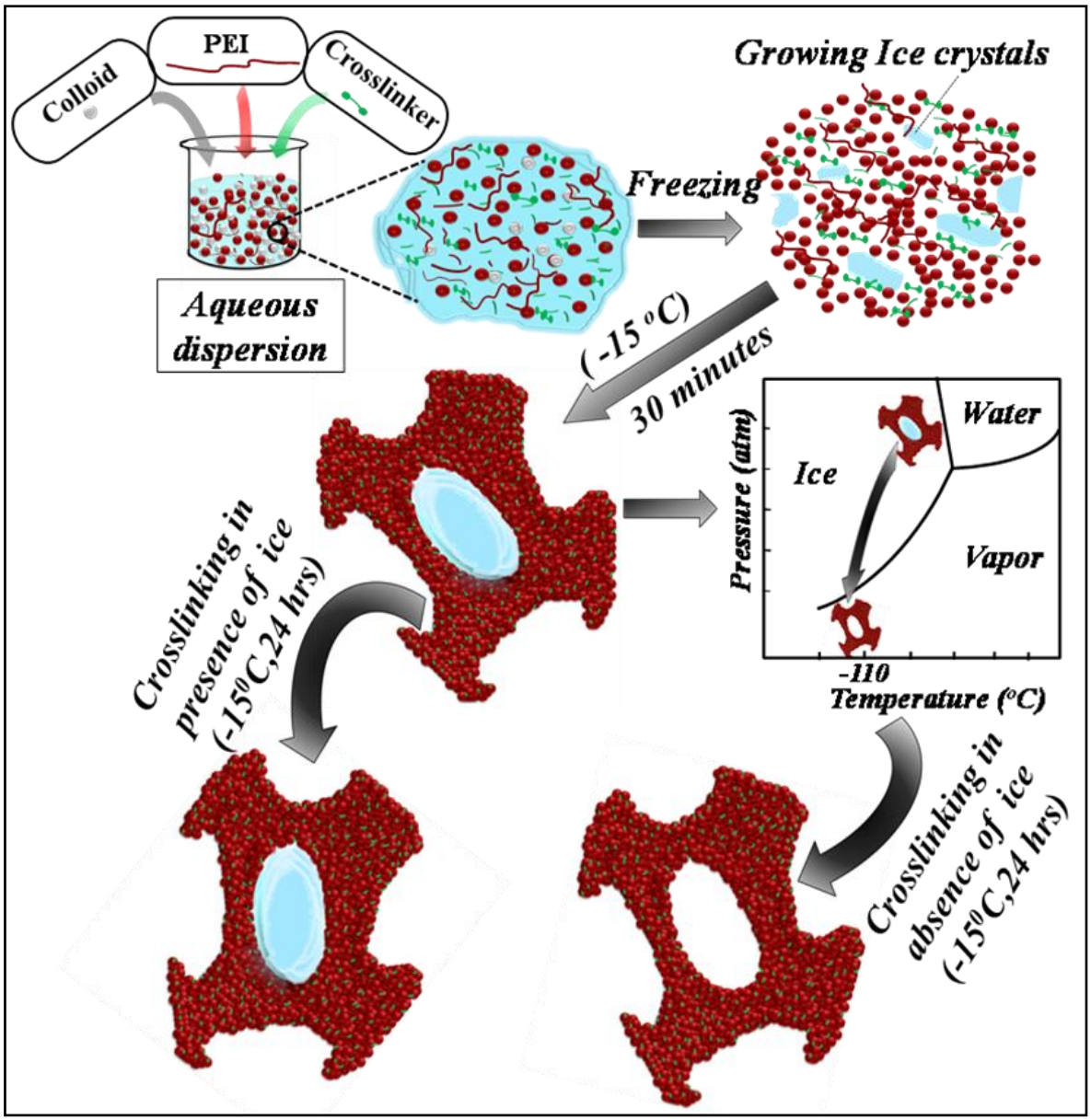

Figure 2.2: Protocol for preparation of "chemically-identical" monoliths. An aqueous dispersion of colloids, polymer (PEI) and crosslinker is frozen (at -15°C, over 30 minutes). Subsequently, either the PEI is allowed to crosslink at -15°C in the frozen state (left, to yield elastic sponges) or, the sample is lyophilized and then the polymer is allowed to crosslink at -15°C (right, to yield a plastic monolith).

2.2.3 Characterization

Compression/expansion experiments and dynamic mechanical rheology is performed using a strain controlled rheometer, TA-ARES G2, equipped with a normal force transducer. The sample morphology was imaged using Hitachi S-4200 field-emission scanning electron microscopy (FE-SEM). Thermogravimetric analysis

(TGA) was performed using an STA 6000. The sample was initially held at 100^{o}C for 5 min to dry it and was subsequently heated in air (50 mL/min) from 100^{o}C to 900^{o}C at a heating rate of 10^{o}C/min. Solid state NMR measurements were carried out on a Bruker Avance 300 spectrometer operating at a static field of 7.04 T, using a 4 mm double resonance MAS probe. Single pulse MAS (HPDEC) spectra were acquired with a 45 degree flip angle and relaxation delay of 10 s at 8 kHz spinning. Small angle X-ray scattering (SAXS) was performed on a XEUSS SAXS/WAXS system by Xenocs equipped with a microfocus sealed tube source (Cu Kα radiation). The X-ray radiation was collimated with FOX2D mirror and two pairs of scatterless slits from Xenocs. The data were collected using an image plate system (Mar 345 detector, calibrated using silver behenate standards) and was processed using Fit2D software. To perform low temperature measurements, we use a XEUSS SAXS/WAXS system equipped with Linkam THMS 600 stage. Data was circularly averaged and the 1D scattered intensity was obtained after background subtraction, and after correction for sample transmission. AFM was performed with a scanning probe microscope (JPK, NanoWizard II). Silicon cantilevers with a spring constant, k of 50 N/m and Q of 100 were used to perform experiments. The cantilever was oscillated at its free resonance frequency (~180 kHz) with free amplitude in the range of 6 to 45 nm. Nominal tip radius was 8 nm.

We are grateful to Dr. Bhoje Gowd (CSIR-NIIST) for allowing us to perform SAXS experiments in his laboratory.

2.3 Results and Discussion

We ice template a 10% (w/v) dispersion of commercially available 22 nm silica nanoparticles to prepare a macroporous material, using the method reported recently.[26] Briefly, an aqueous dispersion of silica nanoparticles, polyethyleneimine (PEI) and diepoxy crosslinker are mixed and this mixture is frozen at -15^{o}C. After holding at -15^{o}C for 24 h, the sample is thawed to afford an elastic macroporous sponge, characterized by pores of the order of 100 μm in size (Figure 2.2). These sponges are largely inorganic–yet, they recover elastically after large compressive strain over several cycles of deformation. It has been previously reported[26] that macroporous sponges, prepared using this technique, recover from compression only when they are swollen with solvent. In this work, we have modified the sample preparation to obtain materials that recover from large compressive strains in either dry or solvent swollen

states. The sponges prepared using this modified protocol are also predominantly inorganic (≈ 80% by weight of silica based on TGA) but, have a higher organic content than in the previously reported sponges. All the results reported in this work refer to measurements on dry sponges.

This synthetic procedure, viz. ice templating of colloids, followed by crosslinking the organic *in the frozen state*, yields elastic sponges, independent of the colloid size and for several polymer-crosslinker chemistries.[26] The remarkable mechanical response of these macroporous colloidal sponges arises from the hybrid structure that forms when the polymeric mesh surrounding the nanoparticles is crosslinked in the presence of the ice crystal templates.

To investigate if elastic materials form only when *aqueous* dispersions are frozen, we prepared macroporous materials by freezing a dispersion of silica particles, PEI and diepoxy crosslinker in a polar solvent, dry dimethyl sulphoxide (DMSO). Here too, the particles and organic were expelled from the DMSO crystals to organize into a macroporous material. After allowing 24 h for crosslinking, the sample was thawed to yield a material that exhibited elastic recovery from large compression (Figure 2.3). Thus, we note that synthesis of elastic macroporous materials is not limited to freezing *aqueous* dispersions. Having established this, in the rest of this Chapter, we describe results from inorganic sponges prepared using ice templating of aqueous dispersions.

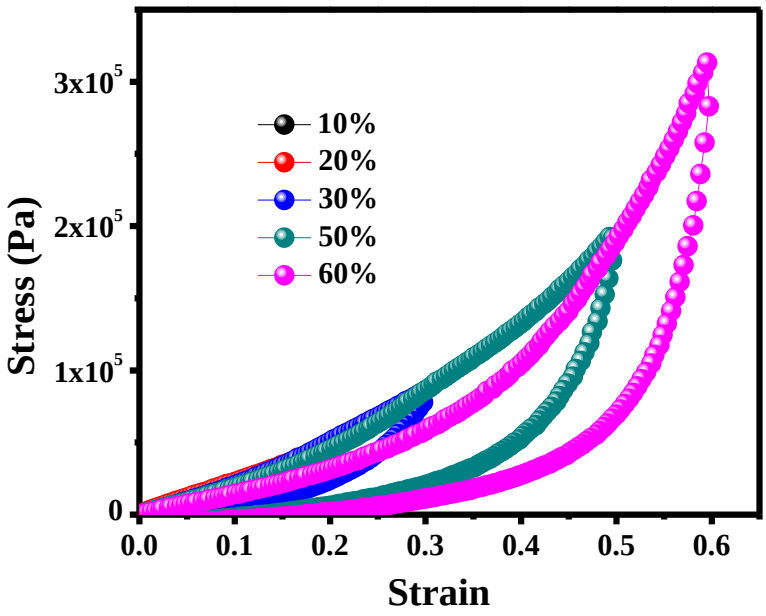

Figure 2.3: Compression-expansion behaviour of monoliths prepared using 1µm silica particles by freezing DMSO dispersion. Monoliths recover elastically from large strains, up to 60%.

We now investigate the role of the crystal templates in rendering the sponges elastic by preparing macroporous materials in the absence of the ice crystals, as shown in Figure 2.2. We begin by freezing the aqueous dispersion of silica nanoparticles, PEI and crosslinker, as earlier. After storage at -15^{o}C for 30 minutes, freezing is complete. During this time, the crosslinking reaction does not proceed to any significant extent since the PEI-diepoxide crosslinking that we employ is a slow reaction, especially at -15^{o}C (Figure 2.4).

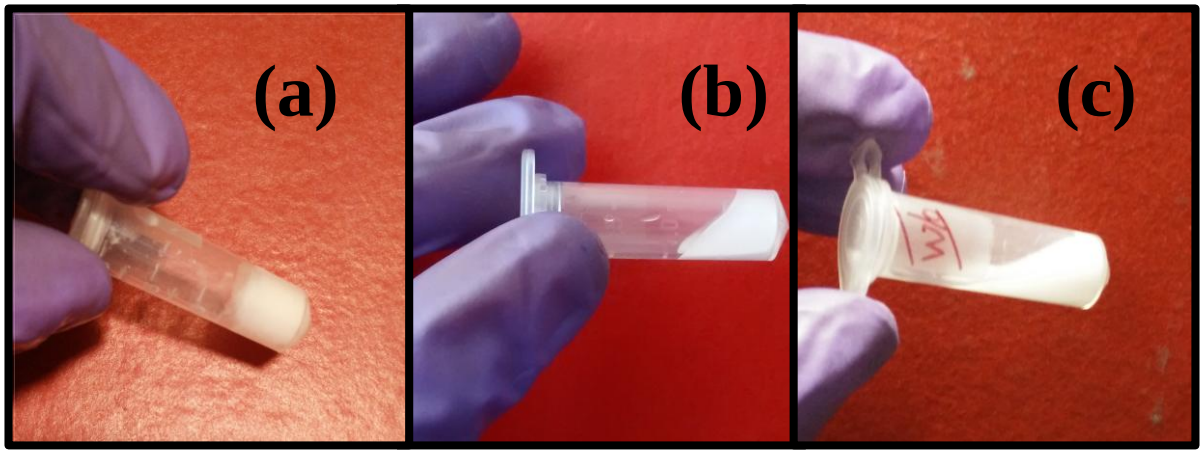

Figure 2.4: (a) Aqueous dispersion containing silica particles, polymer and crosslinker immediately after freezing at -15^{o}C for 30 min. **(b)** Sample thawed after freezing for 30 min. A crosslinked self-standing monolith is not formed when the time allowed for crosslinking is short (~30 min) and the particles re-disperse on thawing. **(c)** The behavior on thawing after crosslinking for a short time (30 min) is similar to an aqueous dispersion of PEI coated particles in the absence of crosslinker.

This frozen sample is then immediately transferred to a lyophilizer and the ice is sublimed by subjecting to a vacuum at -110^{o}C for 6 h (Figure 2.2). At the extremely low temperatures employed during lyophilization, there is no further crosslinking. There is no visual change in the shape or dimensions of the sample due to lyophilization. Subsequently, after lyophilization is complete, the sample is transferred to a -15^{o}C freezer and is allowed to crosslink over 24 hours (Figure 2.2).

There is a qualitative difference in the mechanical response between sponges prepared by crosslinking in the presence of ice and those that are crosslinked after lyophilization. Sponges prepared by freezing the aqueous colloidal dispersion and crosslinking in the presence of the ice crystal templates recover elastically after repeated compression to 80% strain (Figure 2.5 a,c). As the sponge is compressed (at a loading rate of 0.01 mm/s), there is

an initial slow increase in stress, followed by a rapid upturn above ≈ 40% compression. On releasing the stress, the sample recovers its original size. We observe hysteresis in the compression-expansion cycle. There is an increase in hysteresis with compressive strain – however, the sample recovers completely (Figure 2.5 c, inset). The compression-expansion behavior of the dry sponge is similar to that for the solvent swollen sponges that we had reported earlier. For dry sponges compressed to large (80%) strains, there is a small compression set (≈ 6%) immediately after expansion; complete recovery is slow and happens over several minutes. However, wet sponges recover their original dimensions[26] immediately after stress is released.

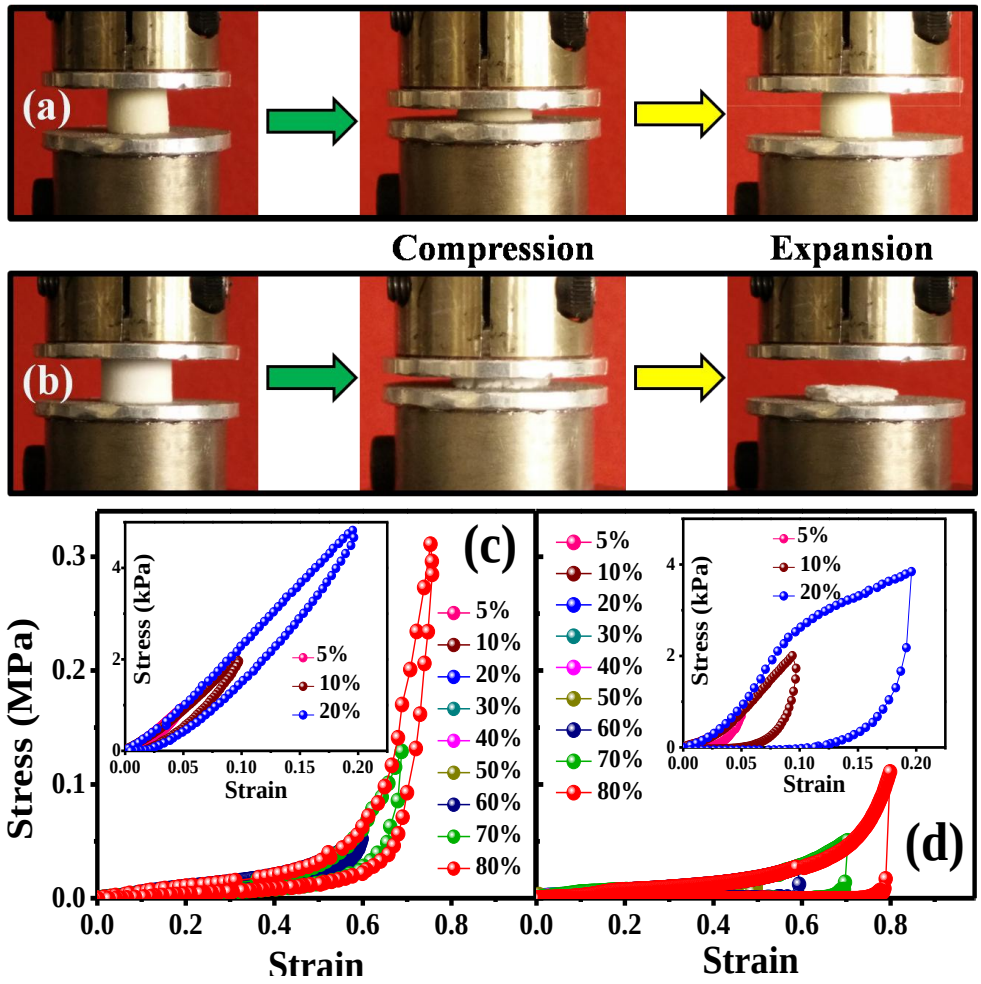

Figure 2.5: When cylindrical monoliths are compressed, **(a)** elastic sponges recover their original size and shape while **(b)** plastic monoliths form cracks and exhibit permanent compression set. The stress-strain behaviour for the monoliths for compressive strains ranging from 5% to 80% is shown for **(c)** elastic sponges and for **(d)** plastic monoliths. Stress-strain data for lower strains for (c) elastic sponges and (d) plastic monoliths are shown as insets.

In contrast to the elastic sponges, monoliths prepared by crosslinking lyophilized samples are brittle and fail catastrophically even at low compressive strains (Figure 2.5 b,d). On compressing, the stress increases with strain. At low strains (<10%), the increase in stress is comparable with the elastic sponge. However, beyond these strains, we observe a slower increase in stress relative to the elastic scaffolds. Further, we observe the formation of cracks in the monoliths and, on releasing compressive strain, the stress drops to zero precipitously (Figure 2.5 d). These samples are unable to recover completely even after modest compression to 10% strain (Figure 2.5 d, inset). We refer to these materials as plastic monoliths, in contrast to elastic sponges. The contrast between the mechanical response of elastic sponges and plastic monoliths is clear when we compare the residual compression set for these materials, as a function of imposed compressive deformation (Figure 2.6). There is minimal, if any, compression set for the elastic sponges even for strains as high as 80%. In contrast, plastic monoliths do not recover after compression to even small strains.

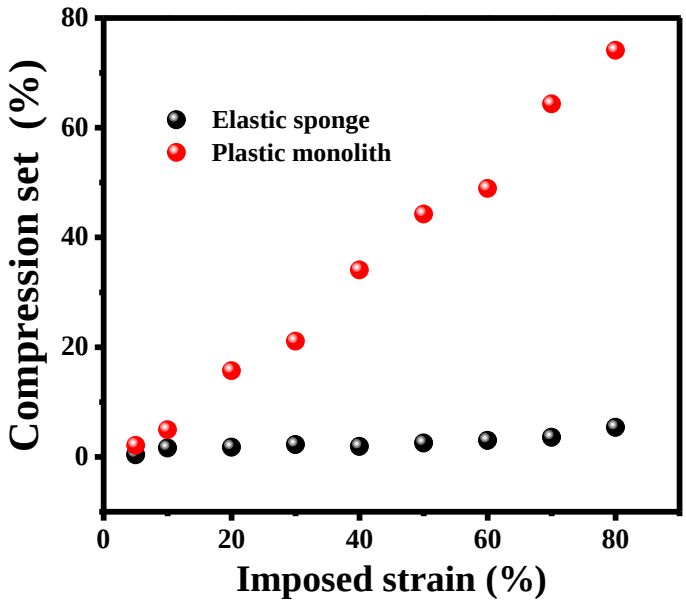

Figure 2.6: Residual compression set as a function of imposed compressive strain for elastic sponge and plastic monolith made from silica nanoparticles.

We note that the qualitative differences in the mechanical response of elastic and plastic monoliths to compression are observed for dry sponges (Figure 2.5) as well as for sponges swollen in water (Figure 2.7). Therefore, these differences are a consequence of the microstructure of the monoliths and cannot be attributed to the presence or absence of trapped water in lyophilized monoliths.

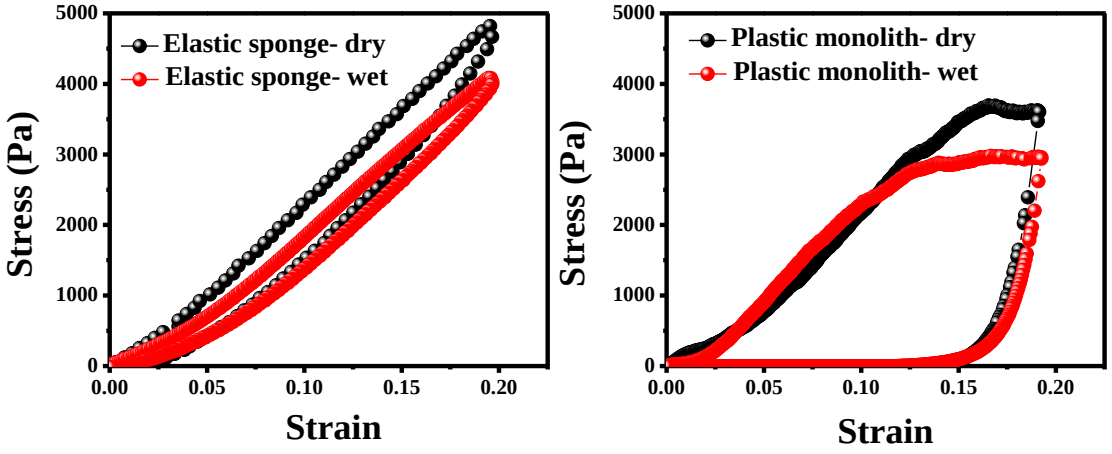

Figure 2.7: Compression/expansion measurements on elastic and plastic monoliths. Measurements are performed on dry sponges (where the voids of the sponge contain air) and are compared with wet sponges (where the sponges are soaked in excess water, so that all the voids contain water).

We now examine the structural origins of the differences between elastic and plastic monoliths. We prepare both monoliths in eppendorf tubes and remove them from the tubes after crosslinking. The physical dimensions and appearance of these samples after crosslinking, are identical. SEM examination reveals that both samples are macroporous, with similar open pore architecture (with pore size ranging from 30 – 60 μm, Figure 2.8a,b).

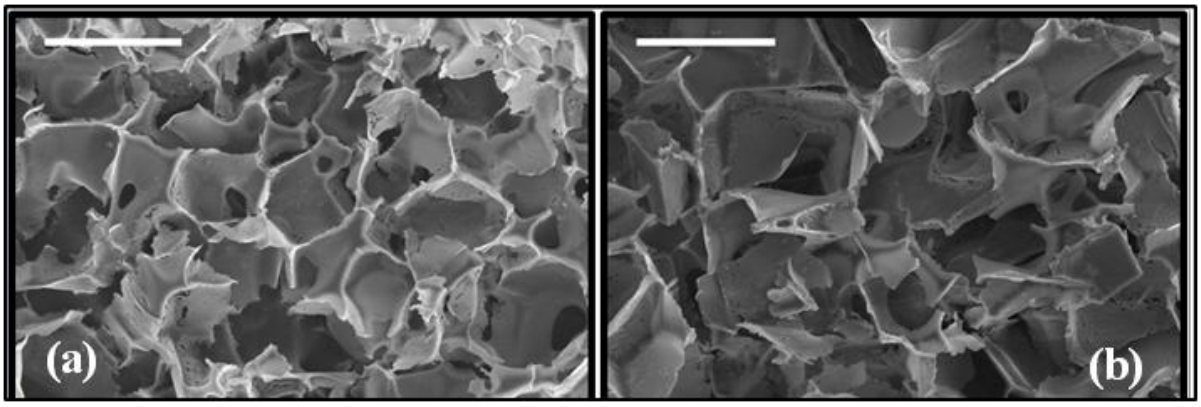

Figure 2.8: SEM images of **(a)** elastic sponge and **(b)** plastic monolith prepared using silica nanoparticles. The scale bar represents 100 μm.

Small angle X-ray scattering (SAXS) is performed on both ice-templated sponges during crosslinking, at -15^{o}C (viz. on the elastic sponges in the presence of ice and on the lyophilized plastic sample). SAXS data from both monoliths appear identical (Figure 2.9). We normalize the SAXS data by scattering from a dilute dispersion of the silica nanoparticles

(Figure 2.9 a) to obtain an apparent structure factor, $S_A(q)$. For densely packed particulate systems, we can estimate[30] the average interparticle spacing from the first peak in $S_A(q)$. We observe that the position of the first peak in $S_A(q)$ is similar, to within experimental error, for the elastic sponge and the plastic composite (Figure 2.9 b) and that the peak position does not change during the crosslinking process. We fit[30] the first peak in $S_A(q)$ to estimate the interparticle distance as ≈ 23 nm (compare with the particle size of 22 nm). Thus, our data indicates that, in both monoliths, the nanoparticles are densely packed together during the ice templating process and that this particle-particle spacing does not change as the organic materials are crosslinked (in the presence or absence of the ice crystal templates).

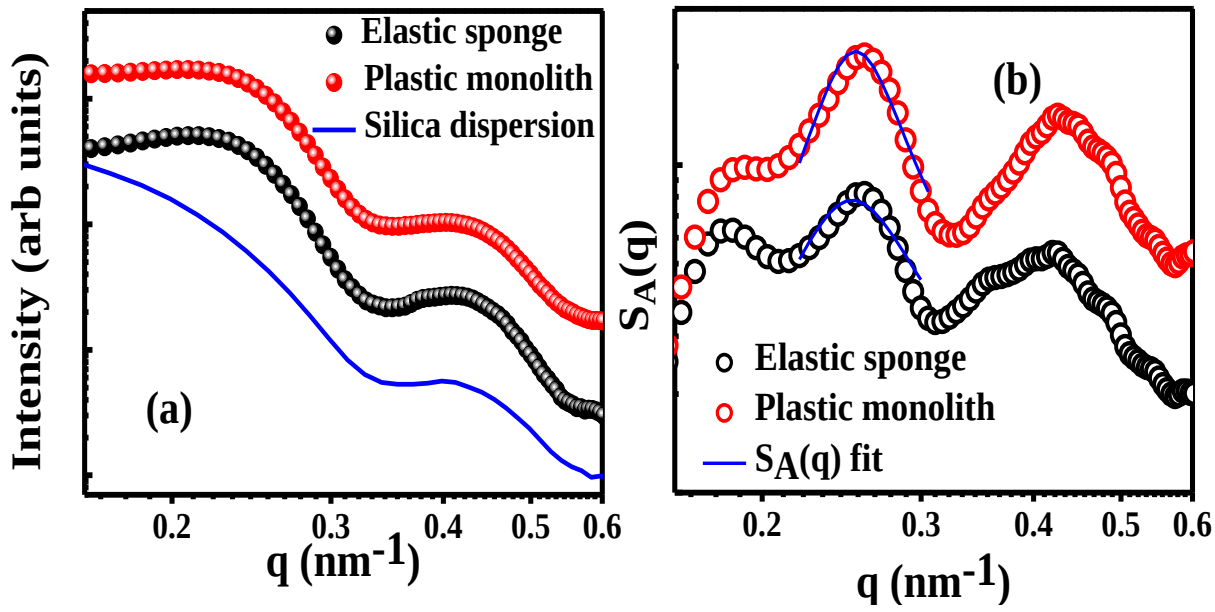

Figure 2.9: (a) SAXS data from an elastic sponge and a plastic monolith while they were held at -15°C to allow the polymer to crosslink. Data are vertically offset for clarity. The solid line represents SAXS from a dilute dispersion of the 22 nm silica particles that were used to prepare the monoliths. **(b)** Normalizing the SAXS data from the monoliths by the dilute solution scattering from silica nanoparticles allows us to determine an apparent structure factor, $S_A(q)$ for nanoparticles in the monoliths. The solid line through the first peak represents a fit[30] to the data to obtain the nearest neighbour spacing. Here too, data is vertically offset for clarity.

Thermogravimetric analysis (TGA) was performed on both samples by first drying at 100°C, followed by heating in air at a ramp rate of 10°C/min. The temperature dependent weight loss profiles for both samples are essentially identical (Figure 2.10 a) and both monoliths have an organic content of ≈ 20%. Next, we perform ^{13}C NMR and use high power proton decoupling

(HPDEC) experiments at a relaxation delay of 10s, to interrogate the organic content in both samples. Since both samples contain polymer, PEI, and the same diepoxy crosslinker, the NMR spectrum shows peaks that correspond to these molecules (Figure 2.10 b). We observe a peak at a chemical shift at 26.3 ppm, that corresponds to the carbon atoms from the -(CH2-CH2)- group present in the crosslinker (1,4-butanediol diglycidyl ether). Since the other signals correspond to either the carbon atoms in the PEI or to the other carbon atoms in the crosslinker, we can obtain the relative proportions of polymer to crosslinker in the monoliths from the ratio of areas of the peak at 26.3 ppm to the other peaks. We obtain a ratio of 1.02 for the elastic sponges and 1.04 for the plastic monoliths, that are identical to within experimental error. Thus, both elastic sponges and plastic monoliths have the same organic content and the same ratio of polymer to crosslinker.

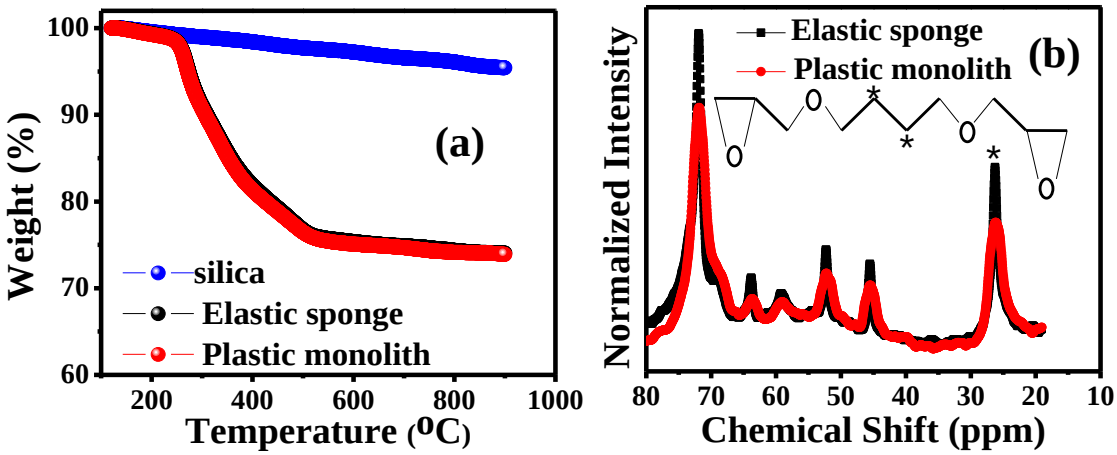

Figure 2.10: (a) TGA temperature-dependent weight loss data for the elastic sponge, the plastic monolith and for the as-received 22 nm silica particles used to prepare the scaffolds. **(b)** ^{13}C NMR spectra of elastic sponge and plastic monolith. The peak at 26.3 ppm (marked *) is attributed to the carbon nuclei in the -(CH2-CH2)- group present in the crosslinker 1, 4-butanediol diglycidyl ether.

To estimate the average crosslink density in elastic sponges and plastic scaffolds, we prepare matched samples by ice templating an aqueous dispersion of uncrosslinked polystyrene (PS) latex particles with PEI and diepoxy crosslinker. In previous work, it was demonstrated[26] that the preparation of elastic sponges using our ice templating method is independent of the particle nature. As in the case of the silica nanoparticle scaffolds, samples prepared by crosslinking the ice-templated latex dispersions in the presence of the ice crystal templates are elastic, while those prepared by crosslinking after lyophilization to remove the ice templates are plastic. We perform dynamic oscillatory shear rheology to investigate the

mechanical response of the elastic and plastic monoliths. At first, we systematically increase the strain to determine the linear response region. We use this to select a strain value in the linear response region and perform small strain (= 0.05%) frequency dependent measurements from 0.1 –100 rad/s. For both monoliths, we observe that the elastic modulus, G′, is essentially frequency independent and is larger than the loss modulus, G″ (Figure 2.11a), as expected for an elastic solid. The difference between the elastic moduli for elastic and plastic monoliths is small relative to sample-to-sample variations. Thus, G′≈ 20 kPa for both elastic sponges and plastic monoliths. However, the loss moduli, G″, for the plastic scaffold is almost an order of magnitude higher that for the elastic sponge (Figure 2.11a).

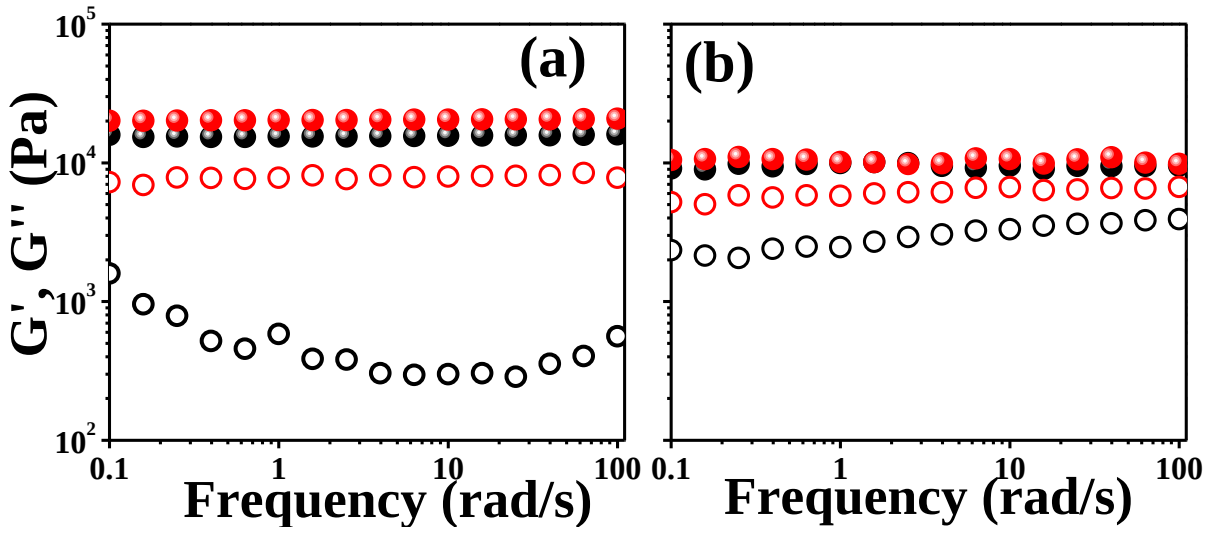

Figure 2.11: Storage (G′, filled circles) and loss moduli (G″, open circles) from rheological measurements in the linear regime for **(a)** elastic sponge (black) and for plastic monoliths (red) prepared using uncrosslinked 1µm polystyrene (PS) particles. **(b)** G′ and G″ for crosslinked PEI gel obtained from elastic sponge (black) and from plastic monolith (red) after dissolution of the PS latex particles.

The elastic and plastic monoliths are soaked in cyclohexane for an extended period to dissolve and remove the polystyrene particles (Figure 2.12). Once the latex particles are dissolved, the crosslinked PEI that is left behind is no longer self-standing. We evaporate the cyclohexane solvent and subject the material that is left behind to rheological measurements in the linear response region. We note that all rheological measurements are performed between roughened 25 mm plates to minimize sample slippage. We observe that the elastic modulus, G′, is frequency independent for both elastic and plastic scaffolds (Figure 2.11b). Also, the value of G′ for this material is of the same order as for the monoliths (compare

Figure 2.11a and b). Further, G′ is larger than the loss modulus, G″ (Figure 2.11b). This rheological response is characteristic of a lightly crosslinked polymer.[31] Here too, we observe that the material derived from the plastic scaffold exhibits a higher loss modulus, G″, as compared to that from the elastic sponge (Figure 2.11b).

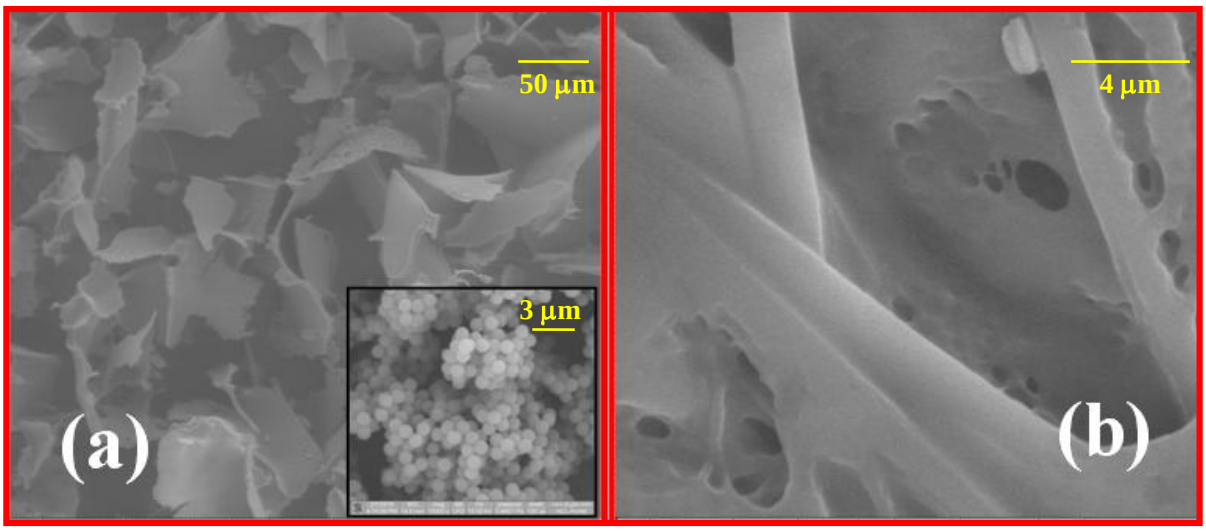

Figure 2.12: (a) SEM micrograph of monoliths prepared using uncrosslinked polystyrene particles of size 1µm (inset: high resolution micrograph of the wall of the monolith) and **(b)** SEM of gel obtained after washing with cyclohexane. Note that the scale bar in this image is 4 µm. The polystyrene particles appear to be completely dissolved and are not observed in this image.

The magnitude and frequency dependence of the elastic modulus, G′, is indicative of the extent of crosslinking in a polymeric matrix. We observe that the G′ for the elastic sponge is similar to that for the plastic monolith. Further, G′ of the crosslinked PEI left behind (after the particles are dissolved from the monoliths) is also similar for the elastic sponge and plastic monolith. Thus, our rheology data suggests that the average extent of PEI crosslinking is similar in both the elastic sponge and plastic monolith. For G′ = 20 kPa, we can estimate the crosslink density[32] in the PEI from $G' = \nu k_B T$, where ν is the number density of effective crosslinks and T is the temperature. This yields a value of $\nu \approx 5$ crosslinks/1000 nm^3 for both the elastic sponge and plastic monolith.

Thus, both elastic sponges and plastic monoliths are indistinguishable based on their pore architecture (from SEM), interparticle spacing in their walls (from SAXS), their organic content (from TGA), ratio of polymer to crosslinker (from NMR) and average crosslink density in the PEI. However, we note that the loss modulus is higher for the plastic monolith

relative to the elastic sponge and for the crosslinked PEI obtained after dissolving the PS latex for the plastic monolith relative to the elastic sponge. Thus, it appears that the plastic scaffolds dissipate more energy when deformed, when compared with the elastic sponges.

We note that, for *pure* PEI sponges, obtained by ice templating higher concentration aqueous PEI/diepoxy solutions, crosslinking either in the presence of ice or after lyophilization, yields elastic sponges that recover from large compressive deformations (Figure 2.13). Therefore, the differences between the elastic sponge and plastic monolith are a consequence of the structure of the hybrid particle/crosslinked PEI monoliths. While no differences are evident in the chemical composition of these monoliths, the plastic monoliths have a higher loss modulus relative to the elastic sponge and, there is a qualitative difference in the response of these monoliths to compression.

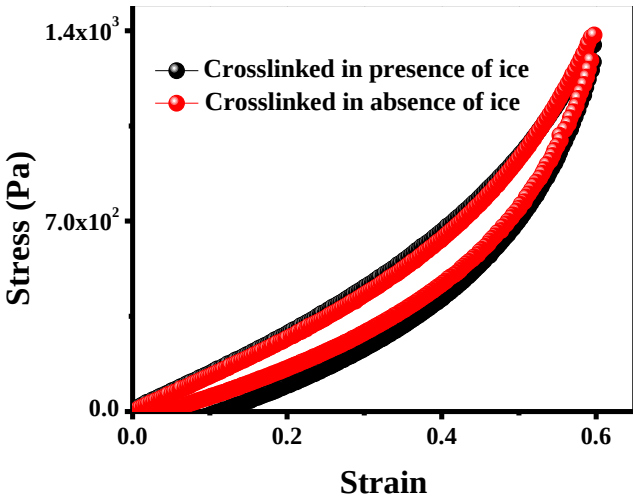

Figure 2.13: Compression-expansion behaviour of pure crosslinked polymer scaffold at 60 % compressive strain. Note that the monoliths recover elastically independent of whether the crosslinking is done in the presence of ice or after lyophilization.

Tapping mode atomic force microscopy (AFM) reveals microscopically-resolved structural differences between elastic and plastic scaffolds. To probe the origins of the higher G″ for the plastic scaffolds, we use amplitude modulation-atomic force microscopy (AM-AFM) [33-36] to create a map of the energy dissipation over the sample surface. Here, an AFM probe is oscillated at its resonant frequency and the amplitude of the cantilever tip is recorded as the tip is moved towards the surface of interest. To quantify the energy dissipation by the cantilever as it interacts with the surface, we measure the phase shift, Φ (relative to the signal that drives the cantilever oscillation) and the amplitude, A, for cantilever motion as the tip is

moved towards the sample. We analyze the data assuming that the cantilever is sufficiently stiff so that its motion can be described by a sinusoidal function, even when it interacts with the sample surface.[37] As in the literature,[33] we equate the external energy per cycle supplied to resonate the cantilever, E_{ext}, to a sum of the energy dissipated to hydrodynamic damping by the medium, E_{med}, and by tip-sample interactions, E_{dis}. Thus,

$$E_{dis}=E_{ext}-E_{med}=(A_0\sin\Phi-A\omega/\omega_0)\pi kA/Q \qquad (1)$$

where, A is the amplitude of the cantilever, A_0 is the cantilever amplitude far away from the sample, ω is the drive frequency, ω_0 is the cantilever resonant frequency (≈180 kHz), k is the cantilever stiffness and Q is the cantilever quality factor.

We anticipate that the differences in the mechanical response of elastic sponges and plastics monoliths can be traced to the nature of the "bonding" between the particles that comprise the scaffolds. Thus, we are interested in using AFM imaging and AM-AFM to probe energy dissipation of the crosslinked polymer mesh in the regions between particles. Performing these experiments on scaffolds prepared using 22 nm silica particles is challenging since the size of the AFM tip probe is comparable to the particle size.

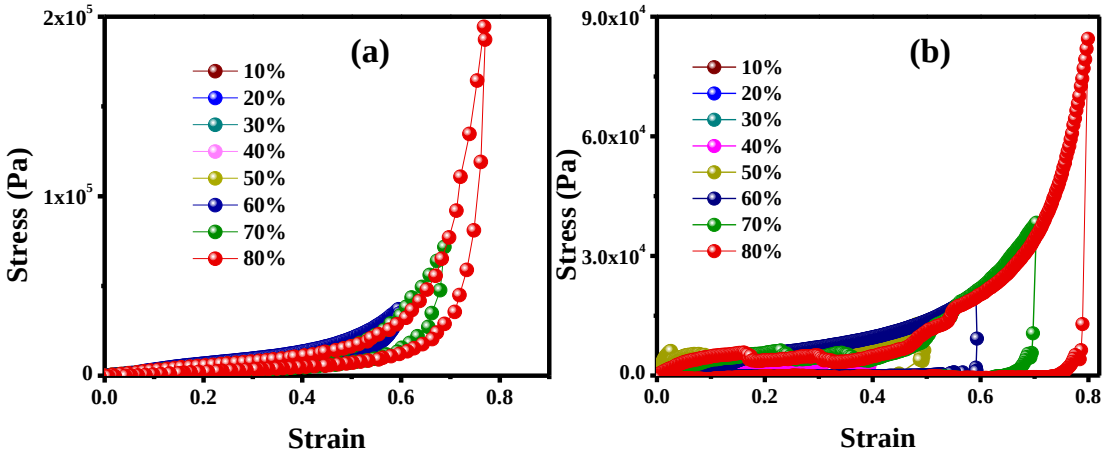

Figure 2.14: Compression-expansion behaviour of monoliths prepared using an aqueous dispersion of 1µm silica particles, where the PEI is crosslinked in the **(a)** presence and **(b)** absence of ice crystals (viz. after lyophilization of the ice). Nominal stress as a function of nominal strain for the compressive strains from 10% to 80%.

Therefore, for AFM measurements, we prepare elastic sponges and plastic monoliths with aqueous dispersions of 1μm silica particles, using the protocols previously described in this Chapter. Again, we confirm that the size of the colloidal particle does not influence the mechanical response: elastic sponges or plastic monoliths are obtained when crosslinking is carried out in the presence of ice or on lyophilized samples, respectively (Figure 2.14).

We begin by imaging in tapping mode and record images based on surface topography and phase shift simultaneously (Figure 2.15). As expected, the topographical height variations across the samples, viz. when going over particles, are similar for the elastic and plastic scaffolds. However, the variations in Φ along line traces are higher, by about a factor of two, for plastic scaffolds relative to elastic sponges. These Φ variations reflect differences in the microscopic material properties of the regions between the particles in elastic and plastic scaffolds.

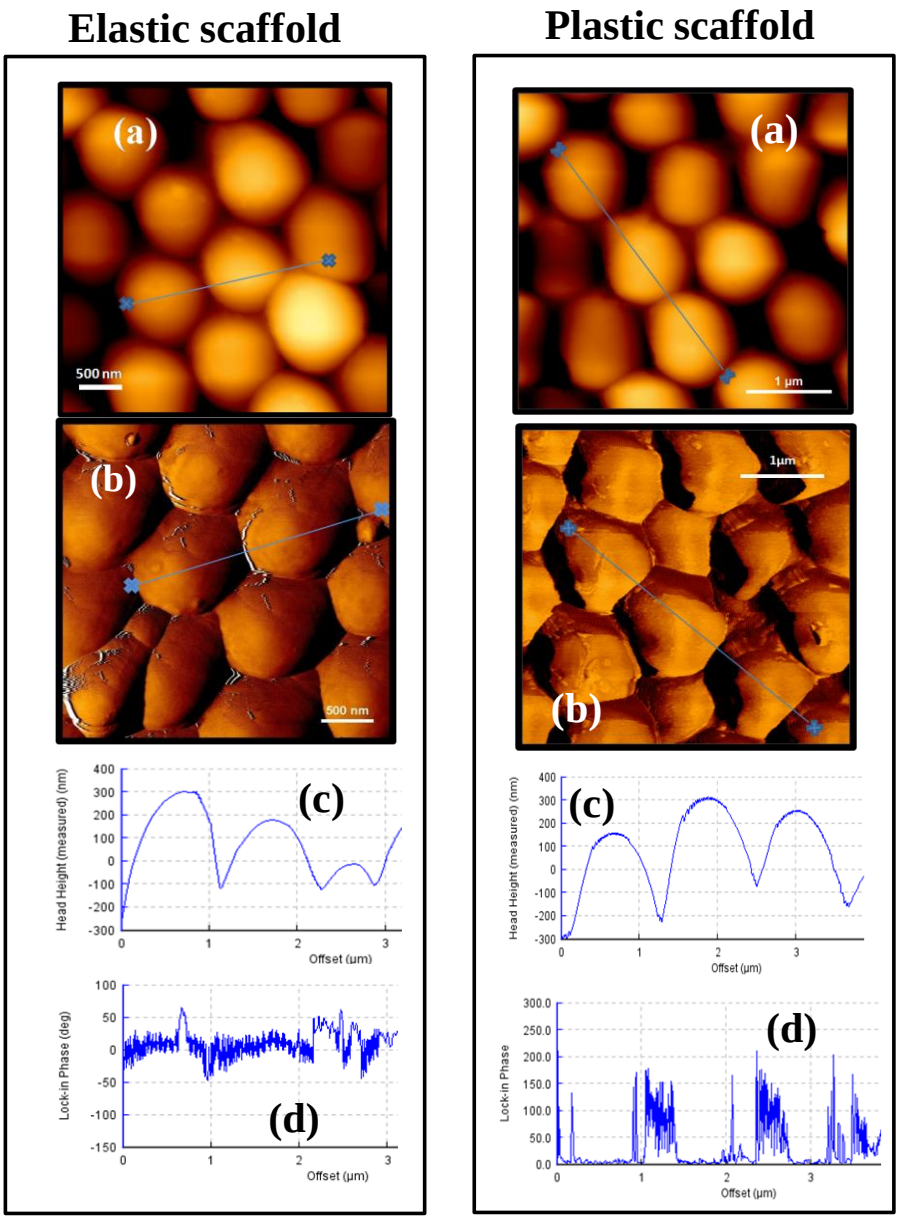

Figure 2.15: (a) Surface topography and **(b)** phase shift images of elastic (left) and plastic (right) monoliths. We extracted height and phase angle profiles along several line cuts across these images. We present one such profile of the **(c)** height trace and the **(d)** phase shift trace as an example. Profiles obtained for other line cuts were qualitatively similar. Comparing the height traces for the elastic and plastic monoliths, we note that there is a similar height variation as we go across the sample (and over multiple particles) for the two scaffolds. When we examine the phase shift trace for the elastic scaffold, we observe a variation from about -50^{o} to $+50^{o}$ as we go across the sample. In contrast, the phase shift trace for the plastic monolith exhibits a larger variation (by a factor of ≈2), from about 0 to 230^{o}. Again, we note that the data presented is representative of differences between elastic and plastic monoliths in Φ–variations across the sample.

We use AM-AFM force curves to probe the region between particles in elastic and plastic samples (Figure 2.16a,b) and to generate dynamic dissipation curves (Figure 2.16c). For both samples, the dynamic dissipation curves are characteristic of viscoelastic tip-sample interactions.[33] We have performed over 50 measurements on interparticle regions on about 10 independent samples (Figure 2.16c) and observe that the peak energy dissipation in the plastic scaffolds is, on average, about three-fold higher than for elastic scaffolds. This is in accord with our macroscopic dynamic rheology measurements on the scaffolds (Figure 2.11). We also note that there is a much wider variation in the peak energy dissipation for the plastic monoliths (from 1100-1900 meV) relative to the elastic sponges (from 500 to 700 meV).

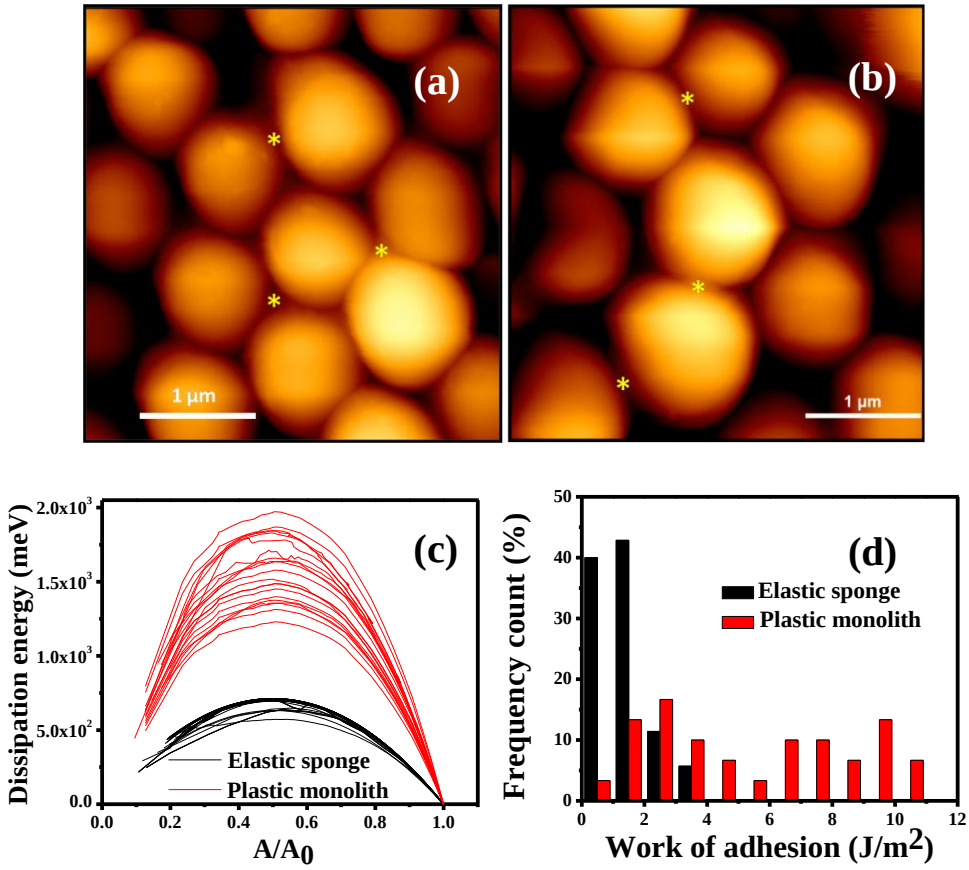

Figure 2.16: AFM height image for **(a)** elastic sponge and **(b)** plastic monolith. We select regions between the particles (marked *) to probe the nature of the crosslinked polymer mesh that bonds the particles in the monoliths. **(c)** Energy dissipation per cycle as a function of normalized amplitude calculated for the interparticle regions in elastic sponges and plastic monoliths. Dynamic energy dissipation measurements are made at several interparticle points using independent samples for both monoliths. **(d)** Distribution of the work of adhesion from contact mode force-displacement measurements performed on several interparticle points on elastic sponges and plastic monoliths.

To help interpret these results, we have performed energy mapping using AM-AFM on films of PEI crosslinked in the solution state with varying amounts of crosslinker. These polymer films are prepared by systematically varying PEI:crosslinker ratio from 1:0.25 to 1:1. Crosslinked polymer films were prepared by solution blending of polymer and crosslinker followed by drying at 55^{o}C. We anticipate that solution blending provides uniform distribution of crosslinker in the polymer matrix. We have observed a systematic increase in energy dissipation per cycle for the films with decrease in crosslinker content (Figure 2.17). The film with 1:1 PEI:crosslinker ratio shows energy dissipation in the region of 60 – 280 meV, 1:0.75 has energy dissipation in the region of 140 – 290 meV, 1:0.5 has energy dissipation in the region of 300 – 410 meV and 1:0.25 has energy dissipation in the region of 360 – 890 meV. We note that we were unable to perform AFM measurements on uncrosslinked PEI films – reliable data could not be generated due to the probe getting stuck in the film during these measurements. Further, as these measurements are performed on thick films, the values for energy dissipation cannot be quantitatively compared with those obtained for the thin polymer meshes probed during AFM investigations of the monoliths. However, we believe that the qualitative trends observed in these experiments hold for the experiments on the monoliths. Our results on the crosslinked polymer films indicate that there is a decrease in the energy dissipation when the crosslinking increases. We compare this with AFM data obtained for the elastic and plastic scaffolds. Plastic scaffolds exhibit a higher variation in the range of values for the energy dissipation compared with elastic scaffolds. In the light of our results on crosslinked PEI films, we interpret this to mean that the variation in the local crosslink density is higher for plastic scaffolds relative to elastic scaffolds.

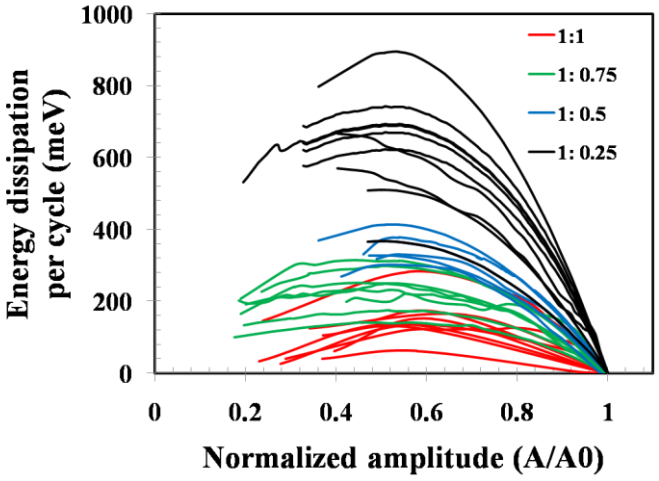

Figure 2.17: Energy dissipation per cycle for polymer films with different crosslinking density.

Extracting viscoelastic parameters for the sample from AM-AFM data is highly model-dependent and makes several severe assumptions, especially when the cantilever is driven at its resonant frequency. Therefore, we have also performed contact mode AFM measurements (independence of the AM-AFM studies) to measure the work of tip-sample adhesion for elastic and plastic samples. Again, measurements were performed on about 50 locations in the inter-particle regions in elastic and plastic monoliths. Here, we measure the force-distance curve as the tip approaches the sample and obtain the work of adhesion as the area in the hysteretic region of the approach-retraction curve (an example is shown in Figure 2.18). We observe that there is a wide distribution in the work of adhesion for plastic samples and, that the values range to over 10 J/m^2 (Figure 2.16d). In contrast, the work of adhesion for elastic samples never exceeds 4 J/m^2 and is peaked at less than 2 J/m^2. Thus, both resonant tapping mode AM-AFM and contact mode work of adhesion data indicate significant differences in the crosslinked PEI mesh that links particles together in elastic sponges and plastic monoliths.

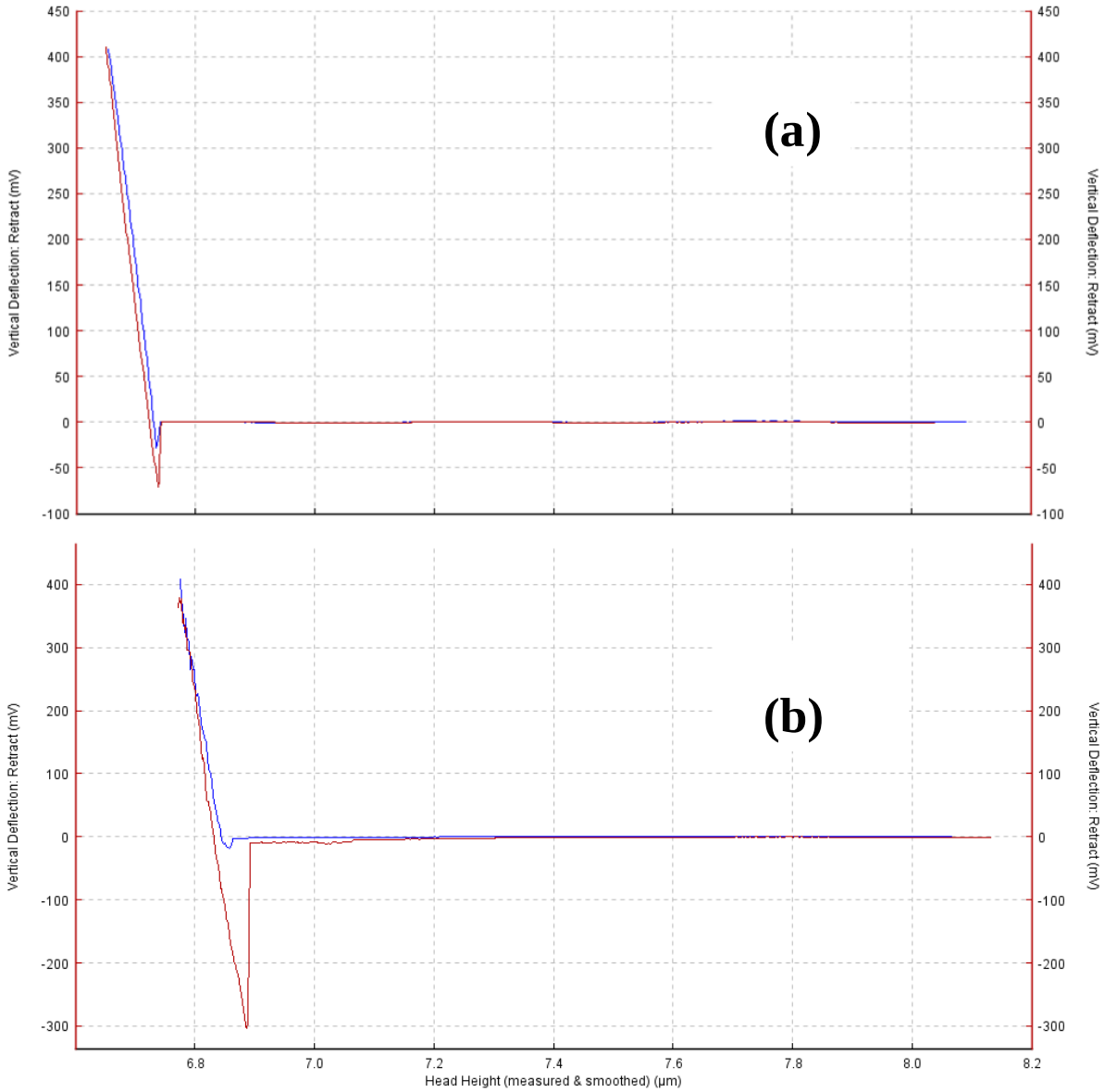

Figure 2.18: Extension (blue)-retraction (dark red) curve showing the dependence of cantilever deflection (that is related to the force on the cantilever) as a function of tip-sample distance for **(a)** elastic sponge **(b)** plastic monolith. The work of adhesion is calculated from the hysteretic area between these extension-retraction curves. This data is shown as an example of how the work of adhesion was calculated. We performed this at over 50 points using 10 independent samples of both elastic and plastic scaffolds.

2.4 Summary

Macroporous monoliths prepared by ice templating an aqueous dispersion of silica nanoparticles and a small fraction of polymer and crosslinker exhibit qualitatively different mechanical response to large compression depending on whether the polymer was

crosslinked in the presence of ice or after the ice was lyophilized. The walls of both elastic and plastic monoliths are comprised mainly of nanoparticles, connected together through a thin crosslinked polymer mesh. Both elastic and plastic monoliths are chemically identical: they have the same organic content, the same ratio of polymer to crosslinker and the polymeric component is characterized by the same average crosslink density. Further, the structure of the monoliths, based on SEM and on interparticle spacing is identical. The origin of the mechanical response of the monoliths arises from the nature of the polymer mesh that surrounds and links the particles. This difference in mesh structure results in greater energy dissipation by the plastic monoliths, as indicated by their higher loss modulus values, relative to elastic sponges. AFM measurements (both AM-AFM and work of adhesion) indicate a wider spatial variation in the properties of the crosslinked polymer mesh for the plastic monolith relative to the elastic sponge. Interestingly, the plastic sponges exhibit significantly higher values of work of adhesion relative to the elastic sponges. It is possible that this high work of adhesion drives the scaffold walls to adhere irreversibly when the monolith is compressed, resulting in plastic deformation of the monolith. Thus, the monolith is unable to recover its original size and form after it is compressed.

The overall ratio of polymer to crosslinker determines the average crosslink density. This is the same for both elastic and plastic monoliths. However, the crosslinked polymer mesh that connects particles in the plastic monolith dissipates more energy compared to the elastic sponge. We speculate that the larger spatial variation observed in AFM measurements of the crosslinked polymer between particles in plastic monoliths might results from greater spatial heterogeneity in the crosslink density, when compared with elastic sponges. This would suggest that the presence (or absence) of ice crystal templates during crosslinking of the polymeric component impacts the spatial distribution of crosslinks. Crosslinks are more uniformly distributed for the polymer mesh in elastic sponges relative to the lyophilized plastic monoliths. We believe that these spatial variations observed in the AFM studies reflect the microstructural underpinnings of the higher dissipation observed for the crosslinked polymer mesh in plastic monoliths. Ultimately, this results in brittle failure of the plastic monoliths obtained by crosslinking after lyophilization. This template-dependent spatial modulation of crosslink chemistry appears to hold, independent of particle type and size for hybrid monoliths comprising predominantly of particles.

2.5 References

1. Cheng, W.; Campolongo, M. J.; Tan, S. J.; Luo, D., Freestanding ultrathin nano-membranes via self-assembly. *Nano Today* **2009,** 4, 482-493.

2. Chen, S., Langmuir-Blodgett fabrication of two-dimensional robust cross-linked nanoparticle assemblies. *Langmuir* **2001,** 17, 2878-2884.

3. Lin, Y.; Skaff, H.; Boker, A.; Dinsmore, A. D.; Emrick, T.; Russell, T. P., Ultrathin cross-linked nanoparticle membranes. *J. Am. Chem. Soc* **2003,** 125, 12690-12691.

4. Mueggenburg, K. E.; Lin, X.-M.; Goldsmith, R. H.; Jaeger, H. M., Elastic membranes of close-packed nanoparticle arrays. *Nat. Mater.* **2007,** 6, 656-660.

5. Cheng, W.; Campolongo, M. J.; Cha, J. J.; Tan, S. J.; Umbach, C. C.; Muller, D. A.; Luo, D., Free-standing nanoparticle superlattice sheets controlled by DNA. *Nat. Mater.* **2009,** 8, 519-525.

6. He, J.; Kanjanaboos, P.; Frazer, N. L.; Weis, A.; Lin, X. M.; Jaeger, H. M., Fabrication and Mechanical Properties of Large- Scale Freestanding Nanoparticle Membranes. *Small* **2010,** 6, 1449-1456.

7. Chen, Y.; Ouyang, Z.; Gu, M.; Cheng, W., Mechanically strong, optically transparent, giant metal superlattice nano membranes from ultrathin gold nanowires. *Adv. Mater.* **2012,** 25, 80-85.

8. Lee, D.; Jia, S.; Banerjee, S.; Bevk, J.; Herman, I. P.; Kysar, J. W., Viscoplastic and granular behavior in films of colloidal nanocrystals. *Phys. Rev. Lett.* **2007,** 98, 026103.

9. Podsiadlo, P.; Krylova, G.; Lee, B.; Critchley, K.; Gosztola, D. J.; Talapin, D. V.; Ashby, P. D.; Shevchenko, E. V., The role of order, nanocrystal size, and capping ligands in the collective mechanical response of three-dimensional nanocrystal solids. *J. Am. Chem. Soc.* **2010,** 132, 8953-8960.

10. Tam, E.; Podsiadlo, P.; Shevchenko, E.; Ogletree, D. F.; Delplancke-Ogletree, M.-P.; Ashby, P. D., Mechanical properties of face-centered cubic supercrystals of nanocrystals. *Nano Lett.* **2010,** 10, 2363-2367.

11. Gallego-Gomez, F.; Morales-Florez, V.; Blanco, A.; de la Rosa-Fox, N.; Lopez, C., Water-dependent micromechanical and rheological properties of silica colloidal crystals studied by nanoindentation. *Nano Lett.* **2012,** 12, 4920-4924.

12. Yan, C.; Arfaoui, I.; Goubet, N.; Pileni, M. P., Soft supracrystals of Au nanocrystals with tunable mechanical properties. *Adv. Funct. Mater.* **2013,** 23, 2315-2321.

13. Klajn, R.; Bishop, K. J. M.; Fialkowski, M.; Paszewski, M.; Campbell, C. J.; Gray, T. P.; Grzybowski, B. A., Plastic and moldable metals by self-assembly of sticky nanoparticle aggregates. *Science* **2007,** 316, 261-264.

14. Raichman, Y.; Kazakevich, M.; Rabkin, E.; Tsur, Y., Inter-Nanoparticle Bonds in Agglomerates Studied by Nanoindentation. *Adv. Mater.* **2006,** 18, 2028-2030.

15. Landman, U.; Luedtke, W. D., Small is different: energetic, structural, thermal, and mechanical properties of passivated nanocluster assemblies. *Faraday Discuss.* **2004,** 125, 1-22.

16. Podsiadlo, P.; Kaushik, A. K.; Arruda, E. M.; Waas, A. M.; Shim, B. S.; Xu, J.; Nandivada, H.; Pumplin, B. G.; Lahann, J.; Ramamoorthy, A., Ultrastrong and stiff layered polymer nanocomposites. *Science* **2007,** 318, 80-83.

17. Tang, Z.; Kotov, N. A.; Magonov, S.; Ozturk, B., Nanostructured artificial nacre. *Nat. Mater.* **2003,** 2, 413-418.

18. Srivastava, S.; Nykypanchuk, D.; Maye, M. M.; Tkachenko, A. V.; Gang, O., Super-compressible DNA nanoparticle lattices. *Soft Matter* **2013,** 9, 10452-10457.

19. Choi, J.; Hui, C. M.; Pietrasik, J.; Dong, H.; Matyjaszewski, K.; Bockstaller, M. R., Toughening fragile matter: mechanical properties of particle solids assembled from polymer-grafted hybrid particles synthesized by ATRP. *Soft Matter* **2012,** 8, 4072-4082.

20. Mulik, S.; Sotiriou-Leventis, C.; Churu, G.; Lu, H.; Leventis, N., Cross-linking 3D assemblies of nanoparticles into mechanically strong aerogels by surface-initiated free-radical polymerization. *Chem. Mater.* **2008,** 20, 5035-5046.

21. Nguyen, B. N.; Meador, M. A. B.; Tousley, M. E.; Shonkwiler, B.; McCorkle, L.; Scheiman, D. A.; Palczer, A., Tailoring elastic properties of silica aerogels cross-linked with polystyrene. *ACS Appl. Mater. Interfaces* **2009,** 1, 621-630.

22. Nguyen, B. N.; Meador, M. A. B.; Medoro, A.; Arendt, V.; Randall, J.; McCorkle, L.; Shonkwiler, B., Elastic behavior of methyltrimethoxysilane based aerogels reinforced with tri-isocyanate. *ACS Appl. Mater. Interfaces* **2010,** 2, 1430-1443.

23. Meador, M. A. B.; Fabrizio, E. F.; Ilhan, F.; Dass, A.; Zhang, G.; Vassilaras, P.; Johnston, J. C.; Leventis, N., Cross-linking amine-modified silica aerogels with epoxies: mechanically strong lightweight porous materials. *Chem. Mater.* **2005,** 17, 1085-1098.

24. Rao, A. V.; Bhagat, S. D.; Hirashima, H.; Pajonk, G. M., Synthesis of flexible silica aerogels using methyltrimethoxysilane (MTMS) precursor. *J. Colloid Interface Sci.* **2006,** 300, 279-285.

25. Kanamori, K.; Aizawa, M.; Nakanishi, K.; Hanada, T., New transparent methylsilsesquioxane aerogels and xerogels with improved mechanical properties. *Adv. Mater.* **2007,** 19, 1589-1593.

26. Rajamanickam, R.; Kumari, S.; Kumar, D.; Ghosh, S.; Kim, J. C.; Tae, G.; Sen Gupta, S.; Kumaraswamy, G., Soft colloidal scaffolds capable of elastic recovery after large compressive strains. *Chem. Mater.***2014,** 26, 5161-5168.

27. Zhang, H.; Hussain, I.; Brust, M.; Butler, M. F.; Rannard, S. P.; Cooper, A. I., Aligned two-and three-dimensional structures by directional freezing of polymers and nanoparticles. *Nat. Mater.* **2005,** 4, 787-793.

28. Munch, E.; Launey, M. E.; Alsem, D. H.; Saiz, E.; Tomsia, A. P.; Ritchie, R. O., Tough, bio-inspired hybrid materials. *Science* **2008,** 322, 1516-1520.

29. Deville, S.; Maire, E.; Bernard-Granger, G.; Lasalle, A.; Bogner, A.; Gauthier, C.; Leloup, J.; Guizard, C., Metastable and unstable cellular solidification of colloidal suspensions. *Nat. Mater.* **2009,** 8, 966-972.

30. Kumari, S.; Kulkarni, A.; Kumaraswamy, G.; Sen Gupta, S., Large Centimeter-Sized Macroporous Ferritin Gels as Versatile Nanoreactors. *Chem. Mater.* **2013,** 25, 4813-4819.

31. Winter, H. H.; Mours, M., Rheology of polymers near liquid-solid transitions. In *Neutron spin echo spectroscopy viscoelasticity rheology*, Springer: **1997**; pp 165-234.

32. Treloar, L. R. G., *ThePhysics of Rubber Elasticity*. Oxford University Press, USA: **1975**.

33. Garcia, R.; Gomez, C. J.; Martinez, N. F.; Patil, S.; Dietz, C.; Magerle, R., Identification of nanoscale dissipation processes by dynamic atomic force microscopy. *Phys. Rev. Lett.* **2006,** 97, 016103.

34. Cleveland, J. P.; Anczykowski, B.; Schmid, A. E.; Elings, V. B., Energy dissipation in tapping-mode atomic force microscopy. *Appl. Phys. Lett.* **1998,** 72, 2613-2615.

35. Payam, A. F.; Ramos, J. R.; Garcia, R., Molecular and nanoscale compositional contrast of soft matter in liquid: interplay between elastic and dissipative interactions. *ACS Nano* **2012,** 6, 4663-4670.

36. Garcia, R.; Magerle, R.; Perez, R., Nanoscale compositional mapping with gentle forces. *Nat. Mater.* **2007,** 6, 405-411.

37. Rodriguez, T. R.; Garcia, R., Compositional mapping of surfaces in atomic force microscopy by excitation of the second normal mode of the microcantilever. *Appl. Phys. Lett.* **2004,** 84, 449-451.

Chapter 3

Single-Particle Tracking to Probe the Local Environment in Ice- Templated Crosslinked Colloidal Assemblies

In this work, we use single particle tracking to investigate colloidal dynamics in elastic sponges and plastic monoliths. Elastic and plastic scaffolds are prepared using ice templating and are macroporous monolithic structures. We investigate microstructure-property relations in assemblies that appear chemically identical, but show qualitatively different mechanical response. Specifically, we contrast elastic assemblies that can recover from large compressive deformations with plastic assemblies that fail on being compressed. Particle tracking provides insights into the microstructural differences that underlie the different mechanical response of elastic and plastic assemblies. Since colloidal motions in these assemblies are sluggish, particle tracking is especially sensitive to imaging artifacts such as stage drift. We demonstrate that the use of wavelet transforms applied to trajectories of probe particles from fluorescence microscopy eliminates stage drift, allowing a dynamical resolution of about 2 nm. In elastic and plastic scaffolds, probe particles are surrounded by other particles– thus, their motion is caged. We present mean square displacement and van Hove distributions for particle motions and demonstrate that plastic assemblies are characterized by significantly larger spatial heterogeneity when compared with the elastic sponges. In elastic assemblies, particle diffusivities are peaked around a mean while in plastic assemblies, there is a wide distribution of diffusivities with no clear peak. Both elastic and plastic assemblies show a frequency independent solid modulus from particle tracking microrheology. Here too, there is a much wider distribution of modulus values for plastic scaffolds as compared to elastic, in contrast to bulk rheological measurements where both assemblies exhibit a similar response. We interpret our results in terms of the spatial distribution of crosslinks in the polymer mesh in the colloidal assemblies.

The content of this chapter is published in,

"*Langmuir* 2018, 34, 4603-4613". (*Reproduced with permission from American Chemical Society)*

3.1 Introduction

Colloidal assemblies are technologically important materials with implications for nanoscale electronics[1], energy conversion/storage devices[2], photonic and plasmonic devices[3], drug and gene delivery systems[4], diagnostic systems[5] as well as for catalysis[6]. However, the fragile mechanical response of colloidal assemblies limits their use.[7] Therefore, there is intense research focused on understanding the structural underpinnings of failure in colloidal assemblies and, into leveraging this understanding to prepare mechanically robust colloidal assemblies.[8-11] Recently, Rajamanickam et al. have demonstrated the preparation of hybrid colloid/polymer assemblies that exhibit remarkable elastic recovery from large compressive strains exceeding 90%, despite an inorganic particle content of 90% by weight.[12] These macroporous assemblies were prepared by ice-templating, and comprise colloids held in a crosslinked polymer mesh to form centimeter-sized monoliths. They have shown that such elastic assemblies are obtained for several different colloids (including polystyrene latex, silica colloids, hydroxyapatite, etc.), for different polymers (including polyethylenimine of different molecular weights, gelatin, etc.) and for different crosslinking chemistries (using glutaraldehyde or diepoxide crosslinkers). Thus, the exceptional mechanical properties of the sponge-like assembly are not a consequence of the chemical composition of the constituents. Rather, they can be attributed to inorganic/organic hybrid microstructure that is formed using the ice-templating protocol, viz., freezing an aqueous dispersion of colloids, polymer and crosslinker, and allowing crosslinking to happen *in-situ* after the water has frozen. This chemistry-independence allows the selection of suitable functional materials to prepare elastic colloidal sponges for applications ranging from flexible supercapacitors[13] to tissue engineering scaffolds[12] and separation media[14].

We have investigated the microstructure that develops in these ice-templated hybrids, to understand its relation to the observed elastic mechanical response. In Chapter 2, we have seen that the mechanical response is sensitive to the preparation protocol employed to prepare the assemblies. For example, if the ice crystals formed by freezing the colloidal dispersion are removed by lyophilization, so that crosslinking happens in the absence of ice, the resultant monoliths are plastic, viz., they fail on compressing even to small strains. Surprisingly, the overall chemical composition of such plastic monoliths is indistinguishable from the elastic sponges. Both are macroporous and are characterized by the same pore size distribution. They are both characterized by the same organic content, same polymer to crosslinker ratio and the same average crosslink density. Therefore, the stark differences between the

mechanical response of elastic and plastic scaffolds must arise from subtle local variations in their microstructure. In the previous chapter, we have reported atomic force microscopy (AFM) investigations of the local structure of elastic and plastic scaffolds. AFM results suggest that elastic sponges are characterized by relatively uniform crosslink density, while there are large spatial variations in the crosslink density in plastic monoliths. Thus, even when the average crosslink density is similar for elastic sponges and plastic monoliths, these subtle local differences in crosslinking result in widely different response to mechanical compression. Therefore, developing sensitive probes that can interrogate local microstructure holds promise for insights into material properties, and material failure. Specifically, such probes can provide independent confirmation of the local microstructural differences between elastic sponges and plastic monoliths.

Probing the dynamics of colloids embedded in the monoliths provides information about the local environment around the colloid. For colloids held in a crosslinked polymer mesh, we anticipate that colloidal motions are highly restricted, rendering microscopy observations of such motions highly challenging. Particle tracking, using optical microscopy is routinely employed to investigate the dynamics of Brownian colloids in low viscosity Newtonian liquids.[15] In contrast, the motion of colloids embedded in monoliths is sluggish, rendering microscopy challenging. The use of direct microscopic observation however has significant advantages and has been used to quantify motions in dense colloidal systems to access local, micron scale dynamics. For example, Weeks et al. employed confocal microscopy to study dynamical changes near the jamming transition of a concentrated colloidal glass.[15] They could identify caging of particle motions in colloidal glasses and reported the observation of dynamic heterogeneities and structural relaxation phenomena near the colloidal glass transition. The microscopic structure of shear thickening or shear thinning colloidal suspensions has also been investigated using microscopy[16], where the thermal motion of several thousand particles are tracked with high spatio-temporal resolution. Such techniques are being used to provide insights into cellular processes in biology[17, 18], local plasticization in polymer matrices[19], adsorption-desorption dynamics[20], local heterogeneity in clay suspensions, polymeric thickener solutions, food gels, etc.[21-25]

Investigating the dynamics of sluggish colloidal systems, where particle motion is highly restricted, requires high resolution optics that are stable over long imaging durations. Remarkable advances have been made in spatial resolution in single molecule microscopy.[26, 27] Of specific interest to us are laser epifluorescence techniques that limit the excitation volume to a very narrow depth, thus reducing the contribution of out of focus, background

light.[28] The spatial resolution that one can achieve using these methods is strongly dependent on the signal to background ratio (SBR). Harnessing these methods to problems in colloid science would make it possible to investigate systems where displacements are too small to be probed using conventional imaging tools. Dekker et al. has shown that non diffraction limited particles imaged using 40X magnification and with SBR ≥20 could be tracked with a spatial resolution of ≈10 nm.[29] However, when imaging colloidal particles (instead of single molecules), the sluggish nature of the systems requires imaging over long durations, typically several minutes or more. In such experiments, unless an extremely stable microscopy setup is used, one has to guard against artifacts in single-particle tracking data. The most common problem is sample stage or focus drift which may arise due to a variety of reasons, including vibrations, acoustic noise and thermal drift.[30, 31] When particle motions are themselves small (~ few nanometers) with respect to the external factors mentioned, even stage drift of a few tens of nanometers could result in erroneous apparent particle motion. To reduce mechanical drift, microscopes are typically mounted on air cushioned optical benches. In addition, several post acquisition techniques have been utilized to correct for stage drift. These rely either on the use of fiducial markers in the sample[32] or marker-less methods such as template matching[33]. Bloess et al.[34] reported optical imaging of single fluorescent molecules with a reproducibility of 3.4 nm in lateral position[34], attained by mechanical drift correction by observing the position of a spatial reference in the sample. Carter et al.[35] further improved the resolution of single-molecule experiments by eliminating drift by referencing with a fiducial mark on the microscope coverslip.[35] In their experiments, drift was corrected through a feedback coupled piezoelectric stage and gave a stability of 0.17 nm for tens of seconds. However, the use of external markers with brightness that is very different from the particles of interest could result in camera pixel saturation, and further, the marker position with respect to the sample cannot be predetermined. Finally, template matching techniques rely on distinct image features, and a consistent background structure that are not always available. Therefore, the use of fiducial markers or template matching to eliminate stage drift cannot be practiced in all experimental situations.

If the number of particles (N) in a frame is large, researchers have suggested subtraction of the average tracer center of mass motion from the particle trajectory. However, this approach introduces an error in the mean square displacement of the order of $1/N$. Therefore, use of this method is advisable only once when the number of tracers in a frame is much greater than 10.[36] Crocker et al.[36, 37] have described another protocol to eliminate stage drift, where they calculate the correlated motion of two particles in a frame along their line of

centers. They used regression techniques to fit this motion to a model, and used this to calculate the two point microrheology.[36, 37] However, application of this process to frames that contain several particles is rather tedious.

In this Chapter, we demonstrate the use of wavelet transforms to eliminate stage drift from single-particle tracking data collected on fluorescent micrometer polystyrene beads which form a part of the network. Wavelet transforms have been used in particle tracking experiments for multiscale detection of particle motions, denoising, 3D deconvolution of fluorescence micrographs and for extending the depth of field.[38] Here, we report a facile method that uses commonly available software tools, and allows for the elimination of stage drift from microscopy data to obtain tracer localization down to few nanometers. We then utilize this method to examine colloidal dynamics in elastic sponges and plastic monoliths and demonstrate differences in the spatial variation of crosslinking density in elastic and plastic scaffolds.

3.2 Experimental Section

3.2.1 Materials:

1μm "Angstrom sphere" spherical silica particles were obtained from Richen Industries (Hong Kong). Monodisperse 1.08 μm (SD=0.04μm) fluorescent polystyrene spherical particles (PS-FluoGreen-1.0, ab/em: 492/519 nm, 2.5 wt %) were obtained from MicroparticlesGmbH (Germany). Branched polyethylenimine (PEI, 25kDa), 1, 4-butanedioldiglycidylether and polyvinylpyrrolidone (PVP, MW- 40kDa) were obtained from Sigma-Aldrich. All materials were used as received. Glass cover slips (No.1, Corning, USA) were used as the substrate in particle tracking experiments.

3.2.2 Sample Preparation:

General protocol for the synthesis of self standing monoliths from colloidal particles: 60 mg 1μm silica particles and 2 mg 1μm fluorescent PS particles were dispersed in DI water (overall particle concentration in the dispersion is 10 wt %). This dispersion was sonicated for 15 min followed by 5 min vortexing. To this aqueous dispersion was added 3 mg of PEI (30 μl of 100 mg/ml polymer stock solution) and was mixed by vortexing for 5 min. To this was added 10 mg of 1,4-butanediol diglycidyl ether followed by 3 min vortexing.

Preparation of elastic sponges: The aqueous dispersion was placed in a freezer maintained at ≈ -15^{o}C for 24 h followed by thawing at room temperature.

Preparation of plastic monoliths: The aqueous dispersion was frozen for 30 min at -15°C followed by lyophilization for 4 h at -80°C, to sublime the ice crystals. After removal of ice, the sample was maintained at -15°C for 24 h to allow crosslinking. After crosslinking, both elastic and plastic scaffolds were washed thoroughly in water (Figure 3.1).

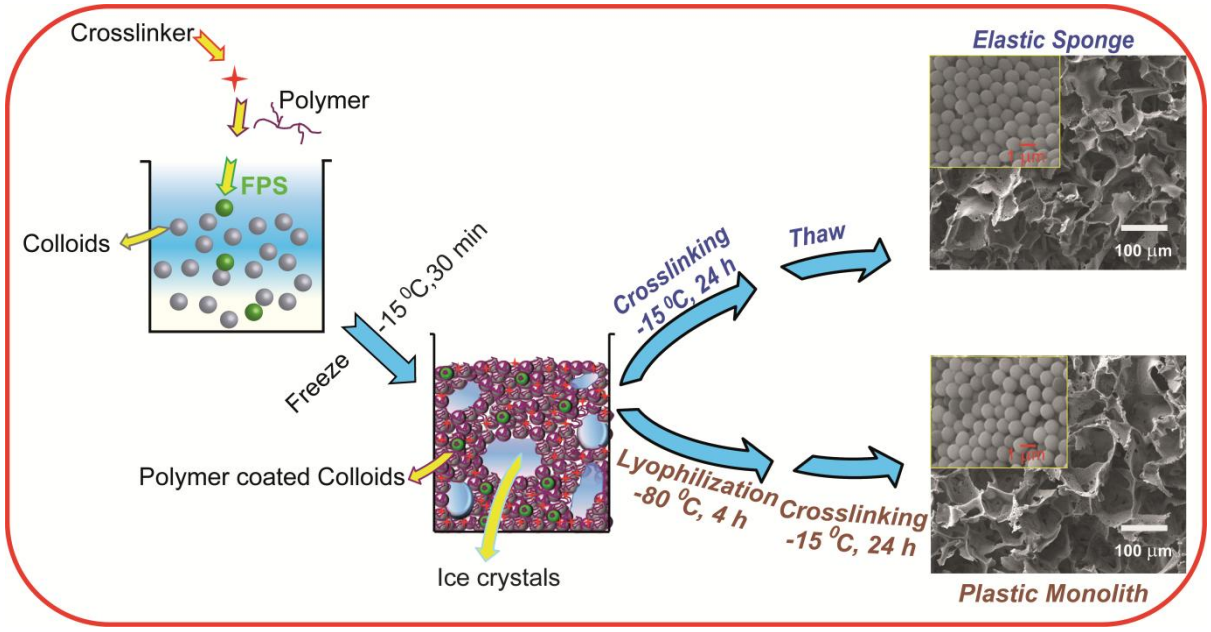

Figure 3.1: Protocol for the preparation of elastic sponge and plastic monolith. Scanning electron microscopy (SEM) morphology shows, both elastic and plastic scaffolds are macroporous, with hybrid pore walls comprising packed colloids held together by a crosslinked polymer mesh.

Preparation of reference glassy sample for calibration of single particle tracking experiment: 1µm PS particles were mixed with 4 wt% aqueous PVP solution. The uniformly mixed solution was drop cast on a clean glass coverslip. The sample was annealed at 80°C for a day under vacuum. The annealed reference sample was placed inside a homebuilt humidifier mounted over the microscope stage and maintained at ambient temperature and pressure. Humidity in the enclosed chamber was controlled by regulating the argon gas flow, that was passed through water and then into the chamber. Temperature and humidity were maintained constant during all measurements. Glass coverslips were cleaned by first sonicating for 10 min in piranha solution and then in 2M NaOH, followed by washing several times with Milli Q water and with methanol. After drying by blowing nitrogen gas, the coverslips were burned in an oxidizing flame to remove any fluorescent impurity on the cover slip.

3.2.3 Characterization

***3.2.3.1 Scanning Electron Microscopy (SEM)*:** The sample morphology was imaged using a Quanta 200 3D scanning electron microscope. Thin slices were cut from the scaffolds using a surgical blade. These were mounted on SEM stubs and were coated by sputtering a thin layer of gold on their surface before imaging.

***3.2.3.2 Single particle tracking*:** Fluorescent particles were imaged using a home built epifluorescence microscope. A 488 nm cw DPSS laser (LaserGlow, 50 mW) was passed through a circular polarizer and was focused onto the back focal plane of a 60X, 1.49 NA oil immersion objective (Nikon, Apo plan TIRF), so as to illuminate a circular area of the sample. Neutral density filters were used to control the excitation power. The light emitted by the sample was collected using the same objective lens and passed through a dichroic mirror. The emitted light was guided through a pin hole and filter wheel and impinged on a cooled (-25^{o}C) interline CCD camera (DVC- 1412AM). Time lapse movies were collected for ten minutes at 1Hz with an exposure time of 150 ms. Image data was collected as a movie using DVC View software.

Detailed procedure for analysis of data from particle tracking experiments

a. Particle tracking experiment

A small piece of the colloidal assembly was cut from the monolith and was placed over a clean coverslip. To ensure that the sample does not experience any load; we place an o-ring around the sample and place the top coverslip on the o-ring. This provides a proper seal for the sample chamber. We collect images at a frequency of 1Hz for up to 10 min.

b. Image processing

We load image sequences in ImageJ and delete the first frame. We then define a region of interest (ROI) that contains one particle. Next, we employ background subtraction in the ROI to enhance the contrast of the particle. This was performed using ImageJ software (NIH). After background subtraction, fluorescent particles appear as bright spots with the signal to background ratio (SBR) of between 20-35 (Figure 3.2).

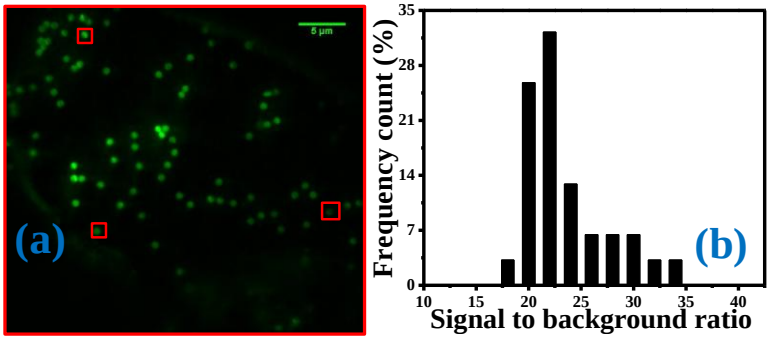

Figure 3.2: (a) Epifluorescence microscopy image of 1μm fluorescent PS (FPS) particles embedded in a glassy matrix. **(b)** Signal to background ratio after background subtraction for multiple particles.

To locate the spatial positions of these bright individual particles over time, we have used single particle tracking program written in Matlab 7.8. The program algorithm is based on the centroid method.[19] Here, we extract X and Y coordinates of the centroids of the bright spots and assign these as the particle center of mass position.

c. Calculating particle coordinates (X and Y) using the centroid method

We have used MATLAB code based on centroid algorithm to track the particles individually to monitor their displacement between successive frames. This algorithm calculates the centre of mass of the object of interest and which provides an absolute position of an object in each image independently. We fit the intensity of the particle in the ROI and determine its centroid. The background subtracted particle movies are used as an input parameter for this program. The centroid of the particle is calculated using the following equations:

$$x_c = \frac{\sum_{i=1}^{n}\sum_{j=1}^{m} x_i I_{ij}}{\sum_{i=1}^{n}\sum_{j=1}^{m} I_{ij}} \qquad y_c = \frac{\sum_{i=1}^{n}\sum_{j=1}^{m} y_j I_{ij}}{\sum_{i=1}^{n}\sum_{j=1}^{m} I_{ij}} \qquad (1)$$

where, x_i is the x coordinate of a pixel , I_{ij} is the intensity of that pixel and similar notationis used for the Y axis.

We track the centroid of each particle of interest and monitor their displacement between successive frames.

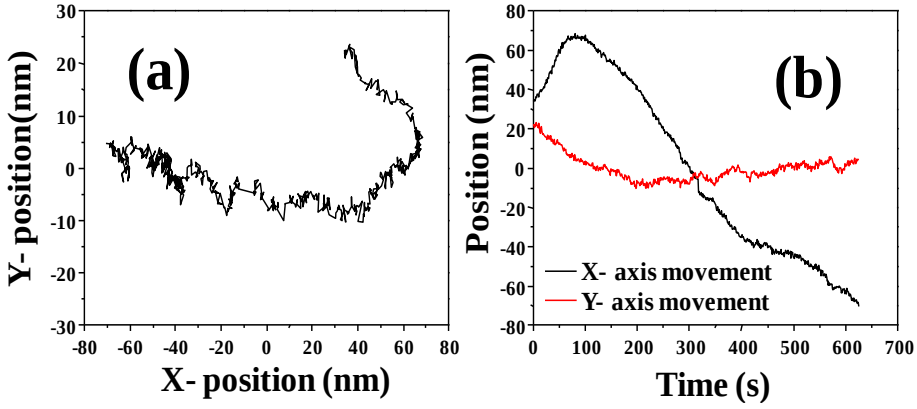

Figure 3.3: Single particle coordinates obtained by centroid method: **a)** Single particle trajectory. **b)** X and Y coordinates obtained for a particle.

Thus, particle coordinates are obtained for all frames of the movie and are used to extract the particle trajectories (Figure 3.3).

All measurements were performed at 23^{o}C temperature and 60% relative humidity. The relative humidity was monitored using RH probe positioned a few mm away from the sample. We maintain a constant temperature of 23^{o}C using an ambient temperature control system. We constantly monitor the temperature during the experiment using a thermocouple connected to the microscope sample stage. The measurements were repeated several times to confirm their reproducibility.

3.3 Results and Discussion

We begin by using epifluorescence microscopy to investigate the reference sample. Individual 1 μm fluorescent polystyrene beads embedded in a glassy PVP matrix appear as bright spots against a dark background (Figure 3.2). Relative humidity is controlled to < 20% during imaging experiments to prevent humidity-induced plasticization of the glassy matrix. Raw microscopy data suggests that the fluorescent polystyrene bead traverses over 100 nm in the PVP matrix over a time span of 10 minutes (Figure 3.4a). Such large length scale motion of micron sized colloids embedded in glassy matrices is physically unrealistic. Literature reports of microscope investigations of the motion of small molecules embedded in a glassy matrix suggest that these molecules are essentially frozen in the matrix, viz., motions, if any, are characterized by sub-nm length scales.[19] Therefore, the apparent trajectories of the 1 μm latex particles, spanning over 100 nm, must arise from experimental artifacts.

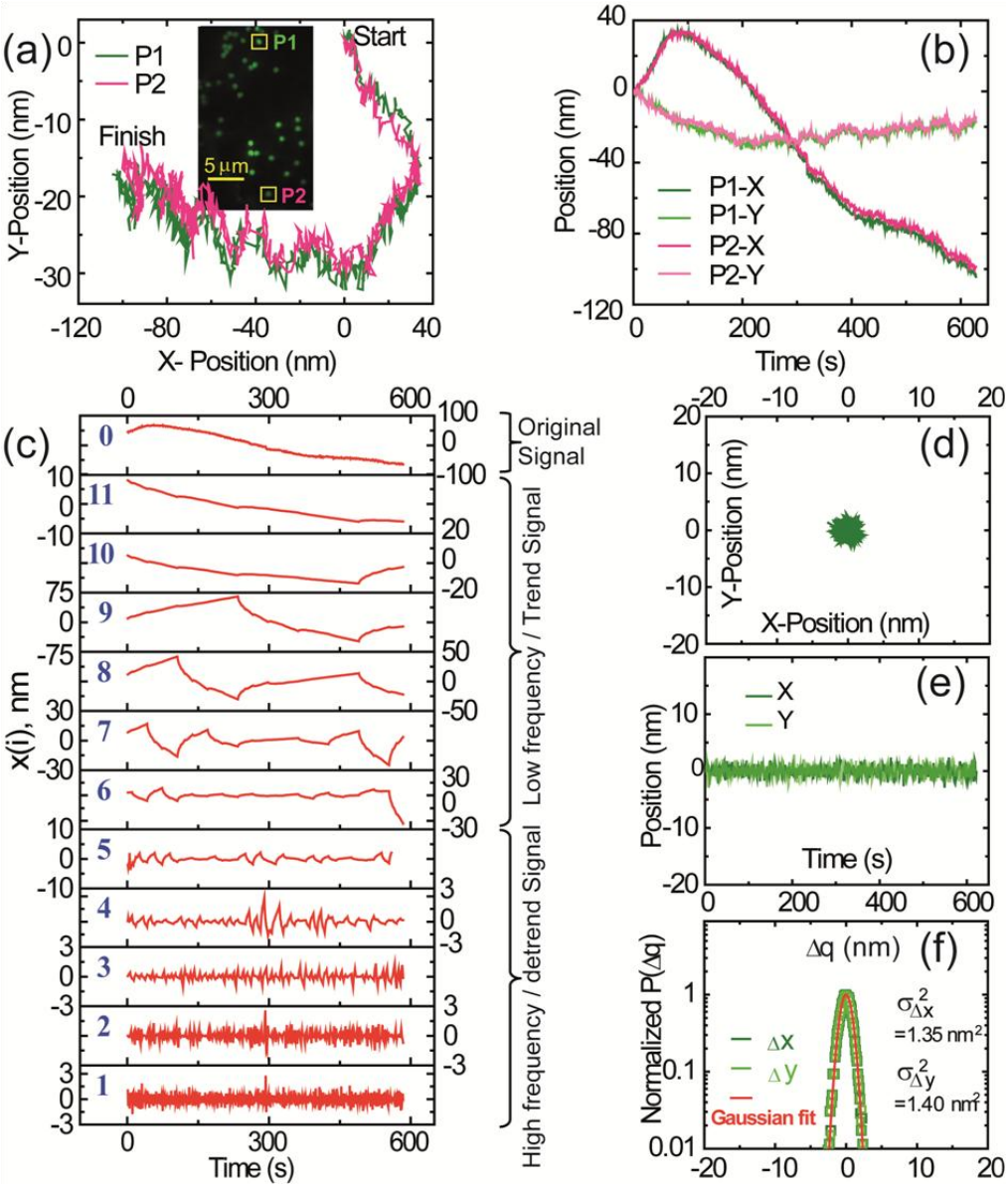

Figure 3.4: Fluorescence microscopy data from tracking of individual probe particles in reference glassy sample. **(a)** Trajectory of two FPS particles embedded in PVP glassy matrix. The inset shows a microscopy image. Note that the probe particles are readily resolved, and are widely separated making it easy to track the motions of individual particles. **(b)** Trajectories shown in (a) are represented as the time-dependent motion of the two particles along arbitrary X and Y coordinates, with coordinate axes as defined in (a). **(c)** Wavelet transform studies of the X- component of the reference data showing scale wise reconstruction, X(i) (i=1,2…11). X(0) is the reconstructed lossless data and equivalent to the X- component. **(d), (e)** The trajectory and time dependent position along X and Y axes of a particle, after removal of stage drift. **(f)** Jump length distribution for particle "jumps" per frame along the X and Y axes. The jump distribution is well fitted by a Gaussian, as shown.

We now discuss the origin for the observed drift in particle motion. It may be seen that widely separated fluorescent particles embedded in the glassy matrix show correlated motion (Figure 3.4b plots particle motion along an arbitrarily determined X and Y coordinates for two particles in the same image frame, but separated by about 30μm). Such slow motion over long experimental time scales, of the order of 10 min, have been previously reported[17] and have been attributed to stage drift. Stage drift can arise from vibrations (despite the use of vibration damping in our experiments), drift in the stepper motors used for sample positioning, temperature fluctuations (for example, induced by environmental changes or variations in laser source intensity), etc. Stage drift represents a persistent experimental challenge when microscopy is used to track motion in samples over long time scales (~ min). We now demonstrate how wavelet transforms can be used to deconvolute stage drift from particle Brownian motion in analysis of microscopy data.

3.3.1: Elimination of correlated motion due to stage drift by using wavelet transform

In long term imaging where we capture the movie for tens of minutes, significant lateral drift is observed as shown in Figure 3.5.

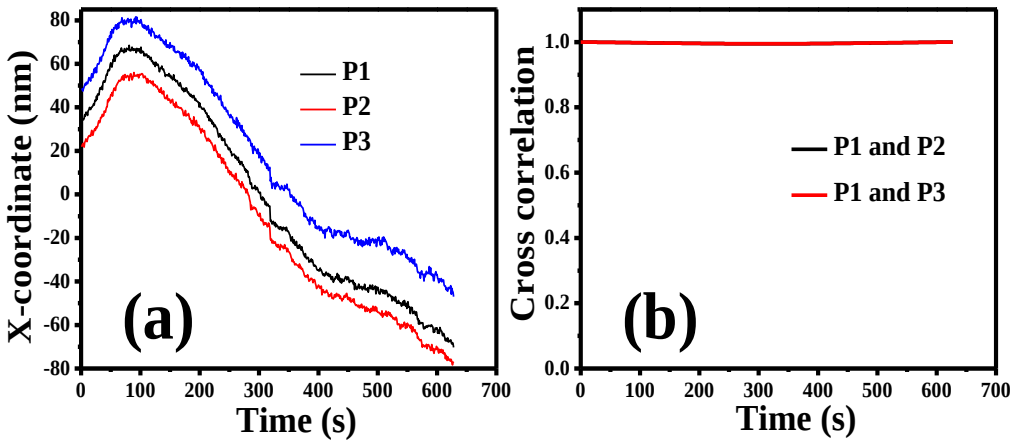

Figure 3.5: X coordinates of three arbitrarily chosen particles obtained from a time lapse images of a single region. **(a)** The three particles have shown a directional movement along with small jumps per frame. **(b)** The cross-correlation between three particles. These three particles are strongly cross-correlated.

To subtract the lateral drift in long term time lapse imaging, we have used wavelet transform to identify the fluctuating component by eliminating the drift from the raw signal. In our system, we term the low frequency signal as the trend signal ($T(n\Delta t)$) and the high frequency signal as the detrend signal ($D(n\Delta t)$).

Unlike the Fourier transform which uses sines and cosines as the basis functions, the wavelet transform uses basis functions that have localized properties in both the analyzed scales and translations (i.e., time in our study). In its most general form, the wavelet transform is carried out to obtain wavelet coefficients at different scales (a) and time (b) as:

$$W(a,b) = \int_{-\infty}^{\infty} f(x)\, \varphi^{*}_{(a,b)}(x)dx \qquad (2)$$

where, *f(x)* is the signal undergoing the convolution with the wavelet function $\varphi^{*}_{(a,b)}$ chosen at scale *a* and translations *b* (the * denotes the complex conjugate symbol).

It should be noted that the wavelet function $\varphi^{*}_{(a,b)}$ at different scales, *a* are chosen to satisfy two basic conditions. The first is the condition of compactness, namely,

$$\emptyset(x) = \sum_{k=-\infty}^{\infty} a_k\, \emptyset(Sx - k) \quad (3)$$

where S is a scaling factor usually chosen as 2 and a_k represent a set of coefficients characterizing the wavelet basis $\emptyset$. The second condition is that the area between basis wavelets at scales *a* are normalized and chosen to be orthogonal to its integer translations, i.e.,

$$\int_{-\infty}^{\infty} \emptyset(x)\, \emptyset(x + l)dx = \delta_{0,l} \quad (4)$$

The discrete wavelet transform (DWT), therefore obtains wavelet coefficients $W(a,b)$ that characterize the discretized signal of length N at dyadic scales *(a)* and translations (b). The use of orthogonal basis functions provides a lossless convolution of the original signal x without any redundancy on deconvolution by the inverse wavelet transform.

For the present signal processing study, we have used the DWT using the Daub4 orthonormal wavelets from the well-known Daubechies set of orthonormal wavelets.[39-41] Daubechies wavelets have been extensively used to represent non linear, non stationary signals.[42, 43] The Daub4 wavelets use 4 non-zero coefficients a_k in their definition and have been generally recommended to analyze spiky signals (as is analyzed here) when compared to the higher order Daub 6, Daub 8, …, Daub 20 etc., where the wavelet basis functions become increasingly smoother. We implement the wavelet transform using the Mallat pyramidal algorithm.[44] In this algorithm two filters - smoothing and non-smoothing are derived and are used repeatedly to obtain wavelet coefficients at all scales. If the length of the data is $D = 2^N$ and the signal length is L then the first coefficient data at scale $L/2^{N-1}$ is computed

followed by $(D/2)/2$ data at scale $L/2^{N-2}$, … , $L/2$. These coefficients are indexed in scales as belonging to the largest scales (lower frequency components) to progressively smaller ones (higher frequency components). This deconvolution yields the scale wise components as shown in Figure 3.4c.

Thus, the DWT can be readily used to separate the fluctuating components in the signal. The principle followed is that if we take a limited number of lowest scale coefficients of the DWT spectrum and perform an inverse wavelet transform, we can obtain the fluctuating component in the signal. To determine the scales to be retained to reconstruct the signal, we chose a method that has been applied to a variety of nonlinear and nonstationary signals arising in different systems. This method analyzes the power distribution characteristics of the wavelet transformed signal at various scales to identify a threshold. As seen in Figure 3.6, we observe that the scales with low power (corresponding to scales 1-5) are related to the fluctuating component in the signal and are masked because of the high power seen in scales 6-11 arising due to experimental drift (trend). Carrying out the inverse wavelet transform using wavelet coefficients for scales i = 1, 2, … , 5 and setting those corresponding to i = 6, …, 11 equal to zero retains only the fluctuating component and the trend signal is eliminated (Figure 3.7). It may be noted that we studied different raw signals and observed similar power behavior as seen in Figure 3.6 for all data sets. Thus for the system under study the threshold scale level was chosen as i=5.

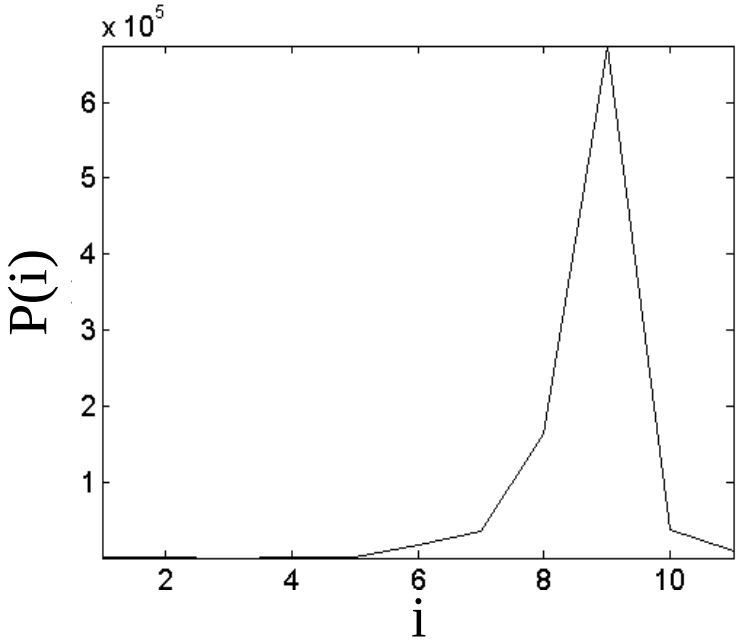

Figure 3.6: Wavelet transform power plot showing the power distribution at different scales. The continuous line has been drawn to aid the eye.

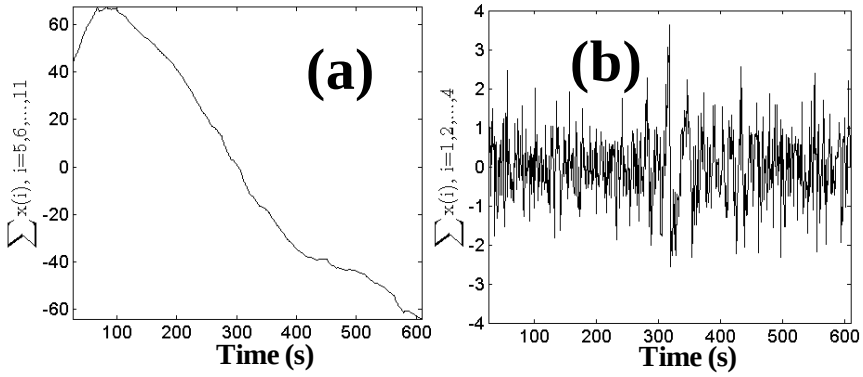

Figure 3.7: (a) The trend in the signal (T($n\Delta t$)); **(b)** detrended signal (D($n\Delta t$)). Note that the original signal, TD ($n\Delta t$)=T($n\Delta t$)+D($n\Delta t$).

The obtained high frequency signal and cross correlation between particles after wavelet transform is shown below (Figure 3.8).

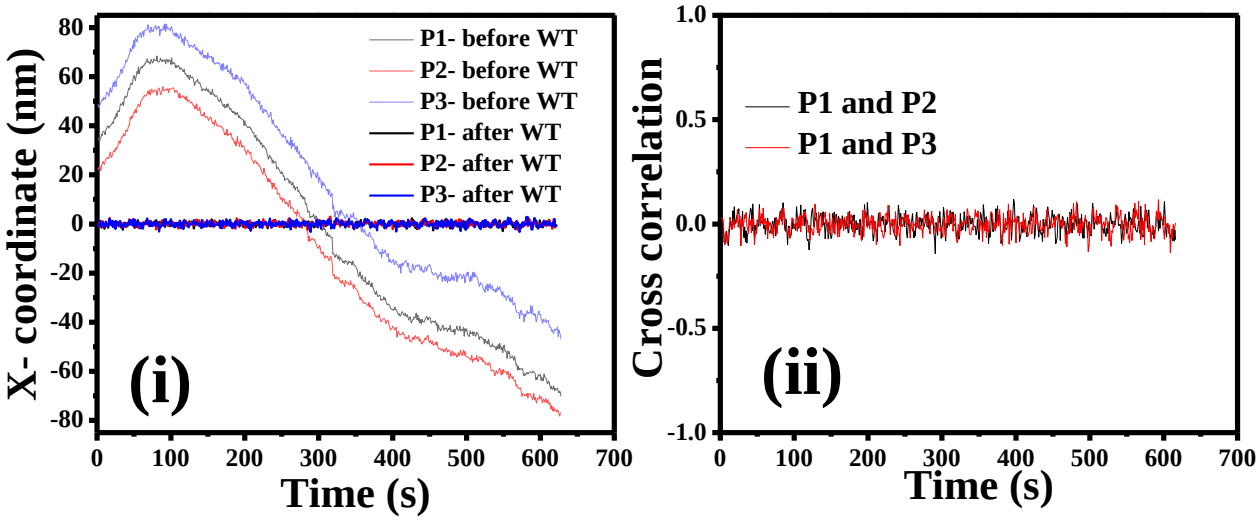

Figure 3.8: (i) The X- coordinate of three particles (P) before and after wavelet transform **(ii)** Cross- correlation between particles after denoising the signal through wavelet transform.

We present analysis of our data by performing Wavelet transforms using code developed by the group of Dr. V. Ravikumar.[45-48] However, such analysis can also be readily performed using several commercial analysis tools. We now show that the results of analysis using commercial routines are consistent with that from our in-house codes.

3.3.2: Wavelet denoising using Origin software

Signal processing using wavelet transforms can also be done using widely available data handling programs. We use Origin software (OriginPro v8) and use the wavelet

transform tool available in the signal processing analysis module. We use wavelet denoising method to separate the drift from the actual particle Brownian motion. As before, we use the DB4 wavelet as a basis set. We choose the appropriate threshold by comparing coordinate trajectories from two independent particles in a frame, and by examining the cross-correlation between the particle trajectories after signal processing. We then systematically vary the threshold level and examine the cross correlation between particle trajectories. For our data, we have determined that a four level decomposition is adequate to ensure that the motions of independent particles are completely uncorrelated after using the wavelet transform to remove stage drift. The effect of different thresholding level in denoising is shown in Figure 3.9.

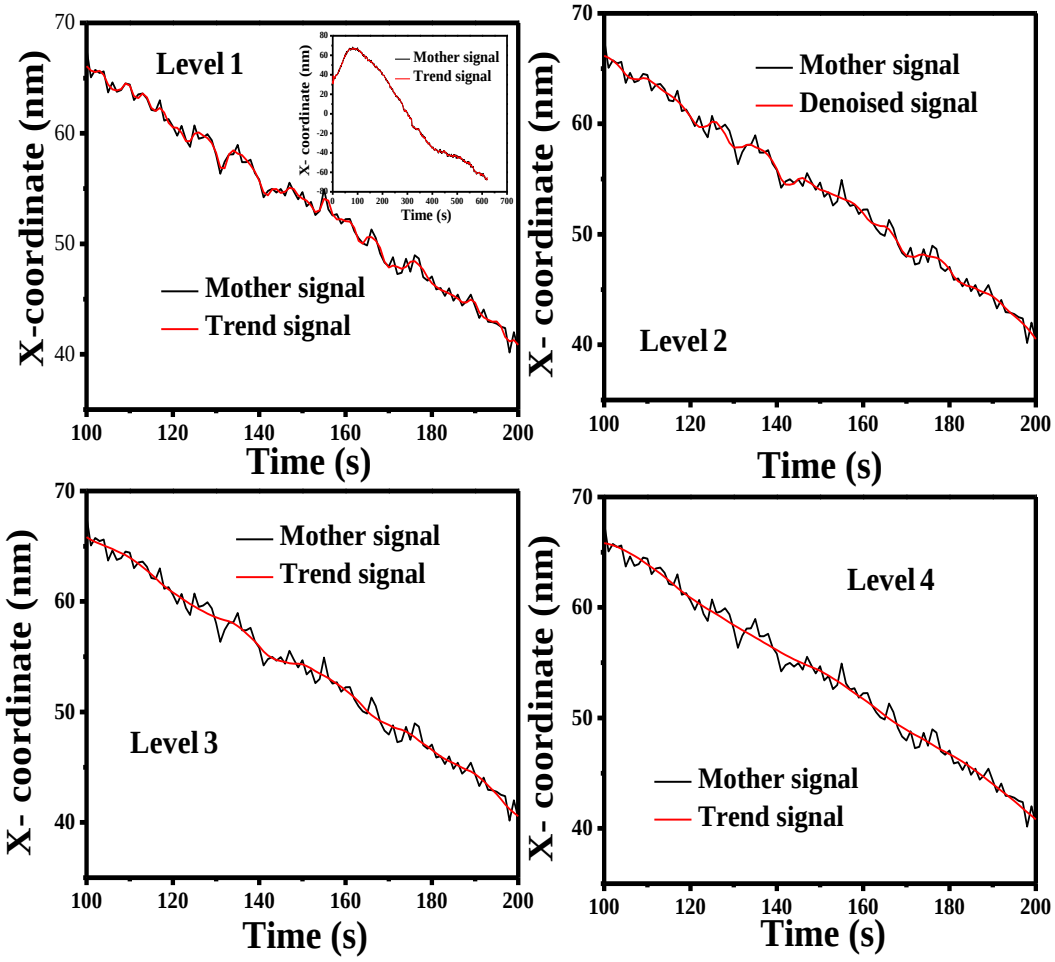

Figure 3.9: The effect of different thresholding levels on the trend signal. The 4 level thresholding showed the best filtering of high frequency signal from low frequency signal.

Comparison between MATLAB and Origin wavelet denoised signals

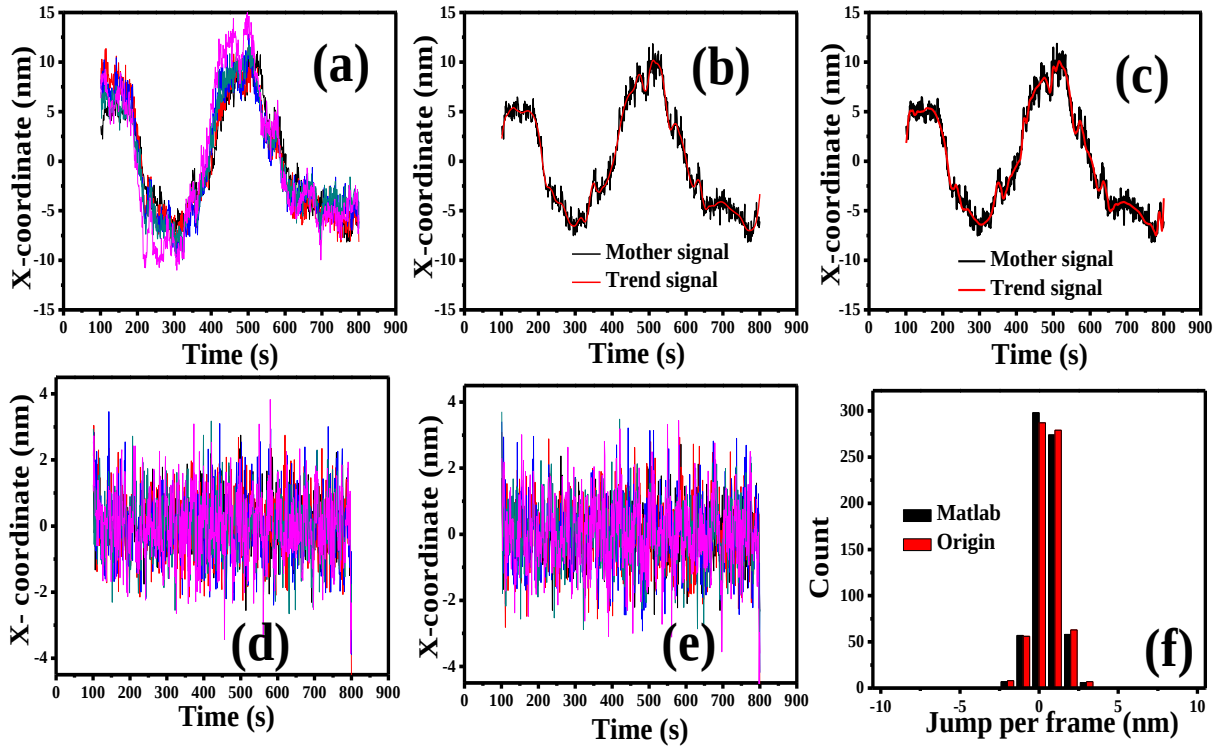

Figure 3.10: Comparison between the results of analysis using the Origin and MATLAB. In Origin we have used 4th order Daubechies basis set and threshold level =4 for denoising the mother signal. In MATLAB, through wavelet transform, the mother signal is deconvoluted into 11 scales. Scales 6-11 represent low frequency signal (trend signal) and scales 1-5 represent detrend signal. (**a**) Mother signals of multiple particles (**b**) and (**c**) taking a representative signal and splitting that signal into trend and detrend signals using MATLAB code and Origin software respectively. (**d**) and (**e**) are the high frequency detrend signals obtained after denoising using MATLAB code and Origin software respectively. (**f**) Comparison between the data obtained through MATLAB code and Origin software in terms of jump distribution. The jump distribution obtained after wavelet transform either through MATLAB code or Origin matches well.

3.3.3: Single particle tracking in reference glassy matrix

We define arbitrary XY coordinate axes for the motion of the polystyrene colloid in glassy PVP and plot motion along these coordinates from the raw microscopy data (Figure 3.4 b). We then subject the X and Y motion to a wavelet transform to subtract the lateral drift in long term imaging. The wavelet transform characterizes the different frequency components present in the original raw signal (mean removed) to obtain the wavelet

scalogram shown in the frequency – time panels of Figure 3.4c. From the lossless nature of the orthogonal wavelet transform using Daub4 wavelets, we obtain the raw signal $x(0,t) = \sum_{i=1}^{11} x(i,t)$ over the entire time period ($t=n\Delta t$, where, Δt is the sampling interval and n=1, 2,⋯.is the discretized data point index), in terms of the scalogram components (i=1,2..11) shown in the panels of Figure 3.4c. Components in higher scales represent the low frequency signal that tracks the stage drift, which is known as the trend signal. Lower scales represent the high frequency "noise" about the drift, referred to as the detrend signal. The scale wise signal power is then given by $P(i) = \sum_t x(i,t)^2$. We observe that the power corresponding to scales (6-11) is significantly higher than those for scales 1-5 (Figure 3.6). Therefore, the signal in scales 1-5 is masked by that in scales 6-11. As mentioned earlier, we use this threshold in power to assign scales 6-11 as the trend signal and scales 1-5 as the detrend signal. Analysis with different colloidal samples showed similar trend and detrend behaviour and a generalized protocol could be obtained. Therefore, we could now subject every individual probe particle to wavelet analysis. Thus by analysing the microscopy data, the excursions of the particles about its mean position could be calculated (Figure 3.4d-e). We also calculated the "jumps" made by the particle over a time interval of 1 s, along the X and Y coordinates by using the formula, $\Delta q = (q_{i+t} - q_i)$, where q is X or Y coordinates and t is the step time (Figure 3.4f) and observed that the jump distributions (or van Hove distributions) along both X and Y coordinates are similar. We fitted the jump distributions to a Gaussian profile and note that they are characterized by a variance of ≈1.4 nm^2. Since we do not anticipate any measurable motion of these large colloidal particles in a glassy matrix, we determine that the resolution limit of measurements is about ±2.5 nm which is the width of the Gaussian at $P(\Delta q)=10^{-2}$. We have also calculated jump distributions for the particles with step sizes of 2 s and 4 s (viz., excursions of the particles across 2 frames or 4 frames), and note that the width of the van Hove distributions islargely independent of the step size (Figure 3.11). Additionally, we have examined the motion of probe particles at different local concentrations, and have confirmed that the resolution from the van Hove distribution is independent of probe particle concentration. We reiterate that to obtain this resolution, we require high signal to background ratio of probes and elimination of artifacts using wavelet transforms.

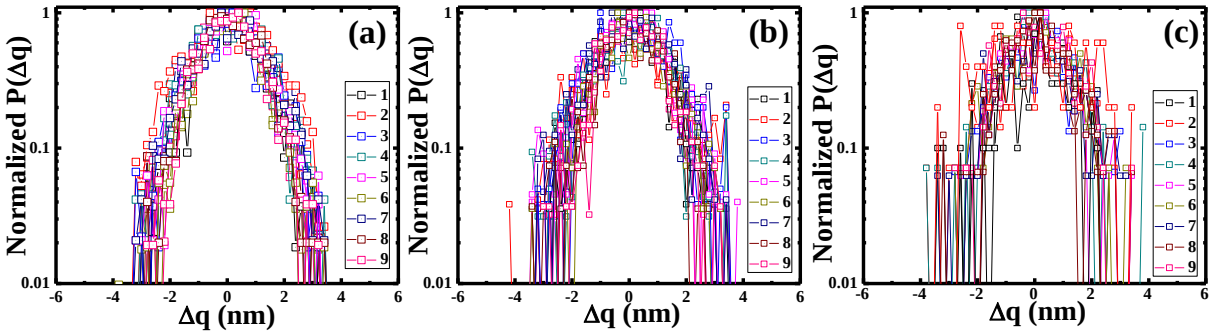

Figure 3.11: The van Hove jump distribution of 9 particles. The jump distribution calculated for time step (**a**) 1 s, (**b**) 2 s and (**c**) 4 s. The comparison of Figures a, b and c shows the resolution is independent of time step and in all cases the dynamical resolution is less than 4nm.

3.3.4 Particle motions in elastic and plastic scaffolds:

Having established a protocol to obtain particle motions by eliminating stage drift, we now apply this to particle tracking data obtained from elastic and plastic scaffolds. Particle scaffolds are prepared by ice-templating a mixture of silica and fluorescent PS (FPS) colloids (Figure 3.1). The scaffolds are macroporous, with ≈50 μm pores bounded by walls comprising colloids bound together in a crosslinked polymer mesh. We use a sparse concentration of fluorescent colloids of size matched with the silica particles. Only the fluorescent particles are visualized in the microscopic image, and as the FPSs are an integral part of the pore walls, tracking their motion provides us insights into how the pore wall microenvironment governs particle dynamics.

We first describe the results obtained from elastic scaffolds. We imaged and tracked multiple (at least 10) FPS particles in the same field of view, and observe that particle motions are correlated, even for widely separated particles (Figure 3.12).

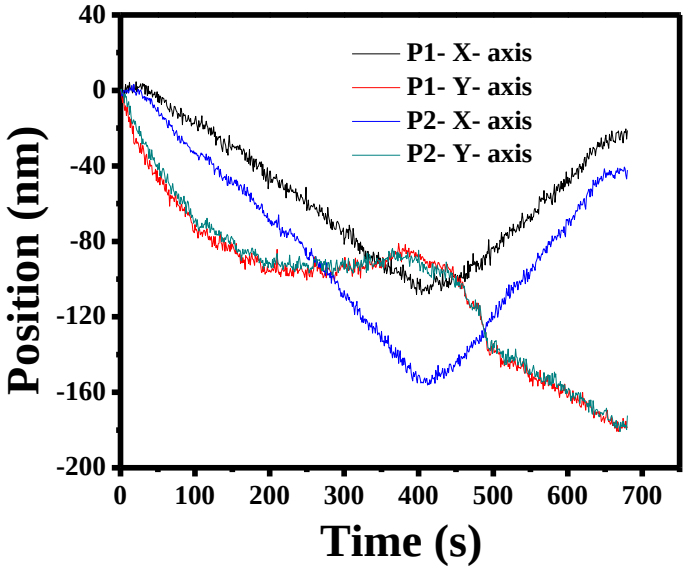

Figure 3.12: X and Y coordinates of two particles present in elastic sponge obtained from a movie. The particles show directional movement along with small jumps per frame.

We attribute these correlated motions to stage drift and employ wavelet transforms, as described in the previous section to eliminate the low frequency correlated motion. Figure 3.13 (a) and (b) shows the time dependent trajectory of one representative particle and the time-dependent particle position along arbitrary XY coordinates, respectively. Using wavelet transform to eliminate the "trend" corresponding to scales 6 – 11, we obtain the position fluctuations due to thermal motion of the particle (Figure 3.13 c, e). It is important to note that the observed fluctuations in position are significantly larger than those observed for the completely immobilized "frozen" reference sample (colloidal PS particle in glassy matrix, compare Figure 3.13 c-e with Figure 3.4d-f). Therefore, the motion observed for the colloidal particles in the scaffolds are above the resolution limit of our technique.

Similarly, we analyze the raw tracking data (trajectory) from plastic scaffold for a representative FPS particle (Figures 3.14 a, b) and use wavelet transforms to eliminate the drift (Figure 3.14 c, d, e). Here too, we find that the thermal fluctuations of the FPS embedded in the walls of the plastic monolith are considerably higher than those for the immobilized (frozen) reference sample (Figure 3.4 d-f) as well as that obtained for the elastic scaffolds (Figure 3.13 c-e). From these trajectories, we obtain the mean square displacement (MSD) in both X and Y directions for probe particles in elastic and plastic scaffolds.

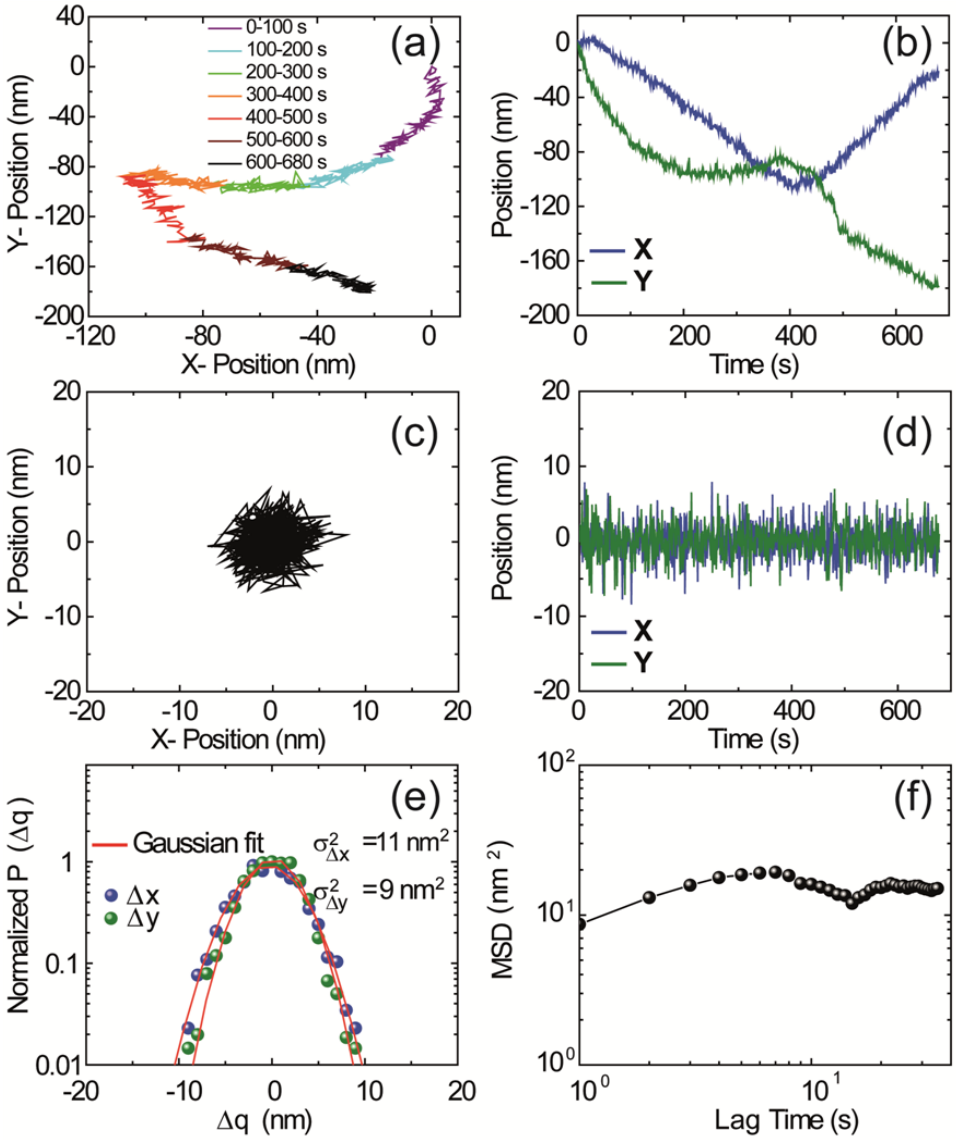

Figure 3.13: Microscopy investigation of elastic sponges. **(a)** Particle trajectory of a single probe particle from fluorescence microscopy. The trajectory is color coded to show the time scale of motion. **(b)** Particle motion along X and Y coordinates (defined arbitrarily, as shown in (a)) as a function of time. **(c)** & **(d)** Trajectory and position of a particle after elimination of stage drift using wavelet transform. **(e)** van Hove jump distribution for a particle along X and Y coordinates, fit to a Gaussian form. **(f)** MSD for particle movement in the X-Y plane. We calculate MSD based on frames collected over about 10 minutes of imaging, but restrict our interpretation to only the first 5% of the lag time, τ, to ensure statistical reliability.

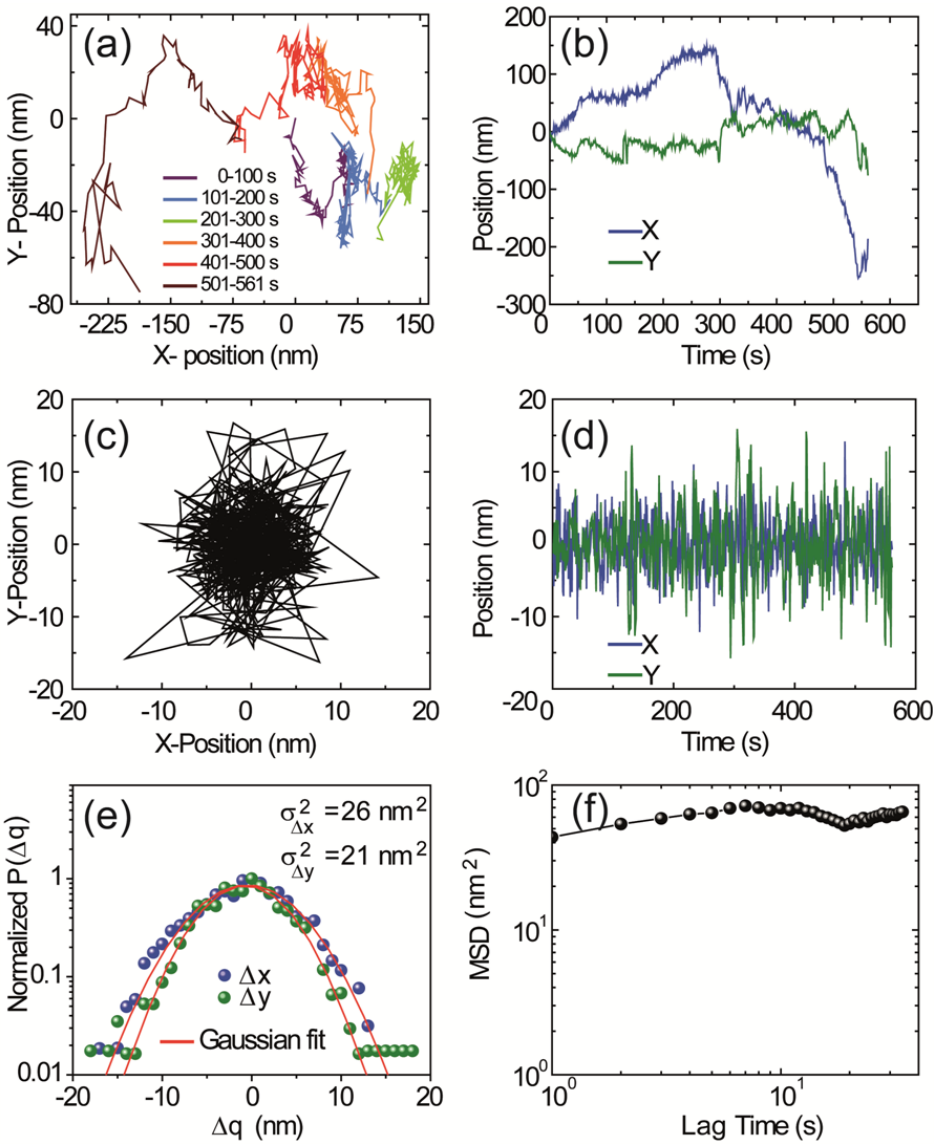

Figure 3.14: Microscopy investigation of plastic monoliths. **(a)** Particle trajectory of a single probe particle from fluorescence microscopy. The trajectory is color coded to show the time scale of motion. **(b)** Particle motion along X and Y coordinates (defined arbitrarily, as shown in (a)) as a function of time. **(c)** & **(d)** Trajectory and position of a particle after elimination of stage drift using wavelet transform. **(e)** van Hove jump distribution for a particle along X and Y coordinates and fit to a Gaussian form. **(f)** MSD for particle movement in the X-Y plane. MSD is calculated and presented as described in the caption for Figure 3.13.

3.3.4.1 Calculation of mean squared displacement (MSD) from detrend signal

MSD is calculated based on the detrend signal obtained from a wavelet transform of the microscopy data. The MSD is calculated as:

$$MSD(\tau) = \langle \Delta r(\tau)^2 \rangle = \langle [r(t+\tau) - r(t)]^2 \rangle \quad (5)$$

where, $r(t)$ is the particle position at time t and τ is the lag time between two particle positions used to calculate the displacement.

X and Y MSDs of elastic sponge and plastic monolith are found to be comparable for all particles (Figure 3.13f and 3.14f respectively). Additionally, we find that the MSD is linear in time for short lag-times, and subsequently plateaus over longer time scales, which is expected for particles embedded in these scaffolds.

To test the reliability of our deconvolution method using wavelet transforms, we have tracked and analyzed more than 100 probe FPS particles in both the elastic and plastic scaffolds. Particles are chosen from widely different spatial locations in each sample, over at least 10 independent samples. This allowed us to construct statistically reliable displacement jump distributions and MSD (τ) for each scaffold. Figure 3.15a and b shows the probability jump distributions (van Hove self correlation functions) of all the FPS particles undergoing a specific distance (Δq, $q = X, Y$) within a minimum time interval of 1 s, for the elastic and plastic scaffolds, respectively, and compared to that of the reference sample where colloidal motions are frozen. It is clear that the motions that we observe in these samples are significantly larger than the instrumental resolution, set by the fluctuations of FPS beads, immobilized probe in a glassy matrix. Further, we can readily observe that the jump distribution spans a much wider range for plastic particles, when compared with the elastic particles. Since the variance of the jump distribution is related to the short time particle diffusivity,[49] we fit each jump distribution to a Gaussian function to extract the distribution of diffusivity for probe particles in the elastic and plastic scaffolds (Figure 3.15 c). We also note that jump distributions for elastic particles from different spatial locations and different samples are relatively similar, with diffusion coefficients spanning from ~1.6 - ~40nm^2/s, and peaking at ≈4 nm^2/s (Figure 3.15c). In contrast, there is considerably more heterogeneity in the diffusivity of particles embedded in plastic samples, ranging from ~2.4 - ~120 nm^2/s, with no clear peak value.

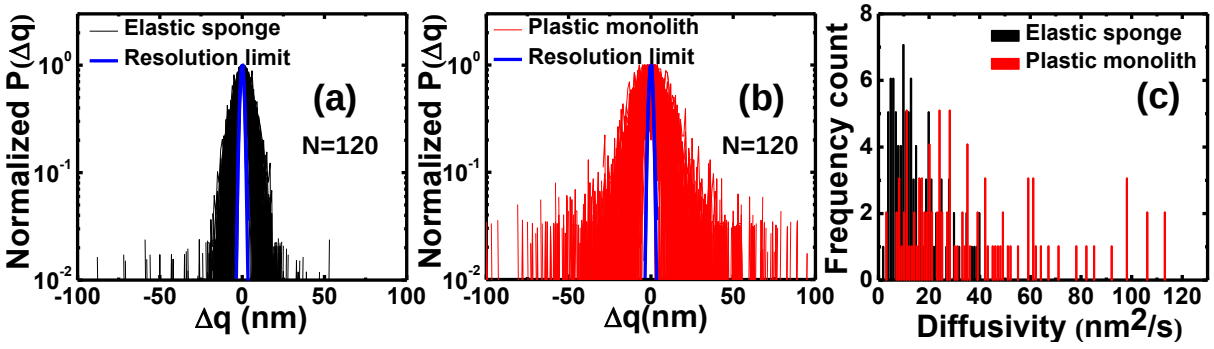

Figure 3.15: van Hove particle jump distribution for multiple (> 100) particles for **(a)** elastic sponge and **(b)** plastic monolith. The resolution limit is set by reference glassy matrix and is about ± 2.5 nm. **(c)** Distribution of particle diffusivity obtained from variance of the jump distribution.

We examined the MSD (for X and Y) for a large number of probe particles in elastic sponges and plastic monoliths. Consistent with the variation of widths of the jump distributions, we observe that there is a significantly greater non-uniformity in the slopes of the MSD(τ) from probe particles in plastic scaffolds, relative to the elastic ones (Figure 3.16a, b). At short times (up to 5 s), the MSD is linear in time, which can be used to estimate the 1D diffusivity, D, using the relation: MSD(τ) = $2D\tau$. This corresponds to the diffusive motion of particles over a time of about 5 s. Therefore, this value of diffusivity does not exactly correspond to that obtained from the breadth of the van Hove distribution. However, the range of diffusivity values obtained from the MSD is comparable to that from the van Hove jump distributions as discussed below. This allowed us to construct the distribution of 1D diffusion coefficients (Figure 3.16c) extracted from all the particles in both elastic scaffold and plastic monoliths. From these distributions, we find that, $D_{Elastic}$ spans from ~1.4-~38 nm^2/s with most probable value of ≈ 3.5 nm^2/s, while the variation of D_{Plastic} is much higher and ranges from ~2.1-~125 nm^2/s with no clear maxima. Thus, the distribution of single particle diffusivities obtained from MSD(τ) (Figure 3.16c) for elastic and plastic scaffolds follows the same trendas those extracted from the analysis of the van Hove correlation functions (Figure 3.15 c).

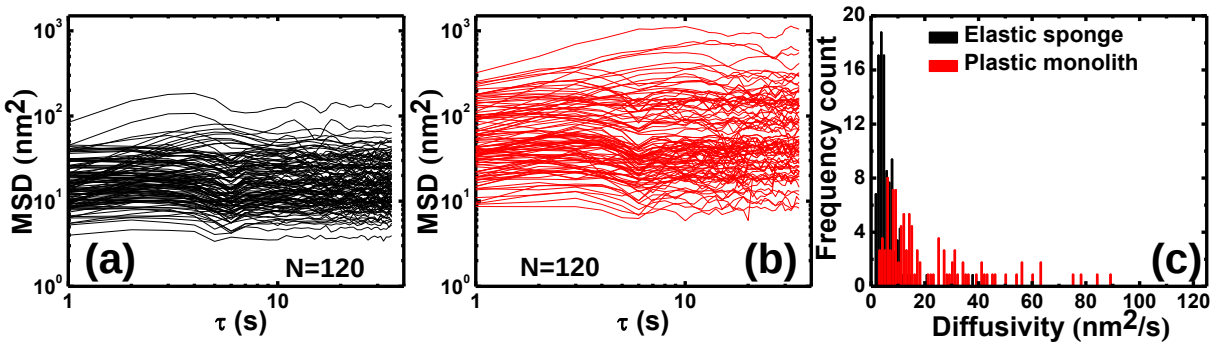

Figure 3.16: Mean squared displacement calculated for **(a)** elastic sponge **(b)** plastic monolith. **(c)** Distribution of particle diffusivity obtained from slope of initial linear regime of MSD.

Using the MSD(τ) data for all the FPS particles, we now calculate local elastic and viscous moduli from the mean squared displacement, following Mason.[50] This microrheological method is based on the generalization of the Stokes- Einstein relation to viscoelastic fluids.

3.3.4.2 Microrheology from mean squared displacement (MSD)

The motion of the Brownian particles has been used to measure the local mechanical properties of the materials. We employ Generalized Stokes- Einstein relation to obtain local shear modulus of scaffolds from MSD.[50]

$$G^*(\omega) = \frac{d\ k_B T}{3\pi a s <\Delta\bar{r}^2(s)>} \qquad (6)$$

where, $s = i\omega$, a is the tracer dimension, d is the number of dimensions tracked in the MSD, k_B is the Boltzmann constant, T is the temperature, i is the imaginary unit and $< \Delta\bar{r}^2(s) >$is Laplace transform of the MSD. The storage and loss moduli of the scaffold have been obtained from real and imaginary parts of the complex shear modulus.

$$G'(\omega) = |G^*(\omega)| \cos(\delta(\omega)) \qquad (7)$$

$$G''(\omega) = |G^*(\omega)| \sin(\delta(\omega)) \qquad (8)$$

where, $\delta(\omega) = \frac{\pi}{2}\frac{d\ ln|G^*(\omega)|}{d\ ln\ \omega}$

We have used micrheo.procode developed by T.G Mason and D.A.Weitz to calculate shear modulus of scaffolds.

We observe that the local elastic modulus (G') is frequency independent for both elastic and plastic scaffolds (Figure 3.17 a, b). G' calculated from the MSD of probe particles in elastic sponges ranges from 20 Pa to 170 Pa. In comparison, the plastic monoliths exhibit a wider variation in local elastic moduli, ranging from 0.2 Pa to 120 Pa. These differences between the elastic and plastic scaffolds are not readily apparent when we compare the average value of G', averaged across all probe particles (compare thick line in Figures 3.17 a, b). Bulk measurements of the elastic moduli, from dynamic shear rheology on macroscopic samples (lines with symbols in Figures 3.17 a, b) reveal that the bulk value of G' is comparable for elastic and plastic scaffolds. This is consistent with our observations for the *average* values of the microscopic G' from microrheology. The values of the bulk elastic moduli are significantly higher than those from microrheological measurements. We discuss possible reasons for this later in the chapter. We have also calculated the damping factor ($tan\ \delta$) as the ratio of the local viscous modulus (G'') to the elastic modulus (G'). For elastic sponges, $tan\ \delta$ varies from 0.04 to 0.2. In comparison, plastic monoliths exhibit a wider range, from 0.04 to 0.5, with most particles showing a $tan\ \delta$ between 0.15 and 0.5.

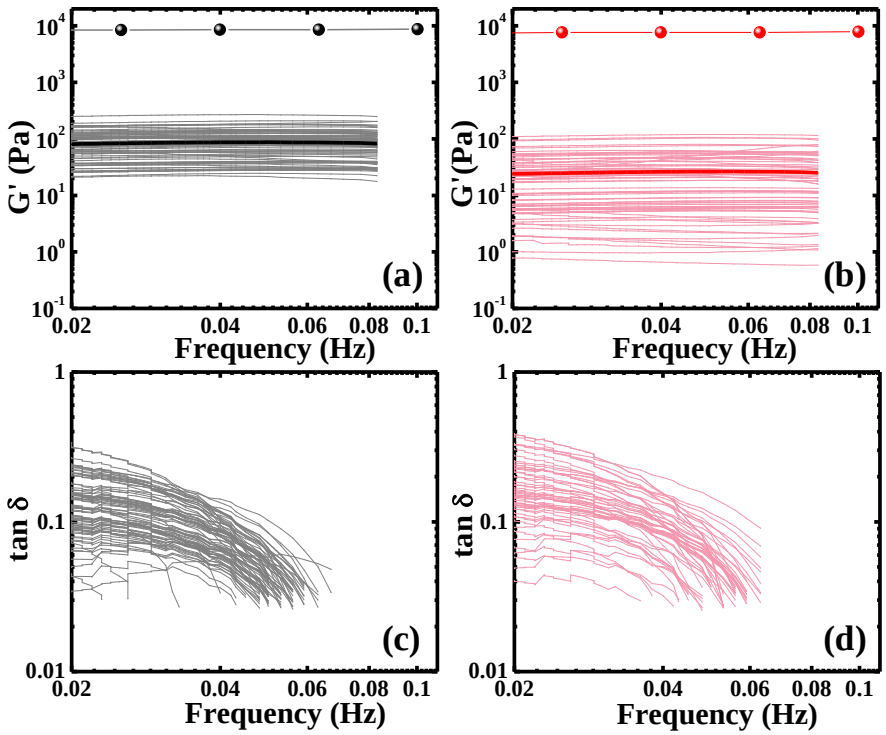

Figure 3.17: Micro and bulk rheology of scaffolds. (**a) & (b**) Elastic modulus (*G'*) as a function of frequency obtained for elastic sponge and plastic monolith. The thick solid lines represent average data. Lines with spherical symbols are obtained from bulk dynamic shear rheology measurements, performed in the linear response region, at 0.25% strain. (**c), (d**) The damping coefficient (*tan δ*) as a function of frequency calculated for elastic and plastic.

MSD(τ) (Figures 3.16a and b) initially increases linearly with time and subsequently plateaus. This is intriguing since the jump distributions follow Gaussian behavior, indicating that the particles are Brownian. Similar observations on anomalous yet Brownian motion of single particles have been reported earlier.[51, 52] We observe that the MSD(τ) saturates over time for all the FPS particles in both elastic and plastic scaffolds (Figure 3.16a, b), which is expected since the particles are trapped in a crosslinked polymer mesh that forms a cage, preventing their free diffusion. For all the FPS particles in the elastic scaffold, the MSD plateaus at relatively short lag-times of within 6 – 10 s, while for plastic scaffolds, there is a much wider variation in the initiation of MSD saturation timescales of ~6- ~30 s.

The particle diffusivity measured using microscopy provides information about the local viscoelastic environment. Variation in the diffusivities reveals spatial differences in this environment in the scaffolds. Further, there are also differences between the time for the MSD to plateau, τ, in elastic and plastic scaffolds. We can estimate the "cage" size that

restricts the motion of particles in the scaffold walls as being of the order of $\sqrt{D\tau}$. Thus, in elastic scaffolds we can estimate cage sizes ranging from 2.9 nm (based on a diffusivity of 1.4 nm^2/s and $\tau \approx 6$ s) to 19.5 nm (D = 38 nm^2/s, τ = 10 s), while for the plastic scaffolds, we estimate a wide variation in cage sizes, ranging from 3.5 nm (D = 2 nm^2/s, τ = 6 s) to 61 nm (D = 125 nm^2/s, τ = 30 s).

To investigate the origin of subdiffusive behavior exhibited by the FPS in elastic and plastic scaffolds, we analyzed single particle trajectories to compute the velocity-velocity autocorrelation functions (VACF), which can provide insights into tracer movement mechanisms.[19]

3.3.4.3 Calculation of velocity autocorrelation function (VACF)

We calculate the particle velocity autocorrelation function, averaged over a time, *t*, as follows:

Normalized velocity autocorrelation function,

$$C_v(\tau) = \frac{\langle \vec{v}(t\ ).\vec{v}(t\ +\tau)\rangle}{<v^2(t\ )>} \quad (9)$$

The velocity, $\vec{v}(\tau) = \frac{[\vec{r}(t+\tau)-\vec{r}(t)]}{\tau}$, is computed from the difference in position of particles between two successive frames, τ being the time gap between two successive frames (minimum τ is 1s).

The velocity autocorrelation function is related to the mean squared displacement through:

$$C_v(\tau) = \frac{1}{2}\frac{d^2\langle \Delta x^2(\tau)\rangle}{d\tau^2} \quad (10)$$

For each particle, the VACF are plotted, as is the average for ease of comparison between the samples (Figure 3.18).

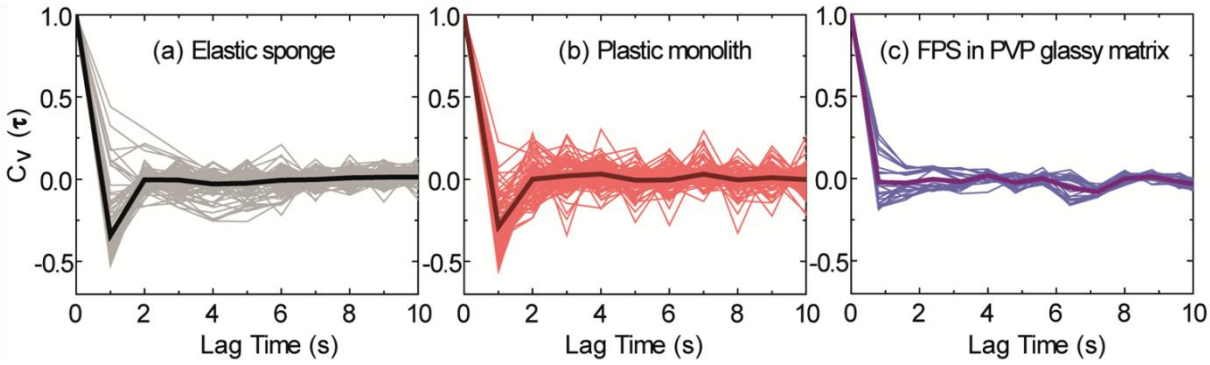

Figure 3.18: Normalized velocity-velocity autocorrelation function (VACF) plotted for **(a)** elastic sponge **(b)** plastic monolith and **(c)** reference sample. VACF of elastic and plastic scaffolds showed sharp negative (or anti) correlations at lag time ~ 1s in contrast to the reference glassy sample.

For particles in both elastic and plastic scaffolds (Figure 3.18 a,b), the VACF demonstrates a sharp negative correlation for short times (τ= 1 s), in contrast to the behavior of the reference sample (FPS in glassy polymer matrix, Figure 3.18c). The negative correlations in initial time period can arise from two different mechanisms; fractional Brownian motion (FBM) or continuous time random walk (CTRW) in confined systems.[53] FBM is associated with the motion of a Brownian particle in a viscoelastic media like polymer. [54, 55] In a viscoelastic medium, when a Brownian walker takes a step in one direction, the elasticity of the medium results in particle rebound. Therefore, velocities of the particle at successive time instants are negatively correlated at short lag times. CTRW arises when the particle stops intermittently for an interval followed by a movement, leading to a broad waiting time distribution. We do not observe any dwell/pause times during particle motion, suggesting that our data is likely to be more appropriately described using a FBM framework. Further, the difference in behavior between the FPS in ice-templated scaffolds versus in the reference sample confirms that particle motions in the scaffolds obtained from our microscopy data are above the resolution limit of the technique.

Particle tracking microrheology further allows us to estimate local viscoelastic moduli. In contrast to our previously reported macroscopic measurements in Chapter 2, there is a difference between the elastic modulus of elastic and plastic scaffolds from microrheology. The values of moduli obtained from microrheology are much lower when compared with bulk rheological measurements. This is not unusual and has been observed for other samples. For example, Caggioni et al. used particle tracking microrheology to study the

effect of shear during gelation of aqueous gellan gum with a monovalent salt. They observed that microrheology underestimates the moduli compared to bulk rheology,[54] and attributed this difference to electrostatic repulsion between tracers and the gellan. They suggest that a depletion layer around tracer particles in their work increases their mobility. This has also been suggested by researchers in the context of other biopolymer solutions.[55] Typically, it is believed that when the length scale characterizing the sample microstructure is small compared to the tracer dimension, then microrheology agrees with bulk measurements.[56, 57] If this is not the case, then tracer particle motion is sensitive to local heterogeneities and microrheological results differ from bulk measurements.[58-60] In our scaffolds, probe particles are integrated into the colloidal assemblies and we do not anticipate that their dynamics will be any different from the matched size silica colloids in the scaffolds.

Bulk rheological measurements show that elastic and plastic monoliths are characterized by similar values of solid modulus, G', and that the loss modulus, G'' for plastic scaffolds is higher than that for the elastic. The particle tracking measurements reported here reveal a more nuanced description of the assemblies when compared with the bulk measurements. In accord with the bulk measurements, microrheology indicates that the local solid modulus for both scaffolds is greater than the loss modulus. However, both scaffolds show a spatial variation in local values of the solid modulus. This variation is larger for the plastic assemblies relative to the elastic. However, the average values of the solid moduli from microrheological measurements of elastic and plastic assemblies vary only by a factor of about 2, since the average values are strongly weighted by the high modulus regions. Thus, the spatially averaged microrheological solid modulus is comparable for elastic and plastic scaffolds, similar to what is observed from bulk rheological measurements. The solid modulus is proportional to the crosslink density. Therefore, the implication of the microrheology data is that there is a wider variation in crosslink density for the plastic scaffolds relative to the elastic. Remarkably, it appears that this variation is averaged so that the bulk solid moduli (and thus, the average crosslink density) are similar for both scaffolds. Finally, we note that the loss tangent, $tan\delta\ (= G''/G')$, that is a measure of energy dissipation, is higher for plastic scaffolds relative to elastic. The variation in $tan\delta$ too is higher for plastic scaffolds. Thus, consistent with previous AFM measurements in Chapter 2, we observe greater energy dissipation for the plastic scaffolds relative to the elastic assemblies.

The van Hove distribution for particle excursions and the MSD provide information about the dynamical environment experienced by FPS particles in the elastic and plastic scaffolds. Our previous investigations of the static structure of elastic and plastic scaffolds used electron microscopy and SAXS to probe morphology, and NMR to probe the chemical composition of these scaffolds. We observed that there were no differences between the morphological structure and average chemical composition of the elastic and plastic scaffolds. However, using atomic force microscope (AFM) to spatially map out the work of adhesion at junctions between particles in scaffold walls, revealed clear differences between the elastic and plastic scaffolds. We observed that the particle junctions in elastic scaffolds are characterized by work of adhesion that is narrowly peaked at ≈ 1.5 J/m^2, while junctions in plastic scaffolds show a wide range of work of adhesion, up to 11 J/m^2, without a peak value. We observe a remarkable similarity between this static description of viscoelastic interparticle junctions from AFM, and the dynamical motions of the colloidal particles obtained from single-particle tracking measurements. Specifically, differences between the elastic and plastic scaffolds with regard to the distribution of particle diffusivities from MSD data and the variance from the van Hove functions are in remarkable consonance with the AFM work of adhesion. Thus, spatial variation in particle dynamics observed with single particle tracking is mirrored by the variation in the local viscoelastic properties of the crosslinked polymer matrix reported using AFM. In Chapter 2, we had speculated that the differences between elastic and plastic scaffolds result from variations in the local crosslink density: elastic scaffolds were characterized by a uniform distribution of crosslinks while plastic scaffolds showed a widely heterogeneous crosslink density. Interestingly, our experiments indicate that the length scale that characterizes the heterogeneity in the samples has to be larger than the probe particle size, viz., 1 μm. We note that this scenario is consistent with the variation in "cage" sizes obtained from particle tracking, for particles in elastic and plastic scaffolds.

3.4 Summary

We have demonstrated that wavelet transforms can be used to eliminate the effect of stage drift during single particle tracking microscopy of samples with slow dynamics. We apply this technique to fluorescence microscopy. For samples with high signal to background ratio, eliminating stage drift using wavelet transforms allows us to track particles with a spatial resolution of ≈ 2.5 nm. We note that high signal to background ratio allow us to accurately

track the particle positions and is essential to obtain the reported spatial resolution. We investigate ice templated colloidal assemblies, and track the motions of fluorescent particles embedded in these. Variations in the preparation protocol for these colloidal assemblies produce materials that have identical overall chemical composition but, that have dramatically different mechanical response. We track the motion of probe colloidal particles to investigate the local microstructure in elastic assemblies that can recover from large compressive deformations and in plastic assemblies that fail at low strains. Since these assemblies comprise of densely packed colloids that are assembled in a crosslinked polymer mesh, the colloidal motions that we observe are slow and of small amplitude. Therefore, high signal to background ratio in imaging and elimination of stage drift using wavelet transforms is critical to analyzing colloidal dynamics in these samples. The use of wavelet transforms to eliminate stage drift is an enabling technique for high resolution particle tracking in samples with slow dynamics, and might be of wide relevance for microscopic studies of dense colloidal systems. We note that this implementation of wavelet transforms to eliminate stage drift relies on eliminating correlated motions between particles. This assumes that long range, low frequency motions are not correlated over long distances in the sample. While this holds true for a large class of dense soft matter systems [61], it is not true for dilute colloidal dispersions, where hydrodynamic coupling decays slowly.

There is a significant difference in the mean squared displacement of probe particles in elastic and plastic scaffolds, as well as the van Hove distribution for particle jumps. The variance from the van Hove distribution is peaked around an average value for elastic sponges, in contrast to plastic monoliths that exhibit a wide variation with no clear peak. This trend is mirrored by the particle diffusivities for elastic and plastic scaffolds, calculated from the MSD data. Therefore, we conclude that the key difference between elastic and plastic scaffolds is that plastic scaffolds exhibit large spatial heterogeneity relative to elastic scaffolds. This spatial heterogeneity is manifested in the wide variation in the motion of probe particles at various locations in the plastic scaffolds. We interpret the spatial heterogeneity in the local environment in terms of variations in local crosslink density for plastic scaffolds. This is consistent with microrheology data that shows greater variation in the local solid moduli for plastic scaffolds than for elastic scaffolds, and lower dissipation for elastic assemblies. Thus particle tracking and microrheology provide a detailed spatial characterization of the local environment in elastic assemblies and plastic monoliths and unambiguously demonstrate the microscopic origin of the differences between them.

3.5 References

1. Sun, B.; Sirringhaus, H., Solution-processed zinc oxide field-effect transistors based on self-assembly of colloidal nanorods. *Nano Lett.* **2005,** 5, 2408-2413.

2. Li, F.; Josephson, D. P.; Stein, A., Colloidal Assembly: The Road from Particles to Colloidal Molecules and Crystals. *Angew. Chem. Int. Ed.* **2011,** 50, 360-388.

3. Ozin, G. A.; Hou, K.; Lotsch, B. V.; Cademartiri, L.; Puzzo, D. P.; Scotognella, F.; Ghadimi, A.; Thomson, J., Nanofabrication by self-assembly. *Mater. Today* **2009,** 12, 12-23.

4. Panyam, J.; Labhasetwar, V., Biodegradable nanoparticles for drug and gene delivery to cells and tissue. *Adv. Drug Deliv. Rev.* **2003,** 55, 329-347.

5. Yager, P.; Edwards, T.; Fu, E.; Helton, K.; Nelson, K.; Tam, M. R.; Weigl, B. H., Microfluidic diagnostic technologies for global public health. *Nature* **2006,** 442, 412.

6. Lewis, L. N., Chemical catalysis by colloids and clusters. *Chem. Rev.* **1993,** 93, 2693-2730.

7. Pierre, A. C.; Pajonk, G. r. M., Chemistry of aerogels and their applications. *Chem. Rev.* **2002,** 102, 4243-4266.

8. Wang, J.; Cheng, Q.; Tang, Z., Layered nanocomposites inspired by the structure and mechanical properties of nacre. *Chem. Soc. Rev.* **2012,** 41, 1111-1129.

9. Jang, D.; Meza, L. R.; Greer, F.; Greer, J. R., Fabrication and deformation of three-dimensional hollow ceramic nanostructures. *Nat. Mater.* **2013,** 12, 893-898.

10. Zheng, X.; Lee, H.; Weisgraber, T. H.; Shusteff, M.; DeOtte, J.; Duoss, E. B.; Kuntz, J. D.; Biener, M. M.; Ge, Q.; Jackson, J. A., Ultralight, ultrastiff mechanical metamaterials. *Science* **2014,** 344, 1373-1377.

11. Lee, L. J.; Zeng, C.; Cao, X.; Han, X.; Shen, J.; Xu, G., Polymer nanocomposite foams. *Compos. Sci. Technol.* **2005,** 65, 2344-2363.

12. Rajamanickam, R.; Kumari, S.; Kumar, D.; Ghosh, S.; Kim, J. C.; Tae, G.; Sen Gupta, S.; Kumaraswamy, G., Soft colloidal scaffolds capable of elastic recovery after large compressive strains.*Chem. Mater.* **2014,** 26, 5161-5168.

13. Das, C.; Chatterjee, S.; Kumaraswamy, G.; Krishnamoorthy, K., Elastic Compressible Energy Storage Devices from Ice Templated Polymer Gels treated with Polyphenols. *J. Phys. Chem. C* **2017,** 121, 3270-3278.

14. Chatterjee, S.; Sen Gupta, S.; Kumaraswamy, G., Omniphilic Polymeric Sponges by Ice Templating. *Chem. Mater.* **2016,** 28, 1823-1831.

15. Crocker, J. C.; Grier, D. G., Methods of Digital Video Microscopy for Colloidal Studies. *J.Colloid Interface Sci.* **1996**, 179, 298-310.

16. Weeks, E. R.; Weitz, D. A., Subdiffusion and the cage effect studied near the colloidal glass transition. *Chem. Phys.* **2002,** 284, 361-367.

17. Cheng, X.; McCoy, J. H.; Israelachvili, J. N.; Cohen, I., Imaging the microscopic structure of shear thinning and thickening colloidal suspensions. *Science* **2011,** 333, 1276-1279.

18. Ruthardt, N.; Lamb, D. C.; Brauchle, C., Single-particle tracking as a quantitative microscopy-based approach to unravel cell entry mechanisms of viruses and pharmaceutical nanoparticles. *Mol. Ther.* **2011,** 19, 1199-1211.

19. Meijering, E.; Dzyubachyk, O.; Smal, I.; van Cappellen, W. A. In *Tracking in cell and developmental biology*, Seminars in cell & developmental biology, **2009**; Elsevier: **2009**; pp 894-902.

20. Bhattacharya, S.; Sharma, D. K.; Saurabh, S.; De, S.; Sain, A.; Nandi, A.; Chowdhury, A., Plasticization of poly (vinylpyrrolidone) thin films under ambient humidity: Insight from single-molecule tracer diffusion dynamics. *J. Phys. Chem. B* **2013,** 117, 7771-7782.

21. Shen, H.; Tauzin, L. J.; Baiyasi, R.; Wang, W.; Moringo, N.; Shuang, B.; Landes, C. F., Single Particle Tracking: From Theory to Biophysical Applications. *Chem. Rev.* **2017,** 117, 7331- 7376.

22. Saxton, M. J.; Jacobson, K., Single-particle tracking: applications to membrane dynamics. *Annu. Rev. Biophys. Biomol.Struct.* **1997,** 26, 373-399.

23. Valentine, M. T.; Kaplan, P. D.; Thota, D.; Crocker, J. C.; Gisler, T.; Prud' homme, R. K.; Beck, M.; Weitz, D. A., Investigating the microenvironments of inhomogeneous soft materials with multiple particle tracking. *Phys. Rev. E* **2001,** 64, 061506.

24. Mason, T. G.; Ganesan, K.; Van Zanten, J. H.; Wirtz, D.; Kuo, S. C., Particle tracking microrheology of complex fluids. *Phys. Rev. Lett.* **1997,** 79, 3282.

25. Anthony, S. M.; Hong, L.; Kim, M.; Granick, S., Single-particle colloid tracking in four dimensions. *Langmuir* **2006,** 22, 9812-9815.

26. Kegel, W. K.; van, B.; Alfons, Direct Observation of Dynamical Heterogeneities in Colloidal Hard-Sphere Suspensions. *Science* **2000,** 287, 290-293.

27. Mortensen, K. I.; Churchman, L. S.; Spudich, J. A.; Flyvbjerg, H., Optimized localization analysis for single-molecule tracking and super-resolution microscopy. *Nat. Methods* **2010,** 7, 377-381.

28. Biteen, J.; Willets, K. A., Introduction: Super-Resolution and Single-Molecule Imaging. *Chem. Rev.* **2017,** 117, 7241-7243.

29. Axelrod, D., Total internal reflection fluorescence microscopy in cell biology. *Traffic* **2001,** 2, 764-774.

30. van Loenhout, M. T. J.; Kerssemakers, J. W. J.; De Vlaminck, I.; Dekker, C., Non-bias-limited tracking of spherical particles, enabling nanometer resolution at low magnification. *Biophys.J* **2012,** 102, 2362-2371.

31. Adler, J.; Pagakis, S. N., Reducing image distortions due to temperature- related microscope stage drift. *J. Microsc.* **2003,** 210, 131-137.

32. Thompson, R. E.; Larson, D. R.; Webb, W. W., Precise nanometer localization analysis for individual fluorescent probes. *Biophys. J.* **2002,** 82, 2775-2783.

33. Lee, S. H.; Baday, M.; Tjioe, M.; Simonson, P. D.; Zhang, R.; Cai, E.; Selvin, P. R., Using fixed fiduciary markers for stage drift correction. *Opt. Express* **2012,** 20, 12177-12183.

34. Brunelli, R., *Template matching techniques in computer vision: theory and practice*. John Wiley & Sons: **2009**.

35. Bloess, A.; Durand, Y.; Matsushita, M.; Van Dermeer, H.; Brakenhoff, G. J.; Schmidt, J., Optical far- field microscopy of single molecules with 3.4 nm lateral resolution. *J. Microsc.* **2002,** 205, 76-85.

36. Carter, A. R.; King, G. M.; Ulrich, T. A.; Halsey, W.; Alchenberger, D.; Perkins, T. T., Stabilization of an optical microscope to 0.1 nm in three dimensions. *Appl. Opt.* **2007,** 46, 421-427.

37. Crocker, J. C.; Hoffman, B. D., Multiple particle tracking and two point microrheology in cells. *Methods Cell Biol.* **2007,** 83, 141-178.

38. Crocker, J. C.; Valentine, M. T.; Weeks, E. R.; Gisler, T.; Kaplan, P. D.; Yodh, A. G.; Weitz, D. A., Two-point microrheology of inhomogeneous soft materials. *Phys. Rev. Lett.* **2000,** 85, 888.

39. Unser, M., Wavelets: on the virtues and applications of the mathematical microscope. *J. Microsc.* **2014,** 255, 123-127.

40. Strang, G.; Nguyen, T., *Wavelets and filter banks*. SIAM: **1996**.

41. Strang, G., Wavelet transforms versus Fourier transforms. *Bull. Amer. Math. Soc.* **1993,** 28, 288-305.

42. Polikar, R., The wavelet tutorial. **1996**.43. Rioul, O.; Vetterli, M., Wavelets and signal processing. *IEEE Signal Process Mag.* **1991,** 8, 14-38.

44. Jensen, A.; la Cour-Harbo, A., *Ripples in mathematics: The discrete wavelet transform*. Springer Science & Business Media: **2001.**

45. Roy, M.; Kumar, V. R.; Kulkarni, B. D.; Sanderson, J.; Rhodes, M.; vanderStappen, M., Simple denoising algorithm using wavelet transform. *AIChE J.* **1999,** 45, 2461-2466.

46. Kulkarni, A. A.; Joshi, J. B.; Kumar, V. R.; Kulkarni, B. D., Wavelet transform of velocity-time data for the analysis of turbulent structures in a bubble column. *Chem. Eng. Sci.* **2001,** 56, 5305-5315.

47. Deshpande, S. S.; Tabib, M. V.; Joshi, J. B.; Kumar, V. R.; Kulkarni, B. D., Analysis of flow structures and energy spectra in chemical process equipment. *J.Turbul.* **2010,** 11, N5.

48. Kumar, V. R.; Kulkarni, B. D.; Dixit, N. M.; Vaish, N. Method and an apparatus for the identification and/or separation of complex composite signals into its deterministic and noisy components. U.S. Patent No.6, 208,951, **2001**.

49. Paul, H.; Andrea, F.; Andrew, J. A.; Matthias, S., The van Hove distribution function for Brownian hard spheres: Dynamical test particle theory and computer simulations for bulk dynamics. *J. Chem. Phys.* **2010,** 133, 224505.

50. Mason, T. G., Estimating the viscoelastic moduli of complex fluids using the generalized Stokes- Einstein equation. *Rheol. Acta* **2000,** 39, 371-378.

51. Wang, B.; Kuo, J.; Bae, S. C.; Granick, S., When Brownian diffusion is not Gaussian. *Nat. Mater.* **2012,** 11, 481-485.

52. Bronstein, I.; Israel, Y.; Kepten, E.; Mai, S.; Shav-Tal, Y.; Barkai, E.; Garini, Y., Transient anomalous diffusion of telomeres in the nucleus of mammalian cells. *Phys. Rev. Lett.* **2009,** 103, 018102.

53. Magdziarz, M.; Weron, A.; Burnecki, K.; Klafter, J., Fractional Brownian motion versus the continuous-time random walk: A simple test for subdiffusive dynamics. *Phys. Rev. Lett.* **2009,** 103, 180602.

54. Caggioni, M.; Spicer, P. T.; Blair, D. L.; Lindberg, S. E.; Weitz, D. A., Rheology and microrheology of a microstructured fluid: The gellan gum case. *J. Rheol.* **2007,** 51, 851-865.

55. Liu, J.; Gardel, M. L.; Kroy, K.; Frey, E.; Hoffman, B. D.; Crocker, J. C.; Bausch, A. R.; Weitz, D. A., Microrheology probes length scale dependent rheology. *Phys. Rev. Lett.* **2006,** 96, 118104.

56. Dasgupta, B. R.; Tee, S.-Y.; Crocker, J. C.; Frisken, B. J.; Weitz, D. A., Microrheology of polyethylene oxide using diffusing wave spectroscopy and single scattering. *Phys. Rev. E* **2002,** 65, 051505.

57. Mason, T. G.; Weitz, D. A., Optical measurements of frequency-dependent linear viscoelastic moduli of complex fluids. *Phys. Rev. Lett.* **1995,** 74, 1250.

58. Wong, I. Y.; Gardel, M. L.; Reichman, D. R.; Weeks, E. R.; Valentine, M. T.; Bausch, A. R.; Weitz, D. A., Anomalous diffusion probes microstructure dynamics of entangled F-actin networks. *Phys. Rev. Lett.* **2004,** 92, 178101.

59. Palmer, A.; Mason, T. G.; Xu, J.; Kuo, S. C.; Wirtz, D., Diffusing wave spectroscopy microrheology of actin filament networks. *Biophys. J.* **1999,** 76, 1063-1071.

60. Gardel, M. L.; Valentine, M. T.; Crocker, J. C.; Bausch, A. R.; Weitz, D. A., Microrheology of entangled F-actin solutions. *Phys. Rev. Lett.* **2003,** 91, 158302.

61. Crocker, J. C.; Valentine, M. T.; Weeks, E. R.; Gisler, T.; Kaplan, P. D.; Yodh, A. G.; Weitz, D. A., Two-point microrheology of inhomogeneous soft materials. *Phys. Rev. Lett.* **2000,** 85, 888.

Chapter 4

Compression-Induced Deformation and Failure of Ice-Templated Inorganic-Organic Hybrid Structures

Ice templating is a fast becoming a preferred method to prepare macroporous materials due to its versatility, environmentally friendliness and economic viability. In this chapter, we will study the cellular mechanics of ice templated inorganic-organic hybrid structures. We have already seen that based on the polymer crosslinking protocol we obtain two materials that are indistinguishable in terms of their static structure but behave qualitatively differently when they are compressed. Crosslinking in the presence of ice crystals gave elastic sponges that can recover from large compressions (~80%). In contrast, crosslinking in absence of ice crystals gave plastic monoliths which fail even when small compressive strain (5%) is imposed. Here, we study the microstructure of elastic sponges and plastic monoliths under compression, using X-ray computed micro-tomography and single particle tracking. We show that crosslinking in presence of ice crystals results in the formation of flexible interparticle bridges which allow elastic deformation of pore walls when compressed. These flexible bridges allow shape recovery during the release of load. However, crosslinking in absence of ice crystals leads to formation of plastic hinges in the interparticle regions. These bridges concentrate stress when compressed and massive failure of these bridges occurs at moderate deformations. Therefore, this allows cracks to propagate through the sample and the entire assembly fails.

4.1 Introduction

Low-density, cellular solids are widely encountered in Nature. Such materials are comprised of an assembly of cellular structures bounded by solid edges or faces, and packed together to fill space. Wood, cork, sponge and coral are common natural cellular solids.[1] Today, synthetic cellular solids have been fabricated using polymers, metals, ceramics and glasses.[2] The remarkable properties of these solids render them very useful. Cellular foams are extensively used from applications ranging from disposable coffee cups (that rely on the low thermal conductivity of Styrofoam®) to the crash padding of an aircraft cockpit (that relies on the extraordinary strength to weight ratio of honeycomb structures).[3-5]

The most commonly reported porous structures are two dimensional (2D) cellular materials called honeycombs and three dimensional cellular foams with either open or closed pore structures.[6] Honeycombs are primarily prepared by casting or extrusion processes whereas foams are prepared either by mechanical stirring, the use of blowing agents or by phase separation of porogens. Cellular foams can also be made by bonding together solid constituents either by sintering or using chemical binders.[6-9]

Among phase separation methods, over past 20 years ice templating has grown as a promising method to make macroporous materials.[10-13] This is because dispersions of almost any material, from polymers to ceramics to metals, can be ice templated. Additionally, this process is easy, scalable and environmentally friendly (since it is water based). Ice templating is suitable for producing anisotropic as well as isotropic macroporous materials with porosity ranging from 40% to just under 100%.[10] Briefly, ice templating is based on freezing of colloidal suspensions and segregation of particles by the solidification front. Depending on the freezing rate and direction of freezing, the resultant material exhibits isotropic or anisotropic pores. After solidification, the frozen solvent is removed, leaving pores whose morphologies replicate the sublimed crystals. To consolidate the ice templated microstructure, the "green body" is typically sintered. Additionally, ice templating provides control over the pore architecture (pore volume, size and morphology) by controlling the initial solid loading, cooling rate or using additives.[10]

The most important processing parameters that control the microstructure of ice templated materials are freezing rate and solid loading.[10, 14, 15] Faster cooling leads to smaller mean pore size and narrower distribution compared with the freezing at slower rates. This is because the magnitude of supercooling ahead of the ice front increases

with freezing rate, while the tip radius of the ice crystals decreases; therefore it leads to finer microstructure. It is also reported that decrease in pore size results from increase in solid loading.[10] The main influence of solid loading on pore size variation is that it affects the number of particles rejected at the solidification front. When the solid loading increases, it becomes more difficult for the advancing solidification front to repel the particles, thus hindering the ice growth and eventually reducing the pore size. There is a critical particle concentration known as breakthrough concentration above which the solid/ liquid interface breaks into the interparticle space. This is the concentration where the balance between the capillary pressure and the osmotic pressure is lost. Ice templating of dispersions having the particle concentration higher than this threshold level leads to materials with low porosity (<40%).[10] If the particle fraction is below this critical concentration, then materials with porosity ranging from 40 - ~100% are obtained. Pore morphology is also strongly influenced by the nature of the solvent.[16] For example, water as a templating medium gives lamellar pore morphology. Incorporation of additives like glycerol, polystyrene, zirconium acetate (ZRA) or sucrose modifies the pore size and shape. For example, the addition of ZRA has been shown to result in a honeycomb pore morphology with a modified pore size distribution without affecting the pore volume.[17]

Recent studies have focused on the relationship between processing, microstructure and mechanical properties of ice templated materials to design materials that optimize performance of porous microstructure. In this context, researchers have investigated the response of ice templated cellular solids to mechanical loading in various geometries and have studied failure mechanisms.[18, 19] Even when the low thermal conductivity of foam is exploited as thermal insulation, or when porosity is exploited for filtration, the mechanical strength and fracture behaviour are important for the end use. The general strategy employed to understand the mechanics of cellular solids is to compare experimentally measured data with model predictions to obtain insights into the deformation mechanisms. Various models have been used to understand the mechanical response of cellular solids. Early models considered structural analysis of a unit cell with hexagonal symmetry (for 2D pores) or a polygon (for 3D structures).[6, 20-22] The most widely used models to predict mechanical response of cellular solids are Gibson and Ashby's models.[6] These models differentiate between open cell, closed cell and honeycomb morphologies. These models have been employed to rationalize the scaling with density of mechanical properties such as fracture toughness, creep

performance or Young's modulus. This approach analyzes the dependence of aforementioned mechanical properties on relative density, $\rho_r = {\rho^*}/{\rho_s}$ where, ρ^* is the density of the cellular material and ρ_s is the density of the cell wall. According to Gibson, materials with $\rho_r < 0.3$ are true cellular solids and above which there is a transition from a cellular structure to a solid with isolated pores.[6] Next we will review the interpretation of various deformation mechanisms of cellular solids in terms of its relative density.

In Gibson's analysis, expressions for moduli; as well as elastic, plastic or brittle collapse stress; fracture toughness and strain at which densification occurs are derived by examining the way in which cell edges or cell faces respond to stress. When a foam is compressed, the stress (σ) -strain (ε) curve shows three regions: linear regime, stress plateau regime and a densification regime. The compression (or tensile) stress-strain curves of an elastomeric honeycomb or foam, an elastic-plastic honeycomb or foam and an elastic-brittle honeycomb or foam exhibit similar shapes but for different reasons. Gibson and Ashby's models are been used to distinguish these three types of deformation mechanisms. Gibson et al. have explained the deformation mechanism in the three regimes of stress-strain curve based on honeycomb model, open cell model and closed cell model.[6] Honeycomb models were used where an array of identical prismatic cells nest together to fill a plane in the material. In-plane and out-of-plane models are the two categories of this honeycomb model. In-plane and out-of-plane models are used when the material is loaded uniaxially either in the plane of the hexagonal cells or along the prism axis in the out of plane direction. Open and closed pore models are used for three dimensional foams by considering the salient features of foams such as relative density and the degree to which the cells are open or closed. Next we will see how these models predict the different deformation mechanisms in the three different regimes of the stress-strain curve.

(a) **Linear elastic regime**– at low strains, the cell deformation is linearly proportional to the deformation. Various deformation mechanisms in this regime are predicted based on honeycomb, open cell and close pore models as follows:

- In-plane honeycomb model:

  When material is loaded uniaxially in the plane of the hexagonal cells, the cell walls of the honeycomb initially deform by bending (if the wall thickness, t is

small compared to wall length,l). In this case the Young's modulus scales with ρ_r as:

$$\frac{E^*}{E_s} \approx (\rho_r)^3 \quad \text{.....(1)}$$

where, E^* and E_s are the Young's moduli of foam and cell wall material respectively.

- Out-of-plane honeycomb model:

  Here, the cell walls of the honeycomb initially compress axially. Therefore, the Young's modulus varies linearly with ρ_r.

$$\frac{E^*}{E_s} \approx (\rho_r) \quad \text{.....(2)}$$

- Open cell model:

  In the linear regime, strut bending is the primary distortion mechanism for low density foams with tetrahedral microstructure.

$$\frac{E^*}{E_s} = C_1(\rho_r)^2 \text{.....(3)}$$

  where, C_1 is the proportionality constant that depends upon the specific strut shape. Shear deformation also manifests in cell wall bending and therefore, the shear modulus also scales in the same way with relative density. However, when the cell wall of the foam compresses axially irrespective of strut bending, this leads to a linear relationship between the effective Young's modulus and relative density.[23, 24]

- Closed cell model:

  Modeling foams with closed cells is more complicated than open pore foams. If the foams are made from liquid components, surface tension can draw the material into the cell edges, leaving only a thin sheet across the faces of the cell. This thin sheet ruptures easily when it is perturbed mechanically. In closed cell foams, stretching of the cell faces also contributes to the mechanical response. In the linear regime, the closed cell modulus is identical to open cell if its stiffness is derived entirely from that of the cell edges. However, if a substantial fraction of the solid is present in the cell faces, it contributes to the stiffness. In this case, the modulus dependence on ρ_r is slightly different than the open cell model. Moreover, pressure coming from cell fluid also can contribute to the cell stiffness.

$$\frac{E^*}{E_s} \approx \varphi^2(\rho_r)^2 + (1-\varphi)\rho_r + \frac{\rho_0(1-2v)}{E_s(1-\rho_r)} \quad \text{.....(4)}$$

where, φ is the fraction of solid in the cell edge and v is the Poisson's ratio of foam. The second term in Eq. 4 represents the membrane stresses coming from cell faces and the third term corresponds to the gas pressure which is due to pore fluid.

(b) **Plateau regime (deformation at almost constant stress)**– this results from either non-linear elasticity, plastic yielding or brittle crushing.[6] In general, linear elasticity is limited to small strains. However, elastomeric foams can be compressed far beyond this point and while the deformation is nonlinear, it is elastically recoverable. Deformation in this regime results in elastic buckling of the columns or plates that make up cell walls or edges. This gives a plateau region in the stress strain curve. This regime is characterized based on the relation between elastic collapse stress of elastomeric foams (σ_{el}^*) and ρ_r.

Plastic yielding also gives a plateau in the σ-ε curve. This occurs if the cell wall material is plastic, viz., for metals and many sub-T_g polymers. Plastic yielding occurs when the moment exerted on the cell walls exceeds a critical value called fully plastic moment, $M_P = \frac{1}{4}\sigma_y t^3$, where, σ_y is the yield strength of cell wall material and t is the side of a beam square section. This leads to large deformation at almost constant stress, σ_{pl}^*.

Ceramics and certain rigid polymers collapse in compression by brittle crushing. This brittle collapse of porous materials also gives plateau regime in the stress strain curve with a crushing strength of σ_{cr}^*.

The scaling relationships of σ_{el}^*, σ_{pl}^* and σ_{cr}^* with ρ_r help to understand the exact deformation mechanism in the porous material which gives rise to the plateau in the stress strain curve. Honeycomb model, open cell model and closed cell model are used to understand the deformation mechanism which leads to plateau regime in honeycomb structure, open and closed foams respectively. The major findings from these models are:

- In-plane honeycomb model:

If the plateau is due to elastic bucking, then the σ_{el}^* varies with wall thickness (t) and wall length (l) as:

$$\frac{\sigma_{el}^*}{E_s} \approx \left(\frac{t}{l}\right)^3 \quad \text{.....(5)}$$

If material undergoes plastic deformation, σ_{pl}^{*} varies with wall thickness (t) and wall length (l) as:

$$\frac{\sigma_{pl}^{*}}{\sigma_{ys}} \approx \left(\frac{t}{l}\right)^{2} \text{.....(6)}$$

where, σ_{ys} is the yield strength of solid cell wall material.

For a brittle honeycomb, the crushing strength scales as:

$$\frac{\sigma_{cr}^{*}}{\sigma_{fs}} \approx \left(\frac{t}{l}\right)^{2} \text{.....(7)}$$

where, σ_{fs} is the failure strength.

- Out-of-plane honeycomb model:

  If there is no elastic buckling, σ_{el}^{*} scales with ρ_r as:

$$\frac{\sigma_{el}^{*}}{E_s} \approx \rho_r \text{ .....(8)}$$

  If there is elastic buckling and which leads to plateau regime, then σ_{el}^{*} scales with t and l as:

$$\frac{\sigma_{el}^{*}}{E_s} \approx \left(\frac{t}{l}\right)^{3} \text{.....(9)}$$

  If the plateau is due to plastic yielding:

$$\frac{\sigma_{pl}^{*}}{\sigma_{ys}} \approx \left(\frac{t}{l}\right)^{5/3} \text{.....(10)}$$

  If plateau is coming from brittle failure of honeycomb during out of plane compression, σ_{cr}^{*} can be expressed as:

$$\frac{\sigma_{cr}^{*}}{\sigma_{fs}} \approx \left(\frac{t}{l}\right) \text{.....(11)}$$

- Open cell model:

  If the elastic buckling gives rise to plateau in the stress-strain curve of open cell foams, then the σ_{el}^{*} scales with ρ_r as:

$$\frac{\sigma_{el}^{*}}{E_s} = C_2(\rho_r)^2 \text{.....(12)}$$

where C_2 is a constant (≈ 0.05). This dimensional argument is valid only for true cellular solids (ρ_r<0.3).[6] At higher ρ_r, cell walls are too short and stocky to buckle.

If plastic yielding takes place in the plateau regime, then σ_{pl}^{*} scales with ρ_r as:

$$\frac{\sigma_{pl}^{*}}{\sigma_{ys}} = C_3(\rho_r)^{\frac{3}{2}} \text{.....(13)}$$

where, C_3 is a constant ≈ 0.3

Plateau in the stress-strain curve due to the crushing of brittle open foams can be expressed as:

$$\frac{\sigma_{cr}^{*}}{\sigma_{fs}} = C_4(\rho_r)^{\frac{3}{2}} \text{.....(14)}$$

where, σ_{fs} is the modulus of rupture of the cell wall material and C_4 is a constant ≈ 0.2

- Closed cell model:

The post yield curve of closed cell foams does not have a flat plateau due to compression of fluid in the pore. Rather, it rises with increasing slope. Therefore, to understand the elastic buckling, plastic yielding and collapse stress of closed pore foams, it is essential to consider membrane stresses coming from cell faces and pressure developed by fluid in the closed cell.

The post yield curve due to elastic buckling of closed pore walls can be expressed as:

$$\frac{\sigma_{el}^{*}}{E_s} = 0.05\ (\rho_r)^2 + \frac{(p_0 - p_{at})}{E_s} \text{.....(15)}$$

where, p_0 is the initial fluid pressure and p_{at} is the atmospheric pressure.

The second term represents the contribution coming from pore fluid.

In closed pore foams, the plastic buckling is a combined effect of plastic bending of cell edges and plastic stretching of their faces. The plastic yield stress can be expressed in terms of ρ_r as:

$$\frac{\sigma_{pl}^{*}}{\sigma_{ys}} = 0.3(\varphi\rho_r)^{\frac{3}{2}} + 0.4(1-\varphi)\rho_r + \frac{(p_0 - p_{at})}{\sigma_{ys}} \text{.....(16)}$$

Here, the second term corresponds to the membrane stress.

The brittle crushing of closed cell walls can be expressed as:

$$\frac{\sigma_{cr}^{*}}{\sigma_{fs}} = 0.2(\varphi\rho_r)^{\frac{3}{2}} + (1-\varphi)\rho_r \text{.....(17)}$$

(c) **Densification regime**: The third regime is due to densification where the σ–ε curve shows an upward trend and reaches a limiting slope of E_s when densification is complete. This regime corresponds to the collapse of cells throughout the material and subsequent loading of the cell edges and faces against one another. The relation between full densification strain (ε_d) relative density (ρ_r) of porous material can be expressed as:

$$\varepsilon_d = 1 - 1.4\rho_r \text{.....(18)}$$

While these models provide a framework to understand model porous structures, ice templated materials are typically characterized by far more complex pore structures. In ice templated materials, the relative density is not the only structural characteristic that determines the mechanical response of the cellular solid. Here, it is necessary to also consider cell shape and anisotropy as important parameters.[18] Cells in ice templated materials are typically neither monodisperse nor isotropic. Rather, they are formed with varying sizes and shapes.[10] Therefore, one needs to account for all these parameters to understand the deformation behaviour accurately in ice templated materials.

Recently, different groups have studied the mechanical properties of ice templated materials.[18, 25-29] Dunand et al. had shown that the open cell model is appropriate for describing anisotropic freeze cast metals especially when the value of intercept is obtained by fitting experimental data to the open-cell model.[30] They have also shown that the open cell model is a statistically better fit for anisotropic dendritic and isotropic equiaxed structures in comparison to other pore structures like lamellar, honeycomb and cellular structures. Moreover, neither open cell nor honeycomb model offers a perfect fit to the lamellar, honeycomb or cellular pore structures. Seuba et al. had shown that the anisotropic ice templated structures collapse by buckling of the cell walls rather than localized bending.[18] Buckling of walls has been reported to be the main failure mechanism in unidirectional porous materials prepared by extrusion,[27] 3D printing[28] and wood pyrolysis.[29] Anisotropic pores with perpendicular struts connecting the main walls are formed during directional ice templating. This architecture prevents shearing by interlocking the lateral motion of the pore walls. Therefore, typically, these materials fail in the middle of the sample, perpendicular to the external load. The stress- strain curve of unidirectionally ice templated sample under compression was observed to show progressive or brittle failure depending on the porosity.[18] When pore volume increases above about 60%, the sample fails progressively through local buckling of the struts. Here, the strength is not strongly influenced by the pore morphology and size distribution. However, for lower porosity, the material fails in a brittle manner with cracks propagating parallel to the load. Here, the distribution of pore wall thickness is important in determining the strength.

In this work, we study the mechanical properties of ice templated inorganic-organic hybrid structures. In contrast to above reports, the pores of these hybrids are isotropic.

Here, we contrast the compression behaviour of two inorganic/organic hybrid macroporous samples, an elastic sponge and a plastic monolith, made by ice templating. As discussed in previous chapters, in these scaffolds, inorganic particles are bridged by a thin crosslinked polymer layer. The mechanical response of these scaffolds is sensitive to the protocol employed to prepare these scaffolds. Elastic sponges are prepared when freezing an aqueous dispersion of colloids, polymer and crosslinker and allowing crosslinking to happen in-situ after the water has frozen. However, if the ice crystals formed by freezing the colloidal dispersion are removed by lyophilization, so that crosslinking happens in the absence of ice, we obtain plastic monoliths which fail at very small compressive strains. Remarkably, the overall crosslinking density and gross structural features of plastic scaffolds are indistinguishable from the elastic sponges. In Chapter 3, spatial mapping of the local environment in elastic and plastic samples using particle tracking and microrheology showed that plastic monoliths exhibit spatial heterogeneity relative to elastic scaffolds. Microrheology showed a greater variation in local solid moduli for plastic scaffolds compared with elastic sponges. We interpreted this spatial heterogeneity in the local environment in terms of variations in local crosslink density for plastic scaffolds.

Here, we compare the response of elastic sponge and plastic monolith to compressive loading. We use bulk rheology to understand the macroscopic response of hybrids to compression. Later, we use this bulk rheology data along with Gibson and Ashby's micromechanical model and X-ray computed microtomography to understand the deformation mechanism of pores in our system. Here, we also use single particle tracking method to study the deformation mechanism within the pore walls. This will help us in understanding the length scale of elasticity and plasticity in these ice templated hybrids.

4.2 Experimental Section

4.2.1 Materials:

'Ångström Sphere™' silica spheres (1μm) were purchased from Fiber Optic Center, USA. Spherical, monodisperse (1.08 ± 0.04 μm) fluorescent polystyrene (FPS) particles (PS-FluoGreen-1.0, ab/em: 492/519 nm, 2.5wt. %) were obtained from Microparticles GmbH, Germany. Branched 25 kDa polyethylenimine (PEI) and 1, 4-butanediol diglycidyl ether were purchased from Sigma-Aldrich. All materials were

used as received. Corning® (No.1, USA) cover glasses were used as the substrate for epi-fluorescence microscopy imaging.

4.2.2 Preparation of scaffolds by ice templating

Aqueous dispersion of silica particles was prepared in a 2 ml round bottom centrifuge tube by sonicating 60 mg of particles in deionised water for 30 min followed by 10 min vortexing. The dispersion concentration was 10 wt. %. 3 mg of PEI (30 µl from 10 wt. % polymer stock solution) was added to this aqueous dispersion and vortexed for 5 min. 10 mg of crosslinker (1, 4- butanediol diglycidyl ether) was added to this dispersion and vortexed for 3 min. Similarly, we have also made aqueous dispersions with 5, 20, 30 and 40 wt.% particle concentrations. In all these compositions, we maintained the particle to polymer and polymer to crosslinker ratio as 1:0.05 and 1: 3.34 respectively.

Elastic sponge preparation: Aqueous dispersion was frozen at -15^{o}C for a day followed by room temperature thawing (Figure 4.1). These wet sponges were dried by lyophilization (LabconcoFreeZone 2.5 Plus, -80^{o}C, 0.1 mBar) for 4 h.

Plastic monolith preparation: Aqueous dispersion was frozen at -15^{o}C for 30 min followed by lyophilization at -80^{o}C and 0.1 mBar for 4 h (Figure 4.1). After sublimation of ice crystals, the sample was stored at -15^{o}C for 24 h for crosslinking.

Preparation of samples for single particle tracking experiment: 60 mg of silica particles and 2 mg of FPS were added to the aqueous phase and the overall particle concentration was 10 wt. %. This aqueous dispersion was used to prepare elastic sponges and plastic monoliths using the aforementioned protocol.

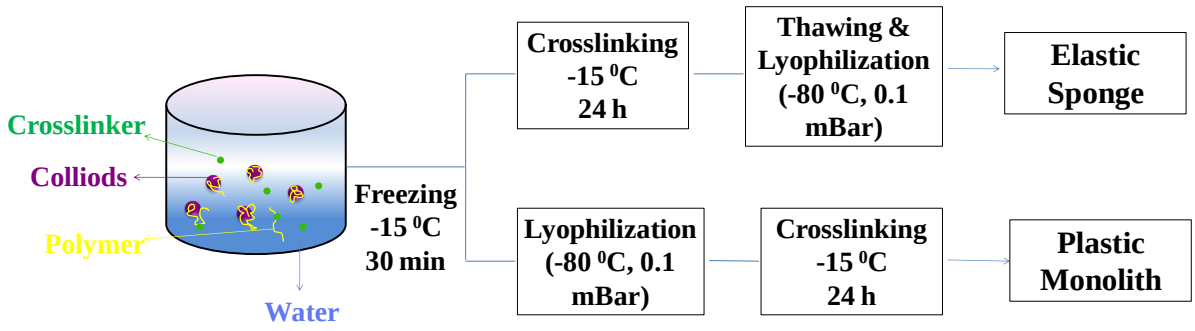

Figure 4.1: Schematic of elastic sponge and plastic monolith preparation.

4.2.3 Characterization

Samples were cut into cylindrical shape using sharp surgical blades and characterized using various instrumental techniques:

4.2.3.1 Scanning Electron Microscopy: Samples were imaged using scanning electron microscopy (SEMQuanta 200 3D). Samples were mounted on the SEM stubs and a thin layer of gold was sputtered on the sample surface prior to imaging.

4.2.3.2 Rheometer: Compression/ expansion studies on the samples were performed using ARES G2 strain controlled rheometer in a dynamic mechanical analysis measurement mode. Samples were placed between two 25 mm diameter roughened parallel plates and 0.5 g preload was applied. Samples were compressed to different % of compressive strains at a constant rate of 0.1 mm/s and the corresponding normal force was measured. Nominal compression stress was calculated by dividing this force with the initial cross-sectional area of the cylinder. We also performed frequency sweep measurements in dynamic mode on the scaffolds (frequency range 1 to 100 rad s^{-1}; strain amplitude of 0.25%, sample loaded with normal force = 1 g).

4.2.3.3 In-situ compression and X-ray micro-computed tomography: 3D imaging was used to study the morphological variation under compressive load. This was done using in-situ micro X- ray computed tomography (μXCT). The CT5000 500N in-situ compression stage for μXCT (Deben UK Ltd, Suffolk, UK) was used as a load frame for in-situ tomography. Control of the sample stage was accessed through MICROTEST drive electronics and Windows^{TM} software. A 500N load cell was used for the experiments and the samples were compressed with a strain rate of 0.1 mm/min. 3D X-ray imaging were conducted on samples compressed to different strain values using Zeiss Xradia 510 versa 3D-X ray microscopes (XRM, Zeiss X-ray Microscopy, Pleasanton, CA, USA). The compression stage was mounted between the X-ray source and detector assembly. Detector assembly consists of a scintillator, objective lens and a CCD camera. Source and detector were 75 and 70 mm away from the sample centre. The source used was a sealed tube operated at a voltage of 40 kV and 3W power. Images were obtained with a 4X objective with a field of view of 3.5 mm^2. Image acquisitions were completed by acquiring 3201 projections over 360° of rotation with a resolution of 3.48 μm and 40 s X-ray exposure per projection. In addition, projections without sample in the beam (reference images) were also collected and averaged. The micrographs were collected using 2kx2k 16 bit charge coupled device (CCD) detector. The images were subsequently reconstructed using Xradia XMReconstructed software. These 3D images were further processed using Geodict software (Math2Market GmbH, Kaiserslauter, Germany).

4.2.3.4 Calculation of bulk densities and porosities of elastic sponges and plastic monoliths.

Volume of the cylindrical dry sample was calculated as $V = \pi r^2 h$ from its known radius (r) and height (h). Mass of the dry sample, m_d, is measured with an accurate weighing balance. The bulk density of the sample is calculated as

$$\rho^* = \frac{m_d}{V} \text{.....(19)}$$

Porosity of the ice templated scaffolds were calculated based on the equation:

$$Porosity = \frac{\frac{m_w - m_d}{\rho_{water}}}{Volume\ \ of\ wet\ scaffold} \text{.....(20)}$$

where, m_w is the weight of wet scaffold and ρ_{water} is the density of water.

4.3 Results and Discussion

4.3.1: Morphology, porosity and relative density of elastic sponge and plastic monoliths

We begin by comparing the cellular features of elastic sponge and plastic monolith. In Figure 4.2, we present SEM images of the elastic sponge and plastic monolith. SEM shows that both elastic and plastic scaffolds are characterized by irregular pores with a distribution of sizes. This is in contrast to the unidirectionally frozen ice templated scaffolds that show aligned pores with perpendicular struts between pores.[10] High resolution images clearly show the inorganic silica particles that comprise the pore walls. We have previously shown (see Chapter 2) that during ice templating, the polymer forms a crosslinked mesh that holds the particle assembly together. The silica particles are polydisperse and show a randomly packed structure. We have also quantified the interparticle spacing in elastic and plastic scaffolds to check whether lyophilization perturbs the particle assembly in plastic scaffolds. The centre to centre distance (*d*) between particles (calculated using ImageJ software by averaging over at least two hundred particles from several high resolution SEM images) is identical for both the scaffolds (Table 4.1). This is consistent with data reported in Chapter 2 for scaffolds prepared using silica nanoparticles, where we calculate "*d*" using small angle X-ray scattering (SAXS).

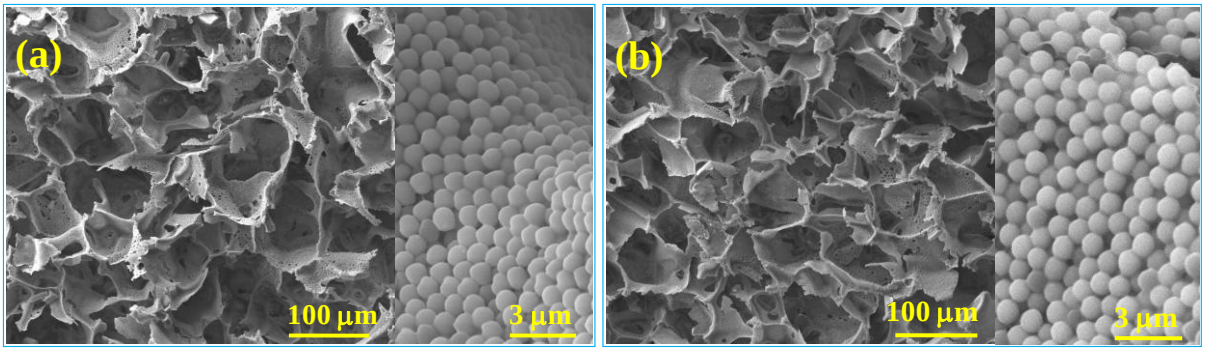

Figure 4.2: Morphology of ice templated scaffolds. SEM images of (a) elastic sponge and (b) plastic monolith. Magnified images of pore walls are shown in the right side of these two images.

Table 4.1: Comparison between elastic sponge and plastic monolith in terms of bulk density, porosity and centre to centre neighboring particle distance of the scaffolds.

Material	**ρ* (g/cc)**	**Porosity (%)** a†	**Particle centre to centre distance (µm)**
Elastic	0.091	88.6	1.005±0.05
Plastic	0.09	88.7	1.005±0.05

a†: from X- ray micro-tomography (averaged over a 1.8 x 1.5 x 3.2 mm^3 and averaged over at least two independent samples)

We have used 3D images of scaffolds obtained from µXCT to calculate porosity (Figure 4.3). "Open and closed porosity" algorithm in the Porodict module of the GeoDict software was used to process the tomography images to obtain porosity. Both elastic sponge and plastic monolith exhibit a volume porosity of about 89% (Table 4.1). The porosities of the two samples are identical, to within experimental resolution. This suggests that the pore structure templates the ice crystals formed during freezing of the dispersion, and there is no change in pore structure during lyophilization and polymer crosslinking. Therefore, there is no difference in the pore morphology between the elastic and plastic samples. Both scaffolds are characterized by the same foam density (ρ^*) ≈ 0.09 (obtained as described in the Experimental Section). The relative density, ρ_r is calculated as, $\rho_r = 1 - fractional\ porosity$ =0.12. Since, $\rho_r < 0.3$, these scaffolds are true cellular solids according to Gibson.[6] Next, we examine the bulk and microscopic response of these two scaffolds to compressive loading.

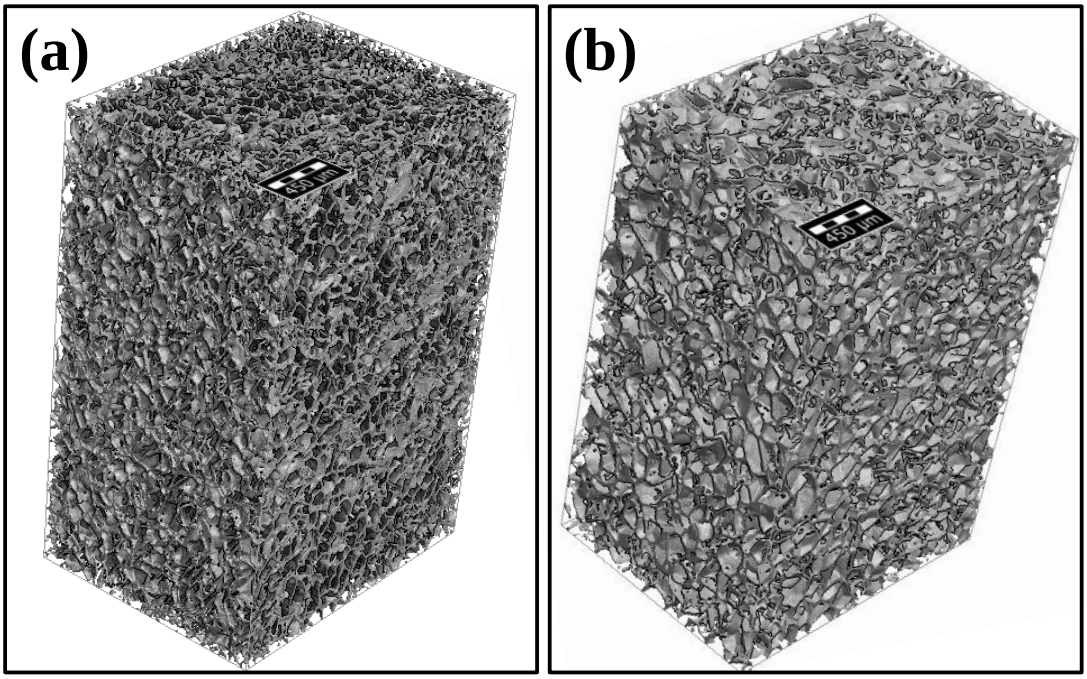

Figure 4.3: X-ray μCT images of **(a)** elastic sponge and **(b)** plastic monolith. Scale bar is 450 μm for both the images.

4.3.2: Bulk response of elastic and plastic scaffolds to compression

Macroscopic behaviour of scaffolds to compression is studied using a rheometer. Here, we have deformed the material to various strains and studied corresponding macroscopic stress builtup in it. First, we discuss the response of scaffolds crosslinked in presence of ice crystals, viz., elastic sponges. Figure 4.4 shows compressive stress-strain curves for elastic sponge compressed to various strain values. The elastic sponge shows linear elastic response at very low strains (<2%, Figure 4.4). Young's modulus calculated as slope of this linear regime gave a value of ≈ 24 kPa. Above 2%, the stress becomes nonlinear in strain (Figure 4.4). Above strain of 30%, the stress strain curves are sigmoidal in shape. This is a manifestation of three deformation regimes typically observed in open cell foams and biocellular materials.[6, 31] At first, there is a linear rise of the stress followed by a region where the slope increases moderately. Finally, at high strains, the stress increases rapidly with strain. The last regime was prominent only above 50% compressive strain. Independent of the original strain, the samples recover to their original size when stress is released.

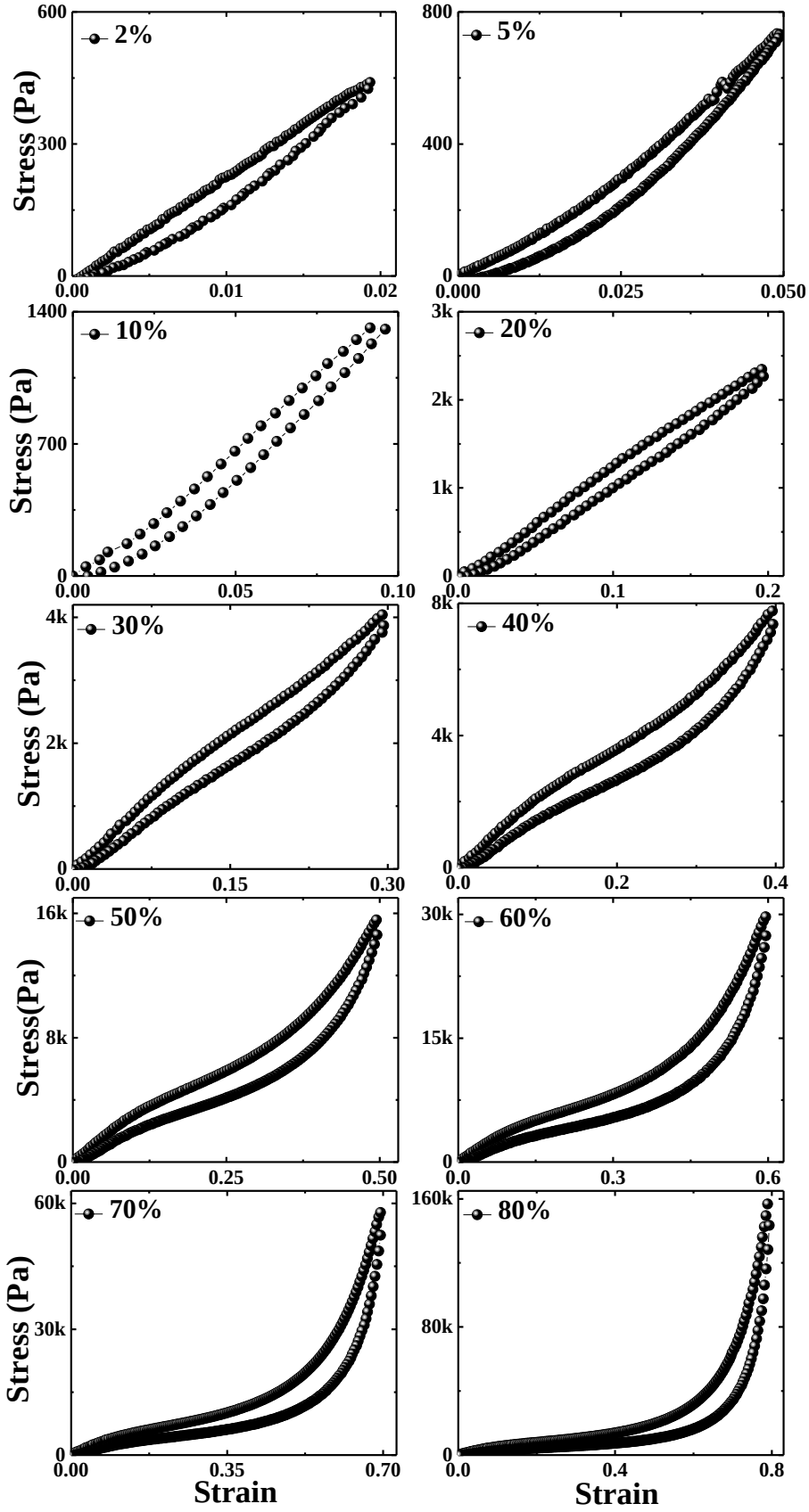

Figure 4.4: Compression-expansion study on elastic sponges. Compressive stress vs. strain plots for various compressive strains. These curves are from the third compression-expansion cycle.

Therefore, the sponge recovers elastically in all three regimes of the stress- strain curve. This is in contrast to the majority of open cell foams that exhibit permanent deformation for moderate strains.[6, 9] However, we observe hysteresis in the compression-expansion cycle from loss of energy to dissipative processes.

Additionally, during compression study, we did not see any noticeable change in sponge diameter with the naked eyes at any of the strains (Figure 4.5a). To quantitative the variations (if any) in scaffold diameter, we analyzed images captured during scaffold compression. Analysis showed that the scaffolds exhibit minor reversible increase in scaffold diameter on compression. For example, we observe 1.03 times increase in diameter at 60% compressive strain (Figure 4.5b). We further calculated the Poisson's ratio ($v = -(\frac{d\varepsilon_{trans}}{d\epsilon_{axial}})$, where, $d\varepsilon_{trans}$ and $d\epsilon_{axial}$ are the transverse and axial strains) for various strain values. At 10% strain the value was 0.05±0.0008 (Figure 4.5c). Interestingly, we did not see any significant change in Poisson's ratio with further increase in strain (30%: 0.047± .012, 50%: 0.040± 0.019, and 60%: 0.060± 0.01).

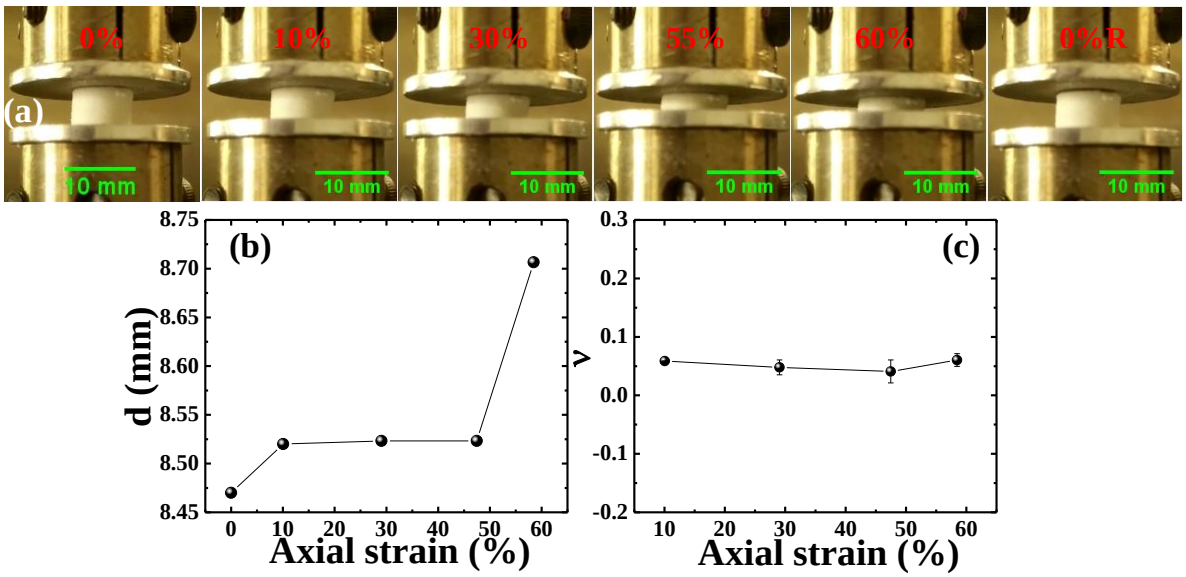

Figure 4.5: **(a)** Photographs of sponge compressed to different strain values. **(b)** Variation of elastic sponge diameter as a function of compressive strain. Reported diameters are the average values of diameters measured from different locations of the scaffold. **(c)** Poisson's ratio as a function of axial strain.

We have also observed that the Young's modulus (E^*=23.9kPa) of this ice templated elastic sponge is approximately double the storage modulus ($G^{'} = 11.2$ kPa at 25 rad/s

frequency) obtained from linear shear rheology (Figure 4.6).[32] Thus, the Poisson's ratio can be calculated as,

$$\nu = \frac{E}{2G'} - 1 = 0.064.$$

Similar observation has been made by Rajamanickam et al. and they have also shown that the pore structures obtained from confocal imaging did not show any difference between 0 and 40% strains.[32]

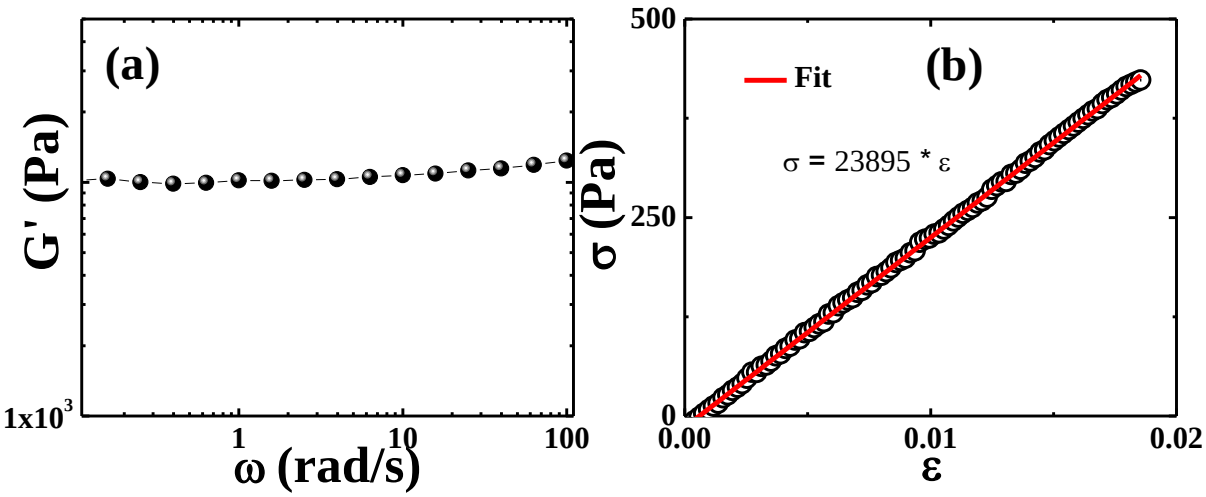

Figure 4.6: **(a)** Storage modulus as a function of frequency. **(b)** Nominal stress- strain curve corresponds to ~ 2% compressive strain.

Obtaining a Poisson's ratio of zero is not unusual for porous materials. It has been suggested that the reason for a Poisson's ratio of zero could be that the dimensional changes due to compression are accommodated by the deformation of cell walls.[33] To obtain further insights into cell deformation mechanisms in the linear elastic regime, we have studied the relationship between foam moduli and relative density (ρ_r). Here, we have made scaffolds with varying bulk density, prepared from 1μm silica colloidal dispersion at different particle concentrations (Φ). We vary Φ from 5 wt.% to 10 wt.%, 20 wt.%, 30 wt.% and 40 wt.%. Further, we have estimated the foam density (ρ^*) and porosity based on equations 19 and 20 respectively. We observe that the foam porosity decreased with increase in Φ (Figure 4.7a) and the foam density (ρ^*) increased with Φ (Figure 4.7b). In addition, the foam Young's modulus (E^*) and shear modulus (G^*) scaled linearly with ρ^*($E^* \sim \rho^*$and $G^* \sim \rho^*$) (Figure 4.7c). In these scaffolds, the ratio of particle, polymer and crosslinker is held constant as we vary Φ. Therefore, we expect the density of pore walls (ρ_s) formed by the consolidation of starting materials will be constant, independent of Φ. Therefore, we can write: $E^* \sim \rho_r$ and $G^* \sim \rho_r$. This clearly

does not follow Eq. 3 based on Gibson's open cell model, indicating that the mechanical response is not dominated by cell edge bending. We attribute the response to the compression of cell walls which gives rise to a linear scaling for the mechanical moduli with foam density.

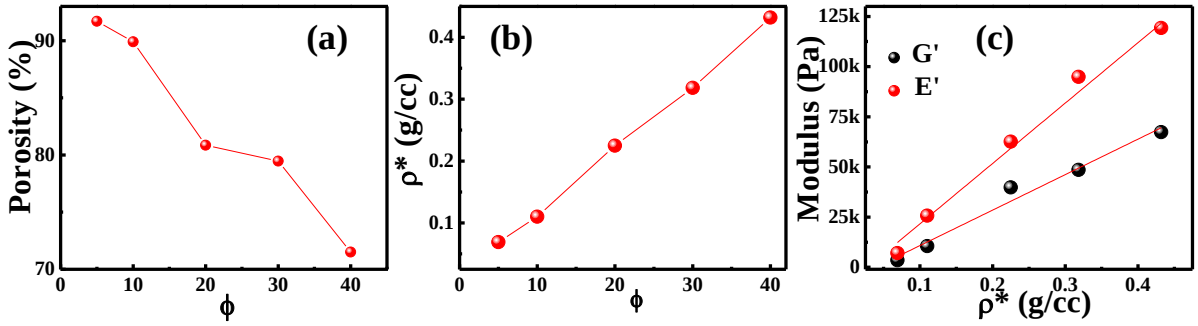

Figure 4.7: Elastic sponge property variation with particle concentration (Φ). Variation of (**a**) porosity and (**b**) foam density (ρ^*) with Φ. (**c**) The scaling of Young's modulus (E^*) and shear modulus (G^*) with ρ^*.

The underlying mechanism for the mechanical response in the higher strain regimes of the stress-strain curve will be discussed later in the chapter.

We now examine the behaviour of plastic scaffolds, viz. monoliths crosslinked in absence of ice crystals during compression (Figure 4.8). Plastic scaffolds also showed a linear increase in stress with respect to strain at very small deformation (<2%, Figure 4.8). The Young's modulus calculated as slope of this linear regime was ≈ 28 kPa, comparable with the equivalent elastic sponge. However, plastic monoliths showed significantly higher hysteresis in compression/expansion experiments compared with elastic sponges. Further, the plastic monolith did not recover completely from 2% compressive strain, and exhibited a permanent set of 0.5%. At 5% strain, the stress-strain curve was qualitatively different from that for an elastic sponge (Figure 4.8, compare with Figure 4.4). Further increase in strain to 20% gave a sigmoidal shape curve (Figure 4.8). Quantitatively, the stress observed on compressing a plastic sponge is lower than that for elastic sponges for strain ≥ 30%. Unlike the steep increase in stress when strain exceeds 50% in elastic samples, the stress build up in plastic samples is relatively modest. For example, on compressing to 60%, the stress for a plastic monolith is 2 times lower than that of an equivalent elastic sponge. Above 10% strain, we note that the stress for plastic monoliths rapidly decays to zero when the load is released, with small strain recovery (~1-2%) in contrast to the complete shape recovery observed for elastic sponges.

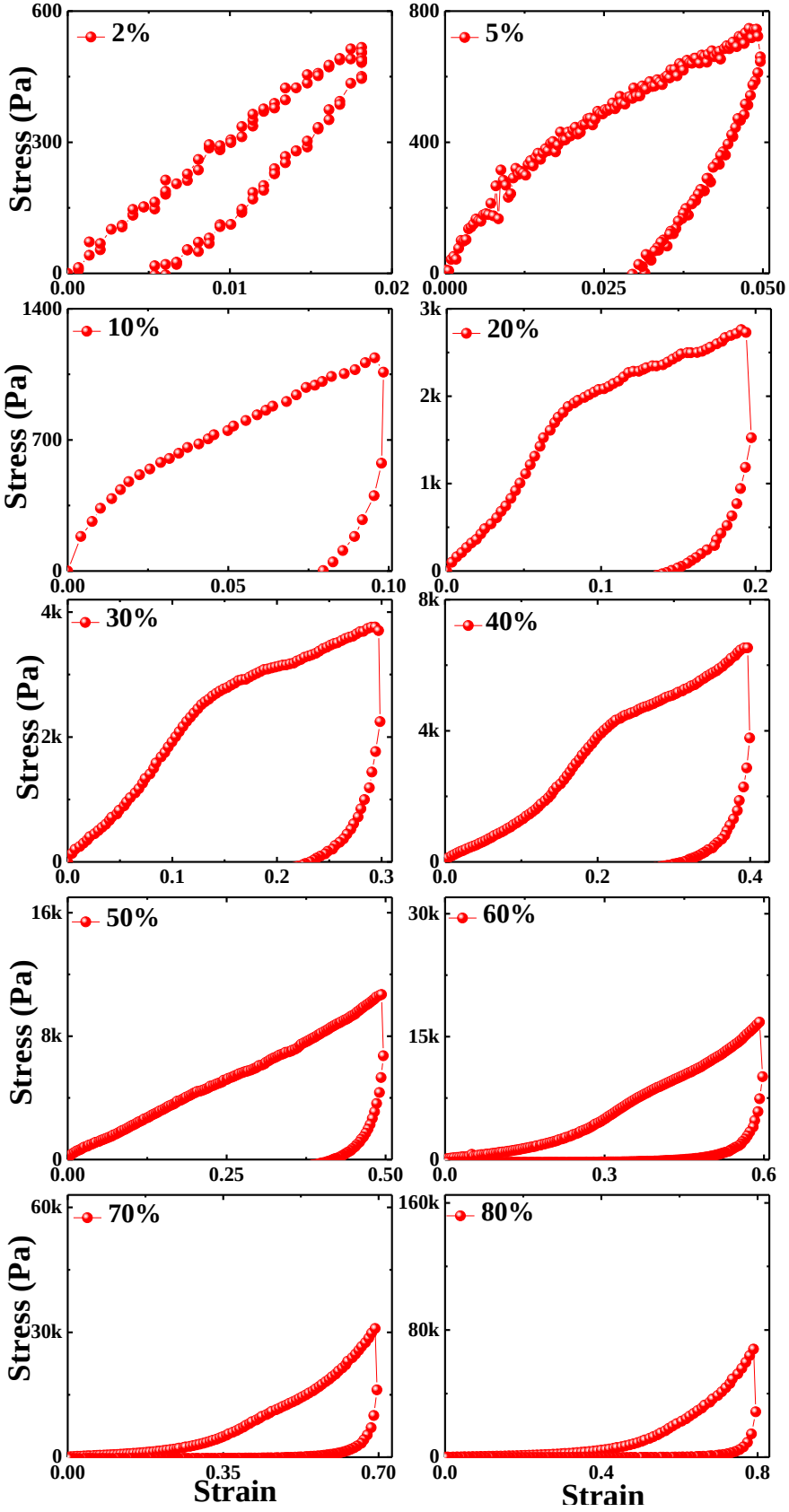

Figure 4.8: Compression- expansion study on plastic monoliths. Compressive stress vs. strain plots for various compressive strains. The Y- axis scales are same as in Figure 4.4 for ease of comparison.

Therefore, while there is some hysteresis during the recovery of elastic monoliths as the stress is released, there is catastrophic failure in plastic monoliths that manifests as large hysteresis in the stress-strain data. Additionally, when plastic samples were compressed to small strains (≈5%), we qualitatively observed sample fragmentation to form small pieces that detached from the sample (Figure 4.9b). At larger strains (typically≥ 50%), we observed propagation of cracks parallel to the loading direction (Figure 4.9c). On releasing the load, we observed that some parts of the sample exhibit modest shape recovery, but there is predominant plastic failure of the sample.

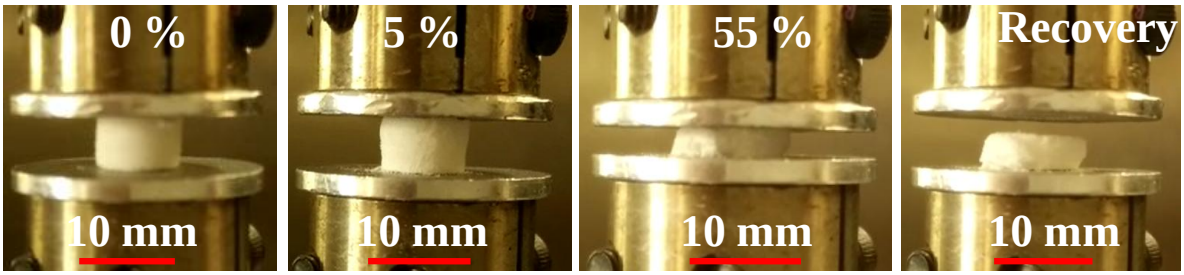

Figure 4.9: Photographs of plastic monolith under compression. At 5% strain, some powder can be seen on fixture plate, coming from the sample during compression. At 55%, on sample surface cracks can be seen. After releasing the load, sample did not recover fully.

Next we look at the microstructure of elastic and plastic scaffolds in the two regimes of the sigmoidal stress- strain curve where there is a moderate increase in stress, and at higher strains where the stress increases rapidly.

4.3.3: Microstructure of elastic and plastic scaffolds under compression

We use μXCT to characterize the microstructural changes in the scaffold on compression. Here, we have studied the effect of compressive strain on porosity and pore size distribution (PSD) by in-situ imaging of scaffolds during compression using μXCT. Samples were imaged at 0, 30 and 60 % compressive strains and after releasing the load (Figure 4.10). The size of the imaged region in all these cases is 1.8 x 1.5 x 3.2 mm^3. Uncompressed, as prepared elastic sponges showed a PSD of ~3.5 μm to ~120 μm with a maximum in the range of 50-70 μm (Figure 4.10e). The PSD remains largely unchanged when the sample is compressed to 30%. However, further increase in strain to 60% leads to a decrease in the size of the largest pores (~3 μm - 85 μm)

and the peak in the PSD decreases to ~ 25 μm. The shift in PSD can be visualized from the μXCT images in Figures 4.10 ac-cc. Specifically, at 60% strain, the blue color which corresponds to small pore sizes (< 20μm) dominates in contrast to the green color which corresponds to larger pores (50-70 μm). Additionally, the uniform color distribution in Figure 4.10cc indicates that the reduction in pore size is not spatially localized but happens uniformly over the entire imaged region of the sample (~1.8 x 1.5 x 3.2 mm^3). We also observe that the PSD is recovered upon releasing the imposed load. Here, we released the load and imaged the sample after a day and the measured PSD was experimentally indistinguishable from the original sample. The volume porosity also showed a reduction with increasing strain. Porosity obtained for uncompressed samples by analysing tomography images was ~ 89%; this value matches with the porosity calculated based on equation 20 (~89%). Sample porosity reduced only marginally from 89% to 86% when strain increased from 0 to 30%. However, at 60% strain, the porosity is reduced to 75%. After releasing the load, porosity increased to ~89%, identical to the initial porosity.

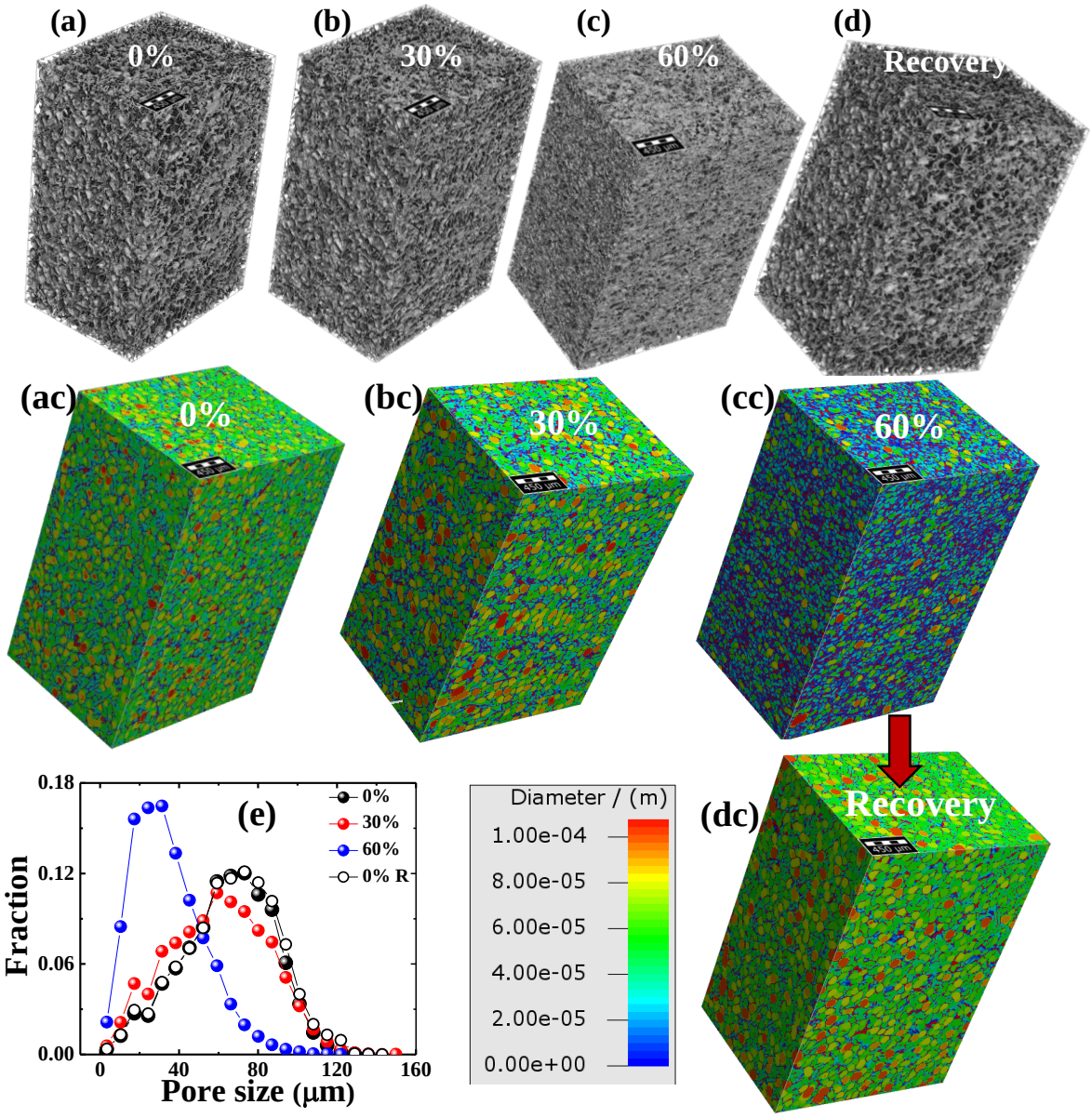

Figure 4.10: Pore size distribution in elastic sponge at different compression levels. X-ray μCT images of elastic sponge under compressive strains of **(a)** 0%, **(b)** 30%, **(c)** 60% and **(d)** sponge morphology after releasing the compressive strain. This image was obtained 24 h after the release of compressive strain. (**ac-dc**) Images a-d color coded based on pore sizes. Scale bar of color code is same for all these figures. Scale bar is 450 μm for all the images. **(e)** Pore size distribution at different compressive strains.

We now focus on deformation of individual pores during compression of the sponges. We analyze 2D slices of sponges obtained from μXCT and examine planes that are parallel (XZ and YZ) or perpendicular (XY) to the loading direction. A few randomly

selected pores are shown with their walls highlighted in the 2D images, for ease of visualization (Figure 4.11). There is no variation in the trends obtained for slices taken at different spatial locations from the imaged region. This is consistent with our observation that there is no spatial dependence of the pore size distribution over the imaged region. To understand the pore shape variation on compression, we have highlighted a few randomly chosen pores by marking their walls red. These pores are highlighted using scribble tool in the Microsoft PowerPoint software. We found that the pores in uncompressed sample are irregular in shape but approximately isotropic. We did not observe any noticeable change in pore size or pore geometry along or normal to the loading direction for strain = 30%. However, at 60% strain, there is a significant reduction in pore size in the XZ and YZ planes. Moreover, for a fixed area imaged, we can see that the population of white lines increased in images corresponding to 60% strain in comparison to 0% or 30% strain images. This indicates that, at 60% strain there is an increase in number density of pore walls compared to 0% strain. The decrease in pore dimensions is much less significant in the XY plane, normal to the loading direction, than for planes along the loading direction. For larger strains (= 60%), we observe a collapse of the porous structure, with folding of the pore walls, predominantly in the XZ and YZ planes (Figure 4.11). Similar wall folding has been reported for cellular structures with very thin cell walls ($t<<l$).[6] Gibson et al. had reported periodic folding of cell walls when honeycombs undergo elastic or plastic buckling.[6] In our case, we do not see periodic folding of pore walls. On unloading the sample, the pore walls "unfold" and elastically recover their original size and shape (Figure 4.11).

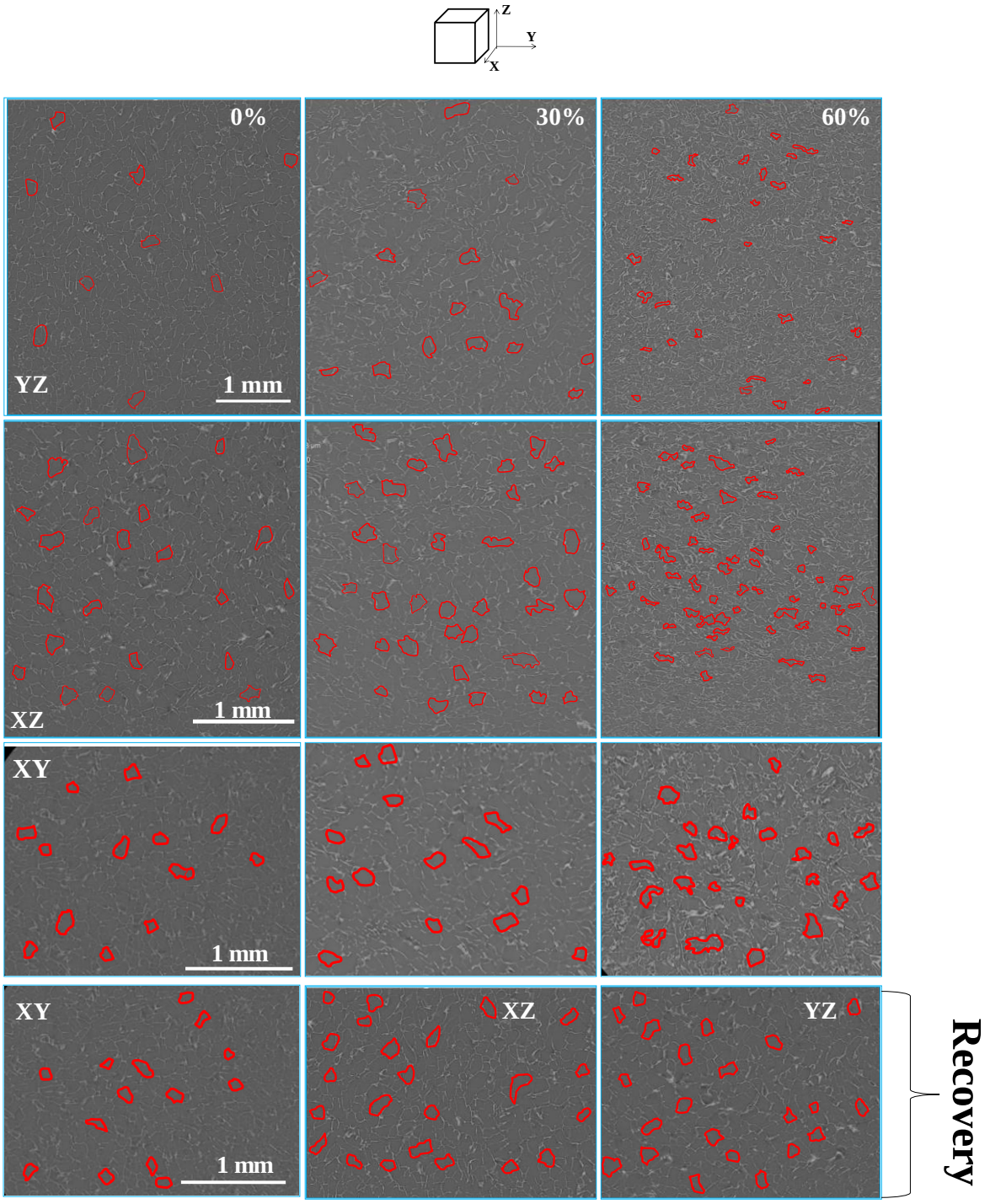

Figure 4.11: 2D slices of elastic sponge correspond to different sample planes obtained from in-situ µXCT at strains 0, 30 and 60%. Images correspond to YZ, XZ and XY planes can be seen in this figure. We have highlighted some randomly selected pore walls with red for better visibility. Pores highlighted are representative and we do not track the same pore with change in strain. The bottom row represents the images obtained 24 h after the release of load.

To understand the pore deformation mechanism responsible for the plateau regime in the stress-strain curve of elastic sponges (Figure 4.4), we have checked the scaling relationship between elastic collapse stress (σ_{el}^*) with relative density (ρ_r) (Figure 4.12). We estimate the plateau stress, σ_{el}^*, of scaffolds containing different particle concentration (Φ) as shown in Figure 4.12.

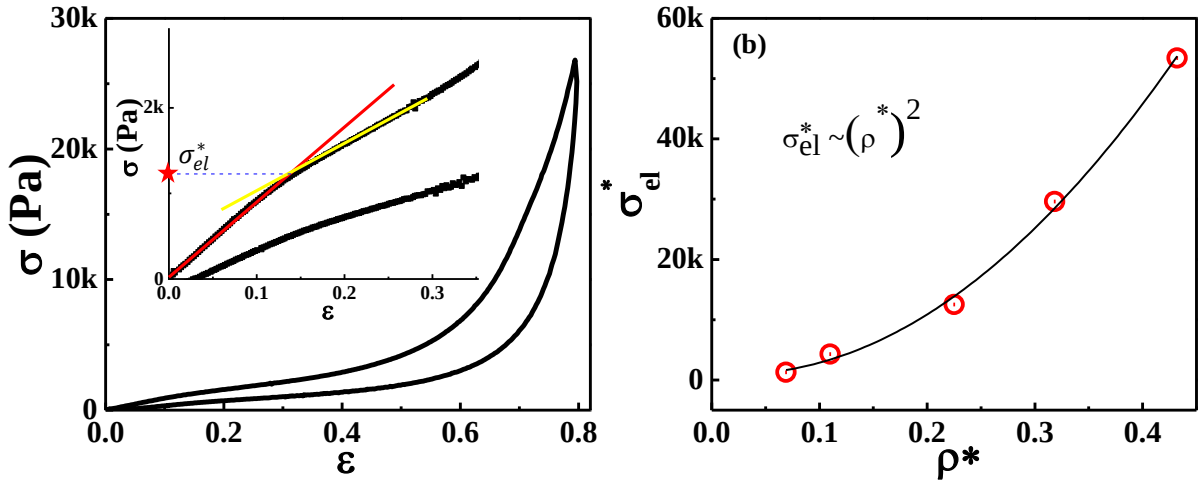

Figure 4.12: **Scaling of σ_{el}^* with foam density (ρ^*).** (**a**) Method to calculate σ_{el}^* from σ-ε curve. This representative σ-ε data corresponds to 5 wt.% scaffold. The stress at the plateau regime is assigned as σ_{el}^* as shown in the inset image. (**b**) Scaling of σ_{el}^* with ρ^*.

Our study shows that the elastic collapse stress varies with foam density as:

$$\sigma_{el}^* \sim (\rho^*)^2$$

As discussed earlier, the cell wall density (ρ_s) is independent of the scaffold particle concentration (Φ). Therefore, the aforementioned scaling relationship can be rewritten as:

$$\sigma_{el}^* \sim (\rho_r)^2$$

According to Gibson's open cell model, the plateau due to elastic buckling gives a scaling relationship of $\sigma_{el}^* \sim (\rho_r)^2$ between σ_{el}^* and ρ_r (Eq. 12). Therefore, our scaling analysis is consistent with the imaging data and suggests that, in the plateau regime, the pore structure collapses by buckling of the cell walls but recovers its shape after removal of stress.

We now analyze μXCT data for plastic scaffolds compressed to 0, 30 and 60% strain (Figure 4.13). At 0% strain, plastic monoliths exhibited a pore size distribution of ~3.5 μm to ~120 μm with a maximum in the range of 50-70 μm, similar to elastic sponges

(Figure 4.13 a, ac, d). However, when strain is increased to 30%, we observe a change in the PSD with a few pores as large as 180 μm to 340 μm (Figure 4.13d). Additionally, we observe that in some locations, the pores are collapsed. Therefore, on compression to 30% strain, there is simultaneously an increase in the fraction of collapsed pores and in the formation of larger pores, presumably from failure of parts of the monolith (Figure 4.13d, inset). On further compression to 60% strain, we observe the opening up of large fissures from 200 μm to 1 mm in size (Figure 4.13c, cc, d), randomly distributed within the imaging volume of 5.3 mm^3 (Figure 4.13 cc). These cracks are sufficiently large that they are visible even to the naked eye.

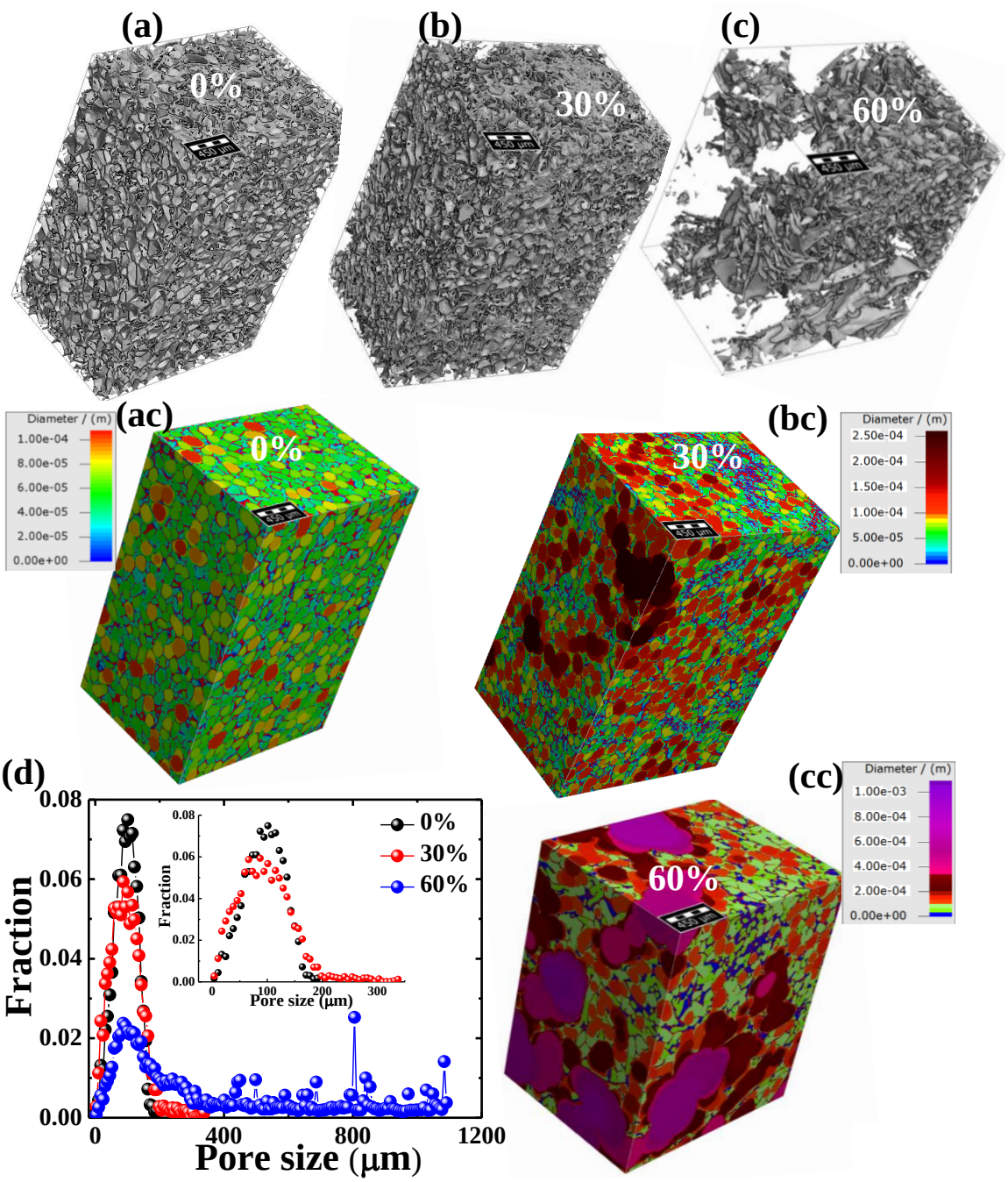

Figure 4.13: Pore size distribution in plastic monoliths at different compression levels. X-ray μCT images of plastic monolith under compressive strains of **(a)** 0%, **(b)** 30% and **(c)** 60%. 60% compression is performed on a fresh sample. Scale bar is 450 μm for all the images. **(d)** Pore size distribution at different compressive strains.

We performed SEM to image crack formation in plastic samples compressed to various strain values. We compressed the samples in the rheometer and then, gently placed them on SEM stubs. Samples were imaged 18 h after compression (Figure 4.14).

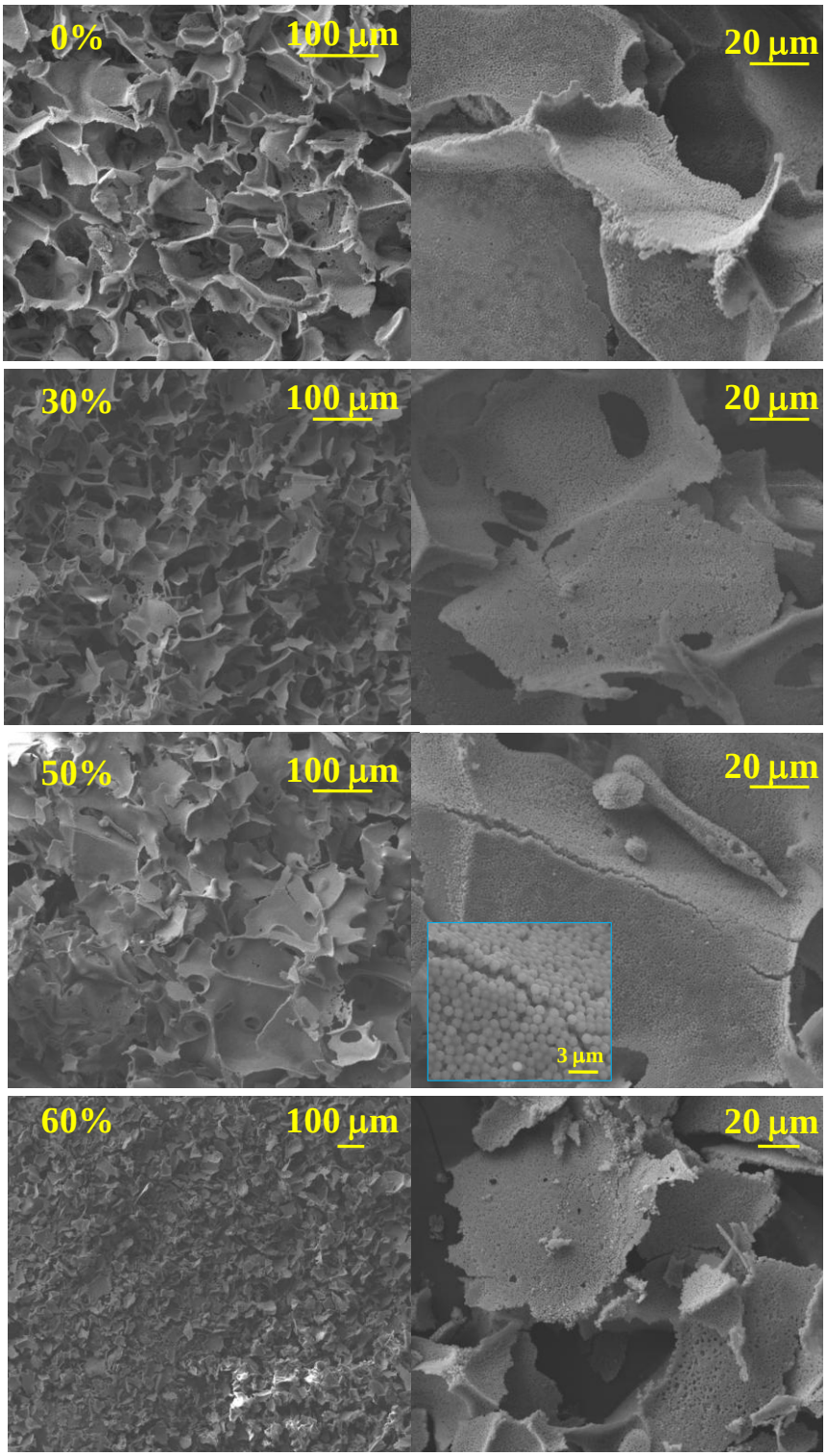

Figure 4.14: SEM images of plastic samples which were compressed to different strains. Samples were compressed to different strain levels using rheometer and were then gently transferred to SEM stubs and imaged after gold sputtering.

For the sample strained to 30%, we observe pore collapse in certain locations of the image. At 50% strain, there was increased pore collapse as indicated by the increase in

number density of collapsed pore walls in a frame. Additionally, we observe that the pore walls are perforated with larger (~ 100 μm) cracks that extend across the entire wall. At even higher strain (= 60%), there is further increase in the density of collapsed walls. Here, we do not see any larger cracks (mm size) because we have imaged a broken piece of the sample. In addition, high resolution SEM image shows many broken pieces of pore walls.

Therefore, our investigation clearly indicates qualitative differences in the response of elastic and plastic scaffolds to compression at macroscopic as well as microscopic length scale. At small strains – elastic sponges exhibit wall thickening and at higher strains > 50%, walls buckle. In contrast, plastic scaffolds show evidence for pore collapse at strains as low as 30%. At 60% strain, the monoliths have completely collapsed and exhibit cracks that are millimeters in size. To understand the implications of this microstructural change at the level of the constituent particles in the pore walls, we use fluorescence microscopy to track and analyze the motion of probe particles in the walls.

4.3.4: Effect of macroscopic stress on particles: Single particle tracking study

Single particle tracking (SPT), as outlined in Chapter 3, is used to probe the dynamics of particles embedded in scaffolds which are deformed to various strain levels. Particle dynamics gives us insights into the local environment around the particle. The use of particle tracking to characterize local mechanical properties is well established in various fields from biology to food to composites.[34] In elastic and plastic scaffolds, particles are held in a crosslinked polymer mesh. Therefore, studying particle dynamics allows us to directly probe how the response of the crosslinked polymer that holds the particles in the assembly.

We prepare scaffolds that incorporate a sparse concentration of size matched fluorescent polystyrene (FPS) probe particles with the silica particles. Probe particles are negatively charged and are incorporated into the scaffold walls in the same way as the silica particles. Therefore, these fluoro-probes are an integral part of the pore walls. We cut a thin piece of scaffold using a sharp surgical blade and place it on a coverslip for imaging. Samples were subjected to controlled stress by loading them by placing a known weight on the coverslip (Figure 4.15). We estimated the stress imposed on the sample from the weight and the sample dimensions. From the stress-

strain data from rheometery, we calculate the strain corresponding to that stress (Table 4.2).

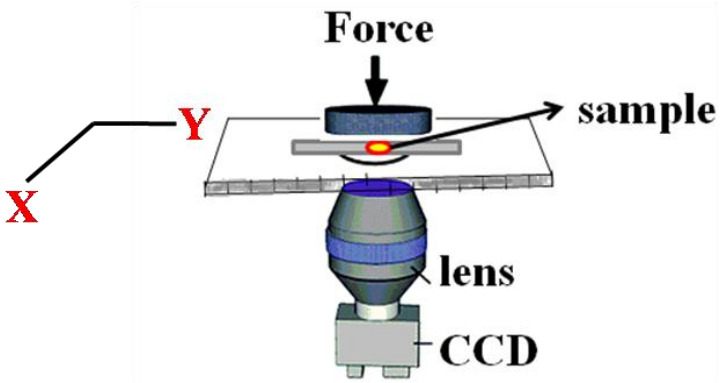

Figure 4.15: Schematic of the experimental setup used for epifluorescence imaging of scaffolds under compression.

Table 4.2: Calculation of strain experienced by the material at known stress values. During epifluorescence imaging, material experiences a known stress value and we obtain the corresponding strain value from the σ–ε curve from bulk studies using a rheometer.

Stress (kPa)	Strain from bulk compression-expansion study (%)	
	Elastic sponge	Plastic monolith
0	0	0
5.47	~ 30	~ 35
10.29	~ 40	~ 50
17.69	~ 50	~ 60

In situ imaging of the compressed sample was done using epifluorescence microscopy. We capture a sequence of images for 10 min at 1 frame/s. We subtract the background from these images and see FPS as bright spots against a dark background (Figure 4.16a,e). As described in Chapter 3, we track the center-of-mass position of the particles in the plane perpendicular to the loading direction (XY plane) using the centroid algorithm. Thus, for each series of images, we obtain X and Y displacements of the particles with reference to an arbitrarily chosen coordinate system centered at the particle. We observe that the trajectories of particle motions in a frame are correlated (Figure 4.16b,f).

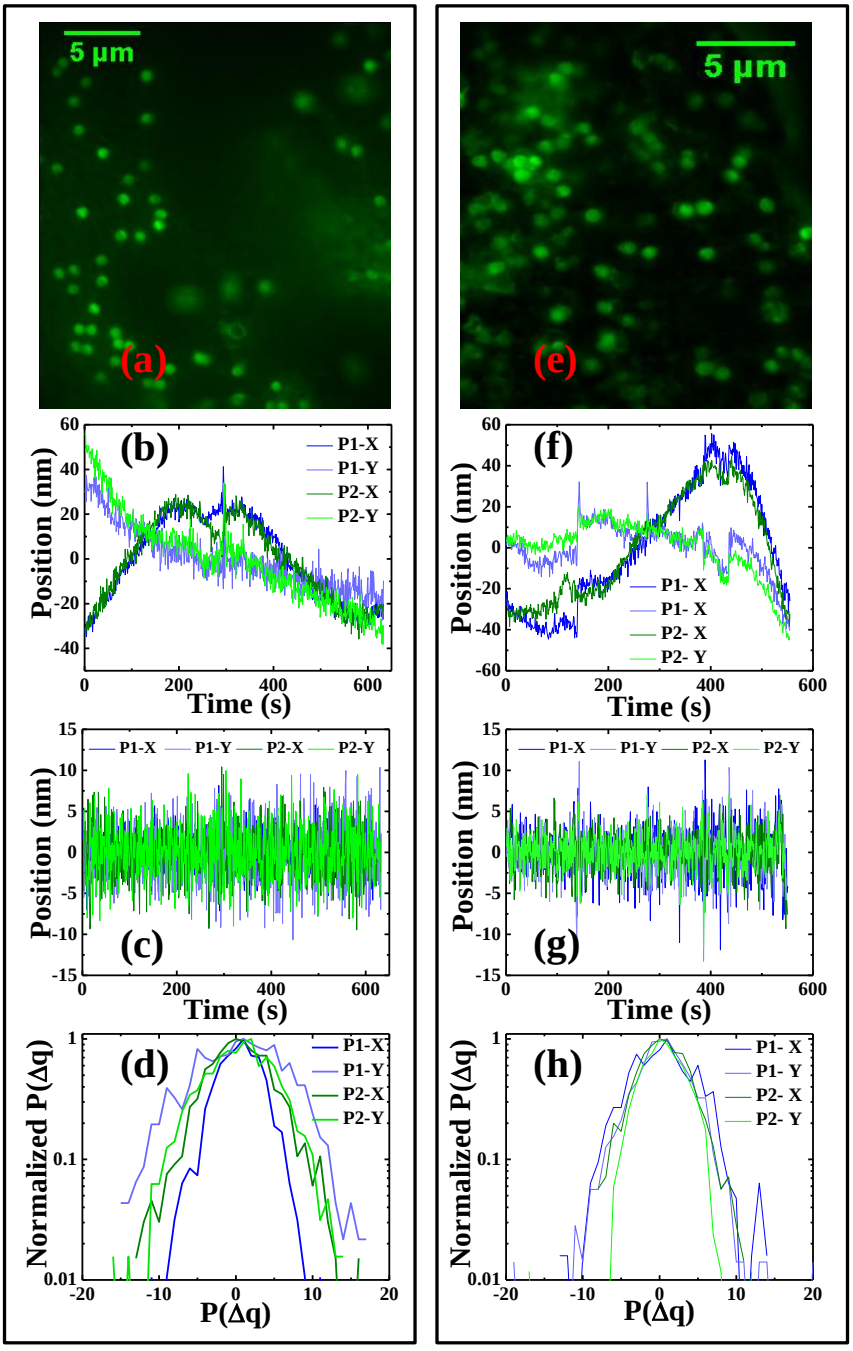

Figure 4.16: Single particle tracking experiment performed on elastic sponge at 30% and plastic monolith at 35% compressive strains. Here, we show the tracking of two representative particles from elastic and plastic samples. (**a,e**) Epifluorescence microscopy image, (**b,f**) particle motion along the arbitrary X and Y coordinates as a function of time, (**c,g**) particle position as a function of time after the elimination of stage drift using wavelet transform. Here, scale 1-5 represents high frequency signal and 6-11 represents low frequency signal. (**d,h**) van Hove jump distribution for particles along the arbitrary X and Y coordinates of elastic and plastic samples respectively.

As discussed in Chapter 3, correlated motion arises from imaging artifacts including stage drift, temperature fluctuation and laser intensity fluctuations. Therefore, these artifacts need to be eliminated to obtain the true thermal motions of the imaged particles. In Chapter 3, we have demonstrated that we can use wavelet transforms to eliminate this artifact. We deconvolute the raw data into a series of time/ frequency scales that allow us to clearly separate the drift from thermal motions. Using a Daubechies wavelet (Daub4)[35] with a threshold value of i = 5 (details in Chapter 3), we can separate the microscopy artifacts (that are carried in the low frequency signals, scales 6-11) from the actual particle dynamics (high frequency range, scales 1-5). This wavelet-filtering methodology appears to work for all our imaging experiments and affords a dynamic resolution of ~ 2 nm.

After obtaining the actual particle trajectory, we calculated the van Hove jump distribution.[36] Here, we calculate the "jumps" made by the particle over a time interval of 1s, along arbitrary X and Y coordinates by using the equation, $\Delta q = (q_{i+t} - q_i)$, where q is the X or Y coordinate and t is the step time (Figure 4.17d,h). We obtain the van Hove jump distribution for multiple particles present at various spatially separated locations in the scaffold.

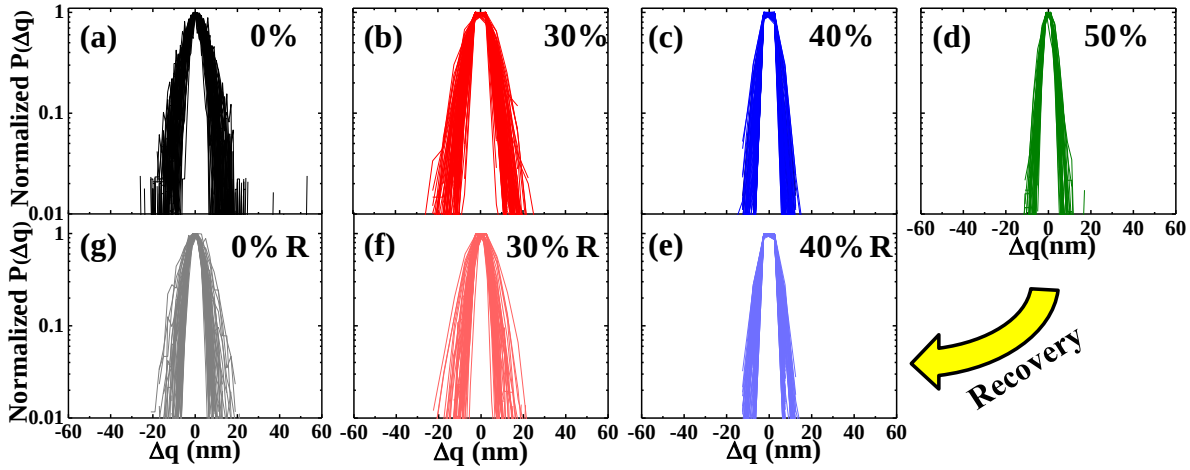

Figure 4.17: van Hove jump distribution of particles in elastic sponges at different % of compressive strains. Data at **(a)** 0% **(b)** 30% **(c)** 40% **(d)** 50% during compression of the scaffold and at **(e)** 40% **(f)** 30% and to **(g)** 0% after loading is released.

The van Hove jump distribution of elastic sponge showed a Gaussian distribution (Figure 4.17). The width of Gaussian distribution at $P(\Delta q) = 10^{-2}$, reduced with increase in strain (Figure 4.17a-d). The variance of jump distribution is related to the short time particle diffusivity.[36] Therefore, we fitted each individual jump distribution

to a Gaussian function and obtained the particle diffusivity. For elastic sponges, the distribution of particle diffusivities did not show any significant variation when the compressive strain is increased from 0 (4.55 nm^2/s– 40 nm^2/s, width of the distribution ≈ 28 nm^2/s and maximum ≈ 20 nm^2/s) to 30% (6 nm^2/s – 45 nm^2/s, width of the distribution ≈ 25 nm^2/s and maximum ≈ 19 nm^2/s) (Figure 4.18a). This is consistent with our observations of changes in porosity and pore size distribution from microstructural studies. Therefore, the stress developed in the pore walls for a nominal compressive strain of 30% (corresponding to ≈ 5 kPa) does not affect local environment for motion of particles embedded in the pore walls. However, further increase in strain to 40 and 50% resulted in reduction in particle diffusivity (at 40%: diffusivities were in the range of 1.35 nm^2/s– 30 nm^2/s, width of the distribution ≈ 7 nm^2/s and maximum ≈ 6 nm^2/s and at 50%: diffusivities were in the range of 2.6 nm^2/s– 15 nm^2/s, width of the distribution ≈ 6 nm^2/s and maximum ≈ 5 nm^2/s, Figure 4.18a).

We have also calculated the mean square displacement (MSD) for each particle from its trajectory ($\{\vec{r}(t_i)\} = \{x(t_i), y(t_i); i = 1,2 \ldots\}$) using the equation:[37]

$$\langle \Delta r^2(\tau) \rangle = \langle [\vec{r}(t_i + \tau) - \vec{r}(t_i)]^2 \rangle$$

where, $\vec{r}(t_i)$ and $\vec{r}(t_i + \tau)$ are positions of the particles at time t_i and $t_i + \tau$ respectively. To ensure reliability of the calculated MSD, we base our calculation only on lag times (τ) upto 5% of the total number of frames acquired. In Chapter 3, we have seen that the particles in an elastic sponge undergo subdiffusive motion. This was confirmed from MSD curves where we see an initial linear regime followed by a plateau. This is intuitive: while the particles can exhibit Brownian motion, there cannot be large scale motion of particles trapped within a crosslinked polymer mesh. We now explore how the imposition of compression affects the particle MSD. At 0% strain, the MSD for particles at multiple locations in the sample showed a plateau in the range of 3– 100 nm^2/s, with most particles showing a plateau in the range of 3-55 nm^2/s (Figure 4.18b). The MSD did not show any appreciable change when strain was increased to 30% (plateau MSD ~ 5– 55 nm^2/s). However, further increase in strain to 40 and 50% showed a reduction in the MSD plateau to 3– 20 nm^2/s and 2.5– 14 nm^2/s respectively. This indicates that the spatial extent of particle motion in the pore walls decreases with increase in strain above 30%. We have already seen that above 30% strain, the stress-strain curve shows a plateau due to elastic buckling of the pore walls.

We believe that the pore wall buckling is the reason for the reduction in particle mobility. However, the applied strain does not influence the particle mobility in the low strain region where E^* scales linearly with ρ_r. Here, the pore walls thicken during compression and there is only a slight shift in the pore size distribution compared to 0% strain (see Figure 4.10e).

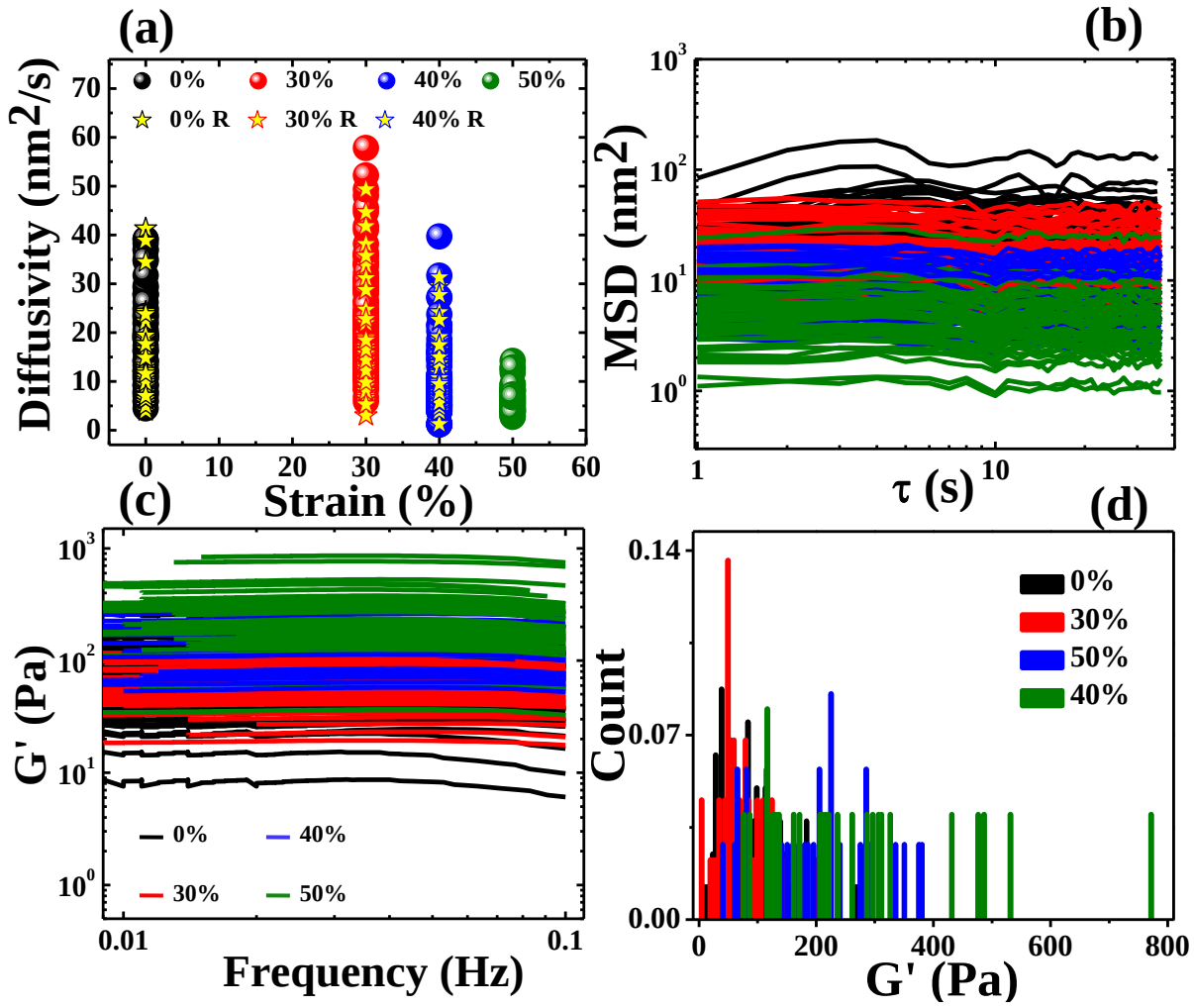

Figure 4.18: Local mechanical properties of elastic sponge while compressing to various strains and on releasing the load. **(a)** Short time particle diffusivity during compression and releasing the load (labeled with 'R' notation). **(b)** MSD and **(c)** local storage moduli ($G^{'}$) calculated for multiple particles tracked from various locations of the sample. (**d**) Distribution of $G^{'}$ values corresponding to 0.04 Hz frequency.

We also use the MSD to calculate the local elastic modulus ($G^{'}$) of pore walls using the generalized frequency dependent form of the Stokes-Einstein equation (Figure 4.18c).[38] We calculate the complex shear modulus ($G^*(\omega)$) using:

$$G^*(\omega) = \frac{k_B T}{\pi a i\omega \mathfrak{L}_u \langle \Delta r^2(\tau) \rangle}$$

where, k_B is the Boltzmann constant, T is the temperature, a is the probe dimension, $\mathfrak{L}_u$ is the unilateral Fourier transform and is effectively a Laplace transform generalized for a complex frequency $i\omega$. The complex shear modulus can be written as the sum of real ($G'(\omega)$) and imaginary ($G''(\omega)$) components; $G^*(\omega) = G'(\omega) + iG''(\omega)$ and thus we obtain local elastic modulus, $G'(\omega)$. These calculations are performed using micrheo.pro code developed by Mason and Weitz.[38, 39]

We observe that the local storage moduli are frequency independent at all strain values (Figure 4.18 c,d). There was no significant difference between the moduli at strain = 0% and 30%. For example, at 0.04 Hz frequency, the unstrained sample shows local G' in the range of 10-270 Pa with a width in stress distribution of 150 Pa. Similarly, at 30% strain, we observe G' in the range of 5-200 Pa with distribution width ~ 97 Pa (Figure 4.18d). However, further increase in strain to 40% resulted in an increase in G'. For example, at 0.04 Hz, G' shows a distribution in the range of 40-390 Pa with a width of ~ 230 Pa. At 50% strain, G' is further increased to 75-775 Pa with a width of 250 Pa. This suggests that the particle motion in pore walls become increasingly restricted with increase in strain beyond 30%. We speculate that this could arise from the buckling and collapse of pore walls at larger strains. This might result in significant distortion of the crosslinked polymer in the interparticle regions. Therefore, particle experiences a rigid local environment that restricts its motions.

We also examined particle diffusivity during the release of strain (Figure 4.17e-g and Figure 4.18a) and imaged samples 20 min after release of load. We observe that particle diffusivity recovers to its original unstrained value after release in stress, indicating complete recovery in the local environment experienced by the particles in the walls.

This data reinforces our picture for the origin of elasticity in our scaffolds. Crosslinked polymer bridges connect particles that make up the pore walls and provide elasticity to the system. They prevent the failure of the particle network upon compression and allow reversible folding of the walls under large compression. During the release of load, these elastic bridges act like springs and allow elastic recovery of the scaffold.

Similarly, we have performed single particle tracking study on plastic monoliths. We have calculated the van Hove jump distribution of plastic monolith at stresses of 0, 5.5, 10.3 and 17.7 kPa, corresponding to compressive strains of approximately 0, 35,

50 and 60%, respectively (Figure 4.19a-d). Short time particle diffusivities were calculated for multiple particles by fitting the jump distributions to a Gaussian form. We obtained a heterogeneous distribution of particle diffusivities (range of diffusivity: 10 nm^2/s– 160 nm^2/s, width of the distribution ≈ 65 nm^2/s peaked at ≈ 57 nm^2/s) at 0% strain (Figure 4.20a). Increase in strain to 35 and 50% led to a reduction in particle diffusivity (35%: diffusivity ranges from 1.3 nm^2/s – 45 nm^2/s, width of the distribution ≈ 10 nm^2/s and peak ≈ 12 nm^2/s and 50%: diffusivity ranges from 2.1 nm^2/s – 33 nm^2/s with width of the distribution ≈ 9 nm^2/s and peak ≈ 12 nm^2/s, Figure 4.20a). Further compression to 60% showed a rapid enhancement in diffusivity of particles located at certain locations such that the overall diffusivity ranged from 2.5–130 nm^2/s (with width ≈ 30 nm^2/s and peak ≈ 22 nm^2/s). Additionally, particle diffusivity further increased to 2.5– 160 nm^2/s (with width ≈ 30 nm^2/s and peak ≈ 21 nm^2/s) when the load was released so that the strain decreased to 50%. Release of strain to 35 and 0% did not result in any further change in diffusivity from 50% strain. This behaviour is apparent in the jump distribution plot as well (Figure 4.19e-g). We note that microscopy images during the unloading cycle were always captured starting 20 min after load was released.

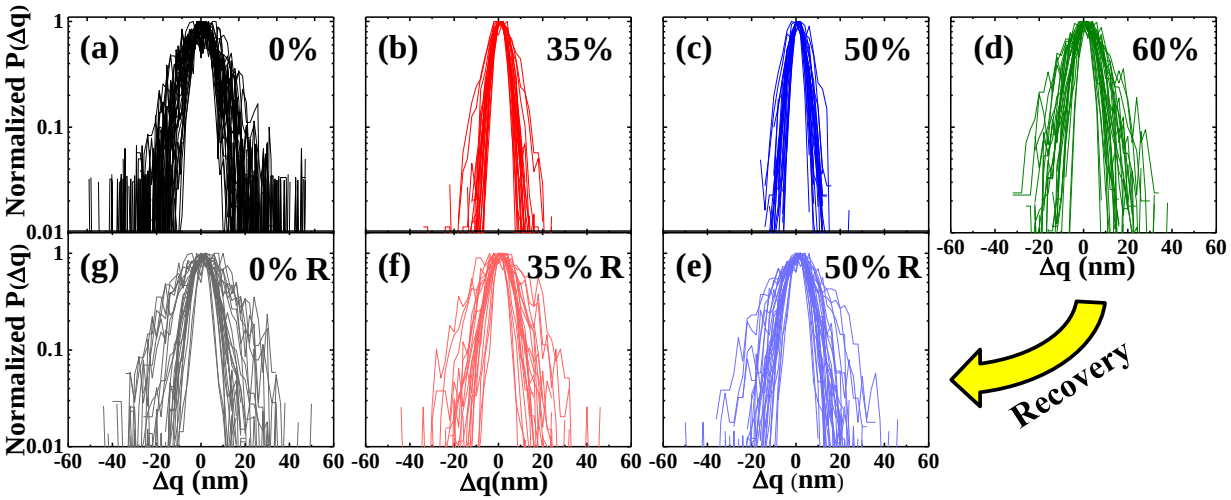

Figure 4.19: van Hove jump distribution of particles in plastic monoliths at different % of compressive strains. (**a**) 0% (**b**) 35% (**c**) 50% (**d**) 60% and during the release of strain to (**e**) 50% (**f**) 35% and to (**g**) 0%.

The MSD exhibited wide heterogeneity at 0% strain (from 7– 1000 nm^2/s, Figure 4.20b) and reduced to 7– 44 nm^2/s and 3– 27 nm^2/s on compressing the sample to 35

and 50% strains, respectively. However, at 60% strain MSD increased to 6– 200 nm^2/s. This indicates an enhancement in particle mobility at 60% strain.

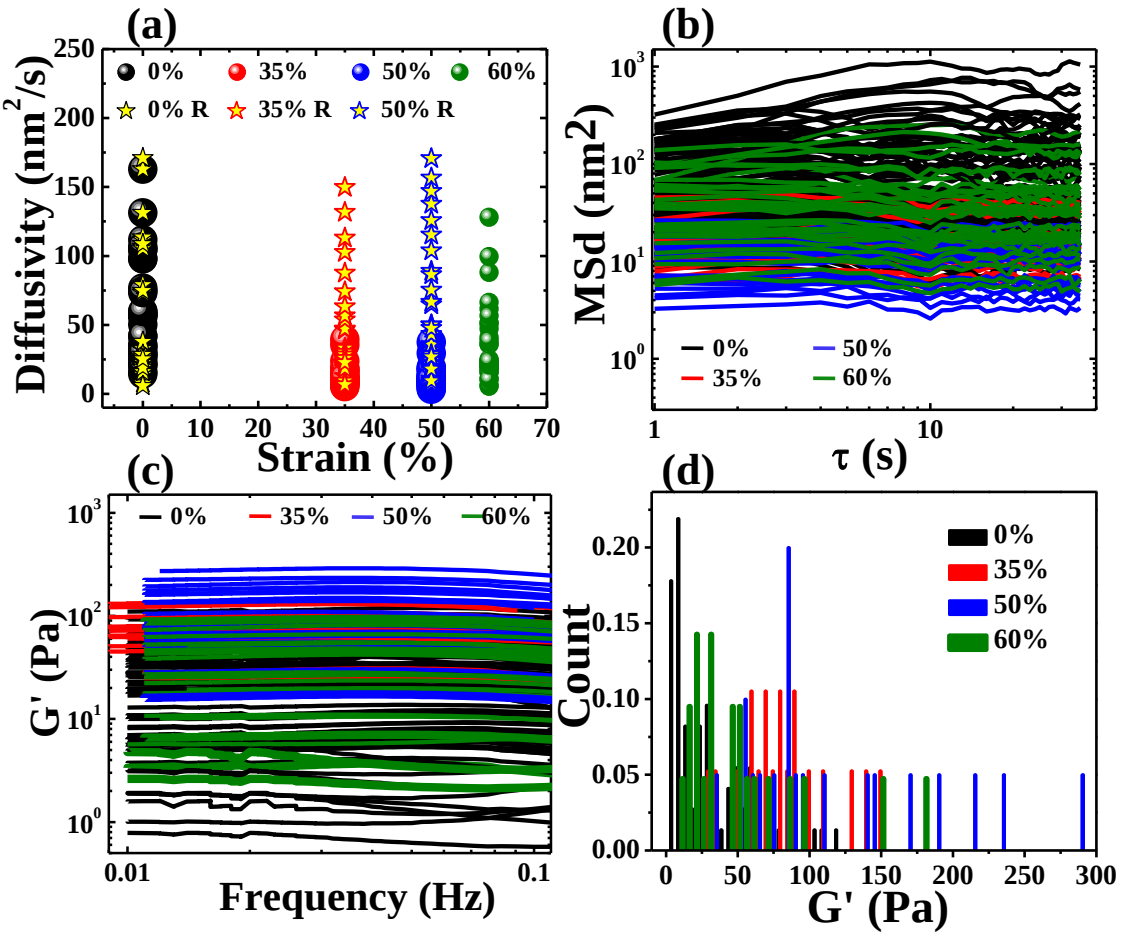

Figure 4.20: Local mechanical properties of plastic monolith while compressing to various strains and releasing the load. **(a)** Short time particle diffusivity during compression and releasing the load (labeled with 'R' notation). **(b)** MSD and **(c)** Local storage moduli (G') calculated for multiple particles from various locations of the sample. (**d**) Distribution of G' values corresponding to 0.04 Hz frequency.

We have also calculated the local storage moduli (G') from MSD (Figure 4.20c,d). At 0% strain, the plastic monolith exhibits a distribution ranging over nearly two orders of magnitude in G' from 5-120 Pa with a peak ~ 10 Pa and width ~ 27 Pa (Figure 4.20d). This range is lower when compared with the elastic sponges (10– 270 Pa with G' peaked at ~ 40 Pa). At 35% strain, the heterogeneity is reduced with a G' distribution in the range of 30– 150 Pa with peak in the range of 60-90 kPa. We also notice that the lower range of G' shifted to higher values compared to 0% strain. The increase in strain to 50% gave a peak in G' ~ 85 Pa and distribution in the range of 35–

290 Pa with width ~170 Pa. At 60% strain, the maximum G' is ~ 25Pa with an overall G' distribution in the range of 10– 180 Pa and width ~ 100 Pa.

Microstructural study had shown that at 30%, pore walls collapse and these collapsed cell walls start densifying at larger strains. The reduction in particle diffusivity and enhancement on storage modulus could be due to the densification of broken pore walls. Additionally, we observed crack growth within pore walls with increase in strain. At 50% strain, we saw cracks with tens of microns length and at 60% strain crack length became hundreds of microns. At 60% strain, cracks result in complete failure of the pore walls, and in fragmentation of the pore walls into individual smaller pieces. At 60%, the enhanced diffusivity of certain particles at some locations is comparable to the 0% strain case. This could be because the crack has relieved the local stress and therefore the sample (locally) is stress free, viz. not under strain. Cracking of pore walls leads to reduction in compressive strength. Therefore, from 30% strain onwards; the maximum compressive stress is less in plastic monoliths compared to elastic. This shows that the origin of plasticity in materials crosslinked in absence ice crystals arises at the particle level, from interparticle bridges.

Therefore, our study shows that the mechanical property of particle- polymer hybrid structure is set by the interparticle linkages. Crosslinking of hybrid in presence of ice crystals gives elastic bridges which makes the particle assembly highly compressible. However, crosslinking in absence of ice crystals leads to weak regions in the scaffolds and these weak points in the scaffold fail under compression – therefore the entire assembly fails.

4.4 Summary

We have studied the cellular mechanics of ice templated isotropic inorganic particle-polymer hybrid systems. Based on the crosslinking protocol we obtained two different hybrid materials. Static structure of these two materials are identical, viz. both are indistinguishable in terms of its pore morphology, porosity, foam density and inter particle spacing. However, the response to these materials to dynamic load was qualitatively different. Crosslinking of hybrid in presence of ice crystals leads to super elastic sponge which can recover from large compressive strains (~80%). However, the hybrid crosslinked in absence of ice crystals showed plastic behaviour and fractures at small compressive strains. During compression, elastic sponge did not

show any structural change upto 30% strain. Further increase in strain gave a plateau in the stress-strain curve due to elastic buckling. Beyond 50% strain, buckling and densification of pore walls gave a steep increase in stress. Particles which are present in pore walls are affected by these changes in the pore wall. Their mobility decreases and the local storage moduli around the particles increase beyond 30% strain. During the release of stress, the particles recover their initial diffusivity. Our study showed that crosslinked polymer bridges allow the folding of pore walls beyond 30% strain and during release of load these elastic bridges push the pore walls back to its initial configuration. However, plastic monoliths showed collapse of pore walls around 30% strain and further increase in strain lead to the densification of collapsed pore walls. Beyond 50% strain, we observed significant crack propagation within the pore walls which led to a reduction in pore wall stiffness. Moreover, failure of pore walls gave a lower densification stress to plastic monoliths compared to elastic sponges.

Our study shows that the flexible interparticle linkages prevent brittle failure of inorganic particle assemblies. Crosslinking of polymer in presence of ice crystals is important to obtain flexible bridges in ice templated particle- polymer hybrids.

4.5 References

1. Gibson, L. J.; Ashby, M. F.; Harley, B. A., *Cellular materials in nature and medicine*. Cambridge University Press: **2010**.

2. Lakes, R., Materials with structural hierarchy. *Nature* **1993,** 361, 511.

3. Bitzer, T. N., *Honeycomb technology: Materials, design, manufacturing, applications and testing*. Springer Science & Business Media: **2012**.

4. Lakes, R., Advances in negative Poisson's ratio materials. *Adv. Mater.* **1993,** 5, 293-296.

5. Prud'homme, R., *Foams: Theory: Measurements: Applications*. Routledge: **2017**.

6. Gibson, L. J.; Ashby, M. F., *Cellular solids: Structure and properties*. Cambridge University Press: **1999**.

7. Colombo, P., Conventional and novel processing methods for cellular ceramics. *Philos. Trans. A Math. Phys. Eng. Sci.* **2006,** 364, 109-124.

8. Inagaki, M.; Qiu, J.; Guo, Q., Carbon foam: Preparation and application. *Carbon* **2015,** 87, 128-152.

9. Gibson, L. J., Biomechanics of cellular solids. *J. Biomech.* **2005,** 38, 377-399.

10. Deville, S., *Freezing colloids: Observations, principles, control, and use: applications in materials science, life science, earth science, food science, and engineering*. Springer: **2017**.

11. Deville, S., Ice-templating, freeze casting: Beyond materials processing. *J. Mater. Res.* **2013,** 28, 2202-2219.

12. Lasalle, A.; Guizard, C.; Maire, E.; Adrien, J.; Deville, S., Particle redistribution and structural defect development during ice templating. *Acta Mater.* **2012,** 60, 4594-4603.

13. Zhou, K.; Zhang, Y.; Zhang, D.; Zhang, X.; Li, Z.; Liu, G.; Button, T. W., Porous hydroxyapatite ceramics fabricated by an ice-templating method. *Scr. Mater.* **2011,** 64, 426-429.

14. Deville, S., Freeze-casting of porous ceramics: A review of current achievements and issues. *Adv. Eng. Mater.* **2008,** 10, 155-169.

15. Gutierrez, M. C.; Ferrer, M. L.; del Monte, F., Ice-templated materials: Sophisticated structures exhibiting enhanced functionalities obtained after unidirectional freezing and ice-segregation-induced self-assembly. *Chem. Mater.* **2008,** 20, 634-648.

16. Qian, L.; Ahmed, A.; Foster, A.; Rannard, S. P.; Cooper, A. I.; Zhang, H., Systematic tuning of pore morphologies and pore volumes in macroporous materials by freezing. *J. Mater. Chem.* **2009,** 19, 5212-5219.

17. Deville, S.; Viazzi, C.; Leloup, J.; Lasalle, A.; Guizard, C.; Maire, E.; Adrien, J.; Gremillard, L., Ice shaping properties, similar to that of antifreeze proteins, of a zirconium acetate complex. *PloSOne* **2011,** 6, e26474.

18. Seuba, J.; Deville, S.; Guizard, C.; Stevenson, A. J., Mechanical properties and failure behavior of unidirectional porous ceramics. *Sci. Rep.* **2016,** 6, 24326.

19. Munch, E.; Saiz, E.; Tomsia, A. P.; Deville, S., Architectural control of freeze-cast ceramics through additives and templating. *J. Am. Ceram. Soc.* **2009,** 92, 1534-1539.

20. Warren, W. E.; Kraynik, A. M., The linear elastic properties of open-cell foams. *J. Appl. Mech.* **1988,** 55, 341-346.

21. Gibson, L. J., The mechanical behaviour of cancellous bone. *J. Biomech.* **1985,** 18, 317-328.

22. Gibson, L. J.; Easterling, K. E.; Ashby, M. F., The structure and mechanics of cork. *Proc. R. Soc. Lond. A* **1981,** 377, 99-117.

23. Gent, A. N.; Thomas, A. G., Mechanics of foamed elastic materials. *Rubber Chem. Technol.* **1963,** 36, 597-610.

24. Hilyard, N. C.; Cunningham, A., *Low density cellular plastics: Physical basis of behaviour*. Springer Science & Business Media: **2012**.

25. Ojuva, A.; Akhtar, F.; Tomsia, A. P.; Bergstrom, L., Laminated adsorbents with very rapid CO2 uptake by freeze-casting of zeolites. *ACS Appl. Mater. Interfaces* **2013,** 5, 2669-2676.

26. Porter, M. M.; Imperio, R.; Wen, M.; Meyers, M. A.; McKittrick, J., Bioinspired scaffolds with varying pore architectures and mechanical properties. *Adv. Funct. Mater.* **2014,** 24, 1978-1987.

27. Isobe, T.; Kameshima, Y.; Nakajima, A.; Okada, K.; Hotta, Y., Gas permeability and mechanical properties of porous alumina ceramics with unidirectionally aligned pores. *J. Eur. Ceram. Soc.* **2007,** 27, 53-59.

28. Bauer, J.; Hengsbach, S.; Tesari, I.; Schwaiger, R.; Kraft, O., High-strength cellular ceramic composites with 3D microarchitecture. *PNAS* **2014,** 111, 2453-2458.

29. Rambo, C. R.; Andrade, T.; Fey, T.; Sieber, H.; Martinelli, A. n. E.; Greil, P., Microcellular Al2O3 ceramics from wood for filter applications. *J. Am. Ceram. Soc.* **2008,** 91, 852-859.

30. Scotti, K. L.; Dunand, D. C., Freeze casting-A review of processing, microstructure and properties via the open data repository, FreezeCasting.net. *Prog. Mater. Sci.* **2018,** 94, 243-305.

31. Nussinovitch, A.; Velez-Silvestre, R.; Peleg, M., Compressive characteristics of freeze-dried agar and alginate gel sponges. *Biotechnol. Prog.* **1993,** 9, 101-104.

32. Rajamanickam, R.; Kumari, S.; Kumar, D.; Ghosh, S.; Kim, J. C.; Tae, G.; Sen Gupta, S.; Kumaraswamy, G., Soft colloidal scaffolds capable of elastic recovery after large compressive strains. *Chem. Mater.* **2014,** 26, 5161-5168.

33. Greaves, G. N.; Greer, A. L.; Lakes, R. S.; Rouxel, T., Poisson's ratio and modern materials. *Nat. Mater.* **2011,** 10, 823.

34. Saxton, M. J., Single particle tracking. In *Fundamental Concepts in Biophysics*, Springer: **2009**; pp 1-33.

35. Daubechies, I., *Ten lectures on wavelets*. Siam: **1992**; Vol. 61.

36. Hopkins, P.; Fortini, A.; Archer, A. J.; Schmidt, M., The van Hove distribution function for Brownian hard spheres: Dynamical test particle theory and computer simulations for bulk dynamics. *J. Chem. Phys.* **2010,** 133, 224505.

37. Bhattacharya, S.; Sharma, D. K.; Saurabh, S.; De, S.; Sain, A.; Nandi, A.; Chowdhury, A., Plasticization of poly (vinylpyrrolidone) thin films under ambient humidity: Insight from single-molecule tracer diffusion dynamics. *J. Phys. Chem. B* **2013,** 117, 7771-7782.

38. Mason, T. G., Estimating the viscoelastic moduli of complex fluids using the generalized Stokes-Einstein equation. *Rheol. Acta* **2000,** 39, 371-378.

39. Mason, T. G.; Weitz, D. A., Optical measurements of frequency-dependent linear viscoelastic moduli of complex fluids. *Phys. Rev. Lett.* **1995,** 74, 1250.

Chapter 5

Elastic and Plastic Scaffolds: The Role of Organic Content

We have seen that the protocol adopted for crosslinking of ice templated particle-polymer composites affects their mechanical properties. Crosslinking of composite in presence of ice crystals leads to the formation of supercompressible sponge despite being primarily composed of particles. However, crosslinking in absence of ice crystals gives a material which undergoes plastic failure even at small deformations. Our single particle tracking and atomic force microscopy studies showed that crosslinking in absence of ice crystals leads to greater heterogeneity in the distribution of local crosslinking density. It is not clear how the ice or air in the particle packing voids influences the crosslinking of these hybrid systems. This chapter addresses this question. Here, we systematically vary the organic to particle ratio in the scaffold by keeping the total solid concentration fixed. We further study the structure, dynamics and mechanical properties of these scaffolds.

5.1 Introduction

The solidification or freezing of colloidal suspension or colloids is commonly encountered in a variety of natural processes such as the growth of sea ice[1] and freezing of soil in cold conditions[2] or in everyday life and engineering situations such as filtration or purification of water,[3] food engineering[4] and cryobiology[5]. It also has implications in various materials engineering processes such as the processing of porous materials using the freezing of colloidal dispersions though a process known as ice templating.[6] This is a well established processing technique for preparing porous ceramics and also for porous hybrid systems including inorganic-polymer porous materials.[7]

Ice templating is a process of segregation of matter by growth of ice crystals in an aqueous dispersion. The removal of ice provides a macroporous scaffold where the pores are replicas of ice crystals. Moreover, organization of matter in the scaffold takes place during freezing.[7] Recently, Rajamanickam et al. have used this method to make a versatile sponge from inorganic particles and polymer.[8] Briefly, they have ice templated an aqueous dispersion containing negatively charged inorganic particles, oppositely charged polymer and crosslinker. This dispersion was freeze casted at -18^{o}C for a day. At this temperature, ice crystals grow isotropically within the system. During this 24 hour period, the polymer reacts with crosslinker and forms a three dimensional self standing scaffold with the walls templating ice crystals. The pores were in the range of 30 to 120 μm and the pore walls were comprised of particles and crosslinked polymer. Polydisperse spherical particles exhibited random close packing in the pore walls. In Chapter 3, we have seen that these particles are enmeshed in a thin crosslinked polymer film (small angle X-ray scattering of scaffolds with particle to polymer ratio 1:0.05 showed a film thickness of about 1 nm). The most interesting feature of this scaffold is its elasticity: it can recover from large compressive strain (> 80% strain) eventhough these sponges are comprised primarily of particles (90 wt% inorganic particles). Moreover, such elastic sponges can be prepared using a wide variety of particles, polymers, crosslinkers and crosslinking chemistry. This versatility opens up wide applications for these sponges. Chatterjee et al. had shown that such sponges are promising materials for fire retardant foam applications[9] and as compressible energy storage devices[10].

In Chapter 2, we have seen that crosslinking of scaffolds in the frozen state is essential to obtain these elastic sponges. We had shown that the crosslinking of

scaffolds after the removal of ice crystals by lyophilisation gives a material which undergoes plastic failure even at small compression (~5% strain). The two scaffolds, viz., elastic and plastic, were identical in terms of their Young's modulus, porous morphology, particle organization in pore walls (identical interparticle distance) and overall crosslinking. However, plastic monoliths exhibit higher local heterogeneity in contrast to elastic sponges. The local storage moduli from microrheology showed a distribution over two orders of magnitude in comparison to a relatively narrow distribution (within an order of magnitude) for elastic sponges. We ascribed this heterogeneity in local storage modulus (G′) to the local crosslinking density. In plastic scaffolds, some regions are weakly crosslinked and therefore exhibit a lower G′ value compared to the tightly crosslinked regimes. Amplitude modulation-atomic force microscopy (AM-AFM) also showed a similar heterogeneity in the interparticle regions (probed using a cantilever tip of size ~ 6-8 nm) of plastic scaffolds. Therefore, our study showed that crosslinking in presence of ice crystals is essential to obtain elastic sponges. However, it is not clear how the presence of 30-120 μm ice crystals influences the crosslinking reaction. In this Chapter, we address this question by investigating the effect of interparticle packing voids in the pore walls on the mechanical properties of elastic and plastic scaffolds. Before discussing the experimental protocol employed, we will review the literature on water in the packing voids during ice templating; freezing of this water and how this freezing changes with the presence of polymer in it.

The process of segregation and concentration of particles during ice templating has been studied using optical[11], confocal[12] and transmission electron microscopy[13] and using X-ray imaging techniques[14]. Dedovets and Deville studied the growth of ice crystals, redistribution of particles as well as the late stages of freezing when ice invades the pores between concentrated particles using confocal microscopy.[12] They have performed in-situ freezing experiments under confocal microscope using 2 μm diameter fluorescent polymethyl methacrylate (PMMA) particles dispersed in water containing a fluorescent dye with a different excitation wavelength. They made several observations about the development of microstructure when they froze dispersions with an ice front growth rate of 20 μm/s and with a temperature gradient of 5 ^{o}C/min maintained over a 2 mm length scale. They observe that isolated particles were engulfed by the growing crystal and they did not see any liquid film around the

particles. They state that there is the possibility of a liquid film with few nanometer thicknesses around the particles. Local defects in particle packing result in smaller pores (smaller than macropores) of different sizes between the particles in the pore walls. They were able to resolve packing voids in the size range of 500 nm to 1μm. They showed that water freezes in these packing voids. The water in the pores between closely packed particles showed depression in freezing point and did not freeze at the temperature at which water froze in the voids of random close packing. Therefore, the freezing temperature is lower as the pore size decreases. Next we will see how pore size affects the freezing point of a liquid in a pore.

Water in small pores will freeze at sub-zero temperatures.[15, 16] Ashworth et al. had studied the freezing of water in small diameter pores.[17] In their study, dynamic thermal analysis of water saturated, porous glass particles with 7.5 nm diameter pores showed a broad exotherm between -9 and -15^{o}C with a large exotherm between -5 to -10^{o}C. The large exotherm corresponds to the freezing of bulk water surrounding the glass particles. Water in the 7.5 nm diameter pores remained liquid for 24h at -10^{o}C and would not freeze until further cooled. Water in the 7.5 nm pores froze between -10 and -15^{o}C. The melting point of water in 300 and 150 nm diameter pores was about 0^{o}C. Reduction in freezing point was observed only for water in pores with a diameter of less than 100 nm.

Homshaw[18] and Mazur[19] have theoretically predicted the melting point depression with pore diameter. Mazur related the melting point of a fluid (ΔT) to the radius of the pore (r, in Å) as: $\Delta T = -{}^{300\cos\theta}/_{r}$, where θ is the angle of the meniscus within a pore. The relation developed between ΔT and r by Homshaw was $\Delta T = -{}^{470}/_{r}$. Next we will review the effect of polymer and its concentration on the freezing point of water.

Freezing point depression, in general, can be derived from the equilibrium condition between a crystalline solid and a solution of its melt with solute. However, if the solute is a long chain polymer molecule, the freezing point depression also needs to account for the thermodynamic interaction parameter (μ), characteristic of the polymer-solvent pair.[20, 21] Therefore, the freezing point of polymer solution has been expressed as:

$$\left[\frac{1}{T}-\frac{1}{T_0}\right]=-\left[\frac{R}{\Delta H_f}\right]\left\{\ln(1-\vartheta_2)+\left(1-\frac{1}{x}\right)\vartheta_2+\mu{\vartheta_2}^2\right\}$$

where, T is the freezing point of solution, T_0 is the freezing of pure solvent, ΔH_f is the molar heat of fusion of solvent. ϑ_2 is the volume fraction of polymer in solution, x is ratio of molar volumes of polymer and solvent.

It has been reported that there is no significant depression in freezing point for solutions containing upto 10% polymer (by volume).[22] Kawai studied the freezing point depression in various polymer solutions and its dependence on polymer concentration.[22] He varied polyvinyl acetate (viscosity averaged molecular weight, $\overline{M_v}$~ 60 kDa) concentration in benzene from 0 to 10 to 30 vol.% and measured the corresponding freezing point of solutions as 278.65 K , 278.58 K and 277.21 K, respectively. Here, the depression in freezing point is due to the change in thermodynamic interaction parameter (μ). This has been explained in terms of entropic contributions arising mainly from the decrease in polymer chain conformational entropy on freezing of solvent and minor effects from imperfect randomness of mixing and changes in the tightness of coiling with concentration.[23] Similarly, cellulose acetate ($\overline{M_v}$~ 65 kDa) solution in acetic acid showed freezing point depression from T_0=289.85 K to 289.64 K at 4 vol% to 288.35 K at 12 vol% and to 284.73 K at 25.7 vol%. In case of polyvinyl alcohol-water system, the depression in freezing point was from 273.15 K at 0 vol% to 272.98 K at 8 vol% to 272.44 K at 10 vol% and 269.27 K at 25 vol%. Therefore, this study showed that the μ markedly changes with polymer concentration.

In this present work, we investigate how polymer crosslinking is influenced when the polymer is crosslinked in the presence of ice. We crosslink the scaffolds in presence of ice crystals or after the removal of frozen ice using lyophilization. Later, we systematically vary the organic content in both the scaffolds by keeping particle amount and total solid concentration (particle and organic) fixed. We further investigate how the variation in organic loading affects the structure, dynamics and mechanical properties of these scaffolds. Our study shows that, above a critical organic loading, both scaffolds show distinct changes in scaffold morphology, mechanical properties and solvent structure in the scaffold. This critical organic concentration corresponds to the amount required to fill the packing voids in the pore walls.

5.2 Experimental

5.2.1 Materials:

Ludox-TM silica particles (manufacturer specified size = 22 nm) are obtained as a 50% (w/v) dispersion. 1μm silica particles were obtained from Richen Industries (Hong Kong). Deuterium oxide (D_2O, 99.9%), polyethylenimine (PEI, 25 kg/mol) and 1,4-butanediol diglycidyl ether were obtained from Sigma Aldrich. All materials were used as received. The structure of polymer and crosslinker is shown in Figure 5.1.

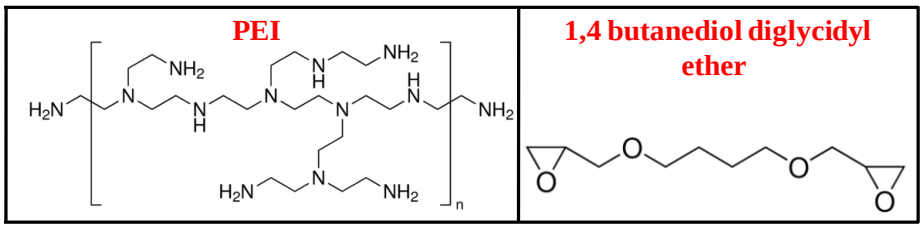

Figure 5.1: Chemical formula of polymer and crosslinker used for scaffold synthesis.

5.2.2 Preparation of scaffolds with varying organic content

60 mg of silica particles (Ludox TM or 1 μm silica particles) was dispersed in deionised (DI) water by sonicating for 30 min. To this was added 'X' mg of PEI stock solution of 10 wt% concentration followed by vortexing it for 10 min. 'Y' mg of crosslinker; 1,4 butanediol diglycidyl ether was added to this dispersion and vortexed for 3 min. Based on this general protocol we have prepared 8 different aqueous dispersions with different organic to particle ratios. The ratios were 0.1, 0.2, 0.25, 0.4, 0.5, 0.75, 1 and 1.5. In these compositions, the 'X' values were 2, 4, 5, 8, 10, 15, 20 and 30 mg respectively. PEI to crosslinker ratio was fixed at 1:2 and the overall solid (i.e. silica particles + organic) concentration was 10 wt% (obtained by adjusting the DI water content). We prepared scaffolds in two different ways using these aqueous dispersions: (i) dispersions were kept at -18^{o}C for 24 h followed by drying of the scaffolds for 10 h using a lyophilizer (LabconcoFreeZone 2.5 Plus, -80^{o}C, 0.1mBar). Here, the polymer-crosslinker reaction takes place in the frozen state, in the presence of ice crystals. (ii) In second case, the dispersions were kept at -18^{o}C for 45 min followed by lyophilisation at -80^{o}C for 10 h. After lyophilisation, samples were transferred back to the freezer (-18^{o}C) for 24 h. Here, the reaction between polymer and crosslinker takes place in absence of ice crystals.

Samples for deuterium solid state NMR were prepared in D_2O rather than DI water and all other steps in the preparation are similar to the aforementioned protocol. Samples were vacuum dried for 24 h at 50^{o}C prior to solid state NMR experiments. Reaction scheme of PEI and 1,4 butanediol diglycidyl ether is shown in Figure 5.2.

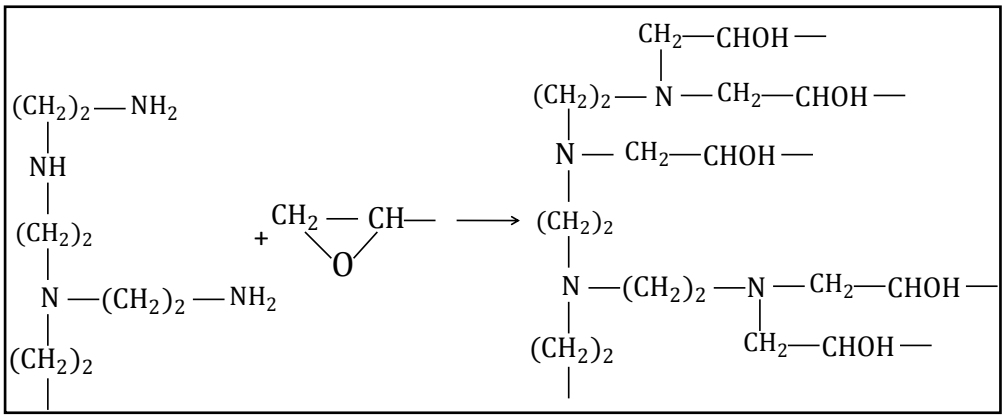

Figure 5.2: Crosslinking reaction of PEI with epoxy containing groups.

5.2.3 Characterization of scaffolds

We have characterised the materials which are crosslinked in presence and absence of ice crystals using small angle X-ray scattering (SAXS), rheometry and solid state nuclear magnetic resonance (NMR).

5.2.3.1 Small Angle X-ray Scattering (SAXS):

Small angle X-ray scattering was performed on a Rigaku system. This instrument is equipped with a micro-focus rotating anode X-ray generator and a confocal max flux mirror, three pinhole collimators and a two dimensional detector (HyPix-3000). The detector is calibrated using silver behenate standard. Experiments were performed at room temperature (~25^{o}C). We performed SAXS on a dilute solution of Ludox silica particles (2 wt%) filled in a capillary tube (diameter 2 mm; wall thickness ~ 10 μm). The data was circularly averaged and the 1D scattered intensity is presented after background subtraction, corrected for sample transmission. SAXS data was analyzed using SASFIT.

5.2.3.2 Rheometry:

Compression/expansion studies on the scaffolds were performed using ARES G2 strain controlled rheometer in a dynamic mechanical analysis measurement mode. Cylindrical samples were placed between two 25 mm diameter roughened parallel plates and 0.5 g pre-load was applied. Samples were compressed to different strains at a constant rate of 0.1 mm/s and the corresponding normal force was measured. Nominal compression stress was calculated by dividing the compressive force with the initial cross-sectional area of the cylindrical sample.

5.2.3.3 ^{1}H and ^{2}H Solid State Nuclear Magnetic Resonance (solid state NMR)

^{1}H solid state NMR: Proton solid state NMR experiments were done on a Bruker AV 700 MHz Avance-III-HD NMR spectrometer equipped with a 1.3 mm double resonance MAS probe. Samples were vacuum dried at 50^{o}C for 24h prior to the

experiments. These dried samples were packed in a 1.3 mm rotor. ^{1}H MAS spectra were recorded at 60 kHz spinning rate using a single 90° excitation pulse. We used pulse lengths of 1.4 μs for proton with 128 transients. In all cases spectra were recorded at room temperature.

^{2}H solid state NMR: Deuterium (^{2}H) solid state NMR experiments were performed on an AV 700 MHz Avance-III-HD NMR spectrometer equipped with a 4 mm double resonance MAS probe, at ^{2}H Larmor frequency 107.47 MHz. ^{2}H NMR experiments were carried out using Hahn Echo pulse sequence with echo delay of 30 μs. Here, the 90° pulse width was 3.5 μs. 64000 transients were used for each sample. Samples for this experiment are made in deuterium oxide (D_2O, 99.9%) as described in the experimental section.

5.3 Results and Discussion

We have ice templated aqueous dispersions having different organic to particle ratio (OP ratio). Here, the ratio was varied from 0.1 to 1.5. For each composition, we crosslinked one sample in the presence of ice and another after lyophilisation to remove the ice crystals. Crosslinking was always performed by storing the sample at -18^{o}C. Three dimensional self standing scaffolds were obtained for all compositions. Here, we will study the effect of OP ratio on structure, dynamics and properties of these scaffolds.

5.3.1 Structural variation with change in OP ratio

We begin by characterising the structure of scaffolds made using Ludox particles with varying organic content. The organization of silica particles in these scaffolds was investigated using small angle X-ray scattering (SAXS). SAXS on a dilute solution of Ludox silica particles (2 wt.%) was fitted to a polydisperse sphere model with Schultz- Zimm size distribution. We obtain a particle radius of 11.09 nm with a polydispersity parameter of 0.14 (Figure 5.3). This is consistent with the manufacturer specified particle diameter of $\approx$ 22 nm.

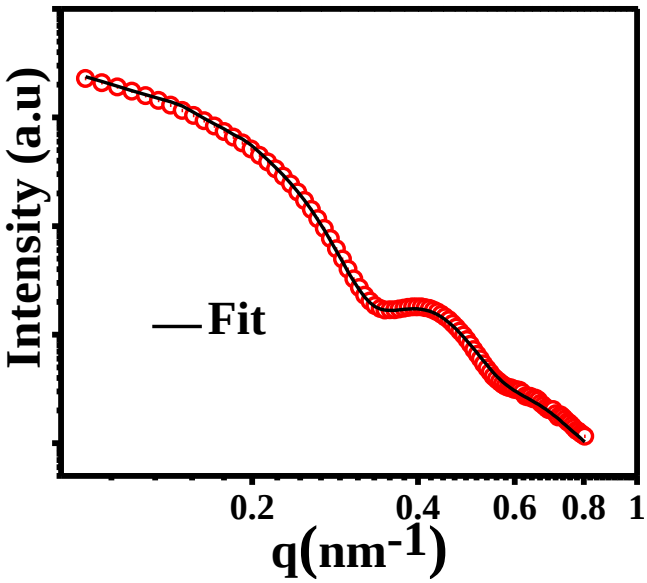

Figure 5.3: Small angle X-ray scattering from a dilute solution of Ludox®-TM silica particles in water (~2 wt.%). Open circles are the experimental data and the solid line is a fit to a polydisperse sphere model.

SAXS from scaffolds prepared using silica nanoparticles show ahump at low q that is not present in the dilute dispersion scattering (Figure 5.4a,c). This comes from particle correlations and represents scattering due to inter-particle interference in dense systems. For scattering from monodisperse spheres, the scattering can be factorized into the form factor for scattering from dilute solutions and a structure factor that represents interparticle interference. These scaffolds comprise of particles that are not monodisperse and are not perfectly spherical. Therefore, here one can calculate an apparent structure factor ($S_A(q)$) by normalizing the SAXS data from scaffolds by scattering from a dilute dispersion of the silica nanoparticles (Figure 5.4b,d). We modeled the first peak of $S_A(q)$ using an interference function which gives the average interparticle distance in the pore walls (Figure 5.5). The interference function is expressed as:

$$S_A(q) = A_2[1 + k\emptyset(q)]^{-1} \qquad \text{(Eq.1)}$$

where,$\emptyset = \frac{3sinqd - qdcosqd}{q^3d^3}$, A_2 is a constant, k is the packing factor and d is the interparticle spacing.[24]

Scattering from scaffolds crosslinked in presence of ice crystals showed a gradual shift of the peak corresponding to particle aggregation towards lower q when the OP

ratio increases above 0.25 (low q peak positions for 0.2 and 1.5 are ~ 0.027 and 0.0224 $Å^{-1}$ respectively). Similar to the samples crosslinked in presence of ice, for lyophilized samples as well we see a gradual shift in correlation peak to low q when the OP ratio increases above 0.25 (low q peak positions for 0.2 and 1.5 are ~0.027 and 0.0217 $Å^{-1}$ respectively), (Figure 5.4c).

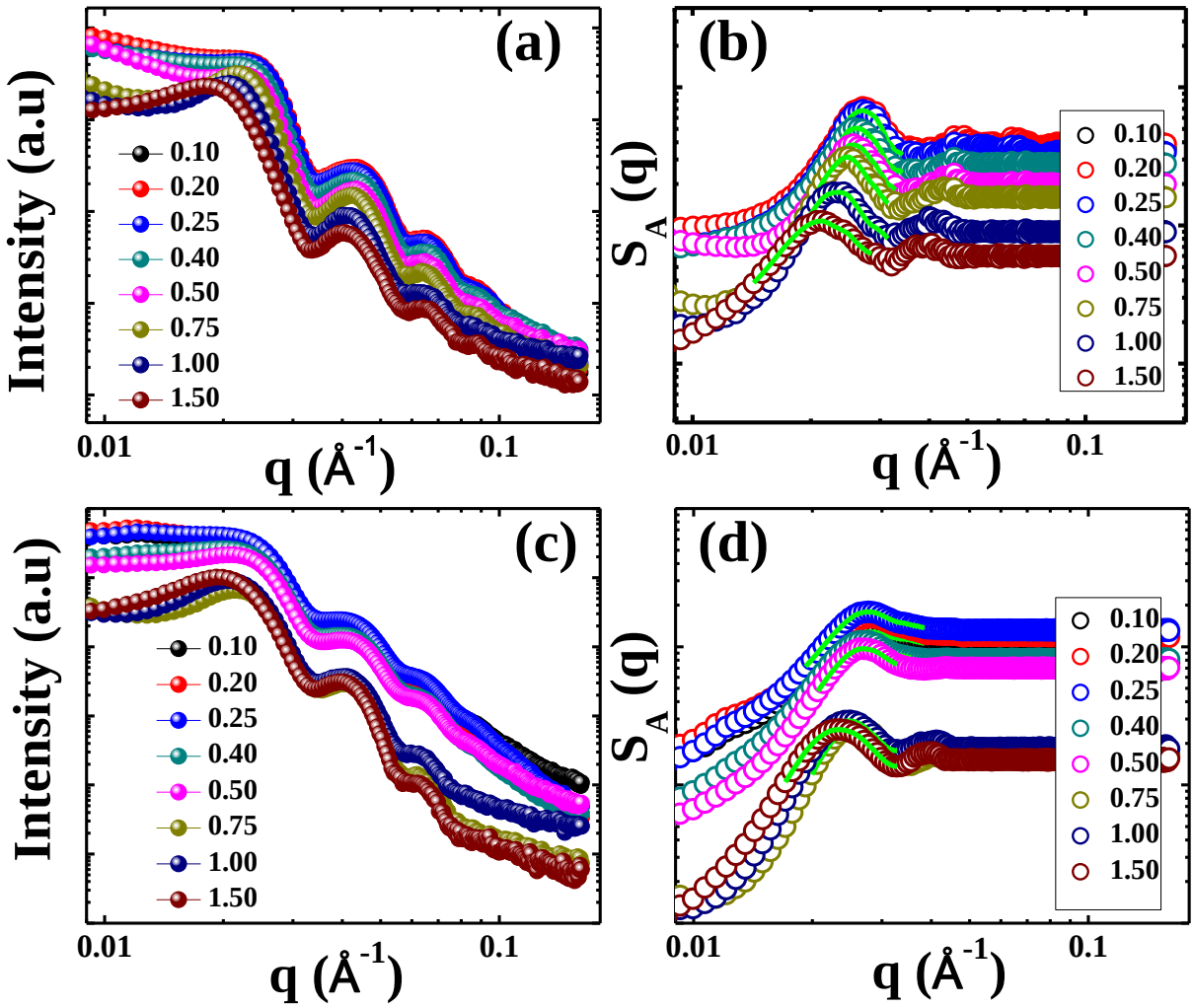

Figure 5.4: (**a,c**): SAXS raw data for scaffolds crosslinked in presence and absence of ice crystals respectively. Legends indicate the organic to particle ratio. (**b,d**) Apparent structure factor $S_A(q)$ calculated for scaffolds crosslinked in presence and absence of ice crystals respectively. $S_A(q)$ obtained by normalizing the SAXS data from scaffolds with scattering from a dilute solution of silica. The green solid line through the first peak of each curve represents a fit to the data to obtain the interparticle spacing.

The interparticle distance 'd' in the scaffolds crosslinked in presence and absence of ice crystals are identical to within experimental uncertainty at all OP ratios (Figure 5.5). The 'd' for scaffolds with 0.1 OP ratio is approximately 23 nm and this value

does not vary upto 0.4 OP ratio. Above 0.4 OP ratio, 'd' increases and reaches 28 nm at an OP ratio of 1. Further increase in organic loading to OP = 1.5 did not show a significant increase in 'd' (at 1.5, d ~ 29 nm). Our study shows that the interparticle distance is independent of the scaffold crosslinking protocol. This indicates that particle assembly by ice crystals is not altered by lyophilisation.

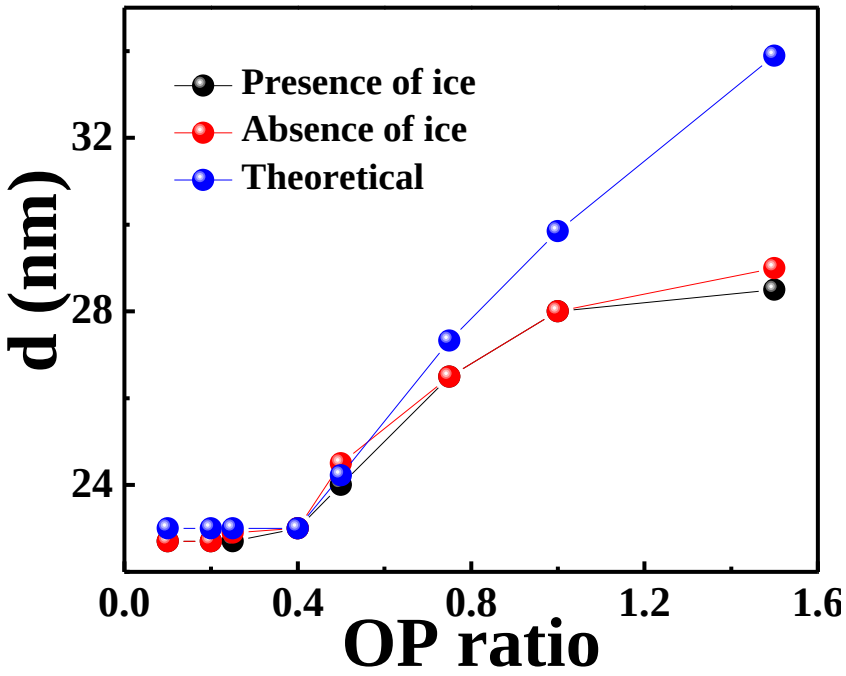

Figure 5.5: Interparticle spacing (d) obtained by fitting interference function to the first peak of $S_A(q)$ plots of scaffolds crosslinked in presence and absence of ice crystals. Here OP ratio indicates organic to particle ratio. The theoretical 'd' values were calculated after accounting for the organic required to fill the packing voids created by 22.5 nm size particles.

We note that the interparticle distance does not vary for organic loading up to 0.4, and then increases with organic content. We rationalize this as follows. Firstly, we observe that when negatively charged silica particles are dispersed in an aqueous solution of the cationic PEI, the polymer adsorbs on the particle surface forming a thin film that is a single molecule thick. This has been extensively documented in the literature[25, 26] and is reflected in the increase in the particle zeta potential after polymer coating. At the lowest organic loading investigated, the average particle spacing from SAXS is about 23 nm. Since the particle diameter is about 22 nm, the thickness of the organic film due to adsorption of the polymer on the particle surface is about 0.5 nm. Further, for random close packing of the slightly polydisperse, monomodal and approximately

spherical silica particles, we anticipate that the void volume fraction is about 36%. Assuming silica density of 2.2 g/cc and organic density of 1.05 g/cc for the crosslinked PEI, we observe that the volume of the organic is significantly smaller than is required to fill the entire void volume between the particles. Thus, the walls of the monolith are perforated with voids between the particles. We can calculate the interparticle spacing in the monolith walls assuming that additional organic in scaffolds with higher OP ratio preferentially fills these voids before the interparticle spacing is increased. This calculation shows that there is no change in the interparticle spacing until an OP ratio of 0.42 (Figure 5.5). For OP ratio above 0.42, there is an increase in the interparticle spacing. The results of these calculations accord remarkably well upto OP ratio 0.5. The discrepancy above 0.5 organic loading is due to an approximation used in our calculations. We did not account for the increase in packing void size with increase in interparticle spacing. Our calculations are based on the packing void size formed with 22.5 nm size particles.

Next we will see how the variation in organic content affects the mechanical performance of scaffolds crosslinked in presence and absence of ice crystals.

5.3.2 Effect of OP ratio on mechanical response of composites

We now investigate the mechanical properties of scaffolds made with different OP ratios. All experiments were performed on thoroughly dried scaffolds. We begin by looking at the mechanical properties of scaffolds crosslinked in presence of ice crystals followed by the analysis of scaffolds crosslinked after the removal of ice crystals.

5.3.2.1 Mechanical properties of scaffolds crosslinked in presence of ice crystals

Scaffolds were compressed to low strains (≈0.025%) and the Young's moduli (E′) were calculated from the slopes of stress-strain curves (Figure 5.6 a). The Young's modulus of a scaffold with 0.2 OP ratio is ≈18.6 kPa. Thus, as noted in Chapter 2, these are soft scaffolds. Further increase in OP ratio to 0.25 and 0.40 did not result in any significant variation in Young's modulus (E′ values for OP ratio of 0.25=21 kPa and OP ratio of 0.40=20 kPa). For higher OP ratios, there is a significant and systematic increase in the Young's modulus with organic content. For example, E′ is almost doubled when the OP ratio increases from 0.4 to 0.5 (at OP=0.5, E′= 39.4 kPa). Further increase of organic content led to a systematic increase in E′ (E′ at OP ratios of 0.75, 1 and 1.5 are 66.4 kPa, 78 kPa and 84 kPa respectively). We note that the qualitative trend in E′ with OP ratio is similar to that for the variation in interparticle

distance (*d*) (compare Figures 5.5 and 5.6b). Thus, for low OP ratios, where there are interparticle voids in the network walls, there is no change in modulus with organic content. This suggests that the monolith mechanical response arises only from the crosslinked shell that forms a mesh around the particles. Only once the voids are completely filled is there an increase in modulus. Thus, counter intuitively, there is an increase in the modulus of the porous monoliths with decrease in inorganic content. The increase in modulus could be due to a transition from two different structures. At low organic loading, the scaffolds comprise a crosslinked polymer shell holding the particles together in the assembly with packing voids between particles in the walls. However, above an OP ratio of 0.4, the walls comprise a continuous polymer phase with silica particles dispersed in it.

Next, we performed loading-unloading experiments on scaffolds made at different OP ratios (Figure 5.6 c,d). At all OP ratios, the scaffolds recover fully even after compressing to large strains (Figure 5.6d). Therefore, these scaffolds are elastic at all OP ratios. In the non-linear elastic regime (strain >0.025%), scaffolds with OP ratios 0.2 to 0.5 did not show any significant difference in the maximum compressive stress for a particular strain. For example, at 0.2s train, the maximum stresses were 6.1 kPa, 6.6 kPa, 7.1 kPa and 8 kPa for 0.2, 0.25, 0.4 and 0.5 OP ratios respectively. However, further increase in OP ratio to 0.75 led to a rapid jump in the maximum stress to 28 kPa (Figure 5.6 c). There wasn't any significant increase in maximum stress for higher OP ratios (for 20% strain, maximum stress = 27.4 kPa and 31.5 kPa for OP ratios of 1 and 1.5 respectively). This trend in the maximum stress values with OP ratio is observed at larger compressive strains as well (Figure 5.6 d).

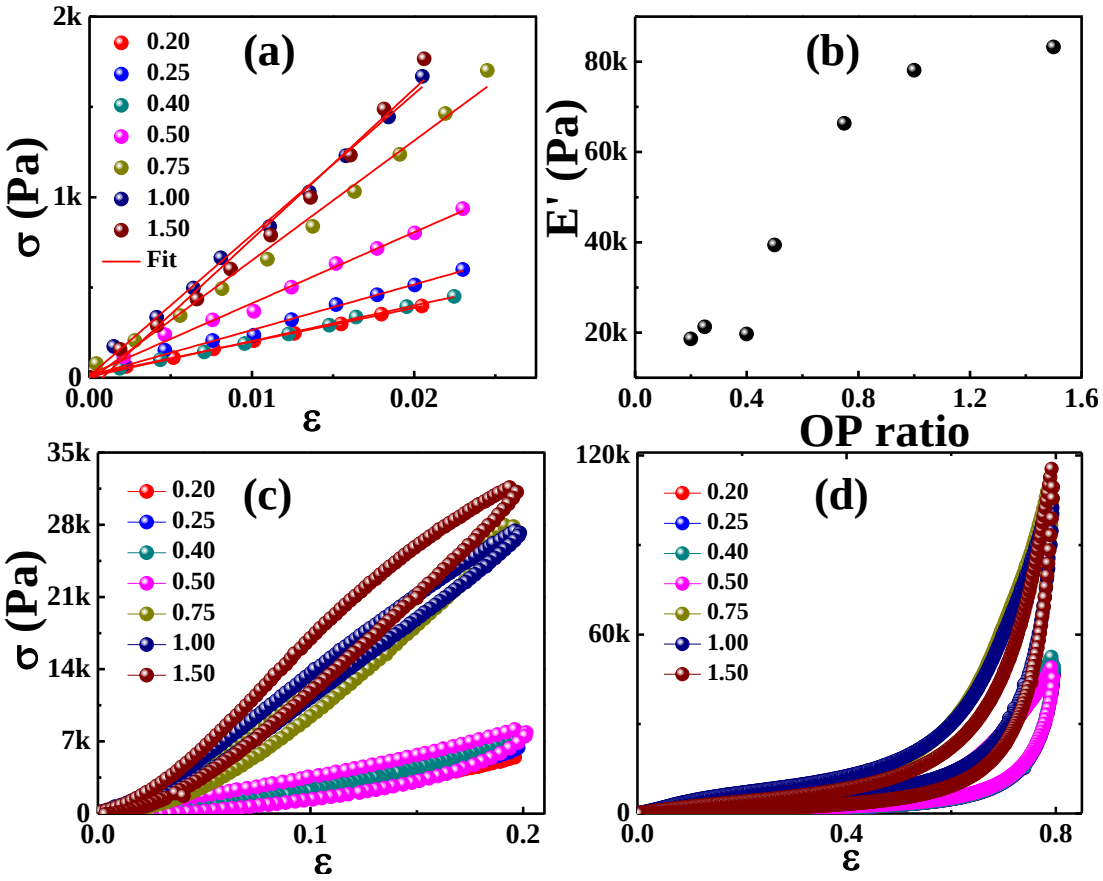

Figure 5.6: Nominal stress- strain curve of scaffolds crosslinked in presence of ice crystals. **(a)** At low strain, the stress varies linearly with strain. The Young's moduli (E′) are obtained from the slopes of stress-strain linear fits. (**b**) E′ variation as a function of OP ratio. Compression-expansion curves correspond to strains of **(c)** 20% and **(d)** 80%. These results are corresponding to scaffolds made from Ludox silica particles.

We have also studied the mechanical response of composites made from 1μm silica particles. Here too, we vary the organic to particle ratio in the composites from 0.2 to 1.5.

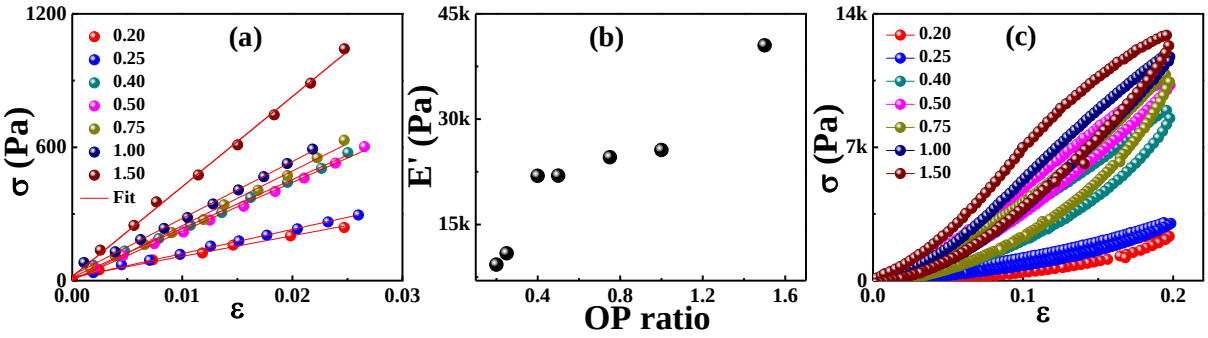

Figure 5.7: Nominal stress-strain curves of scaffolds made from 1μm silica and crosslinked in presence of ice crystals. **(a)** At low strain, the stress varies linearly with strain. The Young's moduli (E′) are obtained from the slopes of stress-strain linear fits. (**b**) E′ variation as a function of OP ratio. (**c**) Compression- expansion curves correspond to 20% strain.

Scaffolds prepared using 1μm silica particles exhibit qualitatively similar behaviour as those prepared using Ludox silica nanoparticles. These scaffolds too are soft, with a Young's modulus of about 10 kPa for OP ratios of 0.2 and 0.25 (Figure 5.7a). Increase in OP ratio to 0.4 doubled the E′ to 22 kPa. There was no significant increase in E′ as the OP ratio is increased to 0.5, 0.75 and 1. For OP = 1.5, the E′ increases further to 40.5 kPa (Figure 5.7b). We note that scaffolds prepared using the Ludox nanoparticles have about two-fold higher modulus when compared with equivalent scaffolds prepared using 1μm silica particles at all OP ratios. Again, similar to Ludox sponges, scaffolds made from 1μm silica particles are elastic and can recover from large deformations. The stress strain plot for scaffolds with OP ratios of 0.2 and 0.25 are similar (Figure 5.7c). There is an increase in stress at comparable strains for OP = 0.4. Further increase in the OP ratio shows only a marginal change in the stress strain behaviour. Thus, the behaviour of the 1 μm silica scaffolds is qualitatively similar to that observed for the Ludox scaffolds. The Ludox silica particles have nearly 40-fold higher specific surface area. When we account for the higher amount of polymer required to form an adsorbed layer on the Ludox, the critical OP ratio for increase in modulus in both monoliths corresponds to the organic fraction required to infill the interparticle pore volume.

5.3.2.2 Mechanical properties of scaffolds crosslinked after lyophilization

Next, we examine the mechanical responseof scaffolds prepared by crosslinking after lyophilisation of ice. We investigate scaffolds prepared using Ludox silica and 1μm particles with varying OP ratio.

At very small strains (< 0.025%), we obtain the Young's modulus from the slope of the stress-strain plot. These are soft monoliths, with moduli comparable to sponges prepared by crosslinking in the presence of ice. In contrast to the scaffolds crosslinked in presence of ice, here we observed a systematic increase in E′ with increase in OP ratio (Figure 5.8a). Scaffolds with OP ratios of 0.2, 0.25, 0.4, 0.5, 0.75, 1 and 1.5 exhibit E′ = 15.2 kPa, 18 kPa, 26 kPa, 44 kPa, 55.3 kPa, 62.6 kPa and 75 kPa, respectively. We have already seen that the interparticle distance in scaffolds is independent of crosslinking protocol (Figure 5.5). Therefore, we do not see a correlation between the interparticle distance and variation in E′ with varying OP ratio. We cycle scaffolds crosslinked after lyophilisation through a cycle of compression, followed by expansion to examine their failure. Scaffolds with 0.2 OP ratio were plastic, as documented in Chapter 2. These scaffolds failed even at small deformations (<20% strain, Figure 5.8c). During compression to 20% strain, the increase in stress for such "plastic" scaffolds is almost 7-fold lower than for the comparable elastic scaffold. When the load is released, the stress rapidly decays to zero and the sample stays deformed relative to the original sample. We define the compression set as the irrecoverable strain residual in the sample when load is released after compressing to 20% strain. For OP = 0.2, the compression set is ≈ 18.5%. Scaffolds with OP ratio = 0.25 also showed plastic failure (Figure 5.8d) on compression to 20%. However, the compression set decreased to 13%. As the OP ratio is increased to 0.4 and 0.5, the stress developed on compression to 20% strain increases relative to lower OP ratios, and is comparable to that for elastic scaffolds (Figure 5.8 b,e). At these higher OP ratios, the compression-expansion cycle exhibits significant hysteresis – however, the samples do not exhibit failure at 20% strain, viz. compression set = 0%. Samples with OP ratio = 0.4 fail at higher strains (= 30%) and exhibit lower compression set (Figure 5.9a). As OP ratio increases to 0.5, the sample fails only at higher compressive strains (= 40%) and shows lower still permanent set (Figure 5.9b).

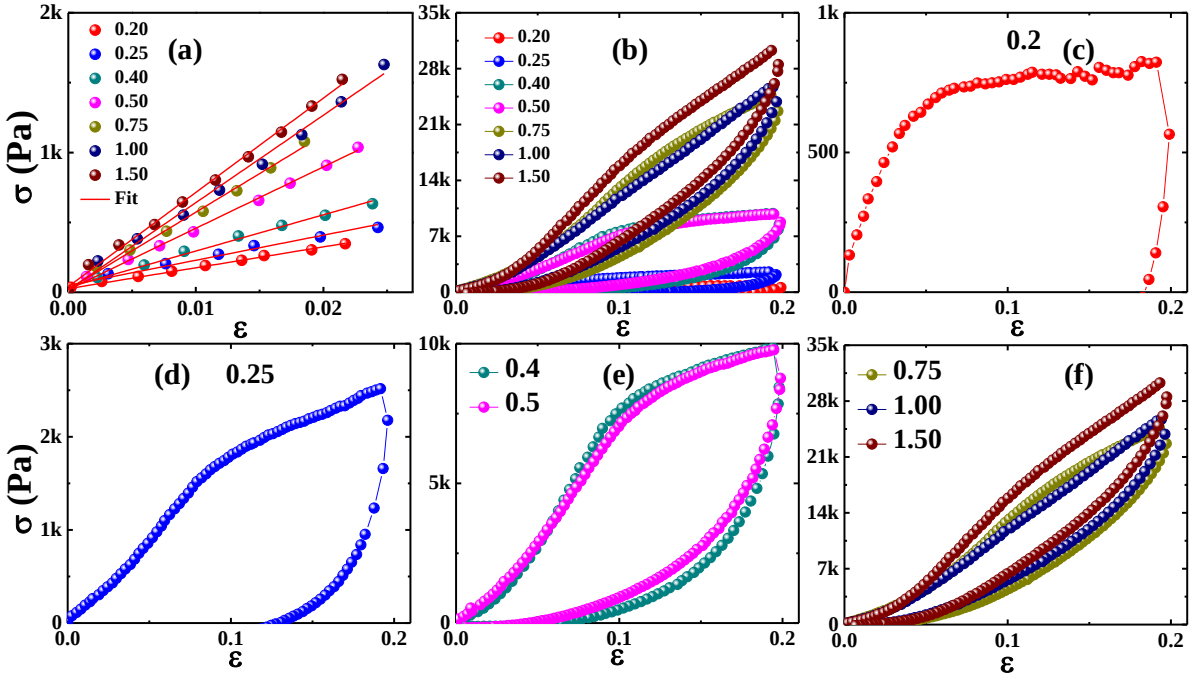

Figure 5.8: Nominal stress- strain curve of scaffolds crosslinked in absence of ice crystals. (**a**) At low strain, the stress varies linearly with strain. Young's modulus is obtained from the slopes of stress-strain curves. Compression-expansion curves correspond to 20% strain for OP ratios **(b)** all **(c)** 0.2 **(d)** 0.25 **(e)** 0.4 and 0.5 and **(f)** 0.75 and above organic loadings.

Scaffolds with OP ratios of 0.75, 1 and 1.5 do not fail even at 80% compressive strain and recover almost completely (Figures 5.8f and 5.9c). In addition, the stresses generated on imposing compressive strain are comparable to those for the corresponding elastic scaffolds (Figure 5.9c).

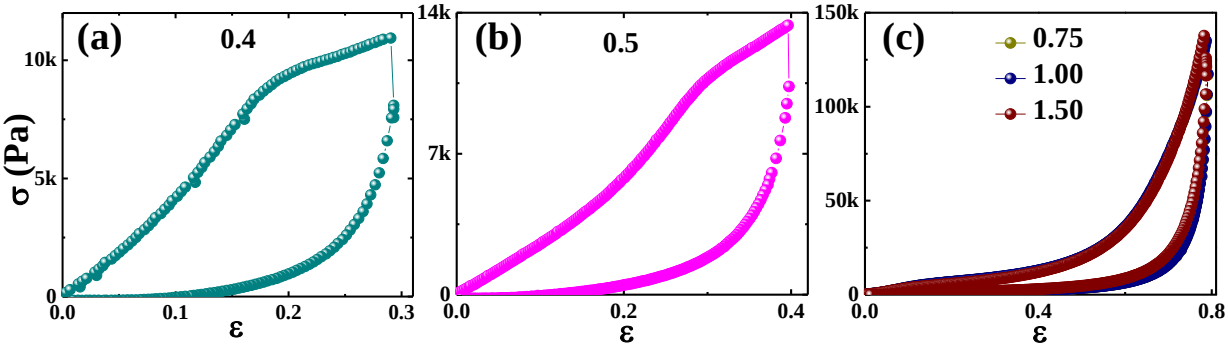

Figure 5.9: Compression- expansion curves of scaffolds with organic loadings **(a)** 0.4 **(b)** 0.5 and **(c)** 0.75 and above obtained at different strain values.

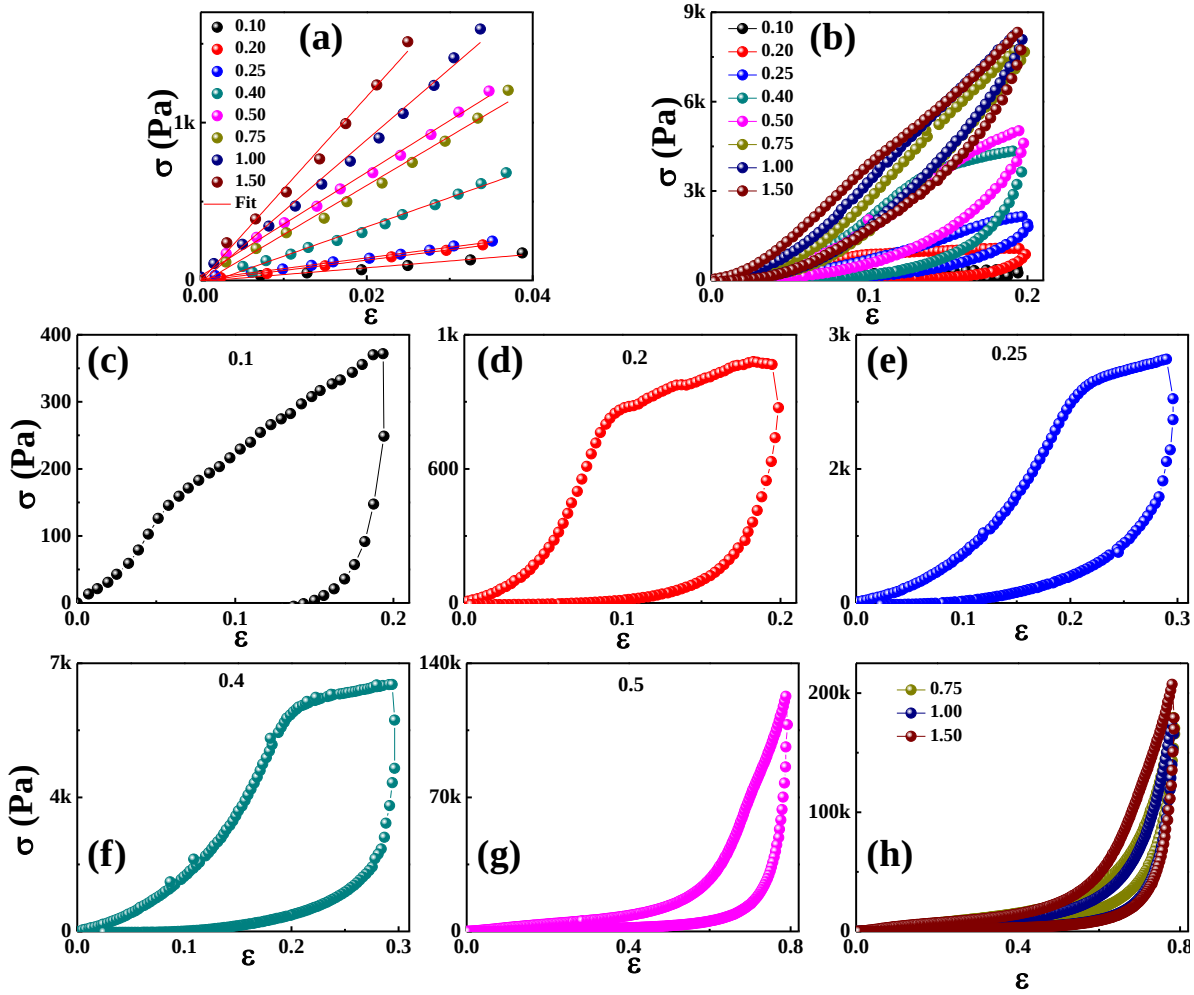

Figure 5.10: Mechanical response of 1 μm silica scaffolds crosslinked after lyophilization. (**a**) Young's moduli calculated from the slope of linear stress-strain curves. Compression-expansion curves of scaffolds with organic loadings **(b-h)** all, 0.1, 0.2, 0.25, 0.4, 0.5, 0.75, 1 and 1.5.

We have also studied the mechanical properties of 1 μm silica scaffolds with different OP ratios and crosslinked after lyophilisation (Figure 5.10). As with the Ludox scaffolds, the Young's moduli of 1μm silica scaffolds crosslinked after lyophilisation increased systematically with increase in organic ratio, with a 2.5-fold jump between OP ratios of 0.25 and 0.4 (Figure 5.10a). Correspondingly, the stress in the sample on compressing increases with OP ratio, the compressive set decreases and the samples are able to recover from larger strains (Figure 5.10b). For example, scaffolds with OP ratio = 0.1 and 0.2 fail at compressive strain less than 20% (Figure 5.10 c,d), with residual compressive set of 14% and 7% respectively. As OP ratio is increased to 0.25 and 0.4, scaffolds fail between 20 and 30% compressive strain with a permanent set of

about 7% at 30% compression (Figure 5.10 e,f). The scaffold with OP ratio = 0.5 did not fail even at 80% compressive strain (Figure 5.10 g) and exhibited a compression set of only ≈ 8% at 80% compression. Scaffolds with OP ratios of 0.75, 1 and 1.5 are also elastic at 80% strain with compression set of only ≈ 5% (Figure 5.10 h).

Remarkably, the transition from plastic failure to elastic recovery for scaffolds crosslinked after lyophilisation happens at OP ratios between 0.4 and 0.5 for scaffolds prepared using 1 μm silica and between 0.5 and 0.75 for the Ludox scaffolds. These values of the OP ratio are near those where the interparticle voids are infilled by organic. In the next sections, we explore the implications of these observations.

Our previous single particle tracking (SPT) study (Chapter 3) showed that plastic monoliths exhibit considerable heterogeneity at the length scale of the probe particles (~1 μm). Spatial variation in particle dynamics observed with SPT was mirrored by the variation in the local viscoelastic properties of the crosslinked polymer matrix from AFM (Chapter 2). To understand how this spatial heterogeneity is affected by increase in organic to particle ratio, we study the particle dynamics in 1μm silica scaffolds crosslinked in presence and absence of ice crystals using single particle tracking (SPT) technique.

5.3.3 Variation in "local" properties with organic loading

We study particle dynamics in samples with three different OP ratios, 0.1, 0.5 and 1for scaffolds crosslinked in presence and in absence of ice crystals. As earlier, we add a small fraction of 1 μm fluorescent polystyrene particles (3.4 wt% of total silica particles) into an aqueous dispersion of 1μm silica particles, PEI and crosslinker. Subsequently, this dispersion is ice templated and the polymer is crosslinked in the presence of ice crystals or after the ice is lyophilized. After crosslinking, the probe particles become an integral part of the scaffold network structure. We track the motions of these fluorescent particles using an epi-fluorescence microscope by capturing images for 10 min. Similar to Chapter 3, we calculate the motion of the particles using centroid algorithm in an arbitrary XY reference frame and obtain particle trajectories.[27] We perform a wavelet transform on these particles trajectories to eliminate stage drift, following the protocol described in Chapter 3, and obtain Brownian particle fluctuations. The particle motion is used to calculate the van Hove jump distribution. We have calculated the van Hove jump distribution of multiple particles located at different locations in the samples.

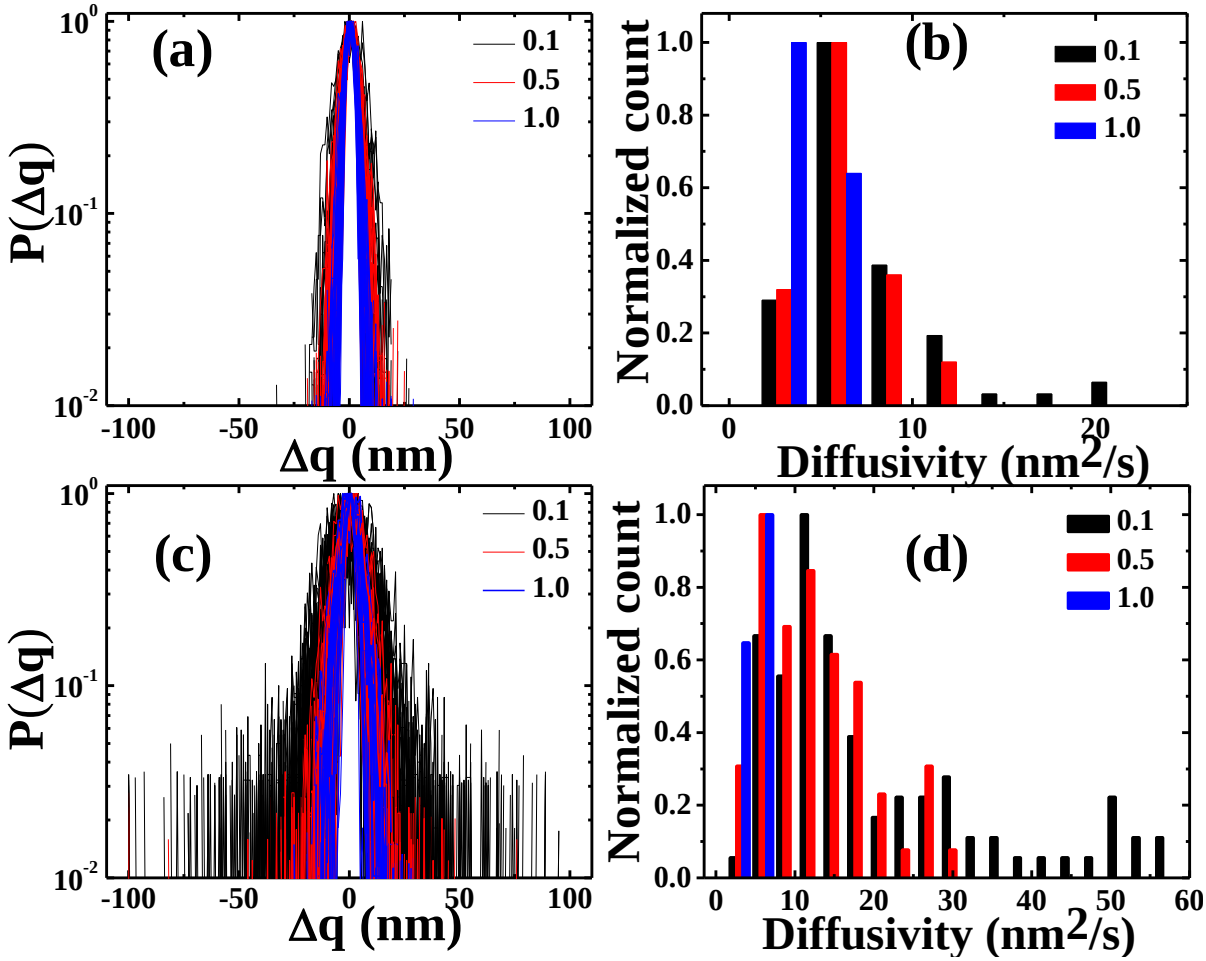

Figure 5.11: van Hove particle jump distribution of scaffolds crosslinked in **(a)** presence and **(c)** absence of ice crystals with 0.1, 0.5 and 1 organic to particle (OP) ratio. Diffusivity calculated from variance which is obtained by fitting a Gaussian function to each jump distribution for scaffolds crosslinked **(b)** in presence of ice and (**d**) after the removal of ice.

Scaffolds crosslinked in presence of ice crystals showed a reduction in the width of jump distribution with increase in organic loading (Figure 5.11a). Specifically, at $P(\Delta q) = 10^{-2}$, the sample with OP ratio = 0.1 showed jumps (Δq) in the range of 6 to 20 nm, whereas at OP ratios of 0.5 and 1, the samples showed Δq in the range of 4– 14 and 5– 10 respectively. We fit each jump distribution to a Gaussian function to extract the distribution of variance for probe particles in these scaffolds. The variance of the jump distribution is related to the short time particle diffusivity.[28] The diffusivity of scaffolds with OP ratio = 0.1 spanned from 1.8 nm^2/s to 22 nm^2/s with a width ≈ 4.2 nm^2/s and peak ≈ 4 nm^2/s (Figure 5.11b). Jump distribution curves of scaffolds with 0.5 organic exhibited diffusivity ranging from 1.8 nm^2 to 13 nm^2/s with a width ≈ 5.4

nm^2/s and a peak ≈ 4 nm^2/s. Scaffolds with OP ratio 1 showed a further decrease in the distribution of diffusivities. Here, the diffusivity spanned from 1.7 nm^2/s to 6 nm^2/s with a width ≈ 3.7 nm^2/s and peak around 3 nm^2/s. We note that the spread in diffusivity decreases with increase in organic loading. Therefore, the local environment experienced by particles at different spatial locations in the samples becomes more homogeneous as the OP ratio increases. In addition, increased OP ratio results in a decrease inthe particle diffusivity.

Scaffolds crosslinked after lyophilization showed a broader jump distribution compared to those crosslinked in the presence of ice. Here too, the spread in the jump distribution curves decreased with increase in OP ratio (Figure 5.11c). Scaffolds with 0.1 OP ratio showed a wide heterogeneity in particle jump distributions and Δq varies from 5– 100 nm at $P(\Delta q) = 10^{-2}$. This Δq range decreased to 5– 47 nm when the OP ratio increased to 0.5. At OP ratio = 1, we observe a drastic reduction in the dynamic heterogeneity. Here, the Δq variation is only 5– 15 nm at $P(\Delta q) = 10^{-2}$. The particle diffusivity in the 0.1 OP ratio scaffolds varied from 1.2 nm^2/s to 60 nm^2/s with a width ≈ 12 nm^2/s (Figure 5.11d). At 0.5 OP ratio, the range of diffusivity distribution reduced and was peaked at ≈ 4 nm^2/s, varying from 1.5 nm^2/s to 30 nm^2/s with a width of 15 nm^2/s. Further increase in OP ratio to 1 reduces the range of diffusivities to 1.6 nm^2/s to 5.5 nm^2/s with a width ≈ 5 nm^2/s and peak ≈ 4 nm^2/s.

Our study shows that the frequency of larger excursions made by the particles reduces with increase in OP ratio. The distribution of diffusivity narrows down with increase in organic loading. Our microrheology investigation in Chapter 3 had shown that the larger jumps correspond to regions with low storage modulus. Thus, increasing the organic loading reduces the number of areas having low storage modulus. Therefore, our SPT study shows that increase in organic content decreases the local spatial heterogeneity in ice templated scaffolds. This reduction is very prominent in the case of plastic monoliths.

At low organic loading, there is insufficient organic to fill the interparticle voids of ice templated scaffolds. For 1 μm silica particles, the packing voids are in the range of few hundreds of nanometers and we anticipate that water in those pores should freeze close to the freezing temperature of bulk water. However, the high concentration of polymer present in the interparticle voids may result in a depression of freezing temperature below that of pure water. The random close packing of smaller particles

like Ludox silica particles, where the particle size is ~ 22 nm, can give packing voids in the range of a few nm. Here, also we should expect the water in packing voids to be frozen at -18^{o}C. Therefore, for samples crosslinked in the presence of ice, we anticipate that the water in interparticle voids will freeze to form ice crystals. For lyophilized samples, the ice is replaced with air. Therefore, in the first case, the organic is exposed to a hydrophilic medium, viz., ice and for lyophilized samples, the organic is exposed to a hydrophobic medium, viz., air. To understand the state of the water content in these two types of scaffolds, we perform deuterium and proton solid state NMR.

5.3.4 Solvent structure in scaffolds: Deuterium and Proton solid state NMR study

The steps involved prior to the NMR experiments are shown in Table 5.1.

Table 5.1: Steps involved in the preparation of scaffolds for deuterium (^{2}H) and proton (^{1}H) NMR experiments.

Crosslinked in presence of ice	Crosslinked in absence of ice
• Freeze for 24 h (crosslinking takes place) • Dry the scaffold by lyophilization (10h, -80^{o}C, 0.1 mBar) • Known quantity of sample is vacuum dried at 50^{o}C for 24 h prior to NMR experiment.	• Freeze for 45 min • After 45 min, samples are lyophilized to remove ice crystals (10h, -80^{o}C, 0.1 mBar). • After lyophilization, sample kept back in the freezer for 24h for crosslinking reaction. • Known quantity of sample (equal to that crosslinked in the presence of ice) is vacuum dried at 50^{o}C for 24 h prior to NMR experiment

5.3.4.1: ^{1}H solid state NMR

We begin by characterising ^{1}H spectra of 1μm silica particles. Dry silica particles showed 4 peaks at 1.39, 2.18, 3.89 and 5.62 ppm (Figure 5.12). Of these, the 5.62 ppm peak was most prominent.

Buntkowsky and coworkers investigated NMR of mesoporous silica particles and showed that the dry silica is characterized by a peak with a chemical shift of 1.74 ppm.[29] They have attributed peaks in the range of the 2– 3 ppm to either germinal hydroxyl ($Si(OH)_2$) or to hydrogen bonded hydroxyl species (SiOH ··· HOSi). They have systematically varied the water content in silica and investigated NMR from OH groups in these samples (Figure 5.13). According to their study, water molecules can either be free or they can be hydrogen bonded to the silica surface or to each other. In addition, they have shown that with increase in water content, different water environments are observed to form in mesoporous silica.

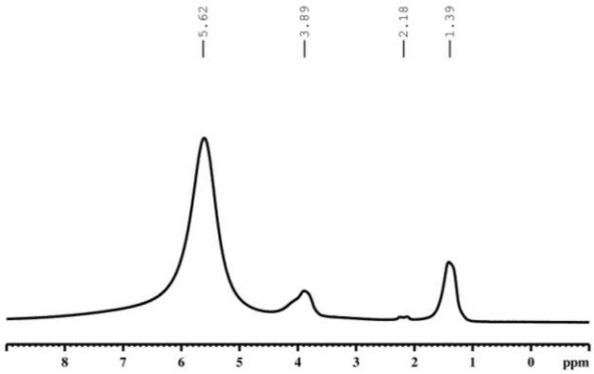

Figure 5.12: ^{1}H NMR of silica particles. Particles were dried at 50 ^{0}C for 24 h prior to the experiment.

This leads to a shift in resonance from 1.74 to 2.5 to 3.9 to 5 ppm with increase in water content. At intermediate water levels, they observed co-existence of peaks at 1.74 and 2.5 or 3.9 ppm. At higher water content, the 1.74 ppm peak intensity reduced due to the increase in water layer around silica. At these high levels of hydration,the number of free surface –SiOH groups reduced until the whole accessible surface is covered by a monolayer of water molecules. In addition, water clusters are observed at 5.5 ppm.

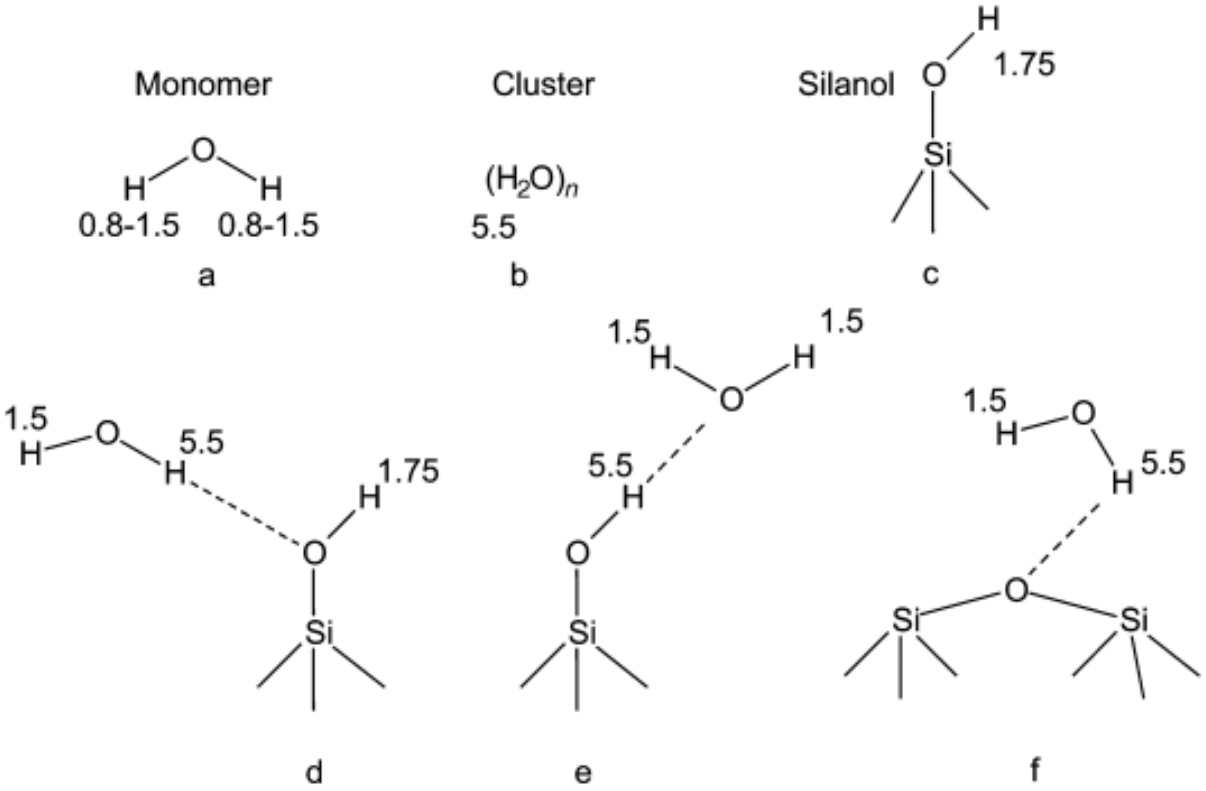

Figure 5.13: Possible OH groups in the silica/ water sample. **(a-c)** chemical shifts of the constituents of monomeric water, water clusters and silanol groups. **(d-f)** various hydrogen bonding scenarios and corresponding chemical shifts. (Taken with permission from reference[29]).

Based on these assignments, the water peak at 1.39 ppm in our samples is attributed to isolated water molecules on the silica surface. We did not observe any dry silica peak at 1.74 ppm. Peaks at 2.18 and 3.89 ppm can be attributed to silica structures with different hydration levels. The peak at 5.62 ppm represents water clusters. Therefore, this study shows that water molecules are adsorbed on the silica particle surface and even vacuum drying at 50^{o}C for 24 h is insufficient to remove these.

We also use ^{1}H NMR to investigate the structure of scaffolds crosslinked in the presence or absence of ice crystals. The observed peak positions of these two classes of materials with different OP ratios (0.2, 0.4 and 1) are listed in Table 5.2.

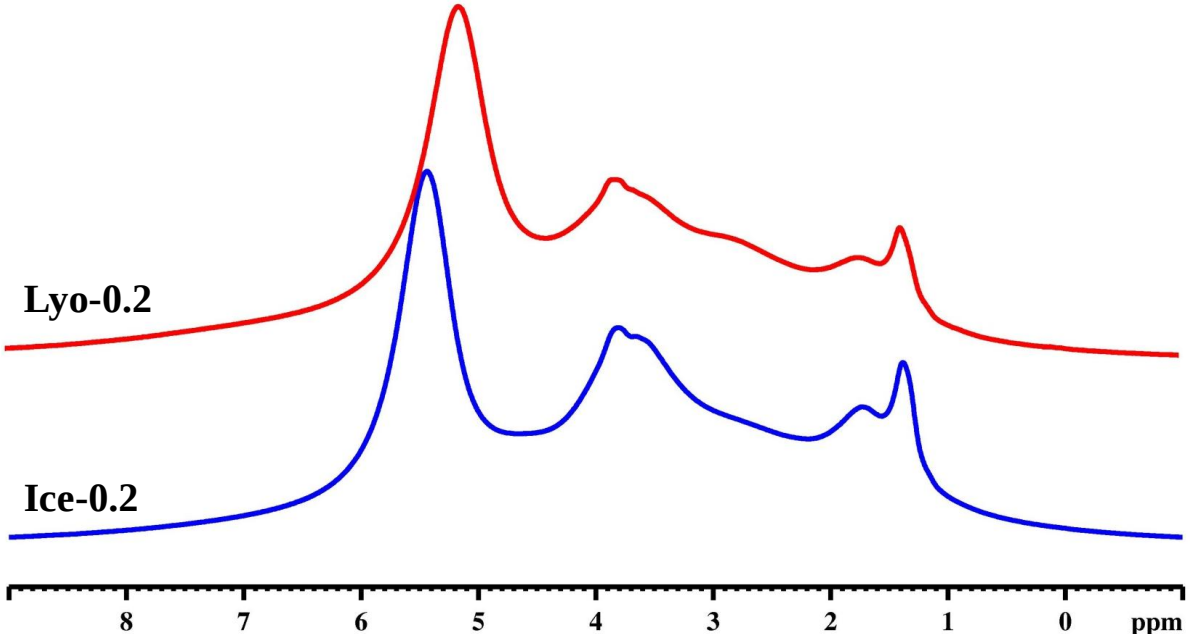

Figure 5.14: ^{1}H NMR of scaffolds crosslinked in presence (labelled as Ice-0.2) and absence (labelled as Lyo-0.2) of ice crystals. The OP ratio in the scaffold is 0.2.

Ice-0.2 (OP ratio = 0.2 and crosslinked in presence of ice crystals) and Lyo-0.2 (OP ratio = 0.2 and crosslinked in absence of ice crystals) exhibited peaks at 1.39, 1.7, 3.6, 3.83 ppm (Figure 5.14). Of these, peaks at 1.39 ppm and 3.83 ppm arise from silica-water interactions. Peaks at 1.7 and 3.6 ppm arise from protons present in the crosslinker molecule (Figure 5.15). In addition to these peaks, we can see an additional prominent peak in Ice-0.2 and Lyo-0.2 samples. In Ice-0.2, this peak occurs at 5.44 ppm while in Lyo-0.2 it is observed at 5.15 ppm.

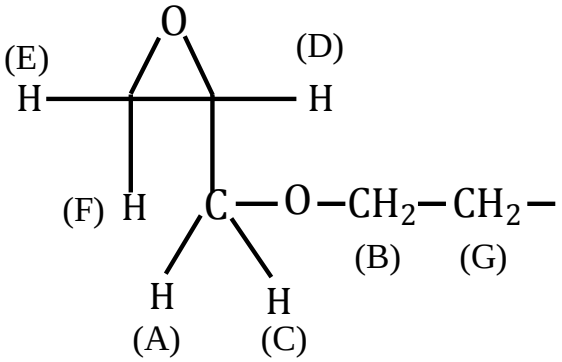

Label	Chemical shift (ppm)
A	3.704
B	3.51
C	3.40
D	3.127
E	2.788
F	2.599
G	1.664

Figure 5.15: Chemical shift of protons present in 1,4 butanediol diglycidyl ether. (Reference: https://www.chemicalbook.com/SpectrumEN_2425-79-8_1HNMR.htm).

Table 5.2: The list of peak positions for samples crosslinked in presence and absence of ice crystals. Peak positions are in units of ppm.

Silica	Ice-0.2	Lyo-0.2	Ice-0.4	Lyo-0.4	Ice -1	Lyo-1
1.39	1.39	1.38	1.39	1.39		
	1.73	1.72	1.73	1.71	1.62	1.66
2.18						
	3.61	3.55	3.64	3.64	3.50	3.53
3.89	3.83	3.81	3.78	3.76		
5.62	5.44	5.15	5.39	4.87	Broad hump between 4.8 and 5.5 ppm	Broad hump between 4.8 and 5.5 ppm

Similarly, for scaffolds with 0.4 OP ratio, we observe a peak for Ice-0.4 at 5.39 ppm and for Lyo-0.4 at 4.87 ppm (Figure 5.16).

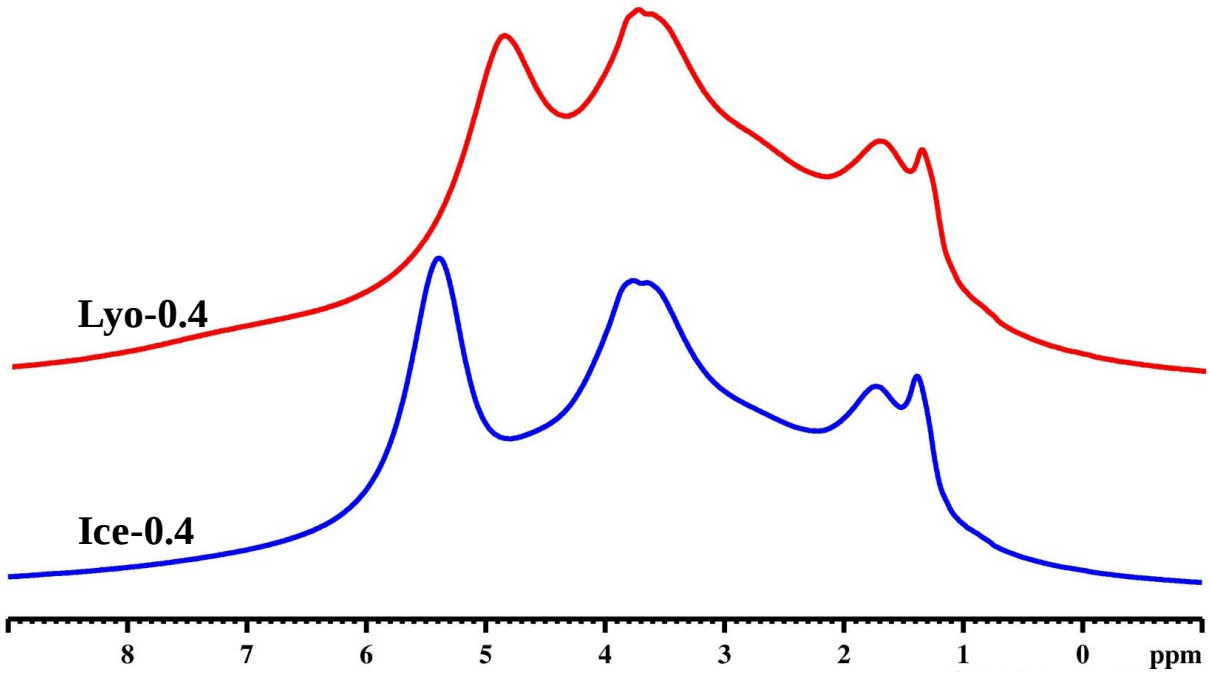

Figure 5.16: ^{1}H NMR of scaffolds with OP ratio 0.4 and crosslinked in presence (Ice-0.4) and absence (Lyo-0.4) of ice crystals.

On further increasing the OP ratio to 1, there were no longer any differences in the NMR from samples crosslinked in presence and absence of ice crystals (Figure 5.17). Here, we observed peaks at 1.6 and 3.5 ppm and a broad hump between 4.8 and 5.5 ppm.

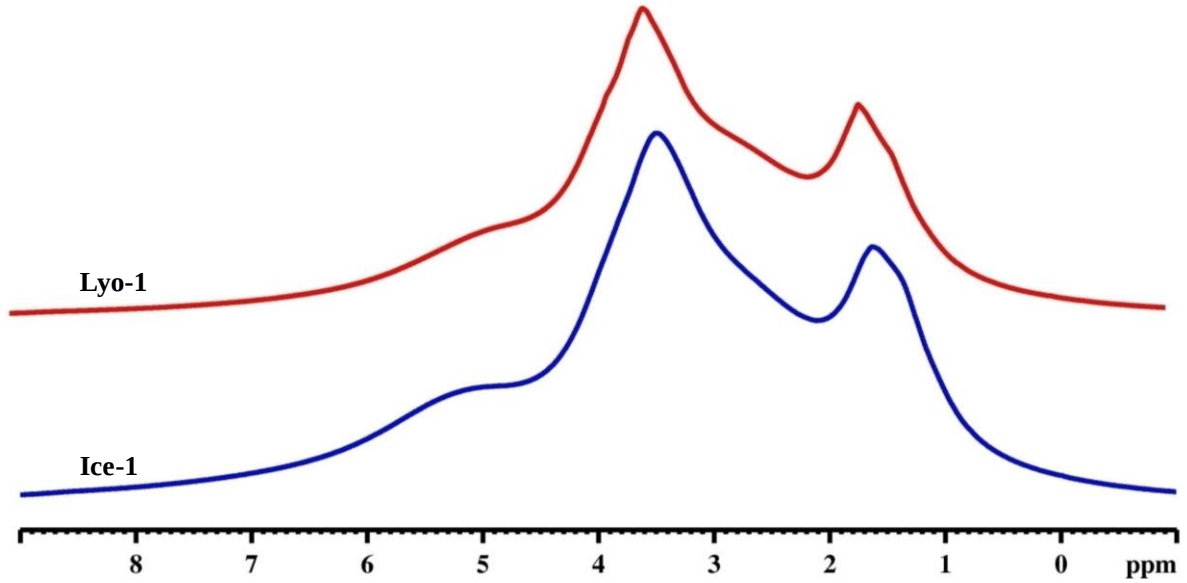

Figure 5.17: ^{1}H NMR of scaffolds with OP ratio 1 and crosslinked in presence (Ice-1) and absence (Lyo-1) of ice crystals.

We have seen that with increase in OP ratio from 0.2 to 1, there is a broadening of the peak near 5 ppm (Figure 5.18). In addition, we observe an increase in peak heights at ~ 1.7 and ~3.6 ppm with increase in OP ratio. This is trivially attributed to the increase in the content of amines and crosslinker with increase in organic loading.

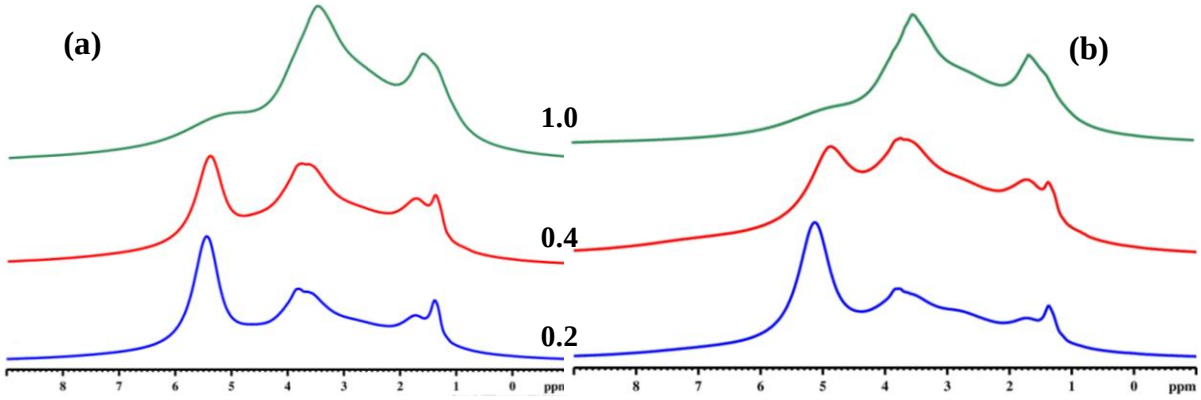

Figure 5.18: Variation in proton spectra with increase in organic loading from 0.2 to 1. (**a**) Scaffold crosslinked in presence of ice and (**b**) in absence of ice crystals.

Our ^{1}H NMR study shows that, whenever there is silica, it is impossible to remove water completely by vacuum drying and we can always see signatures of water associated with the silica surface. In addition to that, at low organic loading, scaffolds crosslinked in presence and absence of ice crystals showed a difference in the peak position corresponding to water clusters (~5 ppm) and all other peak positions were observed in the same positions for both scaffolds. Scaffolds crosslinked in presence of ice crystals showed a shift of the water cluster peak to higher ppm compared to the one crosslinked after lyophilisation. Interestingly, this difference disappears as the organic content increases. This indicates that at low organic loading, there is a difference in water clusters associated with scaffolds crosslinked in presence and absence of ice crystals. To understand the structure of these water clusters we have performed deuterium (^{2}H) solid state NMR.

5.3.4.2: ^{2}H solid state NMR

Deuterium solid state NMR has the advantage that it can distinguish different motional environments based on an analysis of ^{2}H line shapes and provides information about solvent structure. This method has already been used to understand the dynamics of monomer units in a polymer and to obtain motional heterogeneities in glassy systems.[30] Spiess had shown that based on the time scale of molecular motions, ^{2}H NMR spectra exhibits different line shapes.[30] If the motion is very fast, then the centre peak is Lorentzian. At the intermediate molecular motion regime, the signal intensity is spread over the whole frequency range and leads to a broad peak. Slow motions exhibit two symmetric Lorentzian profiles. Terenzi et al. studied the dynamics of water in cellulose fibers using deuterium solid state NMR and have shown that narrow peaks represent mobile water molecules while the broad component is a consequence of slowing down of molecular motion of water adsorbed on the micro fibrils.[31] They also showed that the re-orientational motional averaging in the mobile adsorbed water phase is characterized by a single correlation time that is directly proportional to the line width. Therefore, the mean motional correlation time in the immobile water adsorbed phase is always much longer than that in the mobile water adsorbed phase.

We have performed ^{2}H NMR on scaffolds crosslinked in presence and absence of ice crystals, with OP ratios of 0.2 and 1. Here, particle dispersions for scaffold preparation are made in D_2O rather than in DI water and all other steps in the preparation are similar to the protocol described in Table 5.1. Samples were vacuum dried for 24 h at 50^{o}C prior to solid state NMR experiments. In this experiment we look at the residual

deuterium solvents present in these two samples after lyophilisation (in one case the lyophilisation is prior to crosslinking and in another case after the crosslinking reaction. The lyophilisation conditions are same in both the cases).

Deuterium solid state NMR spectra of scaffolds with 0.2 OP ratio crosslinked in presence and absence of ice crystals showed differences in line shape (Figure 5.19). Ice-0.2 shows a broader peak compared to Lyo-0.2. However, at higher OP ratio, we do not see any difference in line spectra of scaffolds crosslinked in presence and absence of ice crystals. Moreover, Ice-1 and Lyo-1 spectra are broader than the scaffolds with low organic content.

Our deuterium solid state NMR study shows that, at low organic content the D_2O solvent associated with scaffolds crosslinked in absence of ice crystals are more mobile compared to the one crosslinked in presence of ice. At higher organic loading, solvent mobility further decreases and becomes independent of the crosslinking protocol, viz., in presence or absence of ice crystals. Mobility of solvent molecules reflects the environment within the scaffold. We anticipate that solvent molecules in the scaffolds crosslinked in presence of ice crystals are strongly associated with the silica and hydrophilic polymer (PEI) surfaces. We believe that this strong association happens during crosslinking since both the samples are prepared using a similar protocol (Table 5.1).

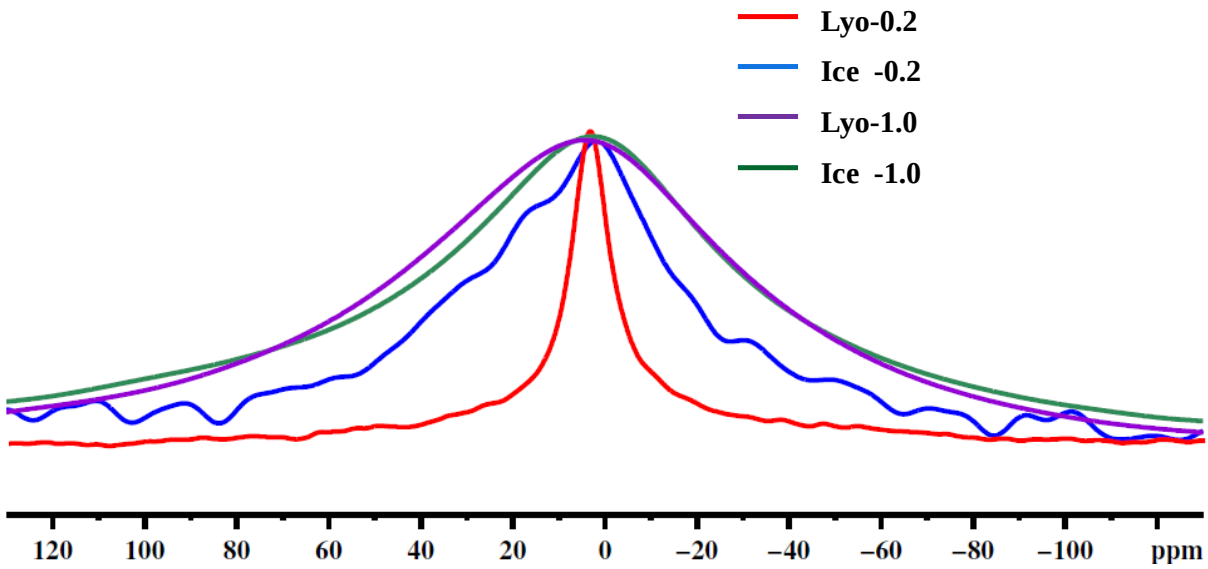

Figure 5.19: ^2H spectra of scaffolds crosslinked in presence and absence of ice crystals with 0.2 and 1 OP ratios.

Based on this understanding, we propose a mechanism for the crosslinking as the scaffolds are synthesized.

At low organic loading, when we crosslink the scaffolds prior to lyophilization, the particle and organic are present in a hydrophilic environment, with frozen or amorphous water molecules in the packing voids, and water adsorbed on the particle surface. Therefore, in this system there is a continuous phase of hydrophilic system during crosslinking. This may lead to a solvent network structure in the crosslinked polymer and on the particle surface. This water network structure is present in the scaffold pore walls and cannot be removed by vacuum drying after the crosslinking reaction.

In contrast, the particle and organic in the scaffolds crosslinked after removal of ice crystals, are exposed primarily to air which is hydrophobic in nature and to water that is not removed by sublimation. Our study tells that the non-frozen solvent which is present in the system exhibits large mobility since these molecules are not strongly associated with the particle-polymer surfaces and likely exist as isolated aggregates than a network structure. We presume that the solvent network structure in scaffolds crosslinked in presence of ice may play a role in the homogeneous distribution of crosslinking density.

At higher organic loading, we have already seen that the interparticle voids within the walls are filled with organic. Therefore, during crosslinking polymers exist in a melt state in all scaffolds. Therefore, at higher organic loadings, the presence or absence of ice does not affect polymer crosslinking. At high OP ratios, the adsorbed water content is higher, which causes a water network to form within the scaffold.

5.4 Summary

We have studied the effect of organic content on the elastic and plastic properties of scaffolds crosslinked in presence and absence of ice crystals. Here, we systematically varied the organic to particle ratio from 0.1 to 1.5 by keeping the total solid concentration fixed. At all OP ratios, we obtained self standing scaffolds and we studied the structure, dynamics and mechanical properties of these materials.

The key finding from these investigations is that there is a qualitative change in the structure and mechanical response of ice templated scaffolds at a critical OP ratio of about 0.5 for scaffolds made from Ludox silica particles. Below this, there is

insufficient crosslinked polymer to form a continuous matrix. Thus, the crosslinked polymer exists as a thin shell around the particles and forms a mesh that imparts elasticity to the particle scaffolds formed by crosslinking in the presence of ice. As the OP ratio is increased, interparticle voids are filled with the organic phase. Above the critical OP ratio of 0.5, there is a significant change in the mechanical response of scaffolds crosslinked in the presence of ice and in the absence of ice. Scaffolds crosslinked in the presence of ice show a significant change in modulus and stress generated on compression. Scaffolds crosslinked in the absence of ice show a transition from being "plastic" below the critical OP ratio to showing complete recovery from large compressive strains. Therefore, the critical OP ratio delineates two qualitatively distinct morphologies. Below the critical ratio, the scaffolds comprise inorganic particles that are held together through a thin shell of crosslinked polymer. Above the critical ratio, there is a continuous crosslinked polymer phase in which inorganic particles are embedded. Therefore, as the OP ratio is increased, there is initially no change in interparticle spacing below the critical ratio. Particle-particle spacings increase only once the interparticle voids are filled with crosslinked polymer at the critical OP ratio.

The change in structure at the critical OP ratio is also reflected in the particle tracking measurements. As the OP ratio is increased above the critical value, there is a narrowing of the distribution of particle diffusivities. This narrowing is especially dramatic for the scaffolds crosslinked in the absence of ice. This reflects a change in the local heterogeneity in the crosslinked polymer, that we believe is a measure of the degree of crosslinking. Thus, there is significant local heterogeneity in the crosslink density for scaffolds crosslinked in the absence of ice that becomes progressively less heterogeneous as the OP ratio is increased above the critical value. Even in scaffolds crosslinked in the presence of ice, there is some narrowing of the distribution of crosslink density with increase in organic content.

Finally, solid state proton and deuterium NMR indicate that the critical OP ratio is also associated with differences in the structure of water present in the scaffolds below the critical OP ratio. These differences disappear above the critical OP ratio. Specifically, water clusters in scaffolds crosslinked in presence of ice crystals showed less mobility compared to those in scaffolds crosslinked after lyophilisation. We attribute this to the strong association of water clusters in a network structure within the scaffolds for scaffolds crosslinked in the presence of ice. In contrast, water clusters

form aggregates that are loosely associated to the scaffolds for scaffolds crosslinked in the absence of ice.

We speculate that for OP ratios below the critical value, polymer chains that are not adsorbed to the particles are dispersed in a swollen state when crosslinked in the presence of ice, but are collapsed when crosslinked in the absence of ice. This results in significantly greater heterogeneity in crosslinking density when crosslinked in the absence of ice, that manifests as plasticity or brittleness of the scaffolds. Once the critical OP ratio is exceeded, the polymer chains fill the interparticle voids and exist as a polymer melt. Crosslinking is uniform in this melt yielding scaffolds that are elastic to large compression, independent of the crosslinking protocol.

5.5 References

1. Weeks, W. F.; Ackley, S. F., The growth, structure, and properties of sea ice. In *The geophysics of sea ice*, Springer: **1986**; pp 9-164.

2. Hohmann, M., Soil freezing-the concept of soil water potential. State of the art. *Cold Reg. Sci. Technol.* **1997,** 25, 101-110.

3. Lorain, O.; Thiebaud, P.; Badorc, E.; Aurelle, Y., Potential of freezing in wastewater treatment: Soluble pollutant applications. *Water Res.* **2001,** 35, 541-547.

4. Goff, H. D., Colloidal aspects of ice cream- A review. *Int. Dairy J.* **1997,** 7, 363-373.

5. Mazur, P., Cryobiology: The freezing of biological systems. *Science* **1970,** 168, 939-949.

6. Deville, S., Ice-templating, freeze casting: Beyond materials processing. *J. Mater. Res.* **2013,** 28, 2202-2219.

7. Deville, S., *Freezing colloids: Observations, principles, control, and use: applications in materials science, life science, earth science, food science, and engineering*. Springer: **2017**.

8. Rajamanickam, R.; Kumari, S.; Kumar, D.; Ghosh, S.; Kim, J. C.; Tae, G.; Sen Gupta, S.; Kumaraswamy, G., Soft colloidal scaffolds capable of elastic recovery after large compressive strains. *Chem. Mater.* **2014,** 26, 5161-5168.

9. Chatterjee, S.; Shanmuganathan, K.; Kumaraswamy, G., Fire-Retardant, Self-Extinguishing Inorganic/Polymer Composite Memory Foams. *ACS Appl. Mater. Interfaces* **2017,** 9, 44864-44872.

10. Das, C.; Chatterjee, S.; Kumaraswamy, G.; Krishnamoorthy, K., Elastic compressible energy storage devices from ICE templated polymer gels treated with polyphenols. *J. Phys. Chem. C* **2017,** 121, 3270-3278.

11. Saint-Michel, B.; Georgelin, M.; Deville, S.; Pocheau, A., Interaction of multiple particles with a solidification front: From compacted particle layer to particle trapping. *Langmuir* **2017,** 33, 5617-5627.

12. Dedovets, D.; Deville, S., Multiphase imaging of freezing particle suspensions by confocal microscopy. *J Eur. Ceram. Soc.* **2018,** 38, 2687-2693.

13. Tai, K.; Liu, Y.; Dillon, S. J., In situ cryogenic transmission electron microscopy for characterizing the evolution of solidifying water ice in colloidal systems. *Microsc. Microanal.* **2014,** 20, 330-337.

14. Deville, S.; Maire, E.; Lasalle, A.; Bogner, A.; Gauthier, C.; Leloup, J.; Guizard, C., In Situ X-Ray Radiography and Tomography Observations of the Solidification of Aqueous Alumina Particle Suspensions-Part I: Initial Instants. *J. Am. Ceram. Soc.* **2009,** 92, 2489-2496.

15. Burke, M. J.; Gusta, L. V.; Quamme, H. A.; Weiser, C. J.; Li, P. H., Freezing and injury in plants. *Annu. Rev. Plant Physiol.* **1976,** 27, 507-528.

16. Everett, D. H., The thermodynamics of frost damage to porous solids. *Trans. Faraday Soc.* **1961,** 57, 1541-1551.

17. Ashworth, E. N.; Abeles, F. B., Freezing behavior of water in small pores and the possible role in the freezing of plant tissues. *Plant Physiol.* **1984,** 76, 201-204.

18. Homshaw, L. G., High resolution heat flow DSC: Application to study of phase transitions, and pore size distribution in saturated porous materials. *J. Therm. Anal. Calorim.* **1980,** 19, 215-234.

19. Mazur, P., The role of cell membranes in the freezing of yeast and other single cells. *Ann. N Y Acad. Sci.* **1965,** 125, 658-676.

20. Huggins, M. L., Thermodynamic properties of solutions of long-chain compounds. *Ann. N. Y. Acad. Sci.* **1942,** 43, 1-32.

21. Flory, P. J., *Principles of polymer chemistry*. Cornell University Press: **1953**.

22. Kawai, T., Freezing point depression of polymer solutions and gels. *J. Polym. Sci.* **1958,** 32, 425-444.

23. Kawai, T., The Third Virial Coefficient in Polymer Solutions. *Bull. Chem. Soc. Japan* **1955,** 28, 679-685.

24. Kumari, S.; Kulkarni, A.; Kumaraswamy, G.; Sen Gupta, S., Large Centimeter-Sized Macroporous Ferritin Gels as Versatile Nanoreactors. *Chem. Mater.* **2013,** 25, 4813-4819.

25. Borkovec, M.; Papastavrou, G., Interactions between solid surfaces with adsorbed polyelectrolytes of opposite charge. *Curr. Opin. Colloid Interface Sci.* **2008,** 13, 429-437.

26. Meszaros, R.; Varga, I.; Gilanyi, T., Adsorption of poly (ethyleneimine) on silica surfaces: Effect of pH on the reversibility of adsorption. *Langmuir* **2004,** 20, 5026-5029.

27. Bhattacharya, S.; Sharma, D. K.; Saurabh, S.; De, S.; Sain, A.; Nandi, A.; Chowdhury, A., Plasticization of poly (vinylpyrrolidone) thin films under ambient humidity: Insight from single-molecule tracer diffusion dynamics. *J. Phys. Chem. B* **2013,** 117, 7771-7782.

28. Pastore, R.; Coniglio, A.; Ciamarra, M. P., Dynamic phase coexistence in glass-forming liquids. *Sci Rep.* **2015,** 5, 11770.

29. Grunberg, B.; Emmler, T.; Gedat, E.; Shenderovich, I.; Findenegg, G. H.; Limbach, H. H.; Buntkowsky, G., Hydrogen bonding of water confined in mesoporous silica MCM-41 and SBA-15 studied by 1H solid-state NMR. *Chem. Eur. J.* **2004,** 10, 5689-5696.

30. Spiess, H. W., Molecular dynamics of solid polymers as revealed by deuteron NMR. *Colloid Polym. Sci.* **1983,** 261, 193-209.

31. Lindh, E. L.; Terenzi, C.; Salmen, L.; Furo, I., Water in cellulose: Evidence and identification of immobile and mobile adsorbed phases by 2 H MAS NMR. *Phys. Chem. Chem. Phys.* **2017,** 19, 4360-4369.

Chapter 6

Effect of Electrostatic Interaction on Structure and Mechanical Properties of Ice Templated Particle- Polymer Composite

We investigate the effect of particle- polymer interaction on structure and mechanical properties of ice templated particle-polymer composites. We have already seen that these composites are macroporous, with pore walls made of polymer coated particles. We tune the surface charge of particles embedded in a macroscopic monolith by immersing the composites in water maintained at different pH. In this way we tune the polymer- particle interaction in the composite. We observe a sudden increase in interparticle distance and subsequent swelling of composite when the pH is decreased below the particle's isoelectric point. Correspondingly, we observe reduction in Young's and shear moduli, compression strength and macroscopic energy dissipation. Interestingly, we did not see any pH dependent changes in pure polymer sponges. Therefore, the pH dependent structural and mechanical property changes arise from the composite structure rather than purely from the crosslinked polymer. We believe that the reduction in mechanical stiffness when the polymer- particle interaction becomes repulsive is because of the reduction in interfacial contacts between particle and polymer. Therefore the mechanical stiffness of ice templated composite is strongly influenced by interactions between the polymer and particle surface.

6.1 Introduction

Controlling the interactions between different constituent components is critical to the performance of a wide variety of systems.[1-4] For example, it has been suggested that electrostatic repulsion in the polyelectrolytes that comprise articular cartilage permits frictionless mechanical motion within joints.[5] Repulsive interactions from magnetic or electrostatic forces are leveraged in maglev trains[6] and in vehicle suspensions[7]. In advanced polymer composites, strong attractive interactions between fillers and the polymer matrix is key to improving mechanical properties.[8] Therefore, it is fair to state that control over interactions between the constituent components of complex systems have implications in Nature as well as for the design of technological devices and novel materials.

In polymer composites, blending a small amount of high performance micro/ nano particle fillers into a polymer matrix as a dispersed phase can improve properties including the mechanical strength, thermal and electrical properties and gas separation efficiency.[8] However, the biggest challenge in realizing the full potential of composite material stems from insufficient control of interfacial contacts between polymer and particle components. Weak binding between polymer matrix and particle causes void structures and particle aggregation, while strong binding can generate densified layers around the particle surfaces.[9]

There are experimental and theoretical studies that relate molecular interactions at the polymer-particle interface with the properties of particle filled polymer composite interfaces at nanoscale.[10-13] Hopkinson et al. have performed lattice Monte Carlo simulation to study the effect of particle- polymer interaction and geometry of particle on density distribution and the free volume of polymer at the interface.[14] They have used particles with smooth and brush like surfaces and polymer chains with different flexibility. They showed that the degree of surface interaction significantly dominates the polymer density in the region close to the particle surface. The effect of surface interaction decreases further away from surface. For neutral interaction between the polymer and surface, the polymer density at the interface and in the bulk are similar, viz. there is no densification near the particle surface. When the surface is weakly repulsive to the polymer, the surface density of polymer becomes slightly lower than that in the bulk. Polymer density at the particle surface decreases much more in the case of strong repulsion. Additionally, Hopkinson et al. have also shown that polymers confined between brush grafted particles show lower polymer density at all types of interactive surfaces due to the disruption in polymer chain packing by the brush structure.[14] Particle- polymer interactions also affect the polymer free

volume near the particle surface.[15] Attraction leads to lower free volume compared to the case where there are no interactions.

Interaction between particle and polymer also leads to polymer conformational changes.[16] In close proximity to particle surfaces, polymers undergo structural deformations due to reduced entropy and decrease in conformational freedom at the interface. When the polymer-surface interaction is attractive, the polymer chains spread on the surface to adopt a compact pancake conformation. However, for repulsive surfaces, the polymer chains can undergo a random walk perpendicular to the surface. Additionally, Hopkinson et al. have shown that the polymer chain length does not significantly influence polymer-particle interfacial properties such as density, free volume and extent of deformation.[14]

Apart from polymer-surface interactions, surface roughness also influences the extent of polymer adsorption on a particle surface. In physical roughness, hills and valleys are present on the particle surface. Local curvature and the nature of surface potential sway the competition between adsorption on hills and valleys. Muthukumar et al. showed that surface roughness in the nanometer length scale plays a role in adsorption- desorption phenomena of a single polymer chain.[13] They had shown that desorption of a chain from rough surface is more difficult than from a flat surface. This is because the number of contacts per chain with the particle surface is higher on rough compared to flat surfaces.

The nature of the interfacial interactions between polymer and particle determines the mechanical stability of composites.[17] Interfacial strength of the composite strongly depends on the stress transfer between particle and polymer. Attraction between polymer and particle leads to strong interfacial bonding. Therefore applied stress can be effectively transferred to the particles from the polymer matrix. This improves the strength and toughness of the composite. However, for particle filled systems, it has been reported that the Young's modulus force is independent of interfacial strength since it is measured at low deformation where there is insufficient dilation to cause interface separation.[17] Repulsive interaction between polymer and particle leads to void formation at the interface. These voids are weak points and initiate failure at the interface when the material is deformed to larger strain. Therefore, polymer-particle repulsion decreases the mechanical strength in contrast to attractive forces. However, in certain cases these voids have been beneficial. For example, articular cartilage strikingly illustrates how electrostatic repulsion can be harnessed to achieve exceptional efficiency.[18, 19] Here, voids allow virtually frictionless mechanical motion within joints even under compression.

In addition to these, interaction between polymer and particle also influences the glass transition temperature (T_g) of polymer composites. Change in T_g is correlated with changes in diverse transport phenomena as well as chain relaxation behaviour.[20] Experimental and theoretical studies have indicated a tendency for highly attractive or repulsive particle–polymer interactions to increase or decrease T_g respectively.[21, 22] This phenomenon has been rationalized in terms of the influence of the particle boundary interactions on the dynamics of polymers within an interfacial layer near the particle surface. In particular, polymer chains in direct contact with the particle shows a slowing down or acceleration of dynamics when the polymer-particle interactions are attractive or repulsive respectively.[22]

However, these all observations were for particle filled composites where we have bulk polymer, interfacial polymer and particle fillers. In 2014, Srivastava et al. have demonstrated the formation of salt tunable two dimensional nanoparticle arrays at the air-water interface.[23] Here, electrostatic attraction between the negatively charged DNA coated gold nanoparticle and positively charged lipid layer at the interface facilitated the formation of a two dimensional hexagonally close packed nanoparticle lattice. They have controlled the interparticle spacing in these 2D arrays by changing the salt concentration. Addition of salt controlled the particle-particle and particle-DNA interactions. In this way they could better tune the particle arrays. However, the effect of these structural changes on mechanical properties of these particle arrays is yet to be understood. In this work, we are trying to understand how the polymer-particle interaction influences the structure and mechanical properties of three dimensional hybrids primarily made of particles.

Recently, Rajamanickam et al. have reported the synthesis of a macroporous three dimensional particle- polymer composite by ice templating.[24] In contrast to conventional polymer composites, these composites are highly filled but do not fail at large deformations. To make these composites, they used cationic, amine containing polymers and negatively charged particles. Here, the polymer forms a thin layer of coating on the particle surface due to electrostatic interactions between them. The excess polymer goes into the interparticle regions during ice templating. Later, the assembly is crosslinked in the frozen state. These ice templated composites are macroporous with pore walls comprised of polymer coated particles. Our previous small angle X-ray scattering study (Chapter 2) showed that the interparticle distance in these pore walls is only about 1- 2 nm even though we add 10-15 times excess amount of polymer as compared to that required for monolayer coverage on particle surface. Rajamanickam et al. had shown that this microstructure results in soft monoliths, with moduli ~O (10^4 Pa), despite the very high particle content in their walls.[24] These soft monoliths can be compressed to larger strains (~90%) and they recover to the initial state while releasing the load in contrast to typical

brittle particle assemblies. It is intriguing to understand how the interaction between polymer and particle influences the mechanical response of these soft colloidal monoliths. To study this we can either compare the performance of materials made from oppositely charged particle and polymer with the material made from similarly charged polymer and particle or tune the surface charge of particle or polymer within the scaffold using external stimuli and study the corresponding mechanical properties. However, at low polymer concentration (<25 wt %), self standing monoliths do not form if the surface charges of particle and polymer are the same. So the first approach does not work in our case. Therefore, here we vary the surface charge of particle present in the monolith by using external stimuli, viz., pH and study the effect of polymer- particle interaction on mechanical properties of these monoliths.

6.2 Experimental

6.2.1 Materials: Ludox®-TM 50, polyethylenimine (PEI, 25 kDa), 1,4-butanediol diglycidyl ether, pH 10,7,4 and 2 buffers were obtained from Sigma Aldrich. 1μm 'Angstrom sphere' spherical silica particles were purchased from Richen Industry Ltd, Hong Kong. Distilled deionised water was obtained from a Millipore Milli- Q unit (18.2 MΩ. cm). All the chemicals were used as received.

6.2.2 Methods:

Synthesis of hematite (Fe_2O_3) particles: *Hematite particles were synthesized by Mr. Hisay Lama from the group of Prof. M G Basavaraj from IIT Madras and were supplied to us.*

Briefly, the synthesis proceeded as follows. Perchloric acid iron (III) salt hydrate ($Fe(ClO_4)_3$. xH_2O, 98%) was obtained from Sigma Aldrich and urea ($(CO(NH_2)_2$, 99.5%) was purchased from Merck, India. Hematite particles were synthesized by the hydrolysis of Fe^{+3} in the presence of urea.[25] 9.246 g of $Fe(ClO_4)_3$ and 1.2012 g of urea were added into 200 ml of Milli-Q water in a clean glass bottle followed by oven heating at 100^{o}C for 24h. The cooled reaction product is centrifuged at 6000 rpm for 30 min and washed with Milli-Q water multiple times. This step is repeated until the supernatant is clear.

Protocol for the synthesis of scaffolds from colloidal particles:

Preparation of sponges from silica particles: 120 μl of Ludox®-TM 50 (50 wt %) silica particles were dispersed in deionised water (overall silica concentration in the dispersion is 10 wt %). This dispersion was sonicated for 30 min followed by 5 min vortexing. To this aqueous dispersion was added 6 mg of polyethylenimine (PEI, 60 μl of 100 mg/ml stock solution) and the mixture was vortexed for 10 min. To this was added 6μl of 1,4-butanediol diglycidyl ether crosslinker by vortexing for 2-3 min. Then the

sample was immediately transferred to a -18 ^{o}C freezer and it was stored at that temperature for 24 h for the crosslinking reaction between amine groups of PEI and epoxy groups of 1,4-butanediol diglycidyl ether. After 24h, the sample was removed from the freezer and washed thoroughly in distilled water followed by lyophilization at -110^{o}C under vacuum for 6 h to thoroughly dry the sponges. To prepare scaffolds from 1μm silica particles, we have used 60 mg silica, 4 mg PEI and 4 mg 1,4-butanediol diglycidyl ether. Scaffolds were prepared using the same protocol as described for the Ludox particles.

Preparation of sponges from hematite particles: 60 mg of hematite particles were dispersed in an aqueous solution of pH 10 (corresponding to a concentration ~ 10% w/v). The amount of polymer and crosslinker used was 5 mg PEI and 5 mg 1,4-butanediol diglycidyl ether. All other steps are the same as in silica sponge preparation.

6.2.3 Characterization:

6.2.3.1 pH and zeta potential measurements: pH of dilute particle dispersion is adjusted by the addition of acetic acid or NaOH solutions of known concentration. pH of the suspension is measured using Mettler Toledo™ SevenCompact™ pH meter. The zeta potential (ζ) of particles at different pH is obtained from electrophoretic mobility of particles measured using Zeta PALS (Brookhaven Instruments Corp., Holtsville, NY, USA). The particle mobility (ν_E) is obtained using dynamic light scattering and is related to the zeta potential at the slip plane through the Smoluchowski equation[26]

$$\nu_E = 4\pi\varepsilon_0\varepsilon_r \frac{\zeta}{6\pi\mu}(1 + \kappa r)$$

where, ε_0, ε_r are the dielectric constant and relative electrical permittivity of vacuum respectively. μ is the solution viscosity, r is particle radius, κ is the Debye- Huckel parameter ; $\kappa = (\frac{2n_0 z^2 e^2}{\varepsilon_r \varepsilon_0 k_B T})^{0.5}$, n_0 is the bulk ionic concentration, z is the valence of the ion, e is the charge of an electron, k_B is the Boltzmann constant and T is the absolute temperature.

6.2.3.2 Rheology: Rheological measurements were performed using TA ARES G2 strain controlled rheometer equipped with normal force transducer. Dry sponges were dipped in different pH solutions for a minimum of 2 days before performing oscillatory shear and compression experiments. To prevent slippage, all measurements were performed using roughened parallel plates. Compression experiments were performed to determine the change in normal force with compression using transient force-gap test. This was performed at strain rate of 0.1 mm/s. Nominal compression stress was calculated from the normal force and using the initial sample cross sectional area. We performed dynamic frequency sweep

measurements in the linear viscoelastic regime from 0.1 to 100 rad/s on scaffolds soaked in water at different pH.

6.2.3.3 Small- angle X-ray scattering (SAXS): Small angle X-ray scattering was performed on a system by Rigaku. This instrument is equipped with a micro-focus rotating anode X-ray generator and a confocal max flux mirror, three pinhole collimators and a two dimensional detector (HyPix-3000). The detector is calibrated using silver behenate standard. Experiments were performed at room temperature (~25^{o}C). The data was circularly averaged and the 1D scattered intensity is presented after background subtraction, corrected for sample transmission. SAXS data was analyzed using SASFIT.

6.2.3.4 Scanning Electron Microscopy (SEM): Sample morphology was imaged using a Quanta 200 3D scanning electron microscope (SEM).

All measurements were repeated at least 7 times to confirm their reproducibility.

6.3 Results and Discussion

6.3.1: Characterization of particles

We begin by characterizing the features of Ludox silica particles. SAXS on a dilute solution of Ludox silica particles (2 wt%) was fitted to a polydisperse sphere model with Schultz- Zimm size distribution. We obtain a particle radius of 11.09 nm with a polydispersity parameter of 0.14 (Figure 6.1a). This is consistent with the manufacturer specified particle radius of ≈ 22 nm.

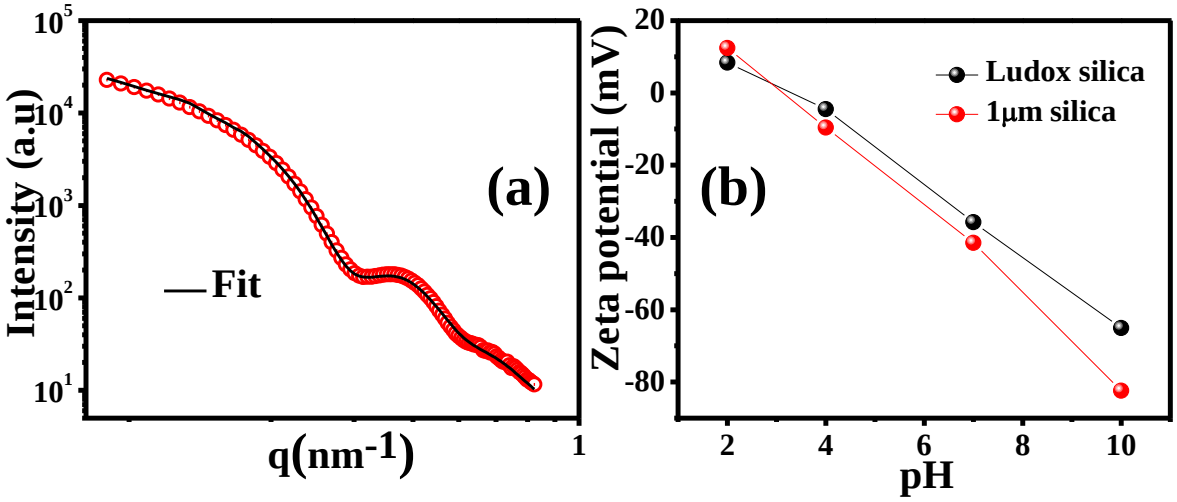

Figure 6.1: Characterization of silica particles. **(a)** Small angle X-ray scattering from a dilute solution of Ludox®-TM silica particles in water (~2 wt%). Open circles are the experimental data and the solid line is a fit to a polydisperse sphere model. **(b)** Zeta potential- pH profiles of Ludox® and 1μm silica particles.

Surface charge of the silica particle is characterized in terms of zeta potential (Figure 6.1b). We observe that the zeta potential decreases with pH. At sufficiently low pH, it is positive (+9 mV at pH = 2), but becomes negative at higher pH (-5 mV, -36 mV and –66 mV at pH = 4, 7 and 10, respectively). This behaviour is independent of silica particle size. As with the case of the Ludox nanoparticles, 1 micron silica particles exhibit a positive zeta potential below pH 3 (+13 mV at pH = 2) and become increasingly negative with increasing pH (-10 mV, -42 mV and –83 mV at pH = 4, 7 and 10, respectively, Figure 6.1b).

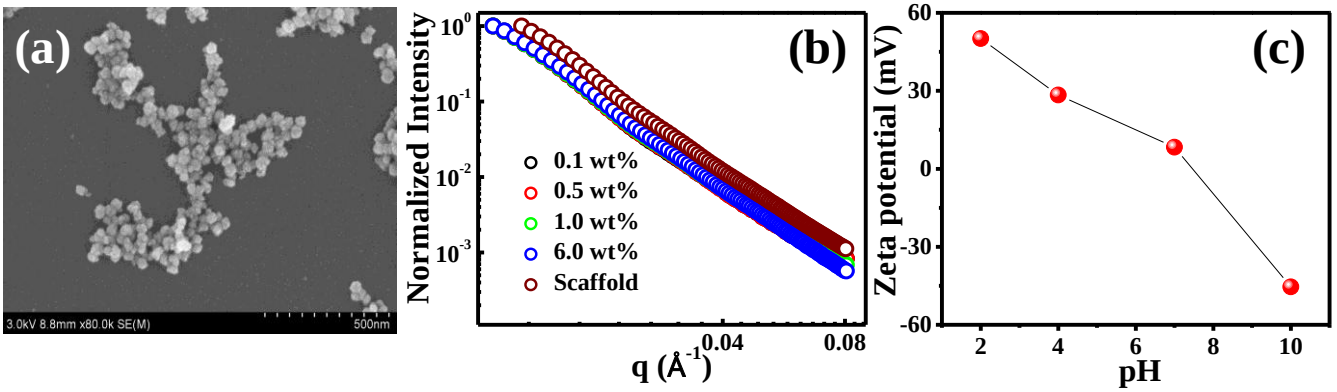

Figure 6.2: Features of hematite particles. **(a)** SEM shows hematite particles are irregularly shaped. Particles are always imaged as clusters with individual particle size ~50 nm. (**b**) SAXS profiles of solutions of hematite particles with different concentrations. The plotted intensity-q profiles are normalized with its concentration. **(c)** Zeta potential- pH profile of hematite particles.

We have also characterized hematite nanoparticles obtained from the group of Prof. Basavaraj, IIT-Madras. SEM image shows these particles form clusters of particles, each of which is ~50 nm in size (Figure 6.2a). To check whether these particles remain clustered in the solution state, we performed SAXS on solutions of hematite particles. We examined four different concentrations of hematite particle dispersions (0.1, 0.5, 1 and 6 wt %) and these were sonicated for 2 h prior to the experiments. We observed a systematic increase in intensity with increase in particle concentration. However, the intensity profiles of these samples normalized with concentration overlapped to within experimental error (Figure 6.2b). This indicates that the particles are clustered even after sonication for a long time and the cluster size is beyond our instrument resolution. Therefore, we did not see any difference in SAXS profiles of dilute and concentrated particle solutions. The increase in scattering intensity with particle concentration is due to the increase in number of scatters in the solution. Zeta potential shows that hematite particles reverse their surface charge around pH ~8 such that the particles are negatively

charged above pH 8 (-46 mV at pH = 10) and are positive at lower pH (9 mV, 29 mV and 50 mV at pH = 7, 4 and 2, respectively) (Figure 6.2c). It has been reported that this is due to the adsorption of H^+ and OH^- ions on the particle surface.[27]

6.3.2: Composites made from these particles and their features at varying pH

a) Scaffolds made from Ludox silica particles

We use Ludox particles to make porous hybrid composites. As discussed in the previous Chapters, particles are coated with polymer in an aqueous media and this dispersion is ice templated to obtain a macroporous scaffold with pore size varying between 30-120 microns (Figure 6.3). Here, we add excess polymer relative to that required for monolayer coverage of particle surface. In Chapter 3, we demonstrate that pore walls are constituted by particles that are enmeshed in the crosslinked polymer. SAXS study in Chapter 2 showed that the interparticle spacing in these composites is ~1-2 nm therefore the crosslinked polymer is highly confined between particles.

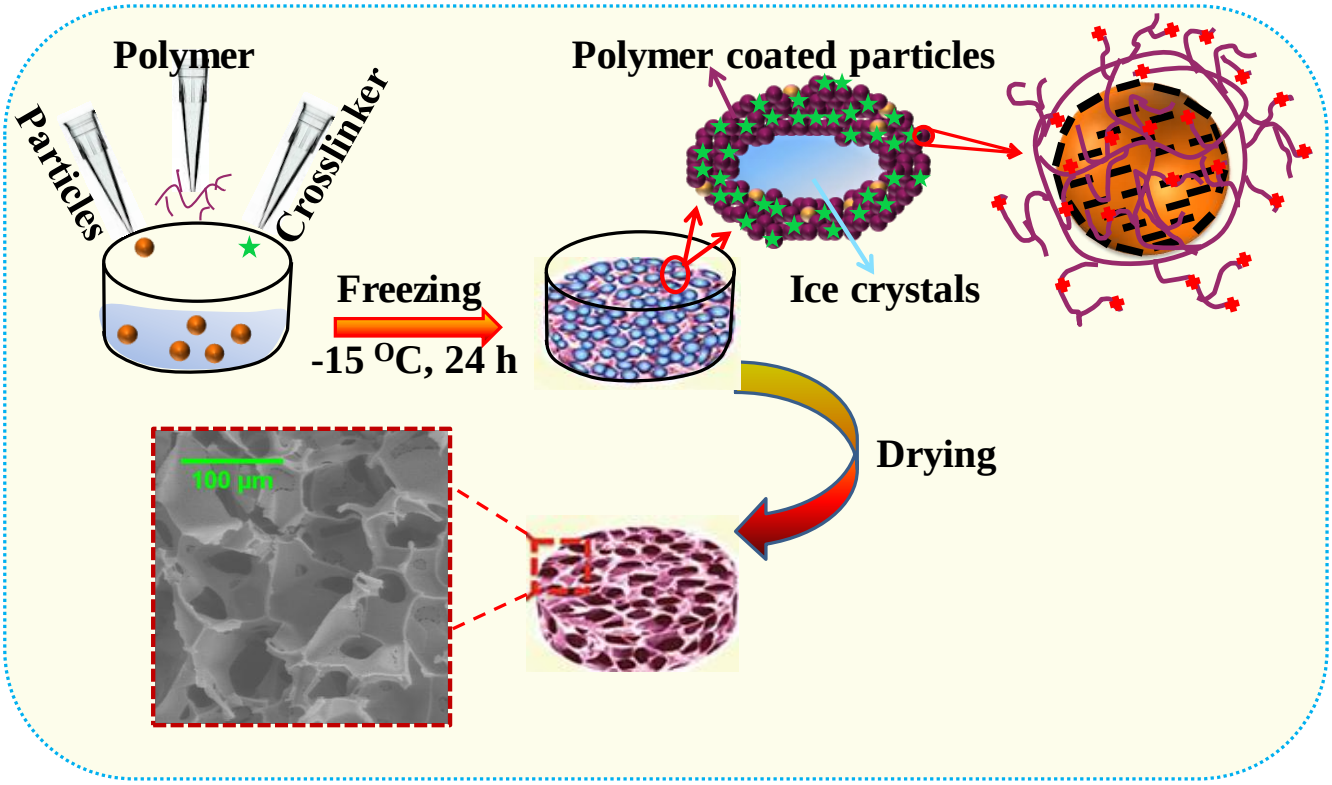

Figure 6.3: Protocol for the preparation of ice templated particle- polymer composite. SEM image depicts the macroporous morphology of particle- polymer composite.

We dipped these dry scaffolds in aqueous solutions of varying pH in the range of 10 to 1. Here, the pH is adjusted using acetic acid and NaOH. Scaffolds were soaked in solutions of the required pH

for over 2 days prior to measurement. Scaffolds expand macroscopically when swollen in water. This expansion in the diameter of the swollen scaffolds is greater for pH < 3 (dry state– 7.9 mm, at pH 2– 8.9 mm) than at higher pH (8.3 mm at pH = 10).

We characterized the structure of scaffolds at different pH using small angle X-ray scattering (SAXS). SAXS from scaffolds shows an extra hump at low q compared with SAXS from dilute silica dispersions (Figure 6.4a). This comes from particle correlations and represents scattering due to interference effects in dense systems. This particle interference can be expressed in terms of structure factor. We calculate an apparent structure factor ($S_A(q)$) by normalizing the SAXS data from scaffolds by scattering from a dilute dispersion of the silica nanoparticles (Figure 6.4b). We modeled the first peak of $S_A(q)$ using an interference function which gives the averaged interparticle distance in pore walls (Figure 6.4c). The interference function is expressed as:

$$S_A(q) = A_2[1 + k\emptyset(q)]^{-1}$$

and $\emptyset = \frac{3sinqd - qdcosqd}{q^3 d^3}$

where, A_2 is a constant, k is the packing factor and d is the interparticle spacing.[28]

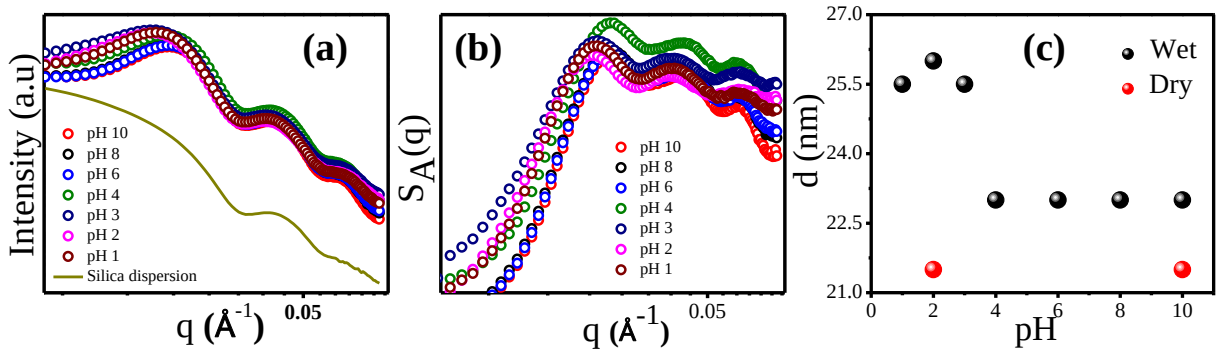

Figure 6.4: SAXS study on composites at different pH. **(a)** SAXS for the scaffolds at different pH: Intensity as a function of scattering vector, q. **(b)** Apparent structure factor calculated for samples at different pH. **(c)** Interparticle distance obtained by fitting the first peak of apparent structure factor. Interparticle distance calculated for scaffolds dried after soaking for several days at pH 2 and pH 10 (red spheres) showed same value.

SAXS data for scaffolds at a pH below 4 shows a slight shift to low q compared to pH 4 and above with a notable broadening in the intensity profile at low q (Figure 6.4a). Similar shift can be seen in the position of first peak of $S_A(q)$ (Figure 6.4b). The interparticle distance, *d*, in the scaffolds is estimated as 23 nm, essentially independent of pH between 10 to 4 (Figure 6.4c). However, there is a rapid jump in *d* from 23 nm to ~ 26 nm as pH is decreased to between 3 and 1. This effect is observed only for scaffolds solvated at different pH. When we lyophilized samples initially maintained at pH = 2 and pH = 10, we observed that both the dry samples had the same interparticle distance = 21.5 nm (Figure 6.4c). Therefore, the discontinuous increase in interparticle distance indicates an expansion at the particle level in a solvent swollen scaffold when it is exposed to pH below 4. This correlates with the observation that the macroscopic dimensions of the bulk scaffold expand below pH 4.

The change in interparticle distance and macroscopic dimensions of the samples as a function of pH is reversible. We sequentially immersed the same scaffold in solutions with pH varying from 10 to 2, then 2 to10 followed by 10 to 2 and measured *d* at each step in this cycle (Figure 6.5). Before each measurement, we washed the sample in Milli-Q water for two days and lyophilized it, and then immersed in solution at the desired pH for 2 days. Interparticle distances in the scaffolds vary from 26.5 nm at pH = 2 to 23 nm at pH = 10 and this variation with pH is reversible.

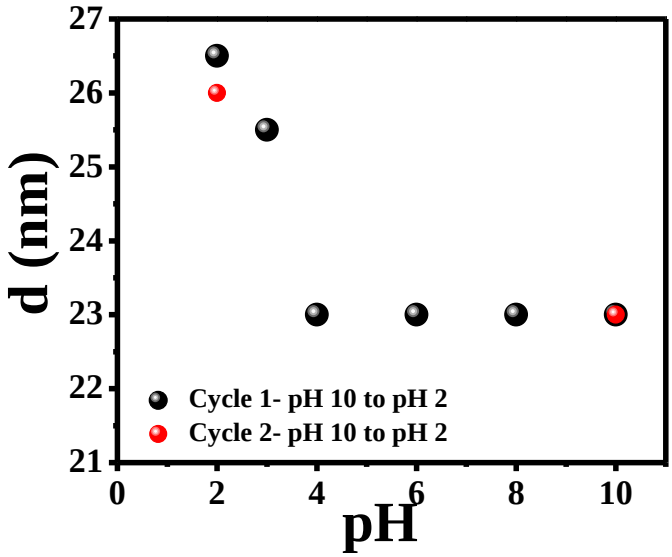

Figure 6.5: Reversibility of interparticle distance. In cycle 1, pH was varied from pH 10 to 2. In cycle 2, the scaffold was thoroughly washed, dried and then immersed in pH 10. Subsequently, the pH was adjusted to 2.

We now examine the mechanical properties of these composite scaffolds at various pH. Scaffolds were compressed to small strains and the Young's moduli (E′) were calculated from the slopes of stress- strain curves (Figure 6.6a). There was a decrease in E', from 80 kPa at pH = 10 to 65 kPa at pH = 4. There was an abrupt decrease in the Young's modulus to 30 kPa for scaffolds immersed at low pH = 3, 2 and 1.

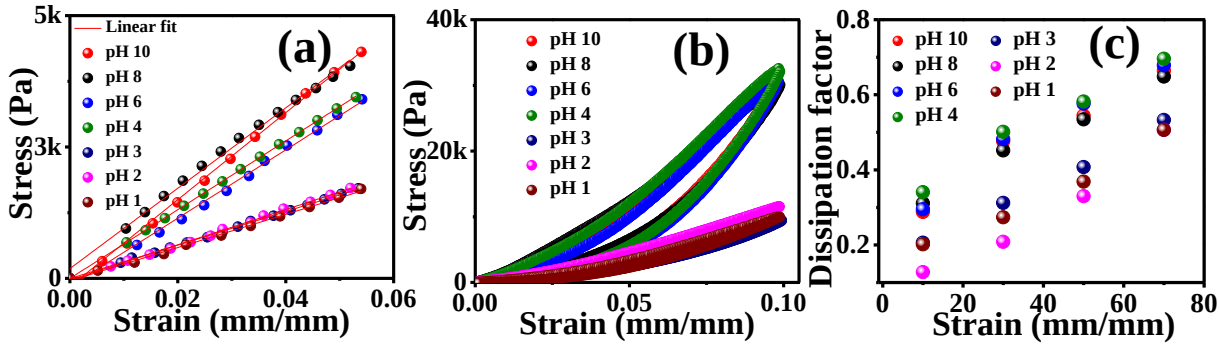

Figure 6.6: Compressive stress-strain measurements on Ludox particle- polymer composites at different pH. (**a**) At low strain, the stress is linear in strain. We obtain the Young's modulus from the stress- strain curve for low strains ~5% (**b**) Nominal stress as a function of nominal strain during compression- expansion of ice templated composite at different pH. (**c**) Dissipation factor: area inside the stress- strain curve of compression- expansion cycle normalized by area of compression cycle is plotted for composites at different pH, and for different extents of compression.

We performed a cycle of compression, followed by expansion to zero strain of these composites at various pH. At all pH the scaffolds recover fully, even after compressing to a large strain (Figure 6.6b and Figure 6.7). Therefore scaffolds are elastic at all pH. However, the maximum stress developed for a particular strain is higher for samples at pH 4 and above. For example, at 10% compressive strain the sample at pH 4 and above showed a maximum stress of 33 kPa and below pH 4 the same sample exhibits a value of 10 kPa (Figure 6.6b).

The compression- expansion curves at all pH showed hysteresis (Figure 6.6c). The area between the compression- expansion curves represents the energy dissipation per unit volume of the monolith during one compression-expansion cycle. We express this quantity in terms of the dissipation factor which is the area between compression and expansion curves normalized by the area under the compression curve. Scaffolds at pH above 4 exhibited larger hysteresis when compared to at lower pH less than 3. For example, the dissipation factor calculated for 50% compressive strain is almost double at pH 10 (0.55) compared to that at pH 2 (0.31). Similar trend is observed for other strain values as well (Figure 6.6c and Figure 6.7).

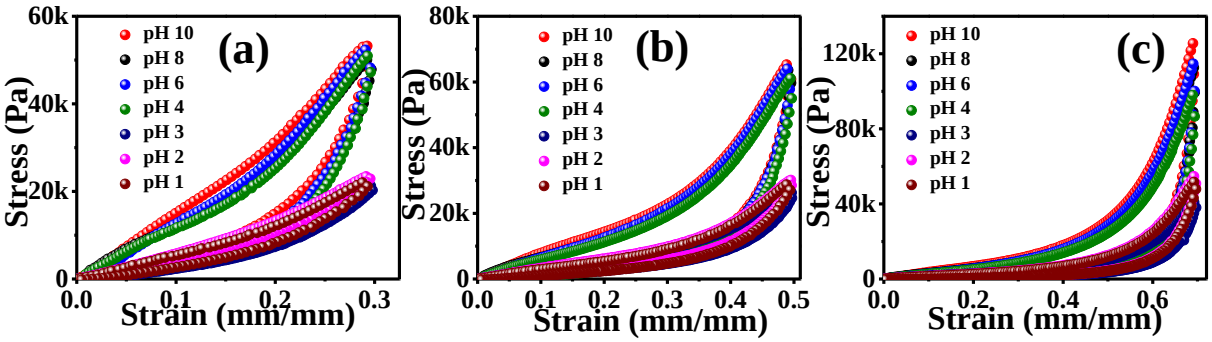

Figure 6.7: Compression- expansion behaviour of Ludox® sponges at different compressive strains: **(a)** 30% **(b)** 50% and **(c)** 70%. At all compressive strains, scaffold shows a decrease in mechanical properties for pH below 4.

The elastic (G′) and viscous (G″) moduli obtained from shear rheology also show significant differences for samples at high and low pH (Figure 6.8). Monoliths at pH 10 exhibit almost 4 times higher elastic modulus and 6 times higher viscous modulus compared to that at pH 2.

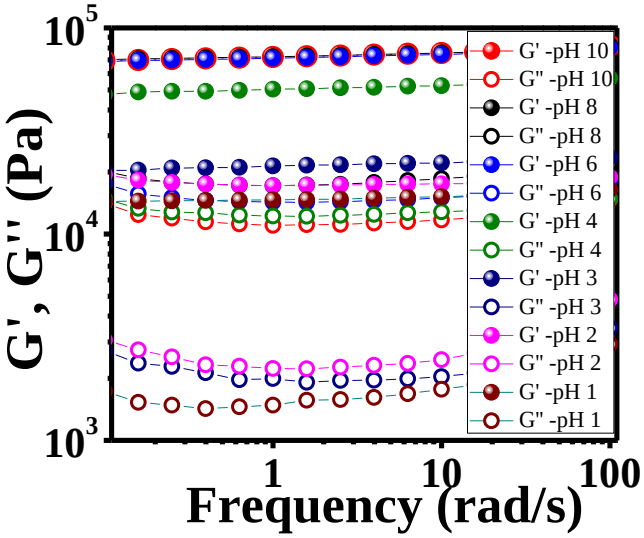

Figure 6.8: Shear rheology of sponges performed at 0.25% shear strain. Below pH 4, elastic (G′) and viscous (G″) moduli show a significant decrease.

We tested the reversibility of the mechanical response by subjecting the same sponge to pH ranging from 10 to 2 and vice versa (Figure 6.9). Hysteresis and maximum compressive stress increased while changing the pH from 2 to 10 and decreased to the initial value, within experimental error, when the pH was decreased to 2 (Figure 6.9a). The Young's (Figure 6.9b) and shear (Figure 6.9c) moduli also showed a similar trend.

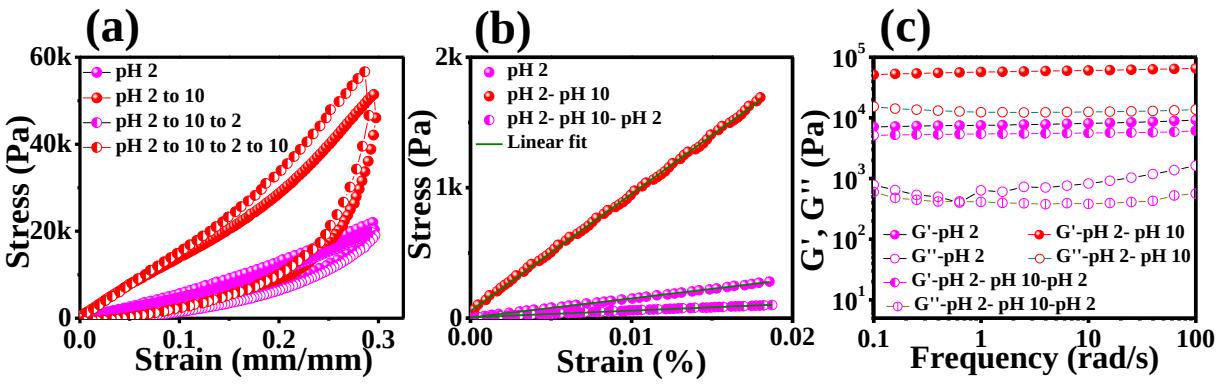

Figure 6.9: Reversibility of the mechanical response of sponges with changing pH: **(a)** Compression- expansion study on a sponge at pH 2 followed by a pH variation to 10. Cycle again repeated by varying pH to 2 and further to 10. Reversibility of **(b)** Young's modulus and **(c)** shear modulus while switching pH from 2 to 10 and again back to pH 2.

We now examine if these findings are restricted to Ludox nanoparticles, or if they are dependent on size, polymer and particle chemistry.

b) Scaffolds made from 1μm silica particles: Effect of particle size and surface chemistry on pH dependent scaffold response

We prepared scaffolds with aqueous dispersions of 1μm spherical silica particles using the same protocol. Ludox and the 1 μm silica are different in terms of their size. Similar to sponges made from Ludox, these scaffolds also exhibited macroporous morphology (Figure 6.10a) and in Chapter 4 we have seen that the majority of pores in this scaffold are in the range of 30– 70 μm.

Mechanical studies of these scaffolds were carried out for samples immersed at different pH. We confirm that the size of the particle used to prepare the scaffold does not influence its mechanical response. We have compressed the scaffolds to small strains so that the Young's moduli (E′) were calculated from the slopes of stress- strain curves (Figure 6.10b). There was a decay in E′ from 72 kPa at pH=10 to 49 kPa at pH=4. The value was further decreased to 23 kPa when the pH was adjusted to 2. Therefore, we observe a ~3.2 times decrease in sample stiffness when pH is decreased from 10 to 2. This is similar to Ludox sponges where we saw 2.6 times reduction in stiffness while changing the pH from 10 to 2. Maximum compressive stress at particular strain also showed a similar trend. For example, at 50% strain, the stress was 52 kPa at pH=10 and the value decreased to 40 kPa for pH= 8, 6 and 4 (Figure 6.10c). Below pH 4, stress further decayed to 20 kPa. Additionally, storage and loss moduli obtained from shear rheology showed a continuous decrease with decrease in pH from 10 (G′=39 kPa, G″= 4 kPa) to 1 (G′=13 kPa, G″= 2.5 kPa) (Figure 6.10d).

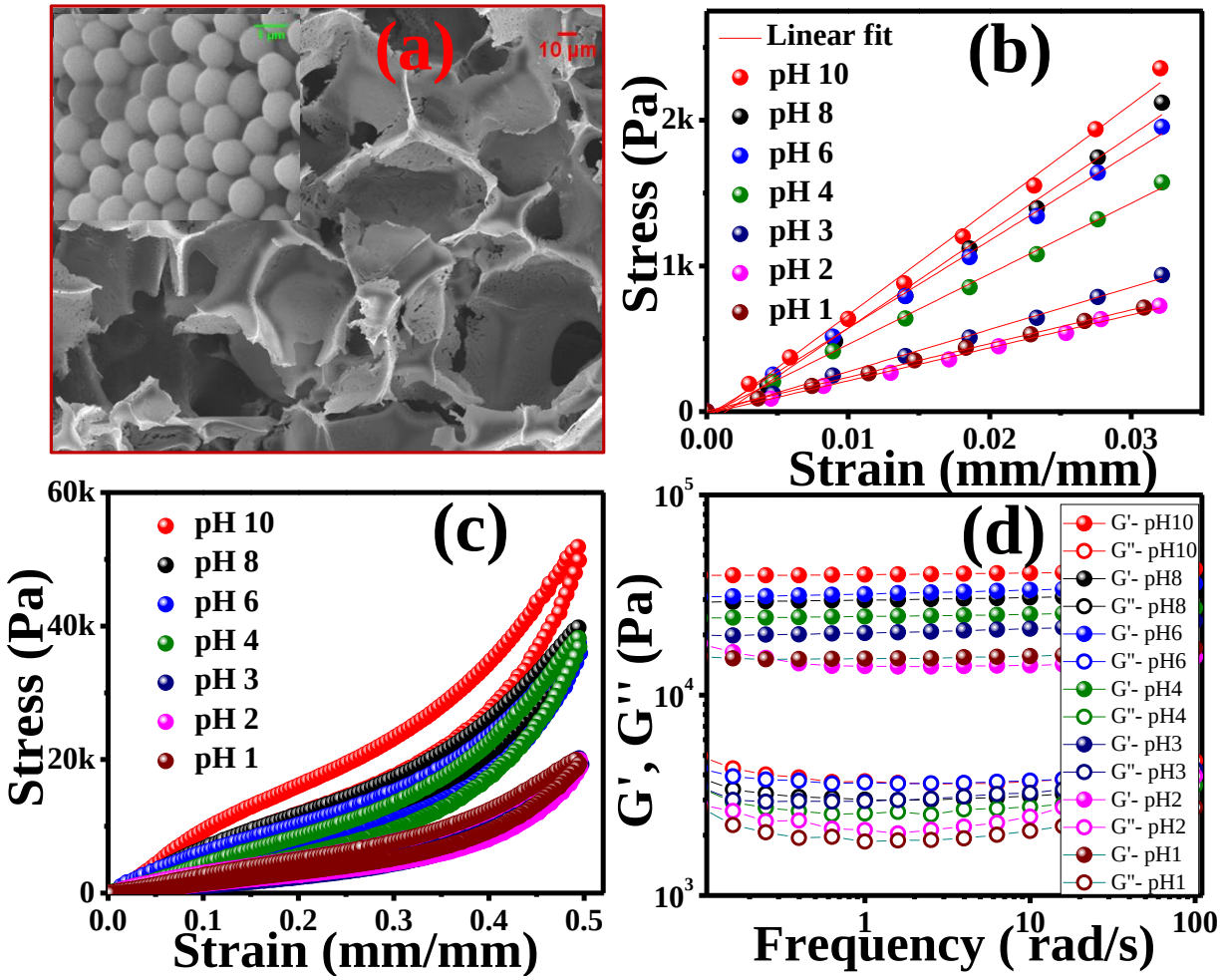

Figure 6.10: Characterization of 1µm silica particles and scaffold prepared from them. **(a)** SEM morphology of scaffolds. Inset SEM shows a magnified view of the pore wall. **(b)** At low strain, the stress is linear in strain. We obtain the Young's modulus from the stress- strain curve for strains ~3.5% **(c)** Compression- expansion behaviour of silica scaffold at 50% compressive strain. Stress- strain curves show an abrupt decay in property below pH 4 as in case of Ludox® sponges. **(d)** Shear rheology of 1µm silica sponges. Elastic (G′) and viscous (G″) moduli show a decrease while reducing the pH from 10.

For composites comprising > 80% by weight of inorganic, the modulus values of the scaffold are very low. Therefore, we believe that the mechanical response of the scaffold is primarily a reflection of the crosslinked polymer mesh that forms a matrix for the particles. Does the pH dependence of the scaffold properties arise from the composite structure, or is it simply a function of the crosslinked polymer mesh? To understand this, we examined the behaviour of scaffolds prepared only from crosslinked polymer at different pH.

c) Behaviour of pure polymer sponges at different pH

Crosslinked PEI sponges were prepared by ice templating aqueous PEI/ di-epoxy solutions in the absence of particles. SEM of the scaffold reveals a foam-like interconnected porous structure with an average pore diameter of 50 μm, with pore walls comprised of cross-linked polymer (Figure 6.11a). We performed compression expansion studies of these sponges immersed at different pH and observe that pH has negligible influence on the mechanical response (Figure 6.11 b-d). Both the Young's modulus (Figure 6.11b) and compression-expansion curve (Figure 6.11c) show no systematic dependence on pH. This is true at all compressive strains (Figure 6.11d). There is, however, a marginal increase in maximum compressive stress when pH is decreased from 10 to 2 (Figure 6.11 d). This suggests that the pH-dependent variation in mechanical properties of the composite scaffolds arises from the composite structure and not just from the response of the crosslinked polymer.

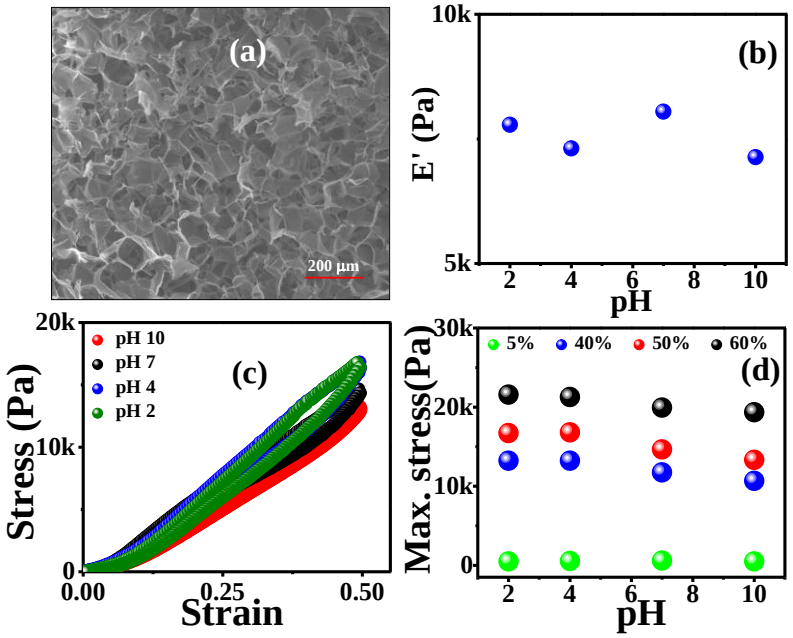

Figure 6.11: Effect of pH on polymer sponges. **(a)** SEM of the scaffold reveals a porous architecture. The pore walls of the scaffold are comprised of cross-linked PEI. **(b)** Young's moduli of polymer sponges at different pH. **(c)** Compression- expansion study at 50% compressive strain for polymer sponge at different pH. **(d)** Variation of maximum compressive stress at different % compressive strains as a function of pH.

d) Effect of particle chemistry on pH dependent scaffold behaviour

Another particle with a different surface behavior compared to silica, was also templated under similar conditions. The particle chosen in this case was hematite and we have already seen that these are clustered particles (Figure 6.2b). To make scaffolds from these particles, a dispersion of the particles in pH 10 aqueous solution was prepared and this was ice templated

as described in the methods section. At this pH, the particles are negatively charged. Therefore, cationic PEI electrostatically adsorbs on its surface. The final scaffolds are macroporous with a majority of pores in the range of 20–70 μm (Figure 6.12). The pore walls are made of irregularly shaped particles (Figure 6.12, inset). We performed small angle X-ray scattering on these scaffolds and the intensity profile matches exactly with the profile obtained from particle dispersions (Figure 6.2b). This again confirms that the particles are clustered. In contrast to the scaffolds prepared using the silica particles, the walls of the scaffolds prepared using hematite are perforated with holes that are a few microns in size. The origin of these pores is not clear at present. However, we speculate that the holes arise due to difficulty in packing the irregularly shaped hematite particle aggregates during ice templating.

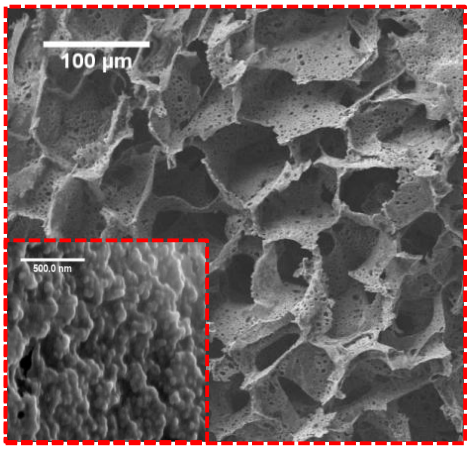

Figure 6.12: Macroporous morphology of hematite scaffold with pore size varies from 20-70 μm. Zommed image of pore wall shows the presence of irregular shaped particles (inset).

Similar to silica sponges, the dry scaffolds were immersed in solutions at varying pH and we observed that the scaffolds at pH 7, 4 and 2 showed an expansion compared to those dipped in pH 10 (scaffold diameters were; pH 10= 8.18 mm, pH 7= 8.83 mm, pH 4= 8.83mm, pH 2= 9.04 mm) (Figure 6.13).

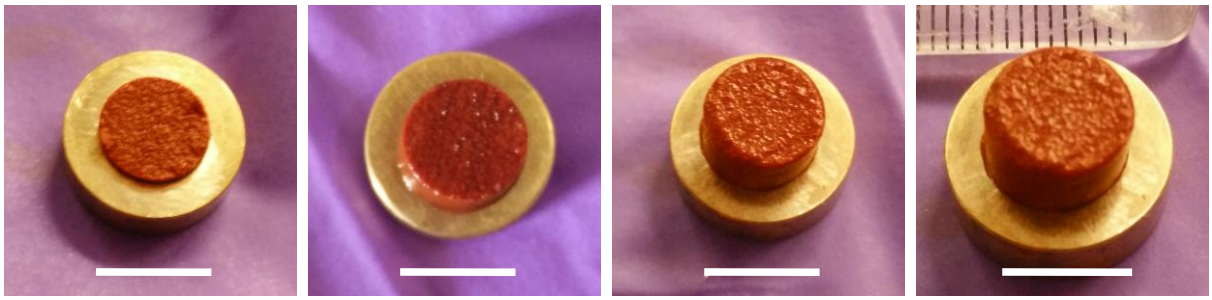

pH 10 pH 7 pH 4 pH 2

Figure 6.13: Hematite scaffold dimension at different pH. Scaffold shows an expansion while soaking in pH 4 and pH 2. White bars indicate the scale bar of 8.4 mm. At pH = 10, the scaffold fits into a metal sleeve with an inner cylindrical diameter of 8.4 mm. For scaffolds at lower pH (= 7, 4 and 2), the scaffold swells so that it no longer fits within the cylindrical opening.

We have also studied the mechanical properties of hematite scaffolds at various pH. We have compressed the samples to small strains and calculated the Young's moduli (E′) by taking the slopes of the stress- strain curves (Figure 6.14a). At pH 10, the scaffold exhibited E′ of 30 kPa which is almost 0.5 times lesser than the E′ values of silica sponges. This could be because of the smaller volume fraction of particles due to high density of hematite compared to silica. The E′ value further decreased to 18 kPa when the pH was reduced to 7 and decreased only marginally with further reduction in pH to 4 and to 2 (E′ = 15 kPa). We have also performed large strain compression- expansion study on hematite scaffolds. Similar to silica sponges, the hematite scaffolds are elastic and are able to recover from large compressive strains at all pH conditions (Figure 6.14b). However, the maximum stress developed for a particular strain showed an abrupt decrease when pH was decreased from 10 to 7. For example, at 30% compressive strain, the sample at pH 10 exhibits maximum compressive stress of 22 kPa. This value decreases to 8 kPa when the pH is changed to 7 (Figure 6.14b inset). The energy dissipation per unit volume, viz., area inside the stress strain curve, also reduced when pH decreased from 10 to 7, 4 and 2. For example, at 30% strain the dissipation factor is ~1.6 and at pH =2 the value reduced to 0.1.

The elastic (G′) and loss moduli (G″) obtained from shear rheology also showed that the hematite sponges are softer than the silica sponges (compare Figures 6.14c, 6.10d and 6.8). At pH= 10 and at 1 rad/s, G′ is about 12 kPa as compared to ~60 kPa and 45 kPa for the Ludox and 1μm silica sponges, respectively. Hematite sponges showed a reduction in G′ to 5.7 kPa when pH was reduced to 7 (Figures 6.14c). The value further reduced to 3.5 kPa

when the pH was reduced to 2 (at all pH, the G′ values are almost independent of frequency and we compare G′ values at 1 rad/s). G″ also reduced in a similar fashion when pH was reduced from 10 to 2.

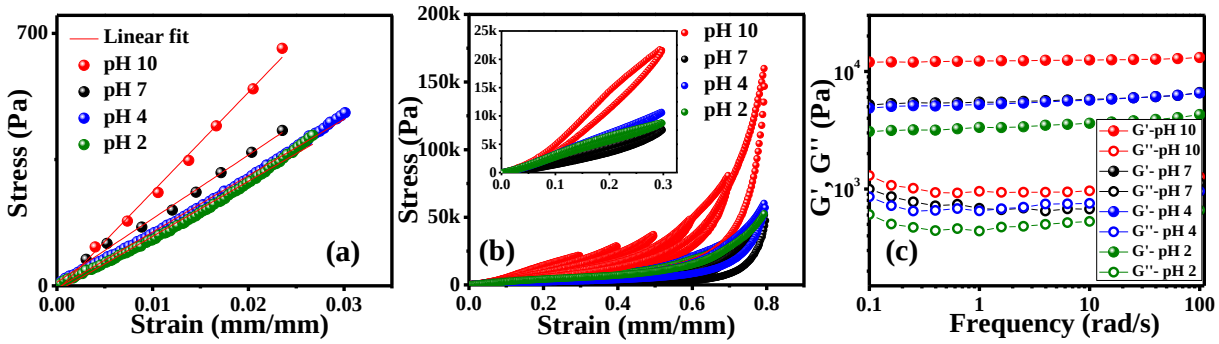

Figure 6.14: Hematite scaffolds at different pH. **(a)** At low strain, the stress is linear in strain. We obtain the Young's modulus from the stress- strain curve for strains ~2.5%. **(b)** Scaffolds at different pH were investigated using compression- expansion tests to different strains. Inset shows compression- expansion study at 30% compressive strain. **(c)** Dynamical mechanical response of hematite sponge soaked in different pH solutions. Experiments were performed in the linear viscoelastic regime with a shear strain of 0.25%. Elastic and viscous modulus shows a decrease from pH 10 to 7.

Our study showed an abrupt decrease in mechanical properties for silica and hematite sponges upon decrease in pH below a certain value. It is interesting to note that although the two sponges are made of different particles, they show qualitative similarities in their pH dependent variation in mechanical properties near the isoelectric point.

The measured interparticle distance of 23 nm in scaffolds made up of 22 nm Ludox silica particles at pH 8 implies that there is a polymer layer of thickness = 1 nm separating the particles. This interparticle distance increases to 26 nm below pH 4. The increase can be attributed to the change in the sign of the surface charge near the isoelectric point (pH 4– pH 3) of silica. Thus, close to pH 3 silica particles will bear positive surface charge. We anticipate that the polyethylenimine which encapsulates these silica particles will have protonated amine groups at this low pH (pKa= 7.11).[29] Thus, the PEI will also be positively charged. We believe that repulsive interactions between the polymer chains and the particle surface cause the inter-particle distance to rapidly increase above pH 4. Expansion at the particle level can lead to an overall expansion of the scaffold. Similar observation has been reported in the case of clay clusters where the presence of cations between negatively charged stacked clay platelets shield repulsive forces between the platelets.[30] It was observed that the

larger the cation concentration smaller is the distance between the platelets and at a macroscopic scale, smaller is the volume of the clay.

The mechanical properties of the ice templated sponges also change when pH reduced below the particle isoelectric point (between pH 3–4 for silica and between pH 8 for hematite). Below the particle IEP, a discontinuous decrease in sponge mechanical stiffness with pH is observed. Ice templated sponges are soft. Therefore, their mechanical response is attributed largely to the crosslinked polymer. However, we note that pure polymeric sponges do not show any variation in mechanical properties with change in pH. Therefore, we conclude that the scaffold response is a consequence of its composite structure. Therefore, for ice templated scaffolds prepared using silica or hematite particles, there is a qualitative similarity in the pH dependence of the mechanical response near the isoelectric point. Thus, it appears that the mechanical response for these scaffolds is largely determined by the attraction between polymer and particle surface.

Above the particle IEP, the polymer is strongly anchored on the particle surface. We presume that, this leads to a large number of polymer –particle contacts. When the pH decreases below the particle isoelectric point, there can be a decrease in the number of polymer-particle contacts due to electrostatic repulsion between the particle surface and polymer. This can lead to the reduction in scaffold stiffness. In addition, a marked decrease in dissipation factor was observed below the particle IEP. This reduction in hysteresis or dissipation factor below IEP could be due to reduction in physical contacts between similar charged components in the scaffold. We note that variations in the structure and mechanical properties of the scaffolds are reversible with change in pH. This suggests that the polymer can physically adsorb or desorb from particle surface in response to the pH and that this structural change determines its mechanical properties.

6.4 Summary

We have studied the effect of electrostatic interactions between polymer and particles on the structure and mechanical properties of ice templated polymer particle composites. We prepared macroporous composites by ice templating and obtained scaffolds with pore walls composed of particles embedded in a crosslinked polymer mesh. We prepare hybrids using silica particles of two different sizes (approximately spherical, ~22 nm and ~1 micron) and irregularly shaped, approximately isotropic clusters of hematite particles. These particles were negatively charged at the pH where ice templating is performed. The cationic polymer used, PEI, adsorbs on the particle surface during scaffold preparation. After scaffold

preparation, we varied the surface charge of particles in the composites by exposing them to varying pH. Composites prepared from 22 nm silica nanoparticles showed an abrupt increase in interparticle distance when the pH was decreased below the particles's isoelectric point. This increase in interparticle distance correlates with a decrease inYoung's and shear moduli, compressive strength and energy dissipation of the composites. At all pH conditions, composites were elastic and recovered fully from compressive strains. The pH dependent mechanical response of the hybrid scaffolds containing silica was independent of the particle size over a range of 22 nm to 1 micron. Since pure polymer sponges do not demonstrate any pH dependence to their mechanical properties, we believe that the variations in the structure and mechanical properties of the composite with pH arise from the polymer – particle hybrid network structure. Thus, the role of the interfacial interaction between the polymer and particle surface is critical. We observe that scaffolds prepared using hematite particles show qualitatively similar behaviour with change in pH. As pH is decreased to below the isoelectric point (= 8 for hematite), the scaffolds expand in size and show an abrupt decrease in Young's and shear moduli, compressive strength and macroscopic energy dissipation. We presume that, when the pH is reduced below the particle's isoelectric point, the interaction between particle and polymer can change from attraction to repulsion. This can be the reason for an increase in interparticle distance in Ludox silica scaffolds when pH goes below silica's isoelectric point. We hypothesize that the repulsion between polymer and particle can reduce the interfacial contact points between particle and polymer and it can lead to the reduction in mechanical stiffness.

6.5 References

1. Waga, S.; Hannon, G. J.; Beach, D.; Stillman, B., The p21 inhibitor of cyclin-dependent kinases controls DNA replication by interaction with PCNA. *Nature* **1994,** 369, 574.

2. Feng, J. Q., Electrostatic interaction between two charged dielectric spheres in contact. *Phy. Rev. E* **2000,** 62, 2891.

3. Trump, J. G.; Van de Graaff, R. J., A compact pressure-insulated electrostatic x-ray generator. *Phy. Rev.* **1939,** 55, 1160.

4. Hull, J. R., Superconducting bearings. *Supercond. Sci. Technol.* **2000,** 13, R1-R15.

5. Eisenberg, S. R.; Grodzinsky, A. J., Swelling of articular cartilage and other connective tissues: Electromechanochemical forces. *J. Orthop. Res.* **1985,** 3, 148-159.

6. Lee, H. W.; Kim, K. C.; Lee, J., Review of maglev train technologies. *IEEE Trans. Magn.* **2006,** 42, 1917-1925.

7. Sharma, R. C.; Dhingra, M.; Pathak, R. K.; Kumar, M., Magnetically levitated vehicles: Suspension, propulsion and guidance. *Int. J. Eng. Res. Tech.* **2014,** 3, 5-8.

8. Balazs, A. C.; Emrick, T.; Russell, T. P., Nanoparticle polymer composites: Where two small worlds meet. *Science* **2006,** 314, 1107-1110.

9. Boluk, M. Y.; Schreiber, H. P., Interfacial interactions and the properties of filled polymers: I. Dynamic-mechanical responses. *Polym. Compos.* **1986,** 7, 295-301.

10. Termonia, Y., Monte-Carlo modeling of dense polymer melts near nanoparticles. *Polymer* **2009,** 50, 1062-1066.

11. Gao, Y.; Liu, J.; Zhang, L.; Cao, D., Existence of a Glassy Layer in the Polymer-Nanosheet Interface: Evidence from Molecular Dynamics. *Macromol. Theory Simul.* **2014,** 23, 36-48.

12. Hsu, H. P.; Binder, K., Effect of chain stiffness on the adsorption transition of polymers. *Macromolecules* **2013,** 46, 2496-2515.

13. Baumgaertner, A.; Muthukumar, M., Effects of surface roughness on adsorbed polymers. *J. Chem. Phys.* **1991,** 94, 4062-4070.

14. Feng, J.; Venna, S. R.; Hopkinson, D. P., Interactions at the interface of polymer matrix-filler particle composites. *Polymer* **2016,** 103, 189-195.

15. Choudalakis, G.; Gotsis, A. D., Free volume and mass transport in polymer nanocomposites. *Curr. Opin. Colloid Interface Sci.* **2012,** 17, 132-140.

16. Schmidt, G.; Malwitz, M. M., Properties of polymer-nanoparticle composites. *Curr. Opin. Colloid Interface Sci.* **2003,** 8, 103-108.

17. Fu, S. Y.; Feng, X. Q.; Lauke, B.; Mai, Y. W., Effects of particle size, particle/matrix interface adhesion and particle loading on mechanical properties of particulate-polymer composites. *Compos. Part B- Eng.* **2008,** 39, 933-961.

18. Scott, J. E., Elasticity in extracellular matrix 'shape modules' of tendon, cartilage, etc. A sliding proteoglycan-filament model. *J. Physiol.* **2003,** 553, 335-343.

19. Dean, D.; Han, L.; Grodzinsky, A. J.; Ortiz, C., Compressive nanomechanics of opposing aggrecan macromolecules. *J. Biomech.* **2006,** 39, 2555-2565.

20. Brown, D.; Marcadon, V.; Mele, P.; Alberola, N. D., Effect of filler particle size on the properties of model nanocomposites. *Macromolecules* **2008,** 41, 1499-1511.

21. Rittigstein, P.; Torkelson, J. M., Polymer-nanoparticle interfacial interactions in polymer nanocomposites: Confinement effects on glass transition temperature and suppression of physical aging. *J. Polym. Sci. B Polym. Phys.* **2006,** 44, 2935-2943.

22. Starr, F. W.; Schroder, T. B.; Glotzer, S. C., Molecular dynamics simulation of a polymer melt with a nanoscopic particle. *Macromolecules* **2002,** 35, 4481-4492.

23. Srivastava, S.; Nykypanchuk, D.; Fukuto, M.; Gang, O., Tunable nanoparticle arrays at charged interfaces. *ACS Nano* **2014,** 8, 9857-9866.

24. Rajamanickam, R.; Kumari, S.; Kumar, D.; Ghosh, S.; Kim, J. C.; Tae, G.; Sen Gupta, S.; Kumaraswamy, G., Soft colloidal scaffolds capable of elastic recovery after large compressive strains. *Chem. Mater.* **2014,** 26, 5161-5168.

25. Ocana, M.; Morales, M. P.; Serna, C. J., Homogeneous precipitation of uniform a-Fe_2O_3 particles from iron salts solutions in the presence of urea. *J. Colloid Interface Sci.* **1999,** 212, 317-323.

26. Hunter, R. J., *Zeta potential in colloid science: Principles and applications*. Academic press: **2013**; Vol. 2, New York.

27. Dugyala, V. R.; Basavaraj, M. G., Control over coffee-ring formation in evaporating liquid drops containing ellipsoids. *Langmuir* **2014,** 30, 8680-8686.

28. Kumari, S.; Kulkarni, A.; Kumaraswamy, G.; Sen Gupta, S., Large Centimeter-Sized Macroporous Ferritin Gels as Versatile Nanoreactors. *Chem. Mater.* **2013,** 25, 4813-4819.

29. Mady, M.; Mohammed, W.; El-Guendy, N. M.; Elsayed, A., Effect of polymer molecular weight on the DNA/PEI polyplexes properties. *Rom. J. Biophys.* **2011,** 21, 151-165.

30. Gajo, A.; Maines, M., Mechanical effects of aqueous solutions of inorganic acids and bases on a natural active clay. *Geotechnique* **2007,** 57, 687-699.

Chapter 7

Summary

This thesis is focused on the structure and properties of ice templated macroporous particle-polymer hybrid assemblies. These hybrid assemblies are formed by isotropic freezing of aqueous dispersions containing particles, polymer and crosslinker. Crosslinking of the polymer is effected in the frozen state. After crosslinking is complete, the sample is thawed to obtain a self-standing monolith with a macropore structure determined by the ice crystal templates. This monolith is primarily comprised of particles (over 80% by weight); however, it can recover from multiple cycles of large compressive strains (>80%). Remarkably, this elasticity is independent of chemistry of the particles and polymer, particle size, polymer molecular weight and crosslinking chemistry. In this thesis, we investigate the origin of this unusual elasticity of particle filled hybrid systems. We have explored the effect of the ice crystal templates on the polymer crosslinking reaction. We prepare an analogous material with the same chemistry of the ice templated hybrids, by lyophilizing the samples after ice templating, but before polymer crosslinking. These two materials, viz., crosslinked in presence and absence of ice crystals, were further characterized from macroscopic to nano-scale using various experimental techniques which include scanning electron microscopy (SEM, morphology), small angle X-ray scattering (SAXS, structure), solid state nuclear magnetic resonance (NMR), bulk and micro rheology, single particle tracking (local mechanical properties) and atomic force microscopy (AFM, nanomechanics). We have also studied the effect of polymer-particle interaction on the mechanical properties of ice templated hybrids. Here, we varied the surface charge of particles by dipping the sponges in different pH buffer solutions. The major observations from our studies are:

- To understand the role of ice crystals during hybrid crosslinking and its effect on elasticity of hybrid assemblies, we have crosslinked the hybrids in presence of ice and compared with hybrids crosslinked in the absence of ice crystals. Monoliths were prepared by ice templating an aqueous dispersion of particles, polymer and crosslinker, followed by polymer crosslinking in presence of ice crystals or after the removal of ice by lyophilization. Hybrids crosslinked in presence and absence of ice crystals exhibited identical structure and same bulk crosslinking density. Both materials exhibited macroporous morphology with pore size ranging from 30- 120 μm. The pore walls of both scaffolds were composed mainly of particles connected together through a thin crosslinked polymer mesh. Interestingly, we found that the macroporous monoliths prepared by ice-templating exhibit qualitatively different

mechanical response to large compression depending on whether the polymer was crosslinked in the presence of ice or after the ice was lyophilized. Scaffolds crosslinked in presence of ice crystals were elastic and could recover from large compressive deformations (~80% strain). However, samples crosslinked after lyophilization showed plastic failure even at very small compressive strains (~5% strain). To understand why crosslinking in presence of ice gives elastic sponges and crosslinking in absence of ice leads to plastic materials, we have characterized the elastic and plastic scaffolds at various length scales.

- We have characterized the mechanical properties of plastic and elastic scaffolds at microscopic length scale using single particle tracking. Here, we have probed the local environment of elastic sponge and plastic monolith by tracking the thermal fluctuations of probe particles. Particles in these assemblies exhibited slow motion because these are surrounded by other particles. Due to this sluggish motion, particle tracking was sensitive to imaging artifacts such as stage drift. We have demonstrated the use of wavelet transforms to filter the thermal fluctuations and to eliminate imaging artifacts. The use of wavelet transform to eliminate stage drift provided us a dynamical resolution of ~ 2 nm.
- Our single particle tracking study shows that the mean square displacement and van Hove jump distributions of particles in the plastic assemblies are characterized by significantly larger spatial heterogeneity when compared with the elastic sponges. In elastic assemblies, particle diffusivities were peaked around a mean value, whereas in plastic assemblies, there was a wide distribution of diffusivities with no clear peak. Both elastic and plastic assemblies showed a frequency independent solid modulus which was obtained from particle tracking microrheology. Here too, there was a much wider distribution of modulus values for plastic scaffolds as compared to elastic, in contrast to bulk rheological measurements where both assemblies exhibited a similar response. We interpreted the distribution of storage moduli in terms of the spatial distribution of crosslinks in the polymer mesh in the hybrid assemblies. Therefore, our microscopy study showed that the plastic monoliths exhibit weak points at a length scale of 1 μm. These weak junctions are the likely regions that result in failure of the monoliths.
- We have also characterized the elastic and plastic scaffolds at nanometer length scale using atomic force microscopy (AFM). Here, we have directly probed the crosslinked

polymer mesh in the interparticle region. We studied the nanoscale energy dissipation using on-resonance amplitude modulation-AFM and the work of adhesion using off-resonance contact mode AFM. Our AFM measurements (both AM-AFM and work of adhesion) showed a wider spatial variation in the properties of the crosslinked polymer mesh for the plastic monolith relative to the elastic sponge. Therefore, our study showed that the origin of the mechanical response of the monoliths arises from the nature of the polymer mesh that surrounds and links the particles.

- We have studied the microscopic behaviour of elastic and plastic scaffolds under compression. We compressed the samples to various strain values and studied the material response in-situ using X-ray computed micro-tomography and single particle tracking. During compression, elastic sponge did not show any structural change upto 30% strain. At low strains, compression results in densification of the pore walls. Further increase in strain gave a plateau in the stress-strain curve. Beyond 50% strain, the pore walls buckle and we observe a steep increase in stress. Our single particle tracking study showed the effect of compression on particles present in the pore walls. Particle mobility decreased and the local storage moduli increased beyond 30% strain. During the release of stress the particles recovered their initial diffusivity. Our study showed that the crosslinked polymer bridges in elastic sponges allowed the folding of pore walls beyond 30% strain and during release of load these elastic bridges pushed the pore walls back to its initial configuration. However, plastic monoliths showed collapse of pore walls around 30% strain and further increase in strain lead to the densification of collapsed pore walls. Beyond 50% strain, we observed the propagation of large cracks within the pore walls which led to a reduction in pore wall stiffness. Flexible interparticle linkages allow the large deformation of elastic sponges without any failure and also help in recovering from large deformations.
- We studied the effect of organic content on the elastic and plastic properties of scaffolds crosslinked in presence and absence of ice crystals. We had systematically varied the organic to particle (OP) ratio from 0.1 to 1.5 by keeping the total solid concentration fixed. At all OP ratios, we obtained self standing scaffolds and we have studied the structure, dynamics and mechanical properties of these materials. The key findings are: there is a qualitative change

in the structure and mechanical response of ice templated scaffolds at a critical OP ratio of about 0.5 for scaffolds made from Ludox silica particles and 0.4 for scaffolds made from 1μm silica. Below this, there is insufficient crosslinked polymer to form a continuous matrix and the crosslinked polymer exists as a thin shell around the particles forming a mesh that imparts elasticity to the particle scaffolds formed by crosslinking in the presence of ice. As the OP ratio is increased, interparticle voids are filled with the organic phase. Above this critical OP ratio, there is a significant change in the mechanical response of scaffolds crosslinked in presence and absence of ice. There is an abrupt increase in modulus and stress generated on compression of scaffolds crosslinked in the presence of ice. Scaffolds crosslinked in the absence of ice showed a transition from being "plastic" below the critical OP ratio to showing complete recovery from large compressive strains. As the OP ratio is increased, there is initially no change in interparticle spacing below the critical ratio. Particle-particle spacing increases only once the interparticle voids are filled with crosslinked polymer at the critical OP ratio. The change in structure at the critical OP ratio is also reflected in the particle tracking measurements. As the OP ratio is increased above the critical value, we observed a narrowing of the distribution of particle diffusivities. This was dramatic for the scaffolds crosslinked in the absence of ice. We interpreted this in terms of distribution in local crosslink density; there is significant local heterogeneity in the crosslink density for scaffolds crosslinked in the absence of ice that becomes progressively less heterogeneous as the OP ratio is increased above the critical value. Our solid state proton and deuterium NMR study showed that the critical OP ratio is also associated with differences in the structure of water present in the scaffolds below the critical OP ratio. These differences disappear above the critical OP ratio. Specifically, water clusters in scaffolds crosslinked in presence of ice crystals showed less mobility compared to those in scaffolds crosslinked after lyophilisation. We attributed this to the strong association of water clusters in a network structure within the scaffolds for scaffolds crosslinked in the presence of ice. In contrast, water clusters form aggregates that are loosely associated to the scaffolds for scaffolds crosslinked in the absence of ice. We speculate that for OP ratios below the critical value,

polymer chains that are not adsorbed to the particles are dispersed in a swollen state for crosslinking in the presence of ice, but are collapsed when crosslinked in the absence of ice. This results in significantly greater heterogeneity in crosslinking density when crosslinked in the absence of ice, that manifests as plasticity or brittleness of the scaffolds. Once the critical OP ratio is exceeded, the polymer chains fill the interparticle voids and exist as an interpenetrated, overlapped polymer solution. Crosslinking is uniform in this concentrated polymer solution yielding scaffolds that are elastic to large compression, independent of the crosslinking protocol.

- Ice templated hybrids are soft monoliths eventhough they are primarily comprised of inorganic particles. We have investigated the source of the scaffold strength: is this derived purely from the crosslinked polymer mesh or do polymer-particle interactions also contribute to this? We have addressed this concern by studying the effect of interaction between polymer and particle on mechanical properties of scaffolds. We tune the surface charge of particles embedded in a macroscopic monolith by immersing the composites in water maintained at different pH. We observed a sudden increase in interparticle distance and subsequent swelling of composite when the pH goes below the particle's isoelectric point. Correspondingly, we observed a reduction in Young's and shear moduli, compression strength and macroscopic energy dissipation. We did not see any pH dependent changes in pure polymer sponges, suggesting that the pH-dependence of structural and mechanical properties of the hybrid sponges arise from their composite structure. Therefore, this study showed that the mechanical stiffness of ice templated composite is strongly influenced by interactions between the polymer and particle surface.

List of Research Credentials, Awards and Conferences

Publications

1. **Suresh, K**.; Patil, S.; Rajamohanan, P. R.; Kumaraswamy, G. The Template Determines Whether Chemically Identical Nanoparticle Scaffolds Show Elastic Recovery or Plastic Failure. ***Langmuir*** 2016, 32, 11623−11630.

2. **Suresh, K**.; Sharma, D. K.; Chulliyil, R.; Sarode, K. D.; Kumar, V. R.; Chowdhury, A.; Kumaraswamy, G., Single-Particle Tracking To Probe the Local Environment in Ice-Templated Crosslinked Colloidal Assemblies. ***Langmuir*** 2018, 34, 4603-4613.

3. **Suresh, K**.; Kumaraswamy, G., et al., Compression-Induced Deformation and Failure of Ice-Templated Inorganic- Organic Hybrid Structures (Manuscript is ready).

4. **Suresh, K**.; Kumaraswamy, G., et al., Elastic and Plastic Scaffolds: The Role of Organic Content (Manuscript is ready).

5. **Suresh, K**.; Kumaraswamy, G., et al., Effect of Electrostatic Interaction on Structure and Mechanical Properties of Ice Templated Particle- Polymer Composite (Manuscript is ready).

Awards

1. Best oral presentation award in NCL RF Annual Student Conference at NCL, 2018
2. Best poster presentation award in Compflu 2017 held at IIT Madras, December 2017.
3. Best poster presentation award in National Science Day celebration at CSIR NCL, 2017.

4. Best poster presentation award in National Science Day celebration at CSIR NCL, 2016.

5. Qualified the Graduate Aptitude Test in Engineering (GATE) in Engineering Science, June 2012.

Conferences, Talks and Poster presentations

1. **S. Karthika,** P. R. Rajamohanan, Shivprasad Patil and Guruswamy Kumaraswamy, "Springy or Crumbly: Depends on crosslinking protocol when we make porous colloid/polymer hybrids", Talk- APS MARCH MEETING 2018, LA, USA

2. **S. Karthika**, Arindam Chowdhury and Guruswamy Kumaraswamy, "Probing the local dynamics in three dimensional colloid- polymer assemblies using single particle tracking", Poster-APS MARCH MEETING 2018, LA, USA

3. **S.Karthika**, "Origin of elasticity in ice templated colloid-polymer hybrids", Talk-Mumbai-Pune Soft Matter Meeting 2018, IIT Mumbai, India

4. **S.Karthika**, "Springy or Crumbly: Depends on how we crosslink colloid-polymer composites", Talk- Macro-Meet, Departmental Seminar, July 2017, CSIR-NCL-India

5. Poster Presentations in CompFlu 2015 , 2016 and 2017

6. Poster Presentations in 2016 and 2017 National Science day celebrations at CSIR-NCL.

7. Attended "SERB school on Rheology of Complex fluids: Advanced computational Methods & Symposium on Rheology of Complex Fluids-2013", organised by IIT Delhi, India, December 2013.